Multi-wavelength Data Analysis and Theoretical Modeling of Blazar Flares

RAJ PRINCE

Under the supervision of

Dr. Nayantara Gupta

Department of Astronomy and Astrophysics
Raman Research Institute,
Bangalore-560 080, India

A thesis
submitted for the degree of

Doctor of Philosophy

to

Jawaharlal Nehru University,

New Delhi - 110067, India

July, 2019

To

My Family and Friends . . .

Declaration

I, Raj Prince, hereby declare that the matter contained in this thesis entitled "Multi-wavelength data analysis and theoretical modeling of blazar flares" is the result of my research work carried out by me at the Raman Research Institute, Bangalore, under the supervision of Dr. Nayantara Gupta. I further declare that the work presented here has not been submitted for the award of any other degree, diploma, membership, associateship, fellowship, etc. of any other university or Institute. I have also run the thesis through the *Turnitin* software.

Dr. Nayantara Gupta
Thesis Supervisor

Raj Prince

Raman Research Institute,
Bangalore – 560 080
INDIA.

Acknowledgements

I want to express my sincerest gratitude to my Ph.D. supervisor, Dr. Nayantara Gupta. She has always inspired me to grow as an independent research scholar during my entire Ph.D. by allowing me to pursue an independent research problem. A special thanks to Dr. Pratik Majumdar from Saha Institute of Nuclear Physics with whom I started the gamma-ray Astronomy.

I would also like to thank the director of RRI and the staff members of Administration, Library, and computer center for providing me all kind of support to continue my research. I would thank Vidya and Harini for helping me to deal with all official and academic works. I thank all members of my doctoral committee for their inputs during various stages of my research.

I thank all my seniors: Nazma, Lijo, Gayathri, Mayuri, Priyanka, Karam, Saurabh, Pragati, Aru, Deepak, Janakee, and many more who were always helpful in my early days of Ph.D. I also thank all my juniors: Sanhita, Aditi, Chaitanya, Saikat, Ranita, Akash, for creating a friendly environment around. I thank Manami, Gunjan, and Ashwin for creating a cheerful environment on Astrofloor.

I thanks all my hostel mates, especially Nancy, Palak, Anand, Chandu, Akash, Varun, Nomaan, Amrita for creating a homely environment in the hostel. Together we have done lots of party/dance that I will miss. Sunday cooking and night walk with them will always be remembered.

I thanks my batch mate: Tiwari, Sagar, Surya from RRI, with whom early days of Ph.D.

was delightful and Siddhartha, Avinash, Akanksha, Shina and Sandeep from IISc for lots of jokes and fun that we have done together.

I will miss my running group Varun and Nomaan, and together we have run a lot of long-distance runs.

I thank to Manashi, Gayathri C., Manami, Gunjan, and Ashwin for thesis proof reading.

A special thanks to Simran for her constant encouragement and support.

I wish to express my gratitude to my family for their constant love and support throughout my life.

Abstract

This thesis is aimed to study the strong and spectacular flares of blazar. Blazars belong to a class of active galactic nuclei (AGN) with one of the jets pointing towards the observer. Blazars are observed in all wavelengths and show chaotic flux variability during flaring states. The spectral energy distribution of blazar is characterized by two hump kind of structures. The first one peaks in low energy band (IR to soft X-ray), which is well explained by synchrotron mechanism caused by the relativistic electrons in the magnetic field of the jets. The second one peaks in the high energy band (hard X-ray to gamma-ray), which is thought to be the product of inverse Compton scattering of low energy photons with relativistic electrons within the jets or from outside the jets.

Here, we study the light curves and spectral energy distributions of four blazars with multi-wavelength data.

Long term study of the light curve of PKS 1510-089 in GeV energies

A study of the long-term gamma-ray light curve of blazar PKS 1510-089 is done for the period of 2008-2016 with *F*ermi-LAT data. Five major flares have been identified within this period. The fastest variability time is found to be 1.30 ± 0.18 hr. This result suggests the size of the gamma-ray emitting region could be as small as 4.85 ± 10^{15} cm. The gamma-ray spectral analysis is performed for all the flaring states and it is found that in most of the flares the log-parabola (LP) distribution gives the best fit to the gamma-ray spectrum. The gamma-ray spectra of the flares can also be fitted with power law with exponential cut-off

(PLEC). In this case the cut-off energies are different for different flares which could be due to different emission regions in the jet of the blazar.

Multi-zone emission modeling of flares of PKS 1510-089

The 2015 gamma-ray flare of PKS 1510-089 is selected as it was observed by MAGIC and HESS along with *Fermi*-LAT. The simultaneous data from Swift-XRT/UVOT telescope was collected and analyzed it for the X-ray and UV/optical spectrum. The variability times found in various energy bands are different which suggests the possibility of multiple emission regions. The gamma-ray and optical/UV variability is found to be in the range of 10 hr to 1 day which suggests their possible co-spatial origin. However, the variability time estimated in X-ray is found to be 2.5 days which is longer than the gamma-ray and optical variability times. This suggests that the X-ray emission is coming from a different region. We have performed the multiwavelength spectral energy distribution (SED) modeling of this flare by considering two emission zones: one zone for gamma-ray and optical/UV emission and another for X-ray emission. The modeling shows two emission zones can be used to explain the multiwavelength emission. The different variability times also constrain the location of the emission regions. In this case, it is found that the gamma-ray and optical/UV emission region is located at the boundary of the Broad Line Region (BLR), whereas the X-ray emission region is further away along the jet in the Dusty Torus (DT) region.

Fermi-LAT observations of the brightest gamma-ray flare ever detected from CTA 102

During the period September, 2016 to March 2017, CTA 102 went in to a long flaring state. The brightest flare was detected from this source with gamma-ray flux of $(30.12\pm4.48)\times10^{-6}$ ph cm^{-2} s^{-1}. The multiwavelength temporal and spectral analysis is done in this thesis to understand this flare. The fractional variability amplitude is estimated to distinguish the different states of the source. It is found that during the flare the source is more variable

compared to the quiescent or pre-flare state. A 73 GeV photon was observed with probability of 99.99% of being from CTA 102. The broadband spectral energy distribution is modeled with the publicly available time dependent code GAMERA. A single-zone emission model is used to model the broadband SED and it is found that a high ($\sim$ 70 times) jet power in electrons is needed during the flare compared to the pre-flare. The increase in jet of power in electrons could be due to enhanced accretion rate of the supermassive black hole of the blazar.

Multi-frequency variability study of Ton 599 during high activity of 2017 and 3C 279 during 2017-2018

A multi-frequency variability study is done for Ton 599 during the flare of 2017. The fractional variability is estimated for all the wavebands. An increase in the fractional variability is noticed with increase in energy of photons which suggests large number of particles are producing the high-energy emission. The correlation study between different wavebands suggests the co-spatial origin of gamma-ray, optical/UV, and X-ray emission. However, the time lag of 27 days found between gamma-ray and radio emission suggests that their emission region are separated by a distance of $\sim$5pc. This also implies that the radio emitting zone is possibly located far away from the AGN central engine.

A broadband spectral study is done for 3C 279 for the period of November, 2017–July, 2018. Three bright gamma-ray flares are identified with a prolonged quiescent state prior to them. The fractional variability reveals that the source is more than 100% variable in gamma-ray followed by X-ray, optical/UV, and radio band. A strong and significant correlation is observed between gamma-ray and optical/UV wavelengths with zero time lag, which suggests their co-spatial origin. For the first time in the history of 3C 279, a significant correlation with zero time lag is noted between gamma-ray and X-ray emission. A single zone emission model is found to be adequate to model its broadband SED during the flare of November,

2017–July, 2018.

The above studies show that some flares could be from single zone and some from multiple zones. Some of the blazars may show similar characteristic features and some could be different.

List of Publications

1. ⋆"Long-term study of the light curve of PKS 1510-089 in GeV energies",
   Raj Prince, Pratik Majumdar, & Nayantara Gupta, 2017, ApJ, 844, 62

2. †"*Fermi*-Large Area Telescope observations of the brightest gamma-ray flare ever detected from CTA 102",
   Raj Prince, Gayathri Raman, Joachim Hahn, Nayantara Gupta, Pratik Majumdar, 2018, ApJ, 866, 16

3. ‡"Multi-frequency variability study of Ton 599 during high activity of 2017",
   Raj Prince, 2019, ApJ, 871, 101

4. ⋆"Two-zone emission modeling of PKS 1510-089 during the high state of 2015",
   Raj Prince, Nayantara Gupta, Krzysztof Nalewajko, 2019, ApJ, 883, 137

5. ‡"Broadband variability and correlation study of 3C 279 during flare of 2017-2018",
   Raj Prince, 2020, Accepted for Publication in ApJ, arXiv:2001.04493

   ⋆Chapter 3

   †Chapter 4

   ‡Chapter 5

Certificate

This is to certify that the thesis entitled **"Multi-wavelength data analysis and theoretical modeling of blazar flares"** submitted by Mr. Raj Prince for the award of the degree of Doctor of Philosophy to the Jawaharlal Nehru University, is his original work done under my supervision and guidance, at the Raman Research Institute. This thesis has not been submitted or published for any other degree or qualification to any other university or institute.

Prof. Ravi Subrahmanyan
Director

Dr. Nayantara Gupta
Thesis Supervisor

Raman Research Institute,
Bangalore – 560 080
INDIA.

Table of contents

List of figures

List of tables

Chapter 1

Introduction

Active galactic nuclei (AGN) are believed to have a supermassive black hole (SMBH) at the center, which accretes the matter surrounded by it and form an accretion disk. It also releases the energy in the form of relativistic jets perpendicular to the disk plane. AGN are observed as most luminous astrophysical objects after GRB in our universe, and it can outshine the whole (host) galaxy with luminosity range of 10^{44} to 10^{47} erg/s. That's the reason to believe that luminosity is not from any star. AGN are observed in all wavebands ranging from radio to gamma-rays and a galaxy hosting an AGN is known as an "active galaxy". The mass of the SMBH in AGN ranging from 10^6 – 10^9 $M_\odot$, is powerful enough to attract the matter from its surroundings. The central part (SMBH+disk+base of the jets) of the AGN is assumed to be surrounded by optically thick molecular gas cloud also called molecular torus or dusty torus. Different parts of the AGN emit radiations in different wavelength through various processes, and as a whole, the emission covers the entire electromagnetic spectrum. So, to get a detailed understanding of accretion physics and particle acceleration in the jets of an AGN, a multi-wavelength approach is essential.

1.1 Historical background

The history of AGN is not very old; it started a century ago with the detection of spectroscopic emission lines from the NGC 1068 by Edward A. Fath (1909) . The jets in AGN were first seen in M87 by Herber D. Curtis (1918), where he describes the jets in the following way "A curious straight ray lies in the gap in the nebulosity in p.a. 20deg, apparently connected with the nucleus by a thin line of matter. The ray is bright at its inner end which is 11″ from the nucleus". In 1943, Carl Seyfert studied several sources like NGC 1068, NGC 4151, NGC 3516, NGC 7469, NGC 1275, and NGC 4051, where he observed the broad emission lines and suggested the presence of a bright nucleus. All these galaxies were then recognized as Seyfert galaxies, after him (Seyfert 1943).

Radio astronomy played an essential role in understanding the AGN. It began in the 1930s when Jansky observed radio emissions from outside the solar system. The earliest detected radio sources are Messier 87 and Centaurus A and in 1954, Baade and Minkowski (1954) observed another radio source called Cygnus A. In 1959, radio astronomy group at University of Cambridge published a catalog called "Third Cambridge Catalogue (3C) of Radio Sources", which includes several new radio sources as well as few radio sources with their optical counterpart. 3C 273 is one of the radio sources in 3C Catalogue whose accurate position was obtained using lunar occultation in 1962 and consequently its optical counterpart was identified.

Some of these sources in optical imaging appear like a star, but their optical spectrum also show a strong emission line which makes these sources different from a star. The star-like appearance of these sources makes us to call them quasi-stellar radio sources (QSR), which later came to be known as quasars. Maarten Schmidt (1963) published the breakthrough result in 1963, where he estimated the redshift of the quasar 3C 273 by studying its optical spectra. After this discovery, optical spectra of quasars have been used as a tool to determine the redshift of the quasars. As the time passed more and more quasars were observed

in radio and optical, and it was noted that some of the quasars lacked strong radio emissions, which implied that not all the quasars were powerful radio emitters. The quasars are divided in radio-loud and radio-quiet quasars, based on their radio emission. The contribution of radio-loud and radio-quiet quasars in the total known population of quasars are $\sim$15% and $\sim$85% (Kellermann et al. 1989) respectively.

X-ray astronomy started during 1960s and 1970s, and it was found that quasars are also a powerful source of X-ray emissions (Byram et al. 1966; Bradt et al. 1967). It is believed that the X-ray emission in quasars comes from the inner part of the disk, surrounding the black hole. The gamma-ray has also been observed in many of AGNs where one of the jets is tilted towards the observer (Thompson et al. 1993). In general, the multi-wavelength emission from AGN is dominated by non-thermal processes like synchrotron and inverse-Compton mechanism.

1.2 Physical picture of AGN

Detection of AGN in different wavelengths across the entire electromagnetic spectrum paints a broader picture of AGN. In the last 30 years all possible electromagnetic radiation has been observed, from different parts of the AGN. Combining all the information gathered from different emission part suggest an AGN could be a combination of a SMBH, jets, accretion disk, dusty torus, etc (Padovani et al. 2017; Blandford et al. 2019).

The presence of SMBH at the center of galaxy Messier 87 is confirmed by event horizon telescope (EHT Collaboration et al. 2019) which completes the physical picture of AGN. Before this discovery, the presence of a SMBH at the center of AGN was indirectly known from the galaxy rotation curve and movement of individual stars in the central region of the galaxies. Gleaning from the data collected for the last 30 years, it can be said that: AGN have a SMBH at the center, which accretes matter from its surrounding, by its strong gravitational pull. Through the accretion disk, the surrounding matter moves inwards towards

the black hole and loses its angular momentum through viscous or turbulent processes. In this process of formation of the accretion disk, the matter gets compressed and heated, and as a result, disk emits thermal radiation in the ultraviolet (UV) and X-ray wavebands. The photons emitted from the disk also affects the matter in the immediate vicinity of the central engine, and as a result, different wavebands emissions are produced, which covers almost the entire electromagnetic spectrum. From different observations of the AGN, the mass of the SMBH is considered in the range of 10^6-10^9 $M_\odot$ (Salpeter 1964; Shakura and Sunyaev 1973).

1.2.1 Accretion Disk

From the AGN perspective, the accretion disk is formed by cold and diffused matter moving around the central SMBH and the huge luminosity observed from AGN is believed to be dominated by accretion of matter into the SMBH. Different models have been proposed in the past to describe the accretion process in terms of low and high accretion rates. Currently, a well-accepted model is proposed by Shakura and Sunyaev (1973), which describes the accretion disk as a geometrically thin and optically thick structure and which also suggests the quasi-Keplerian motion of materials around the SMBH. The disk emission is believed to be purely thermal and the spectrum peaks in optical-UV energy range. The accretion disk photons can be scattered by hot material present just above the accretion disk called corona, through inverse-Compton (IC) process up to X-ray energies.

1.2.2 Broad Line Region

Broad line region (BLR) is typically at a distance of 0.1–1 pc away from the central SMBH, which is believed to be the source of broad emission lines, at optical and UV wavelengths, observed in AGN spectra. There is no direct evidence of BLR since it is spatially unresolved even in the nearest AGN. It is believed that the BLR is a cold gas cloud and directly exposed

to the intense radiation from the disk and heated to a high temperature. The clouds also move around the jet and due to Doppler broadening broad emission lines are observed. The orbital speed is estimated by measuring the width of emission lines, which is ∼1000–10,000 km/s.

1.2.3 Dusty Torus

A dusty or molecular torus is a warped disk of a mixture of molecular gases and dust located, several parsecs away from the SMBH. It is believed that the fraction of radiation from disk absorbed by torus and re-emitted in infrared (IR) wavebands. The central part (SMHB+disk+BLR) of the AGN gets completely obscured by dusty torus because of its huge size, and as a result, various spectral features are observed in different types of AGN. The shape of the torus is not known though there are different predictions about it. The distribution of clumpy cloud and dust around the nucleus is a well-accepted description of the torus (Nenkova et al. 2002).

1.2.4 Narrow Line Region

Similar to BLR but slow-moving and less dense clouds of ionized plasma are also found further away from the torus, which produces narrow width emission lines. These clouds are called narrow line region (NLR) located at $\sim$ 10 pc–1 kpc from the SMBH. This region lies outside the dominating effect of central SMHB, and as a result, narrow emission lines are observed with line width lesser than the typical BLR line width. The typical NLR velocity width is in the range of $200 < \mathrm{FWHM} < 500$ km s^{-1}.

1.2.5 Relativistic Jets

Relativistic jets are formed along the poles of the accretion disk. They are characterized as a medium of radiation and highly energetic charged particles moving along the jet axis. In

radio-loud AGN, the jets can extend up to hundreds of kpc to several Mpc. Jets in AGN were first confirmed in radio frequency, where it is described as a giant radio structure associated with a central SMBH. Generally, jets are made up of plasma of electron-protons or electron-positron which are moving relativistically (Rees 1966) along the jet axis and this has been confirmed in observations by Jorstad et al. (2001), where they have observed the superluminal motion of plasmas. Jets plow into extragalactic medium and interact with surrounding matter consequently decelerating them, by producing giant structures called lobes. The interaction between jets and its surroundings restrict the jets till Mpc and which defines the size of the jets. The emission produced inside the jets is boosted along the jet axis due to relativistic beaming effect. The mechanism behind launching of the relativistic jets from central part of the AGN is still hotly debated. Two leading theories were proposed in the 70s and 80s by Blandford and Znajek (1977) and Blandford and Payne (1982). According to Blandford and Znajek (1977), jets are launched by accretion disk through the process of electromagnetic extraction of energy and angular momentum from an accretion disk and according to Blandford and Payne (1982) jets are a result of the extraction of rotational energy from the spinning SMBH. So the direction of the jet's ejection can be determined either by the angular momentum axis of the accretion disk or by the spin axis of SMBH. A schematic picture of radio-loud AGN is shown in Figure 1.1.

1.3 AGN Types and Unification Scheme

AGN are observed across the entire accessible electromagnetic spectrum ranging from low energy radio band to high energy gamma-ray band. Based on radio and optical emissions, the AGN are broadly categorized in two different class called radio-loud and radio-quiet AGN. Roughly the $\sim$ 85% of the total amount of AGN are radio-quiet AGN because they have very less or no radio emission and a minority of them ($\sim$ 15%) are called radio-loud AGN because they emit more in radio band and also have large jet structures. This classifica-

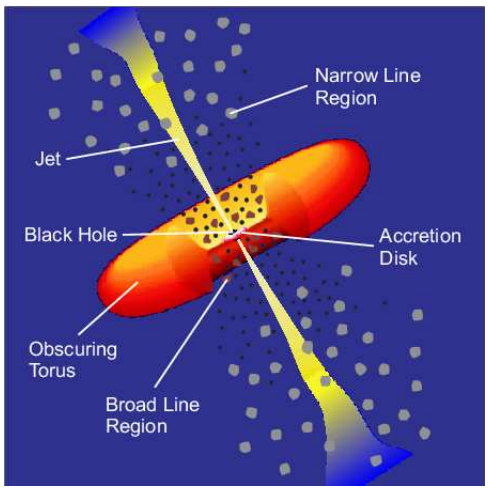

Fig. 1.1 A schematic picture of the radio-loud AGN. The SMBH presented at the center is surrounded by an accretion disk. The broad line region surrounding the disk produces the broad emission lines. BLR and the central part is obscured by a droughnut shaped structure called dusty torus. The narrow emission regions are very far from the central engine (Urry and Padovani 1995)

tion is based on a parameter called *radio-loudness parameter*(R) that is defined as the ratio of radio flux density at 5 GHz and the optical flux density at B-band (Urry and Padovani 1995):

$$R = \frac{f_{5GHz}}{f_B} \tag{1.1}$$

AGN with R $\geq$ 10 are classified as radio-loud AGN and rest with R $\leq$ 10 are classified as radio-quiet AGN (Kellermann et al. 1989). The main difference between these classes is the presence of relativistic jets, the radio emission in radio-loud AGN are dominated by the powerful relativistic jets, which are generally absent in radio-quiet AGN (Miller et al. 1993). According to Pier and Krolik (1992) and Pier and Krolik (1993) gas or dust is distributed in the form of a torus whereas Sanders et al. (1989) suggested the distribution in the form of a wrapped disk around the central region. The emission from AGN is anisotropic because most of the emission is boosted along the jet axis due to the relativistic effect. Therefore, along with the obscuration of the central region by a torus, other phenomena like relativistic

effect and superluminal motion also play an important role in modifying the appearance of an AGN.

1.3.1 Types of AGN

Radio-loud and radio-quiet AGN are further divided into different sub-classes depending on the strength of emission lines present in their optical spectra. One class of AGNs that have narrow emission lines (FWHM $\sim$ 1000 km s^{-1}) are called *type 2* objects and other class in which both narrow and broad emission lines are present called *type 1* objects and the broad emission lines in *type 1* objects can have line widths of up to 10,000 km s^{-1} (Netzer 2015). According to Urry and Padovani (1995), the classification of AGN is done based on the orientation of the jet axis with respect to the line of sight. If the AGN are viewed at a smaller angle from the polar axis of the accretion disk ($\theta_v \leq 60$ degree), both the BLR and NLR are visible and AGN appears as *Seyfert 1* galaxy in case of radio-quiet AGN and broad line region galaxy (BLRG) in case of radio-loud AGN. In case of large viewing angle (looking edge-on) the BLR region is obscured by dusty torus, and hence only narrow line region is visible, and these AGN appear as *Seyfert 2* galaxy in case of radio-quiet AGN, and in case of radio-loud AGN, it is called a narrow line region galaxy (NLRG). If the jets are oriented in such a way that one of the jets is pointing towards the observer ($\theta_v \leq 5$ degree), due to the relativistic beaming effect, its non-thermal featureless continuum emission will start dominating the entire source spectrum. This type of radio-loud AGN is called blazar. Among the different type of AGN, this thesis focusses on radio-loud AGN of blazar types.

1.3.2 The Unification model

The unified model proposes that different observational classes of AGN are a single type of physical objects observed under different conditions. The currently favored unified models are ‘orientation-based unified models’ implying that the apparent difference between differ-

ent types of AGN arise simply because of their different orientation to the observer.

The presence of obscuring materials in the form of gas and dust around the central part of the AGN were first reported by Rowan-Robinson (1977), stating that the emission from the central region is contaminated by the surrounding materials (gas and dust). Later, Pier and Krolik (1992) and Pier and Krolik (1993) and Sanders et al. (1989) proposed two different views on the distribution of gas and dust around the central region. According to Pier and Krolik (1992) and Pier and Krolik (1993) gas or dust is distributed in the form of a torus whereas Sanders et al. (1989) suggested the distribution in the form of a wrapped disk around the central region. The emission from AGN is anisotropic because most of the emission is boosted along the jet axis due to a relativistic effect. So, along with the obscuration of the central region by a torus, other phenomena like relativistic effect and superluminal motion, also play an important role in modifying the appearance of an AGN. Finally, an AGN can appear different at different viewing angles.

The observed variety of AGNs arises from two degrees of freedom: (1) Dust opacity, which differentiates between Seyfert galaxies of type 1 and type 2; (2) viewing angle of the relativistic jet, which differentiate between *Type 1* AGN and blazars. The unification scheme says that, if the AGN is oriented in a way that an edge-on view is seen, then, BLR will completely be obscured by the torus of gas and dust and this type of AGN is known as *Syefert 2* AGN. If one of the jets of AGN is along the line of sight of the observer, i.e., face-on view, then, both BLR and NLR can be seen without any obstruction and observer can also see the related features of the central engine. The observed property of radio-loud and radio-quiet AGN are characterized by the presence or absence of relativistic jets, respectively. When the line of sight of the observer is along the radio jet axis within the < 5 degree viewing angle, those type of sources are called blazar, and in this case, the relativistic boosting along the jet axis strongly amplifies the observed luminosity of blazar and produces strong variability, polarization, and superluminal motion.

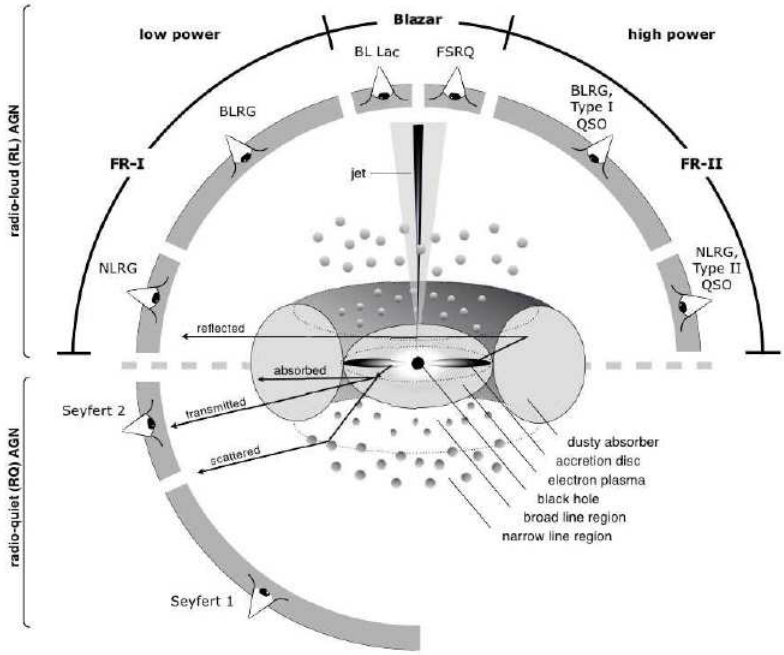

Fig. 1.2 A current representation of AGN unification scheme. The radio-loud and radio-quiet AGN are divided in upper and lower part of the picture (from Beckmann and Shrader 2012.

The current unification scheme is proposed by Urry and Padovani (1995), and according to them, radio-loud and radio-quiet AGN are defined based on different observational properties. The whole picture of classification is shown in Figure 1.2, where the narrow line radio galaxies (NLRGs), broad-line radio galaxies (BLRGs), radio-loud quasars and blazars are categorized as a radio-loud AGNs. According to the model, NLRGs are seen at large angle with respect to the line of sight of the observer, BLRGs, and radio-loud quasars are seen at a modest angle whereas blazars are seen close to the line of sight of the observer. On the other hand, radio-quiet quasars, Seyfert galaxies, and LINERs, etc. are categorized as a radio-quiet AGN.

1.4 Blazar

Blazars are the class of radio-loud AGN exhibiting strong and chaotic variability across the entire electromagnetic spectrum (Heidt and Wagner 1996; Wagner et al. 1996 etc.). The emission from blazars are highly beamed along the jet axis and non-thermal in nature, ranging from low energy radio frequency to high energy gamma-rays. Blazars also produce highly polarized emission in radio and optical wavebands (Fan et al. 1997; Jorstad et al. 2001), and superluminal motion in radio band (Rees 1966; Gubbay et al. 1969). According to the unification model by Urry and Padovani (1995), blazars jets are oriented close to the line of sight of the observer within a few degrees and its observed properties are usually attributed to these large scale relativistic jets.

Blazars are classified in two sub-classes, based on presence or absence of optical emission lines, called Flat Spectrum Radio Quasars (FSRQs) and BL Lac objects. FSRQs generally show broad emission lines in their optical spectrum with equivalent width (EW) > 5 Angstrom whereas the BL Lac objects show either a featureless optical spectrum or very weak emission lines in their optical spectrum. In FSRQs and BL Lac objects, the presence or absence of optical emission lines could be linked to the accretion mechanisms. The optical and UV photons produced by the accretion disk are mostly responsible for the broad emission lines observed in the blazars optical spectrum, and therefore the difference found in the strength of emission lines could be a result of the different accretion process. Efficient accretion process can produce strong, broad emission lines, and on the other hand, weak or no emission lines could be due to inefficient accretion process. It is believed that strong and broad emission lines produced in the blazar optical spectrum originate in broad line region. So, in other words, the presence or absence of BLR can be used to classify the FSRQs and BL Lac objects. Broadly, FSRQs are the source of strong emission lines because they are linked to radiatively efficient accretion process such as Shakura and Sunyaev (1973) disk, whereas BL Lac objects are related to inefficient accretion process like

the advection-dominated accretion flow discussed by Narayan et al. (1998).

Blazar as a source of high energy gamma-ray is known since the EGRET (Energetic Gamma-Ray Experiment Telescope; Thompson et al. 1993) era. The launch of *Fermi* Large Area Telescope (*Fermi*-LAT; Atwood et al. 2009) in 2008 confirms that the extragalactic sky is dominated by high energy gamma-ray mostly from blazars. *Fermi* fourth source catalog (The Fermi-LAT collaboration 2019) has reported more than ∼5000 blazars as a high energy gamma-ray emitters between energy range of 50 MeV–1 TeV. The powerful gamma-ray emissions from blazars is also considered as another characteristic property.

Blazars emit across the entire electromagnetic spectrum ranging from low energy radio frequency to high energy gamma-ray and the total spectral energy distribution (SED) shows two broad hump structures, first one peaking in low energy band ranging from mm to soft X-rays and the second one peaking in high energy band between X-rays to gamma-rays (Fossati et al. 1998; Ghisellini et al. 1997; Giommi et al. 1995), an example is shown in Figure 1.3. Depending upon the exact location of the first peak in SED, BL Lac objects are sub-classified into low energy peaked blazars (LBLs) and high-energy peaked blazars (HBLs) (Padovani and Giommi 1995), and also in intermediate peaked blazars (Sambruna et al. 1996). A detailed study about the blazar was done by Nieppola et al. (2006), and he found that the object with peak frequency $\nu_{peak} = 10^{13-14}$ Hz can be classified as LBLs, peak frequency with $\nu_{peak} = 10^{15-16}$ Hz as intermediate peaked blazar (IBLs), and peak frequency with $\nu_{peak} = 10^{16-17}$ Hz as HBLs. FSRQs in general show the low energy peak at $\nu_{peak} = 10^{14}$ Hz, and the BL Lac objects contain all HBLs and IBLs blazar.

In the past, various models have been proposed to explain the broadband emission in blazars. The low energy peak in SED is well described by synchrotron radiation produced from relativistic electrons moving in the jet magnetic field. On the other hand, the high energy peak in the SED can be produced by two different processes, e.g., leptonic and hadronic processes.

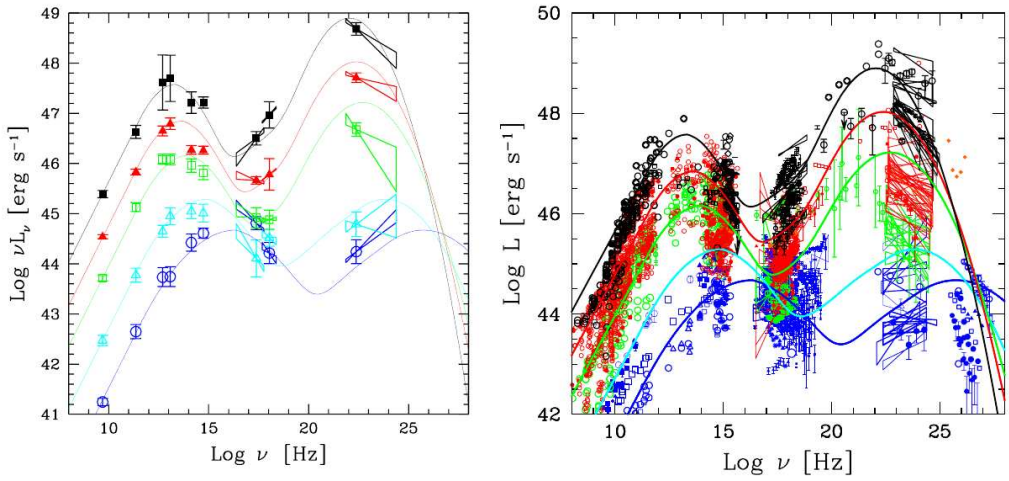

Fig. 1.3 Typical SEDs of blazar and blazar sequence (Fossati et al. 1998; Donato et al. 2001; Ghisellini et al. 2011).

Details about the different processes involved in blazar emissions are discussed in the next section 1.5.1.

1.5 Emission Processes

The broadband spectral energy distribution (SED) of blazars cover the entire electromagnetic spectrum starting from low energy radio emission to high energy gamma-ray emission. One of the reasons behind this wide range of SED is that the blazars emits both thermal and non-thermal radiation. A well-accepted scenario to explain the low energy peak in the SED is attributed to the synchrotron emission. Relativistic electrons produced at the base of the jets travels along the magnetic field lines inside the jets and loses energy in the form of synchrotron radiation. To explain the high energy peak of SED, two different models are proposed, one involving electrons and other involving protons called leptonic and hadronic models. Detail description of different models is presented in the next section [1.5.1 and 1.5.2].

1.5.1 Leptonic Models

According to the leptonic model, the low energy and high energy peak observed in broad-band SED is produced by synchrotron and inverse-Compton (IC) scattering of relativistic electrons present inside the jets. It is believed that a spherical blob of non-thermal electrons produced at the base of the jets moving down-stream (away from the SMBH) in the jet emits both the synchrotron and inverse-Compton radiation.

Synchrotron self-Compton

Synchrotron self-Compton or SSC model says that the relativistic electrons first interact with the jet magnetic fields and produces the synchrotron photons and later these synchrotron photons act as a seed photons for IC emission, where the synchrotron photons get upscattered to high energy photons by the same population of electrons via the IC process (Konigl 1981; Marscher and Gear 1985; Ghisellini and Maraschi 1989). It is a widely accepted and a popular emission model for TeV blazar. This model is mostly used to explain the high-frequency peaked BL Lacs sources.

External Compton

As the name suggests, external Compton (EC) involves the low energy photons from outside the jets. According to the EC model, high energy peak of SED can be explained by the IC scattering of low energy external photons (Begelman et al. 1987; Melia and Konigl 1989; Dermer et al. 1992) with relativistic electrons present inside the jets; while the low energy peak still can be explained by the synchrotron emission. The source of external photons for EC can be from the accretion disk (Dermer and Schlickeiser 1993; Boettcher et al. 1997), from the BLR (Sikora et al. 1994; Ghisellini and Madau 1996), and from the dusty torus (Błażejowski et al. 2000). The EC mechanism is mostly used for FSRQs to explain the high

energy peak.

In general, FSRQs show prominent thermal components, and they can act as a seed photons for the EC process. Thus, the high energy emission in FSRQs is likely to be dominated by an EC mechanism. On the other hand, the lack of thermal radiation in BL Lac objects suggests fewer sources of external photons to be used for IC scattering. Therefore, the high energy emission in BL Lac objects is most likely to be produced by SSC not by EC.

1.5.2 Hadronic Model

In the hadronic model, the jets are assumed to be composed of electrons and protons, and both electrons and protons are accelerated to relativistic energies. Inside the jets, the low energy photons interact with the high energy protons (photo-pion interaction) and produce charged and neutral pions, further the charged pions decay into the charged mesons and charged mesons decay into the electron-positron pairs along with high energy gamma-ray photons (Mannheim 1998; Mücke et al. 2003; Böttcher et al. 2009). The neutral pions produced at the first stage can directly decay into high energy gamma-ray photons and neutrinos. In photo-pion interactions the targets could be synchrotron photons from coaccelerated electrons (Mannheim 1993), inverse Compton emission of electrons, and also photons outside the jet, from BLR or dusty torus region (Protheroe 1997; Bednarek and Protheroe 1999; Atoyan and Dermer 2001). In the hadronic model, to produce sufficient amount of gamma-ray flux, the protons need to accelerate above 10^{18} eV. A large value of magnetic field ($\sim$ 100 G) is required in the emission region to produce the gamma-ray emission from the proton synchrotron process. While the leptonic scenario predicts the correlated variability in X-rays and gamma-rays, the hadronic models predict the production of neutrinos. Detection of neutrinos by IceCube along with multi-wavelength study can confirm hadronic interactions in blazars. The neutrino detected in IceCube was in coincident with a gamma-ray flare from the blazar TXS 0506+056 (IceCube collaboration 2018). This finding certainly

supports the hadronic models which predicts the simultaneous production of high energy gamma-rays and neutrinos.

1.6 Relativistic Effects

In blazar jets, when an emitting region is moving along the line of sight of the observer with a relativistic velocity, a series of relativistic effects happen. If the emission region is moving nearly at the speed of light, and at a small angle with the line of sight of the observer, the time intervals between two successive photons measured in observer's frame reduce , and the emitting region will appear to move faster than its actual velocity (Blandford and Königl 1979). This effect is known as *superluminal motion* and the apparent velocity of the emitting region is given by

$$v_{app} = \frac{\beta c sin\theta_v}{1 - \beta cos\theta_v} \tag{1.2}$$

where θ_v is the angle between the direction of motion of the emitting region and the observer line of sight, $\beta = \upsilon/c$, where υ is the actual velocity of the emitting region, and c is the speed of light in vacuum.

Due to this relativistic effect the radiation will be boosted along the direction of motion into a cone with opening angle $\theta_j \sim 1/\Gamma$, where $\Gamma = (1\text{-}\beta^2)^{-1/2}$, called bulk Lorentz factor. The relativistic beaming will amplify the intensity of radiation along the direction of motion. In special relativity, the relativistic beaming quantified by Doppler factor (δ) can be seen as a function of Lorentz factor (Γ) and viewing angle (θ_v) as given below

$$\delta = \frac{1}{\Gamma(1 - \beta cos\theta_v)} \tag{1.3}$$

Due to the relativistic effect, the observed flux density from a moving emission region will be modified as (e.g., Rybicki and Lightman 1979)

$$f(\nu) = \delta^{3+\alpha} f^{'}(\nu^{'}) \tag{1.4}$$

where the primed quantities are representing the rest frame of the source and α is the photon spectral index. So, it is clear that what is observed is not the same as what is emitted by the source. Hence, the relativistic effect plays a key role in the appearance of AGN and form the backbone of the unification model.

1.7 Variability in AGN

AGN are known for strong and chaotic variability across the entire electromagnetic spectrum (Wagner and Witzel 1995; Ulrich et al. 1997) and the time scale of variability can be as long as years and as short as minutes (Smith 1996). The flux variability in AGN was known from the beginning itself, soon after the discovery of Quasars (Matthews and Sandage 1963; Fitch et al. 1967). The flux variability is more prominent in blazar as the jet is pointing towards the observer. Blazar shows minutes (Aharonian et al. 2007; Shukla et al. 2018) to year (Raiteri et al. 2013) scale of variability across the entire electromagnetic spectrum. However, the short-term variability observed in different blazars is still remain elusive to the AGN community. Many efforts had been made in this direction, but still, there is no clear understanding of the physical process behind this strong flux variability. The variability time is used as a tool to probe the innermost region of the blazar, which is not accessible to any direct imaging techniques. Studying the variability time in a different part of the spectrum can be used to constrain the size of the emission region that is responsible for the particular waveband of the spectrum. The observed variability time (t_{var}) is related to the size of the

emission region (R_s) by the following equation:

$$R_s < \frac{ct_{var}\delta}{1+z} \tag{1.5}$$

where z represent the redshift of the source and δ is the Doppler factor.

1.8 Motivation behind blazar study

Blazars are known to be one of the brightest objects of the extragalactic sky, and their jets are found to be excellent laboratories to study the radiative environment. A significant part of the observed non-thermal emissions from blazars have originated from the jets, and the total emission covers the entire electromagnetic range from radio to high energy gamma-rays. Their extreme flux and spectral variability on multiple time scales over an entire waveband range are not understood very well. However, multiwavelength flux and spectral variability studies have made substantial progress in the direction of understanding the jets. Since blazar emits in all wavelength, so to understand the exact physical mechanism behind its broadband emission and short variability time, a multi-wavelength approach is essential. To accumulate the densely sampled data both in time and energy is one of the most challenging tasks to understand AGN physics.

However, significant progress has been made in the past several years to understand the blazar physics, with several key questions are still unanswered. Some of the unanswered questions are (i) what is the jet composition in blazars, is it composed of electron-proton plasma or electron-positron plasma; (ii) the location and structure of the emission region; (iii) the origin of observed strong flux variability on timescales of minutes to years; (iv) what is the role of external photon fields in gamma-ray production; (v) how the distribution of the particles are responsible for the observed radiation and their acceleration mechanism; and (vi) the role of magnetic fields in origin, confinement, and propagation of relativistic

jets. The main reason behind these mysteries is the lack of good quality of observational data across the entire wavebands. Now, the collection of multiwavelength data sets, from different telescopes or observatories, from low energy radio wave to high energy gamma-rays, is possible. Using good quality of publicly available data, an effort has been made in this thesis to answer some of the above-mentioned questions.

1.9 Thesis goals

This thesis mainly focuses on understanding the physical properties of the gamma-ray flaring blazars. Broadly the studies are divided into two parts: The discussion in the first part is focused on the temporal and spectral study of blazar flares in gamma-ray as well as in X-rays and optical bands. This will help us to constrain the size and location of the emission region and also provide information about the spectral properties. The second part is mostly the modeling of multiwavelength emission, which helps us to understand the physical mechanism behind the broadband emission and fast variability time.

1.10 Thesis Summary

We present a multiwavelength study of four FSRQs blazars on their flaring states across the entire electromagnetic spectrum. The gamma-ray observation has been done with the *Fermi*-LAT between 0.1 – 300 GeV, and X-rays and optical is done by *Swift-XRT/UVOT*, and other multiwavelength data are obtained from various data archives. Using the multiwavelength data from different telescopes and observatories, an attempt is made to understand the broadband SED of blazars.

Following is broadly the chapter section of my thesis:

Chapter 1 gives a brief introduction about the AGN and blazars and also address the challenging problems persisting in the field.

Chapter 2 provides the detailed information about the telescopes and observatories that have been used in this thesis and their data reduction process.

Chapter 3 discusses the historical behavior of the FSRQ PKS 1510-089 and broadband SED.

Chapter 4 explains the brightest gamma-ray flare ever detected from CTA 102.

Chapter 5 discusses the correlation between different wavebands for Ton 599 and 3C 279.

In **Chapter 6**, conclusions are drawn from the work presented in this thesis and future directions are mentioned.

Chapter 2

Multi-Wavelength Observations: Data Reduction and Analysis

The physical property of blazar can be well understood by combining both observational and theoretical tools. Blazars are observed in almost all wavebands from radio to gamma-rays by various space and ground-based telescope that were used to cover the observational aspects of our study presented in this thesis. Radio observations from ground-based radio telescope and optical, UV, X-ray and gamma-ray observations from space based Swift-XRT/UVOT and *Fermi*-LAT telescopes were used to carry out the study of blazars.

The data from Swift-XRT/UVOT and *Fermi*-LAT telescope have been analyzed, and the entire procedure of data reduction and analysis are discussed in this Chapter. Also, fully analyzed optical and IR archival data from Steward and Smarts observatory, radio archival data at 15 GHz and 230 GHz from Owens Valley Radio Observatory (OVRO) and Sub-millimeter Array (SMA) are used.

2.1 Observations and Data Reduction

2.1.1 Fermi Gamma-ray Space Telescope

The *Fermi Gamma-ray Space Telescope* was launched by NASA on a Delta II Heavy launch vehicle on June 11, 2008, into a near earth orbit at an altitude of ∼550 km with an orbital period of ∼96 minutes. Initially, it was named as Gamma-ray Large Area Space Telescope (GLAST), but was renamed to *Fermi*-LAT just after its launch in 2008. The *Fermi Gamma-ray Space Telescope* has on-board two instruments called Large Area Telescope (LAT) and Gamma-ray Bursts Monitor (GBM) to look for the galactic and extragalactic gamma-ray sources. Among these two, the LAT is the primary instrument, and the GBM is the secondary instruments. The primary goal of GBM is to look for the sudden gamma-ray flares produced by Gamma Ray Bursts (GRBs) and solar flares.

Large Area Telescope

LAT is a pair(e^-,e^+) conversion gamma-ray detector and it tracks the electron-positron pairs produced by an incident gamma-ray photon to measure the direction of incident photons. LAT has a CsI(Tl) crystal calorimeter to measure the energies of the incident gamma-ray photons. It has an array of a total of sixteen trackers to construct the direction of incident gamma-ray photons and has a calorimeter to store and measure the energies of incident photons. A thin anti-coincidence detector covers the whole detector for background rejection. A gamma-ray passes through the anti-coincidence detector and interact with the tungsten foils inside the detector and produces the electron-positron pairs. These pairs travel with the silicon strip detectors, which are used for the purpose of tracking, and produces ions at the base of the detector. A cesium iodide calorimeter is present at the base of the detector, which stops the charged particles and measures the total energy deposited (Figure 2.1). The information gathered from the anti-coincidence detector, tracker, and calorimeter are com-

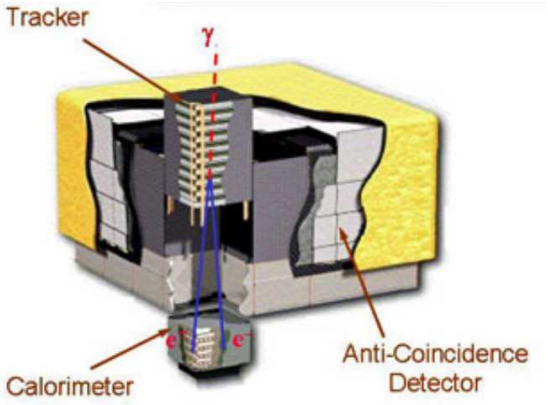

Fig. 2.1 Schematic representation of Large Area Telescope on-board *Fermi*-LAT.

bined together to measure the direction and energy of incident gamma-ray photons. The working energy range of LAT is between 20 MeV to greater than 300 GeV (Atwood et al. 2009). LAT has a field of view (FoV) of ∼2.4 sr and covers about 20% of the sky at any point of time. The *Fermi* operates in sky survey mode and covers the entire sky every 3 hr (orbital period ∼ 96 minutes).

The point spread function (PSF), effective area, and angular resolution of LAT are the function of incident photon's energy, its incidence angle, and the event class. The PSF for an on-axis gamma-ray photon has 68% contaminant radius of about 3 degree at 100 MeV and 0.04 degree at 100 GeV. The observed photon count rate is the product of the effective area and incident photon flux with live-time fraction. So, the systematics on measured flux is mainly governed by the uncertainty in the effective area and also depends on energy. The uncertainty measured in flux is 10% for below 100 MeV, 5% between 316 MeV and 10 GeV, and 10% above 100 GeV. The details about the performance of LAT can be found at Atwood et al. (2009).

LAT data reduction and analysis procedure

The *Fermi*-LAT archival data can be obtained from the webpage of *Fermi Science tools*[1] and the data for a particular period contains the list of photon files and information about satellite in spacecraft (SC) files. The event file contains the list of photons and information about the time of observation. The spacecraft file contains the information about the satellite pointing, direction, and position in orbit in addition to information from the period when the spacecraft passes through the South Atlantic Anomaly (SAA). SAA is seen as a location of charged particle background. To avoid this charged background, the LAT does not collect data when the satellite is passing through SAA. The detailed procedure of analyzing the LAT data is provided on *Fermi Science tools* webpage[2] by *Fermi*-LAT team. The technique used for analyzing the *Fermi* LAT data is based on maximum likelihood optimization technique developed by Mattox et al. (1996). This technique is used for detection, computing flux and obtaining the spectral parameters from the target sources.

To analyze the *Fermi*-LAT data, two types of likelihood analysis techniques are available: "binned" and "unbinned". The unbinned likelihood method is recommended for point sources, and for short time periods where the source count is expected to be small. However, the binned analysis is preferred for long time bins or when the source is close to the very bright background region such as the Galactic plane. Both methods are performed by a set of tasks which are fully compatible with Python and provided with the ScienceTools software.

To perform the *Fermi*-LAT analysis, a circular region was chosen around the source for event reconstruction. This circular region is called the region of interest (ROI), and generally, its size should be larger than the PSF of the LAT. A circular region with a size larger than the ROI was also selected so that it can include more sources while doing the likelihood analysis. This larger circular region with more sources is called the "Source Region". While

[1] https://fermi.gsfc.nasa.gov./ssc/data/analysis/scitools/
[2] https://fermi.gsfc.nasa.gov/ssc/data/analysis/scitools/

studying the point source using unbinned likelihood analysis method, an ROI with a radius of 10 degree and source region with a radius of 15–20 degree is reasonable to use. Further, a model file can be generated which contains the best guess information about the location and spectral forms of all the sources lying within the "Source Region". The source model file can be produced using the "Modeleditor" a GUI-tool, or by running a user-contributed python script[3]. This produces a "model.XML" file which includes all the information about all kind of sources lying within the ROI and the Source Region from the *Fermi* Catalog (e.g., Acero et al. 2015).

A zenith-angle cut of 90 degree is generally applied to remove the contamination from the earth's limb gamma-rays. Time intervals when the satellite was passing through the South Atlantic Anomaly (SAA) were also removed. A Galactic diffuse emission model and isotropic background model provided by the ScienceTools are also used while analyzing the LAT data.

The maximum likelihood test statistic is used to determine the significance of the gamma-ray signal. It is defined as TS = 2 Δ log(L), where L is the likelihood function between models with and without a point source at the position of the source of interest (Paliya 2015). In the likelihood analysis, all the parameters of the sources lying within the ROI are kept free to vary. The parameters of the sources which are lying outside the ROI but inside the Source Region, are fixed to the values given in the catalog. Generally, the sources with TS $<$ 25 (correspond to $\sim 5\sigma$ detection; Mattox et al. 1996) were removed from the model file to perform the further temporal and spectral analysis.

All the steps that have been used in unbinned likelihood analysis to obtain the flux and spectrum from the point gamma-ray sources are presented below.

[3] https://fermi.gsfc.nasa.gov./ssc/data/analysis/user/

1. *gtselect*: The user-specific cuts, such as cuts on the position in the sky, choosing the ROI, selection on energy bin, observation period, and cuts on maximum zenith angle value are all done by this tool.

2. *gtmktime*: This tool is used to generate the Good Time Intervals (GTI) from the total observational period. It also excludes the time where the ROI is outside the FoV by choosing the appropriate zenith angle cut.

3. *gtltcube*: Since the LAT operates in the survey mode, so it makes an angle in the sky with the position of the source. The number of events detected by LAT from a particular region of the sky or a source depends on the amount of time that the source spent at a given inclination angle during an observation. The LAT response function also depends upon the inclination angle between the observed position of the sky (source) and the z-axis of the LAT. The livetime is the time that the LAT observed a given position at a given inclination angle. The task *gtltcube* is used to estimate the livetime cubes.

4. *gtexpmap*: The total exposure to a given source in the sky in the ROI during observations is defined as an exposure map. This is the combination of effective area and time over which source is observed by LAT. The exposure map can be created by task *gtexpmap*.

5. *gtdiffrsp*: This task is used to produce the diffuse source response. It uses the source model file and the event file. The model file must contain all the diffuse sources to be fit. This tool modifies the event data file by adding one extra column for all the diffuse sources present in the ROI. It also uses the instrument response function (IRF).

6. *gtlike*: The likelihood fitting is done by this task "gtlike". It is used to obtain the best fit model parameters between the given input model and the observed data. The input model contains all the information like position and the spectral parameters about the

sources lying within the Source Region. To find the initial values of the parameters, an optimizing algorithm DRMNFB is used and then to get the final results and more accurate set of parameters another optimizing algorithm NEWMINUIT is used.

2.1.2 Neil Gehrels Swift Observatory

Swift is a first-of-its-kind multiwavelength observatory primarily designed to study the gamma-ray bursts (GRBs) (Gehrels et al. 2004). It has three instruments on board to work simultaneously to observe a source in gamma-ray, X-ray, ultraviolet, and optical bands. All three instruments are mentioned below.

1. Burst Alert Telescope (BAT): Its working energy range is 15 – 150 keV
2. X-Ray Telescope (XRT): The working energy range is 0.2 – 10 keV
3. Ultraviolet and Optical Telescope (UVOT): It works in frequency range 170 –650 nm.

Burst Alert Telescope

The BAT is used for sky survey, and it has a large FoV of $\sim$2 sr. The details about the instrument can be found in Barthelmy et al. (2005). Its working principle is based on coded aperture imaging using CdZnTe detector. The working energy range for imaging is 15 – 150 keV while it can extend up to 500 keV for a no-coded response.

X-Ray Telescope

The main goal of XRT is to estimate the fluxes, light curves, and spectra of X-ray sources in the energy range of 0.2 – 10 keV. It uses a grazing incidence Wolter Type I focusing X-ray telescope which focuses the X-rays onto a CCD. The CCD in XRT is located at the focal plane of the X-ray mirrors, has an image area of 600$\times$600 pixels (40$\times$40 microns) and a storage region of 600$\times$600 pixels (39$\times$12 microns). XRT can be used as an instrument

for imaging, window timing (WT), and photon counting (PC) mode. The PC mode is the most sensitive and primary mode of XRT. The time resolution of XRT is only 2.5 sec, but it has full imaging and spectroscopic resolution. The PC mode of observation is preferred when the source has very low flux (below one mCrab), and on the other hand, the WT mode is used for extremely bright sources. More details about the instruments can be found in Burrows et al. (2005).

The XRT data can be found on HEASARC data archive[4] webpage for all kinds of observed sources. The tool *xrtpipeline* is run for each observation to produced the cleaned event files. The latest calibration files (CALDB) and standard screening criteria are used to reprocess the raw data. The source and background region are generally chosen around the source and away from the source of size 25 arcsec. The X-ray spectra are extracted in *xselect*, and the tool *xrtmkarf* is used to produce the ancillary response file. The spectra are loaded in *grppha* for grouping the data. Finally, the grouped spectra are used as an input in *XSPEC* for further spectral fitting.

Ultra Violet and Optical Telescope

The UVOT is a diffraction-limited 30 cm (12 arcsec aperture) Ritchey-Chrétien reflector. It is sensitive to the magnitude 22.3 in a 17 minute exposure. The telescope has an f/2.0 primary mirror that is re-imaged to f/13 by the secondary mirror. This results in pixels that are 0.502" over its $17'$ square FoV. There are two micro-channel intensified CCD detectors which are photon counting devices and capable of detecting very low signal levels, and enables UVOT to detect even very faint objects over 165 – 650 nm.

The UVOT data can also be obtained from HEASARC data archive[5], which is then processed by standard task *uvotimsum* and *uvotsource*. The task *uvotimsum* sums the images from different observations and is used as input in *uvotsource* to extract the source magni-

[4]https://heasarc.gsfc.nasa.gov/docs/archive.html
[5]https://heasarc.gsfc.nasa.gov/docs/archive.html

tudes and fluxes. A source region of radius 10" are chosen around the source, and a 30" circular region is selected away from the source as a background region. The extracted magnitudes are corrected for galactic extinction (Schlafly and Finkbeiner 2011) and further converted to flux units using the zero points and conversion factors given in Breeveld et al. (2011) and Larionov et al. (2016) respectively.

2.1.3 Publicly Available Archival Data

Many telescope facilities have been established to provide the regular monitoring of *Fermi*-LAT sources in different energy bands as part of *Fermi* multiwavelength support program. We have used the multiwavelength data from some of these observatories, in our thesis, which are Publicly available. The details about these observatories are presented below.

SMARTS

A sample of gamma-ray blazars discovered by *Fermi*-LAT is continuously being monitored by Small and Moderate Aperture Telescope System (SMARTS; a 1.3 m telescope). It is located at the Cerro Tololo Inter-American Observatory at Chile operated by Yale University. It observed the gamma-ray blazars in different bands of optical and IR; the available bands are B, V, R, J, and K. The details about the data reduction and calibration can be found in Bonning et al. (2012). The magnitudes in different filters are corrected for galactic extinction by following Schlafly and Finkbeiner (2011) and converted to flux using the zero points mentioned in Bessell et al. (1998). The details about the sources can be found on SMARTS official page[6].

[6]http://www.astro.yale.edu/smarts/glast/form.html

Stewards Observatory

It is an optical telescope operated by the University of Arizona, which observes the *Fermi*-LAT detected blazar in V and R bands as a part of *Fermi* multiwavelength support program. It is one of the telescopes which also measures the optical polarization in V and R bands, and along with that, it also makes optical photometric, spectrophotometric, and spectropolarimetric observations. The details about the data reduction and calibration process are mentioned in Smith et al. (2009). The photometric data are corrected for galactic extinction by following Schlafly and Finkbeiner (2011) and finally converted to flux (Bessell et al. 1998).

Owens Valley Radio Observatory

The Owens Valley Radio Observatory is a 40 m disc telescope operated at 15 GHz in support of the *Fermi* Gamma-Ray space telescope. It is monitoring more than 1800 blazars about twice per week. Details about the data reduction and calibration process can be found in Richards et al. (2011). The Publicly available data from this telescope is used in our thesis.

Sub-millimeter Array

The Sub-millimeter Array (SMA) working range is between 180 GHz to 418 GHz. It is a radio interferometer located at Maunakea in Hawaii. The SMA observer center provides the 230 and 345 GHz data which (Gurwell et al. 2007) is used in this thesis.

Chapter 3

Long-term Study of PKS 1510-089

3.1 Introduction

PKS 1510-089 is an FSRQ type blazar, located at a redshift of 0.361 (Burbidge and Kinman 1966; Thompson et al. 1990), is one of the most variable sources in 3FGL catalog. It has been observed in gamma-ray energies up to 400 GeV by MAGIC and HESS (H.E.S.S. Collaboration et al. 2013; Aleksić et al. 2014, MAGIC Collaboration). *Fermi*-LAT is continuously monitoring PKS 1510-089 for last eight years (2008-2016), and it is still a part of the *Fermi* monitoring program. The variability time is among the main characteristic properties of the blazar PKS 1510-089.

The multiwavelength observations of PKS 1510-089 during its high state between 2008 September and 2009 June showed variabilities in timescales of 6–12 hours (Abdo et al. 2010a, Fermi LAT Collaboration). They have also estimated the isotropic luminosity in gamma rays of $\sim 2 \times 10^{48}$ erg/s on 2009 March 26, which was found to be more than the estimated Eddington's luminosity $L_{Edd} = 6.86 \times 10^{46}$ erg/s. The Eddington luminosity is calculated by using the black hole mass given in Abdo et al. (2010a). Various studies in the past on PKS 1510-089 have shown that the source is strongly variable in GeV gamma-ray emission (Abdo et al. 2010a; Saito et al. 2013; Aleksić et al. 2014). Many FSRQs have

been detected in the very high energy (VHE) gamma-ray range during their flaring episodes (MAGIC Collaboration et al. 2008; Aleksić et al. 2011; Ahnen et al. 2015). In May 2015, PKS 1510-089 showed a strong GeV gamma-ray flare observed by *Fermi*-LAT, followed by the high state in optical (Jankowsky et al. 2015; Mirzoyan and MAGIC Collaboration 2015) and IR bands (Sameer et al. 2015; Carrasco et al. 2015). Further, the source was observed by the MAGIC telescope which detected an enhanced VHE gamma-ray activity during May 2015 (Mirzoyan and MAGIC Collaboration 2015). The VHE gamma-ray emission has also been seen by the HESS telescope reported in Zacharias et al. (2017b). The May 2015 flare observed by the MAGIC telescope along with telescopes in other wavebands was studied by (Ahnen et al. 2017). They suggest that it is hard to find any correlation in emissions at different frequencies (Ahnen et al. 2017; MAGIC Collaboration). The multiwavelength emission of PKS 1510-089 has been modeled previously in the framework of both leptonic and hadronic models. The study of the light curve and the identification of flares (Tavecchio et al. 2010) are of much interest due to the availability of the excellent quality of flare data as observed by *Fermi*-LAT. The possibility of multiple simultaneously active gamma-ray emission regions along the jet of PKS 1510-089 has been suggested before by Brown (2013).

Many exciting results have been seen from the light curve of PKS 1510-089 in the past, like multiple flares and substantial flux variability, and has been studied before by several authors (Abdo et al. 2010a, Foschini et al. 2013, Zacharias et al. 2017b, Ahnen et al. 2017). However, most of these work focused on the variability studies and finding the short timescales (of a few hours to few tens of minutes) of variability. Till present, no effort has made on studying the long-term behavior of the source. In this chapter, we aim to address the long-term light-curve of the PKS 1510-089 in the gamma-ray band using the *Fermi*-LAT data collected over a period of eight years.

In the eight years light curve of PKS 1510-089, many flaring states have been recognized, and we have specifically selected those high states or flares to compare their spectral and

temporal properties. Although some of them have been studied before by other authors, a comprehensive study including all the high states observed by *Fermi*-LAT Collaboration till 2016 December and a comparison of their spectral and temporal characteristics is not available in the literature. Thus this Chapter provides a detailed, complete, and updated analysis of the flares of PKS 1510-089 as detected by *Fermi*-LAT in the past eight years.

3.2 *Fermi*-LAT Data Analysis

Fermi-LAT has continuously monitored PKS 1510-089 since August, 2008. Here, we have analyzed the *Fermi*-LAT data for PKS 1510-089 from 05 August 2008 to 31 December 2016 (MJD 54683–57753). The data analysis is done with the help of *gtlike/pyLikelihood* method, which is part of latest version (v10r0p5) of *Fermi ScienceTools* software package. The analysis is performed over the energy range between 100 MeV to 300 GeV. Gamma (γ) rays are also produced in the upper atmosphere by the interaction of cosmic rays with ambient medium, matter or radiation. To reduce the contribution from these γ rays (also called Earth limb γ rays), our analysis is restricted to a maximum zenith angle of 105°. The instrument response function (IRF) "P8R2_SOURCE_V6" has been used in the analysis, which is also the part of *Fermi ScienceTools*. The photons are extracted from a circular region of 10° around the source, known as the region of interest (ROI). The third *Fermi*-LAT source catalog (3FGL; Acero et al. 2015) has been used to include all the sources lying within the ROI. The spectral parameters of the sources which are lying within the 10° radius are kept free while doing the model fitting. Several other sources are also present in the 10–20° ROI and their spectral parameters are kept fixed to the 3FGL catalog value. The maximum likelihood (ML) test is done to determine the significance of gamma-ray, which is defined by TS=2Δ log(L), where L is the likelihood function between models with and without a point source at the position of the source of interest (Paliya 2015). We first performed the ML analysis over the period of interest, and for further analysis, we removed the sources of

low TS (TS<9) value (TS = 9, corresponds to $\sim 3\ \sigma$ detection; Mattox et al. 1996). The standard background model provided by the *Fermi ScienceTools* are used to extract the spectral information. In our analysis, we have also used the latest isotropic background model, "iso_P8R2_SOURCE_V6_v06", and the Galactic diffuse emission model, "gll_iem_v06" (available on *Fermi ScienceTools* website[1]). The source variability over a particular time period can be seen by producing light curves with different time bins (7 days, 1 day, 12 hr, 6 hr, and 3 hr). In Figure 3.1, we have shown the 7 day bin light curve for a period of more than eight years, which clearly reveals the source variability. Further, we have also performed the spectral analysis in the energy range 0.1–300 GeV over several periods of the flaring states, detected in the light curve, by using the *unbinned likelihood analysis*. The gamma-ray photon spectra have been fitted with three different spectral models, whose functional forms are presented below:

- A power law (PL), defined as

$$dN(E)/dE = N_p(E/E_p)^{-\Gamma}, \tag{3.1}$$

with E_p = 100 MeV (constant for all the SEDs).

- A log-parabola (LP), defined as

$$dN(E)/dE = N_0(E/E_0)^{-\alpha-\beta\ln(E/E_0)}, \tag{3.2}$$

with E_0 = 300 MeV (constant for all the SEDs), where α is the photon index at E_0, β is the curvature index, and "ln" is the natural logarithm.

- A power law with an exponential cut-off (PLEC), defined as

$$dN(E)/dE = N_0(E/E_p)^{-\Gamma}\exp(-E/E_c), \tag{3.3}$$

[1]https://fermi.gsfc.nasa.gov/ssc/data/access/lat/BackgroundModels.html

with E_p = 200 MeV (constant for all the SEDs).

- A broken power law (BPL), defined as

$$dN(E)/dE = N_0(E/E_{break})^{-\Gamma_i}, \tag{3.4}$$

with i = 1 if $E < E_{break}$ and i = 2 if $E > E_{break}$.

3.3 Identification of Flares

The variability of PKS 1510-089 can be seen in Figure 3.1, which shows the weekly light curve history observed by the *Fermi*-LAT from August, 2008 to December, 2016 . It is observed that, most of the time the source is in the quiescent state or low flux state, accompanied by occasional periods of high activity or flaring state. During the high activity state the flux suddenly increases to several times the low state flux value. Generally, the flares happen for a very short time duration (ranging from a few days to a couple of weeks), and after the flaring period the source returns to its quiescent state.

The *Fermi*-LAT light curve history is shown in Figure 3.1, which shows that so far five major flares have happened in PKS 1510-089. These flaring states are identified as Flare-1, Flare-2, Flare-3, Flare-4, and Flare-5 and their time durations are MJD 54825–55050, MJD 55732–56015, MJD 56505–56626, MJD 57082–57265, and MJD 57657–57753 respectively. The finer time binning of 1 day, 6hr, and 3hr is done for all the five flares observed in Figure 3.1. The 1 day bin light curve does not show any substructures whereas the 6hr bin light curve reveals many substructures which are finally used for the temporal analysis. The 3hr bin light curve has been used to find out the variability time scale. The 6-hour bin light curve reveals that there are substructures inside each flare, and each substructure can be divided into various phases (pre-flare, plateau, flare, and post-flare). For further study, we concentrated on the 6-hour bin light curve. Two substructures have been identified during Flare-1, labeled

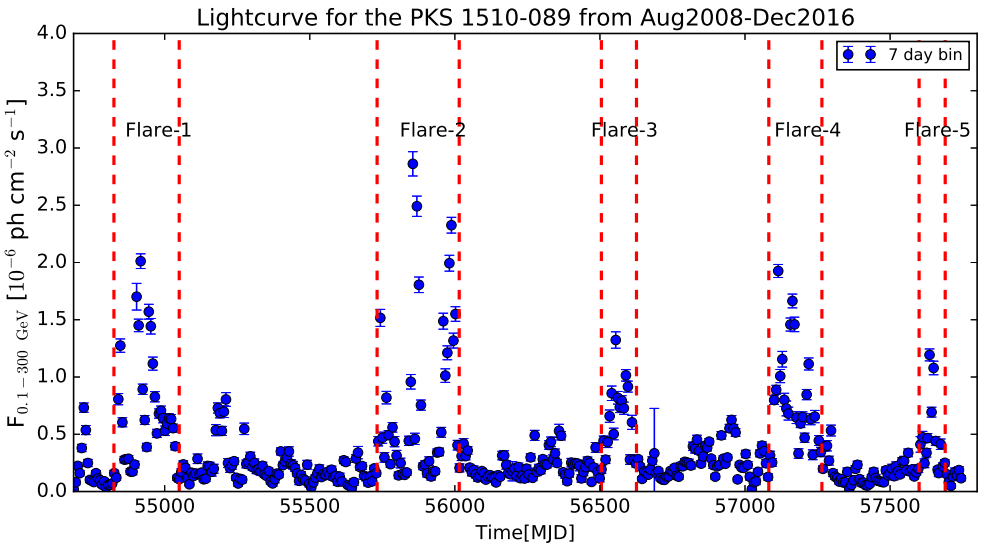

Fig. 3.1 Light curve history of the PKS 1510-089. Five flare episodes have been identified and further studied. Their time durations are the following: MJD 54825–55050, MJD 55732–56015, MJD 56505–56626, MJD 57082–57265 and MJD 57657–57753, which are shown by broken red lines.

as flare-1(A) and flare-1(B). Flare-2 comprises of five substructures, defined as flare-2(A), 2(B), 2(C), 2(D), and 2(E). No substructure found during Flare-3 and Flare-5 while three substructures were seen during Flare-4 and defined as flare-4(A), 4(B), and 4(C). All the different phases of activity have been separated by vertical broken red lines (see Figure 3.2 to Figure 3.13).

3.4 Temporal Analysis

Five major flaring states have been observed in Figure 3.1. The temporal evolution of each flare have been studied separately and the peaks observed in different substructures are fitted with a function called sum of exponentials. The temporal fitting provides the decay and rising time for the different peaks shown in the light curve. The quiescent state (designated by light gray line in the Figures (3.2–3.13)) is also fitted with the peaks of the flaring states.

The sum of exponentials is defined as,

$$F(t) = 2F_0[exp(\frac{t_0 - t}{T_r}) + exp(\frac{t - t_0}{T_d})]^{-1} \quad (3.5)$$

(Abdo et al. 2010a), where F_0 is the flux observed at time t_0 representing the approximate flare amplitude, and T_r and T_d are the rise and decay time of the flare.

3.4.1 Flare-1

Figures 3.2 & 3.3 shows the 6hr bin light curve of flare-1(A) and flare-1(B) corresponding to the flaring activity during MJD 54890–54927 and MJD 54935–54965 respectively. The different phases during these flaring episodes have also been carefully outlined in Figures 3.2 & 3.3.

Flare-1(A)

In Figure 3.2, *Fermi*-LAT has not detected any photons during time interval MJD 54901.2–54905.6. This maybe due to some technical issue, but it must be noted that before MJD 54899.0 the source was in a quiescent state. This quiescent state is named as the pre-flare epoch of the source. The flaring activity in flare-1(A) can be further divided into three parts: flare(I), plateau, and flare(II). The flare(I) phase is observed during MJD 54899.0 to 54910.3, and within this time interval, two strong peaks (P1 & P2) were observed with flux F_{GeV} = 2.34±0.40 and 2.92±0.45 at MJD 54906.4 and 54909.1 respectively. After this, the source spent almost five days (MJD 54910.3-54915.0) in a state where the flux exceeded the constant flux value (0.64±0.07). This particular state, which is neither the quiescent state nor a fully-fledged flaring state, is referred to as the "plateau". After spending five days in plateau state where the average flux was found to be 1.38±0.06, the source flux again started rising and showed one major peak P3 at MJD 54916.9 with a flux of F_{GeV} =

5.73±0.50. Finally, the source returned to its quiescent state. This quiescent state is named as post-flare phase, for the period between MJD 54921 to 54927. The decay and rising time of all the peaks are fitted by equation 3.5 and are presented in Table 3.1.

Flare-1(B)

Similar to flare-1(A), flare-1(B) has also been divided into different phases depending upon the behavior of the source. In flare-1(B), a pre-flare phase is observed during time period MJD 54935 to 54944 with average flux F_{GeV} = 0.61±0.04, which is close to that of the quiescent state flux value. The time period considered for flaring phase is between MJD 54944–54951.5 and four major peaks P1, P2, P3, and P4 are observed. The maximum flux achieved during this period is F_{GeV} = 4.49±0.52 at MJD 54947.9, which corresponds to peak P2. The flux observed corresponding to peak P1 at MJD 54947.4 is F_{GeV} = 3.85±0.55. The second peak P2 is followed by two other peaks P3 and P4 at MJD 54948.6 and 54949.6 with the flux value of F_{GeV} = 3.25±0.39 and 3.31±0.40 respectively. Two peaks were also observed in the post-flare phase. However, They are not considered as the part of a flare since the amplitude of the first peak is very low compared to the peaks observed during flaring phase and the second peak is much farther away from the main flaring period. However, the reduced χ^2 of the fit improves significantly if these additional small peaks are included in the fit. A few small outliers were also observed during this epoch for a very short time period (6 hr). The decay and rising time estimated for various peaks are mentioned in Table 3.1.

3.4.2 Flare-2

Similar to Flare-1, the 6 hr binning carried out for Flare-2 (MJD 55732–56015) observed in Figure 3.1. Several substructures were observed in 6hr bin light curve, and each substructure has been divided into several phases (pre-flare, plateau, flares, and post-flare). Various

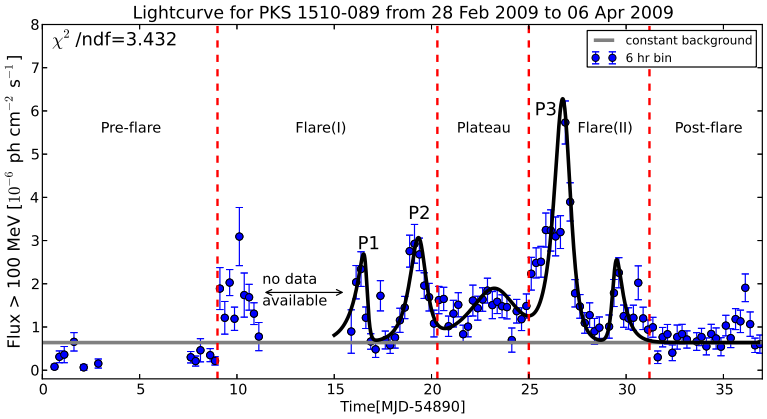

Fig. 3.2 Light curve for the flare-1(A) fitted by the sum of exponentials (see text for details). The fitted parameters are given in Table 3.1. All the different periods of activity have been separated by broken red lines and the light grey line represents the constant state/flux.

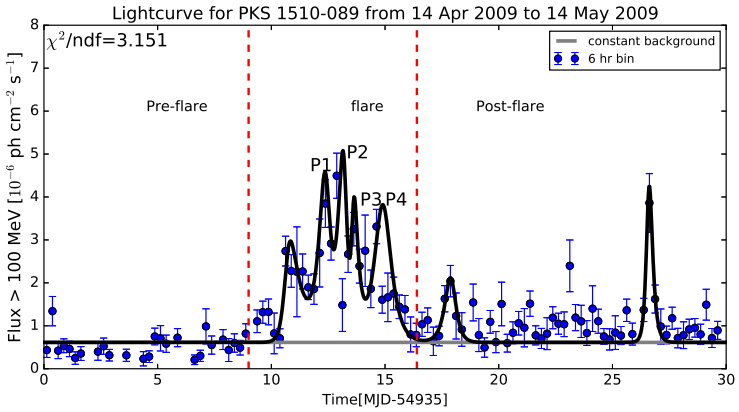

Fig. 3.3 Light curve for the flare-1(B) fitted by the sum of exponentials (see text for details). The fitted parameters are given in Table 3.1. All the different periods of activity have been separated by broken red lines and the light grey line represents the constant state/flux.

Table 3.1 Results of temporal fitting with sum of exponentials (equation 3.5 in the text) for differents peaks of the flares (here Flare-1). Column 2 represents the time (in MJD) at which the peaks are observed and the peak fluxes are given in column 3. The fitted rise (T_r) and decay (T_d) times are mentioned in columns 4 & 5.

flare-1(A)				
Peak	t_0 [MJD]	F_0 [10^{-6} ph cm^{-2} s^{-1}]	T_r [hr]	T_d [hr]
P1	54906.4	2.34±0.40	13.76±7.30	2.06±1.27
P2	54909.1	2.92±0.45	10.97±2.32	7.26±2.25
P3	54916.9	5.73±0.50	10.56±1.58	7.75±0.98
flare-1(B)				
P1	54947.4	3.85±0.55	6.43±2.66	4.04±2.52
P2	54947.9	4.49±0.52	5.71±2.73	2.99±1.23
P3	54948.6	3.25±0.39	1.93±1.98	4.83±2.08
P4	54949.6	3.31±0.40	7.86±2.55	7.85±1.64

substructures and their multiple phases are shown in Figures 3.4, 3.5, 3.6, 3.7, and 3.8, respectively. Five substructures have been observed in Flare-2, and named as flare-2(A), flare-2(B), flare-2(C), flare-2(D), and flare-2(E).

Flare-2(A)

The total time duration of flare-2(A) has been divided into five phases, defined as pre-flare, flare(I), plateau, flare(II), and post-flare, shown in Figure 3.4. The observed flux during the pre-flare phase is very much close to the quiescent state flux value, shown in Figure 3.4 by the gray line. The time duration for the pre-flare phase is chosen between MJD 55732.0 to 55737.5. Just after the pre-flare, the source went into a higher state for a period of four days between MJD 55737.5–55741.0, and named as flare(I). The flux started rising from MJD 55737.9 and exceeded the flux value 2.0. The flare(I) was comprised of several peaks, and the maximum flux attained at MJD 55738.9, is denoted as peak P1. After spending three days in the flare(I) phase, the source returned to the quiescent state. However, the quiescence lasted for a very short time interval ($\sim$ 6 hr), and the flux rose slowly and a clear

peak was observed. The slow rising part is considered as a plateau with time duration of MJD 55741.0 to 55743.5. The average flux observed during plateau is F_{GeV} = 0.79±0.10. A clear flaring state observed between MJD 55743.5 to 55751.0, and named as flare(II). Three major peaks was observed during flare(II), recognized as P2, P3, and P4 at MJD 55743.9, 55744.9, and 55746.4. The maximum flux observed during these three peaks are F_{GeV} = 2.37±0.55, 3.67±1.02, and 5.40±0.60 respectively. The fitted parameters of all the four peaks are provided in Table 3.2.

Flare-2(B)

Three different phases, pre-flare, flare, and post-flare, are observed during flare-2(B) (Figure 3.5). The pre-flare phase was observed for a period of seven days from MJD 55758 to 55765 and the flux was found to be close to the quiescent state flux value. A small peak was also observed during the pre-flare phase. The amplitude of peak was very low, and it was also disconnected with the main flare. Therefore, considered as a part of the pre-flare phase.
A flaring activity was observed during MJD 55765 to 55771. A bright and major peak was seen during the flare, represented as peak P1 at MJD 55767.4 and the peak flux was noted as F_{GeV} = 3.81±0.46. The source spent five days in its flaring state and returned to it's quiescent state, where the flux was almost similar to that of the pre-flare epoch flux value. The source resided in this quiescent state for a long time, and considered as a post-flare. The time duration chosen for post-flare is from MJD 55771 to 55777. Details of the parameters found in the flare fitting are described in Table 3.2.

Flare-2(C)

A similar three-phase pattern was also seen in flare-2(C) Figure 3.6. A small flux variation was noticed during the pre-flare phase, similar to flare-2(B). The time duration for pre-flare was considered between MJD 55846 to 55851, and flux observed was close to the quiescent

state flux value. A Four day flaring period was observed during flare-2(C), and a clear major peak P1 was observed at MJD 55853.9 with a flux value of F_{GeV} = 17.56±1.15. Incidentally, it was recorded as one of the brightest flares in the history of PKS 1510-089 (Foschini et al. 2013). After showing spectacular flare during MJD 55851 to 55855, the source returned to it's quiescent state, named as post-flare. The chosen time interval for post-flare is MJD 55855–55860. The rise and decay time of the peak P1 is presented in Table 3.2.

Flare-2(D)

As expected flare-2(D) also shows the typical phase of pre-flare, flare & post-flare during the total time duration from MJD 55860 to 55890 (Figure 3.7). The pre-flare and post-flare were observed during MJD 55860–55866 & MJD 55878–55890. Three major peaks, P1, P2, and P3, were found during the flaring episode at MJD 55867.9, 55868.4 and 55872.9. The corresponding fluxes were recorded as F_{GeV} = 6.38±0.63, 7.62±0.73, and 8.88±0.77 respectively. Peak P3 is the 2nd highest peak ever observed from PKS 1510-089. The best fitted parameter values for peaks P1, P2, and P3 are described in Table 3.2.

Flare-2(E)

The total time duration (MJD 55965–56013) of flare-2(E) is divided into four phases pre-flare, flare(I), flare(II), and post-flare (Figure 3.8). Small fluctuations in flux are noticed during the pre-flare phase, around the flux value 1.0. Four clear significant peaks were observed during flare(I), defined as P1, P2, P3 & P4. These peaks were found at MJD 55980.4, 55982.9, 55988.7 and 55990.6 with the flux values of F_{GeV} = 4.20±0.51, 4.37±0.51, 3.36±0.44 & 4.19±0.51 respectively. After the flare(I), the source was observed to be in a quiescent state for around four to five days. Soon after, the flux started rising again from MJD 55998. A bright and major peak P5, at MJD 56002.4 with a flux value of F_{GeV} = 2.90±0.57, was observed as a part of flare(II) phase. During MJD 56005 to 56013, a post-flare was observed

Table 3.2 All the columns represent the same parameters as mentioned in Table 3.1, here results are shown for Flare-2

		flare-2(A)		
Peak	t_0 [MJD]	F_0 [10^{-6} ph cm^{-2} s^{-1}]	T_r [hr]	T_d [hr]
P1	55738.9	2.26±0.52	1.90±1.00	2.67±1.99
P2	55743.9	2.37±0.55	4.70±1.42	3.72±1.44
P3	55744.9	3.67±1.02	4.25±0.93	4.11±0.92
P4	55746.4	5.40±0.60	7.86±0.96	3.98±0.61
		flare-2(B)		
P1	55767.4	3.81±0.46	7.38±0.73	5.10±0.72
		flare-2(C)		
P1	55853.9	17.56±1.15	2.92±0.89	2.50±0.27
		flare-2(D)		
P1	55867.9	6.38±0.63	6.07±1.16	4.74±2.67
P2	55868.4	7.62±0.73	7.08±2.50	3.81±1.43
P3	55872.9	8.88±0.77	5.49±0.75	5.62±0.68
		flare-2(E)		
P1	55980.4	4.20±0.51	8.41±1.36	8.78±1.42
P2	55982.9	4.37±0.51	6.91±1.32	2.02±0.65
P3	55988.7	3.36±0.44	7.06±2.86	9.39±1.96
P3	55990.6	4.19±0.51	8.64±1.42	4.46±1.03
P4	56002.4	2.90±0.57	15.07±2.72	9.50±2.29

whose flux instead of attaining a fixed value, keeps fluctuating in the vicinity of the quiescent state flux value. The best fitted values of the parameters of different peaks are presented in Table 3.2.

3.4.3 Flare-3

It is the first time that a detailed study about the flaring period from September 10 to October 13, 2013 has been presented. This flaring period was defined as Flare-3. The entire flaring period of Flare-3 is divided into four phases like pre-flare, flare(I), flare(II) and post-flare.

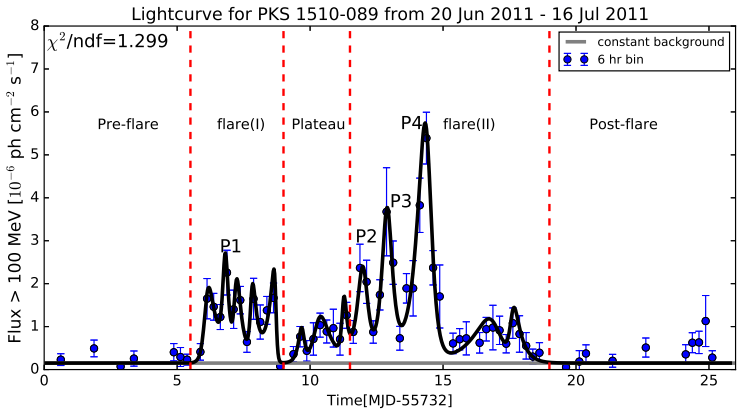

Fig. 3.4 Light curve for the flare-2(A) fitted by the sum of exponentials (see text for details). The fitted parameters are given in Table 3.2. All the different periods of activity have been separated by broken red lines and the light gray line represents the constant state/flux.

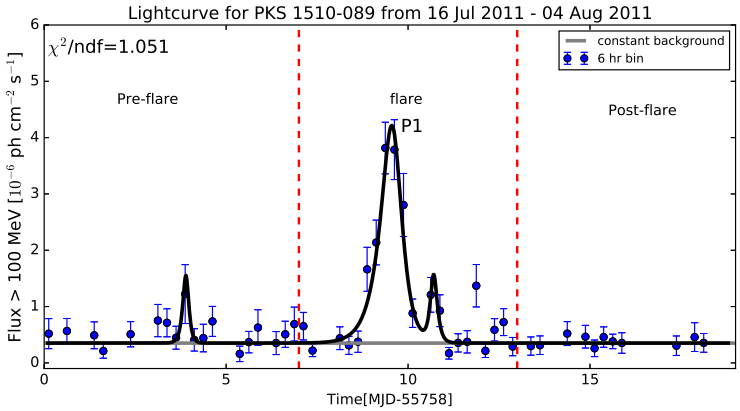

Fig. 3.5 Light curve for the flare-2(B) fitted by the sum of exponentials (see text for details). The fitted parameters are given in Table 3.2. All the different periods of activity have been separated by broken red lines and the light gray line represents the constant state/flux.

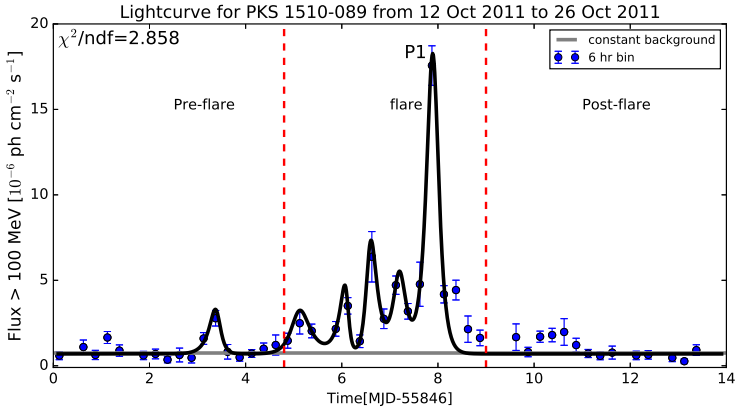

Fig. 3.6 Light curve for the flare-2(C) fitted by the sum of exponentials (see text for details). The fitted parameters are given in Table 3.2. All the different periods of activity have been separated by broken red lines and the light gray line represents the constant state/flux.

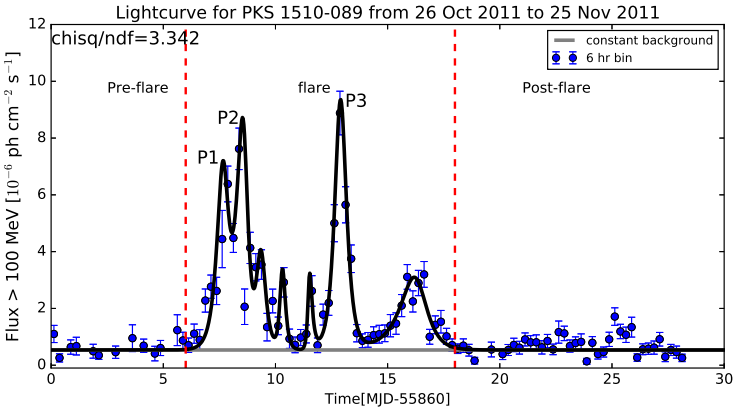

Fig. 3.7 Light curve for the flare-2(D) fitted by the sum of exponentials (see text for details). The fitted parameters are given in Table 3.2. All the different periods of activity have been separated by broken red lines and the light gray line represents the constant state/flux.

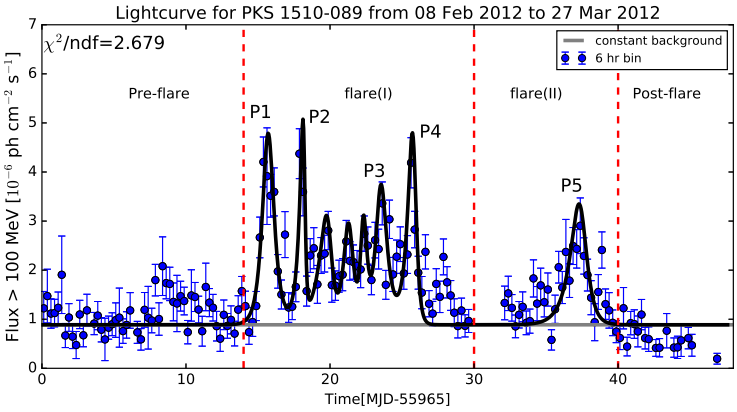

Fig. 3.8 Light curve for the flare-2(E) fitted by the sum of exponentials (see text for details). The fitted parameters are given in Table 3.2. All the different periods of activity have been separated by broken red lines and the light gray line represents the constant state/flux.

The light curve of flare-3 is shown in Figure 3.9. The pre-flare phase was defined for a period between MJD 56545 to 56552 and the average flux obtained during this period was F_{GeV} = 0.54±0.02. After spending seven days in the pre-flare state, the flux suddenly rose to 3.5, and the source resided for around nine days in this higher state. The period of high state during MJD 56552–56561 was considered as flare(I).

Three significant peaks P1, P2, and P3 were observed during the flare at MJD 56554.1, 56556.4 and 56557.9. The maximum fluxes corresponding to each peak was recorded to be F_{GeV} = 3.47±0.47, 2.72±0.43 and 1.99±0.49 respectively. The flux decreased to it's quiescent state and stayed low for two days with an average flux value F_{GeV} = 0.54±0.02. The flux again started rising from MJD 56562.9 and reached close to 3.0, with a fluctuating behavior seen in flux. This period is defined as flare(II) and the time duration was between MJD 56561 to 56570. A clear and major peak P4 was observed during the flare(II) at MJD 56563.9 with flux value of F_{GeV} = 2.71±0.45. A post-flare phase was observed just after the flare(II), and the time duration was between MJD 56570 to 56578. The flux found during post-flare was below 1.0. The fitted parameters corresponding to peaks are presented in Table 3.3.

Table 3.3 All the columns represent the same parameters as mentioned in Table 3.1, here results are shown for Flare-3

Flare-3				
Peak	t_0 [MJD]	F_0 [10^{-6} ph cm^{-2} s^{-1}]	T_r [hr]	T_d [hr]
P1	56554.1	3.47±0.47	3.88±0.89	5.16±0.97
P2	56556.4	2.72±0.43	3.94±0.96	7.02±1.28
P3	56557.9	1.99±0.49	3.12±1.21	1.31±0.94
P4	56563.9	2.71±0.45	4.76±0.92	4.88±0.96

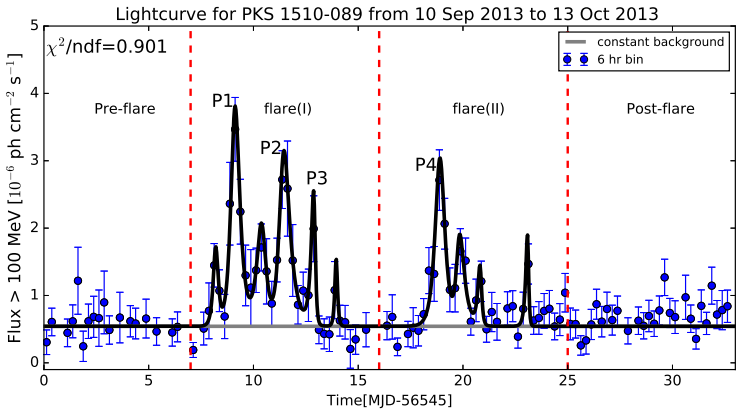

Fig. 3.9 Light curve for the flare-3 fitted by the sum of exponentials (see text for details). The fitted parameters are given in Table 3.3. All the different periods of activity have been separated by broken red lines and the light grey line represents the constant state/flux.

3.4.4 Flare-4

We also carried out a 6 hr binning of Flare-4 during MJD 57082 to 57265. Three sub-structures were observed during this period, named as flare-4(A), flare-4(B), and flare-4(C). These substructures, along with different phases, are shown in Figures 3.10, 3.11, and 3.12, respectively.

Flare-4(A)

Flare-4(A) exhibit the usual three-phase pattern known as pre-flare, flare, and post-flare (Figure 3.10). A significant amount of variations seen in the pre-flare and post-flare phase, but they are disconnected from the main flaring event and hence are not included in the analysis. The duration of pre-flare and post-flare were chosen as MJD 57106–57113 and MJD 57118–57128. The main flare was observed for five days during MJD 57113 to 57118. Two major peaks P1 and P2 were found during flare with fluxes of F_{GeV} = 3.84±0.46 and 4.47±0.44 respectively. The Peak P1 and P2 are found to be at MJD 57114.4 and 57115.9. The details about the fitting parameters of the peak P1 and P2 are described in Table 3.4.

Flare-4(B)

The total time duration of flare-4(B) can be divided into four phases, as shown in Figure 3.11. The phases were defined as pre-flare, flare(I), flare(II), and post-flare. A significant peak was observed during the pre-flare phase, but it was disconnected from the main flare, and hence was not considered as a part of the flare. The pre-flare phase was considered between MJD 57143 to 57155 and after that a flare(I) was observed during MJD 57155 to 57163. The flare(I) is consisted of several peaks, defined as P1, P2, and P3. The maximum flux observed during the flare(I) is F_{GeV} = 3.28±0.41, which corresponds to the peak P3 at MJD 57159.9. The other peaks P1 and P2 are observed at MJD 57156.4 and 57158.4 with the peak fluxes of F_{GeV} = 2.10±0.34 and 2.02±0.33 respectively. The source spent around seven days in the flaring state and after that returned to it's quiescent state. The quiescent state continued for about two and a half days, and the observed flux was comparable to the pre-flare phase flux value. The source again started showing the activity, defined as flare(II) phase. Three bright and significant peaks were observed during the flare(II) phase and named as P4, P5, and P6. The maximum flux reached during this period was F_{GeV} = 3.56±0.47, which corresponds to the peak P5 at MJD 57167.4. The fluxes observed corresponding to the peaks, P4 and P6 are F_{GeV} = 2.32±0.37 and 3.10±0.47 at MJD 57165.1 and 57170.4 respectively. The post-flare epoch observed just after the flare(II) phase, lasted from MJD 57171 to 57177 with a flux of around 1.0. The fitted parameters of all the peaks observed during flare(I) and flare(II) are provided in Table 3.4.

Flare-4(C)

The flare-4(C) was observed to be the third-brightest flare from PKS 1510-089. As usual, three different phases were observed and named as pre-flare, flare, and post-flare. During pre-flare and post-flare phases, the fluxes were almost similar (below 1.0) and close to the quiescent state, as shown by a horizontal gray line in Figure 3.12. Two major peaks were

Table 3.4 All the columns represent the same parameters as mentioned in Table 3.1, here results are shown for Flare-4

		flare-4(A)		
Peak	t_0 [MJD]	F_0 [10^{-6} ph cm^{-2} s^{-1}]	T_r [hr]	T_d [hr]
P1	57114.4	3.84±0.46	8.29±1.69	4.93±2.40
P2	57115.9	4.47±0.44	8.27±2.98	18.10±2.27
		flare-4(B)		
P1	57156.4	2.10±0.34	6.83±2.12	9.50±3.99
P2	57158.4	2.02±0.33	11.77±4.48	9.49±3.84
P3	57159.9	3.28±0.41	8.00±2.27	5.35±2.92
P4	57165.1	2.32±0.37	9.87±1.83	3.99±1.56
P5	57167.4	3.56±0.47	6.35±2.09	11.82±1.61
P6	57170.4	3.10±0.47	8.53±1.60	2.67±0.87
		flare-4(C)		
P1	57244.6	8.58±1.03	7.59±0.85	2.66±0.98
P2	57245.4	6.09±0.58	7.11±1.68	2.86±0.80

observed during the flaring state and named as P1 and P2. The fluxes observed corresponding to peak P1, and P2 are F_{GeV} = 8.58±1.03 and 6.09±0.58 at MJD 57244.6 and 57245.4 respectively. The parameters found in flare fitting are presented in Table 3.4.

3.4.5 Flare-5

The last flare in our study was found between August, 2016 and September, 2016 during MJD 57628–57646, and defined as flare-5. The phases like pre-flare, flare, and post-flare were observed during this period. The flux observed during pre-flare and post-flare phase are low and very similar to each other. A bright and major peak P1 was observed during the flaring phase, shown in Figure 3.13. The maximum flux observed during peak P1 is F_{GeV} = 3.15±0.47 at MJD 57634.625. The model parameters for fitting the peak P1 is provided in Table 3.5

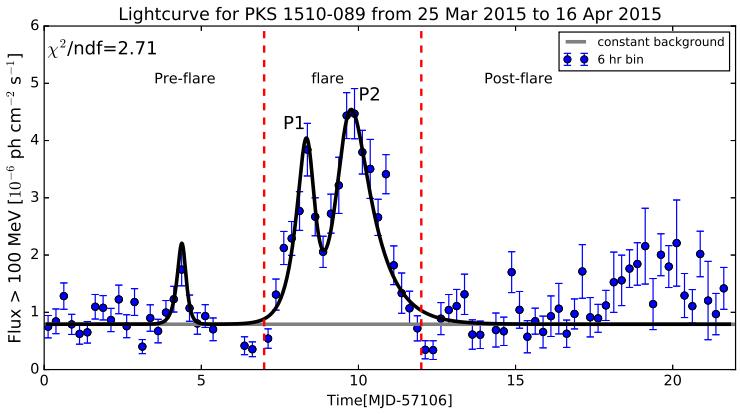

Fig. 3.10 Light curve for the flare-4(A) fitted by the sum of exponentials (see text for details). The fitted parameters are given in Table 3.4. All the different periods of activity have been separated by broken red lines, and the light gray line represents the constant state/flux.

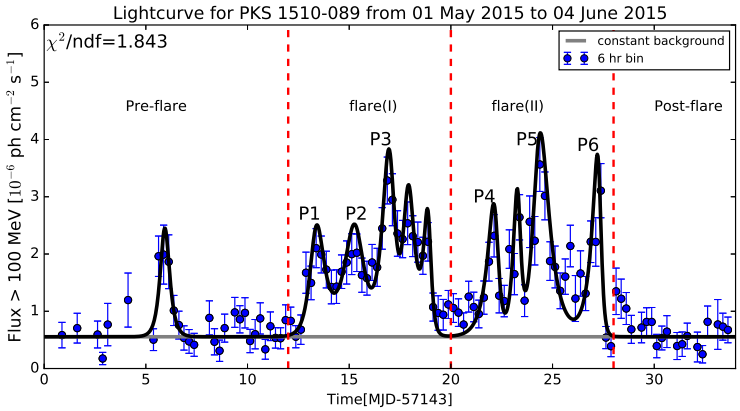

Fig. 3.11 Light curve for the flare-4(B) fitted by the sum of exponentials (see text for details). The fitted parameters are given in Table 3.4. All the different periods of activity have been separated by broken red lines, and the light gray line represents the constant state/flux.

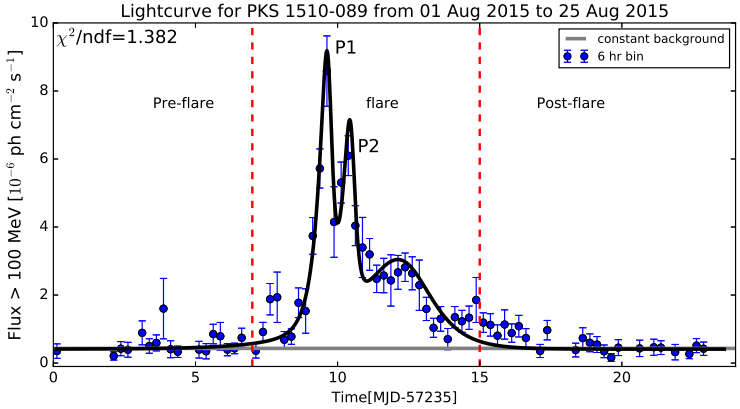

Fig. 3.12 Light curve for the flare-4(C) fitted by the sum of exponentials (see text for details). The fitted parameters are given in Table 3.4. All the different periods of activity have been separated by broken red lines, and the light gray line represents the constant state/flux.

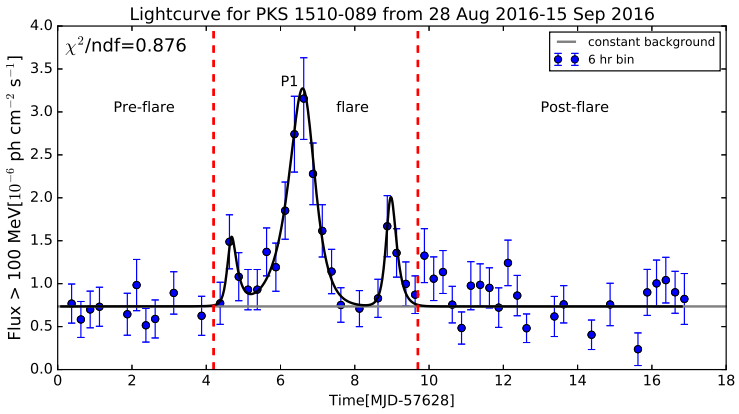

Fig. 3.13 Light curve for the flare-5 fitted by the sum of exponentials (see text for details). The fitted parameters are given in Table 3.5. All the different periods of activity have been separated by broken red lines and the light gray line represents the constant state/flux.

All the above peaks during the flaring episodes were fitted along with the constant flux state (value), and their parameters are mentioned in Table 3.6.

Table 3.5 All the columns represent the same parameters as mentioned in Table 3.1, results are shown here for Flare-5.

Flare-5				
Peak	t_0 [MJD]	F_0 [10^{-6} ph cm^{-2} s^{-1}]	T_r [hr]	T_d [hr]
P1	57634.6	3.15±0.47	8.96±1.06	6.28±0.89

3.4.6 Histogram plots

Figure 3.14 shows the histogram of the peak fluxes of all the peaks observed during various flares (left panel). The right panel represents the histogram of the rise and decay times of the peaks. These values are also enumerated in Table 3.1–3.5. The flux corresponding to each peak from all the flares (Flare-1 to Flare-5) are distributed around a mean of 3.54±0.08 with a standard deviation of 1.69. The histogram of rise and decay times are distributed around a mean of 6.04±0.22 hr and 3.88±0.16 hr with a standard deviation of 2.40 hr and 2.20 hr

Table 3.6 The values of constant flux which are also fitted with the above peaks in the light curve. A histogram of the constant fluxes in different periods is shown in left panel of Figure 3.15.

Flares/Sub-flares	Constant flux Flux $F_{0.1-300\ GeV}$ [10^{-6} ph cm^{-2} s^{-1}]
Flare-1(A)	0.64±0.07
Flare-1(B)	0.61±0.04
Flare-2(A)	0.15±0.03
Flare-2(B)	0.35±0.03
Flare-2(C)	0.74±0.09
Flare-2(D)	0.53±0.05
Flare-2(E)	0.88±0.04
Flare-3	0.54±0.02
Flare-4(A)	0.69±0.05
Flare-4(B)	0.50±0.04
Flare-4(C)	0.41±0.04
Flare-5	0.74±0.04

respectively.

Histogram of the constant flux, shown in Figure 3.1–3.13 as a horizontal gray line and displayed in Table 3.6, are shown in the left panel of Figure 3.15. They are distributed with a mean of 0.51±0.01 and a standard deviation of 0.20, which implies that the quiescent state of the source is pretty stable.

A histogram is also produced for all the flux data points, shown in Figure 3.1, and plotted in the right panel of Figure 3.15. A peaked distribution, with the slow rising part before the peak and a fast decaying part beyond the peak, was observed. The peak of the histogram signifies the flux where the source spends most of the time. Beyond the peak, the flux values fall rapidly along with a few outliers which can be associated with large flux variations in the source. Tavecchio et al. (2010) have studied flux variations and duty cycles with 1.5 years of data in two of the most variable sources, PKS 1510-089 and 3C 454.3. Our findings with a much larger data set also show very similar behavior to their study.

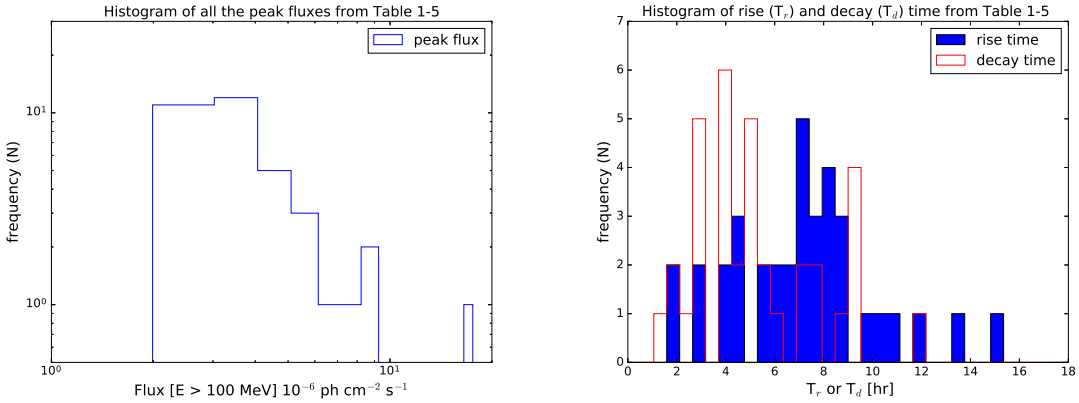

Fig. 3.14 Histogram of peak fluxes (left panel) and rise and decay time (right panel) from Tables 3.1–3.5 are plotted here.

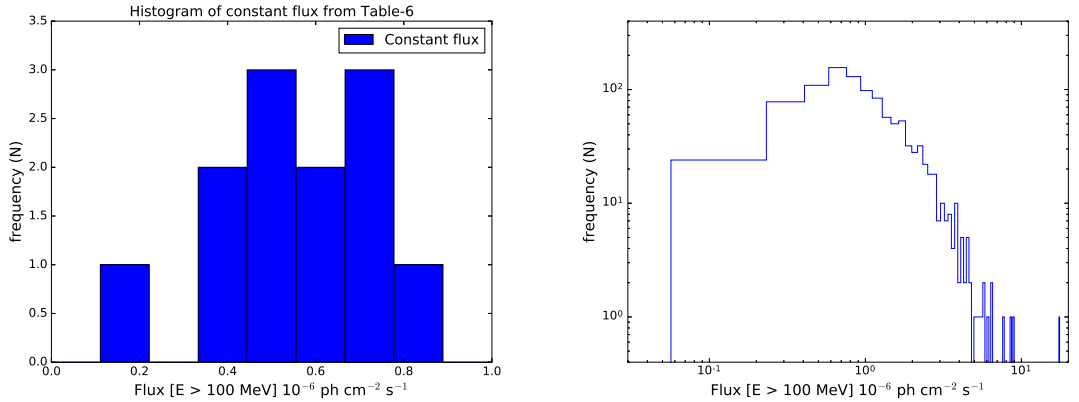

Fig. 3.15 Histogram of constant flux (left panel) from Table 3.6 and all the flux data points (right panel) are shown here.

3.4.7 γ-ray Variability and Emission Region

The variability time is a measure of flux variations over time. It tells us about how fast the flux is changing with time, during the flaring periods. To estimate the variability time, we have produced the 3 hr bin light curves of all the flares and their substructures. All the substructures identified in different flares are scanned separately by using the following equation,

$$F(t_2) = F(t_1).2^{(t_2-t_1)/t_d}, \tag{3.6}$$

to calculate the minimum time of doubling/halving of flux between two consecutive instants of time t_1 and t_2. $F(t_1)$ and $F(t_2)$ are the fluxes measured at time t_1 and t_2 respectively, and t_d represents the flux doubling/halving timescale. The variability time estimated for all the substructures are presented in Table 3.7. The chosen flux points $F(t_1)$ and $F(t_2)$ must satisfy the criteria $F(t_2) > F(t_1)$, and also the criteria of significant detection by TS > 25 ($\sim 5\sigma$ detection), while scanning the light curve with equation 3.6. Among all the observed substructures, the shortest variability time for the rising and decaying part of the peaks are found during flare-1(B) and flare-2(C). The fastest variability time for the rising part was observed to be t_{rise} = 1.43$\pm$0.22 hr between MJD 54945.438 and 54945.563 (flare-1(B)), and for the decaying part it was found to be t_{decay} = 1.30$\pm$0.18 hr between MJD 55852.063 and 55852.188 (flare-2(C)). There are also several time intervals where the flux changed by a factor of two but they did not satisfy the requirement of TS > 25. These time intervals were not included in the variability time calculation. PKS 1510-089 is considered as a highly variable source and an hour scale of variability time was observed before also by Brown (2013) and Saito et al. (2013). The variability time is mainly, used in estimating the size and location of the emission region. If one knows the Lorentz factor and Doppler factor of the source, then the size and the location of emission region can be easily estimated. The variability time t_{var}, size of the emission region (R) and Doppler factor (δ) are related to

each other by the following equation,

$$R \leq ct_{var}\delta(1+z)^{-1} \tag{3.7}$$

where z represents the redshift of the source and c is the speed of light in vacuum. The radio observations of ultra-relativistic jets of PKS 1510-089 is done by Jorstad et al. (2005), and they have found the apparent speed up to 46c, and which also suggest the very high Doppler factor for this source. The Doppler factor, δ = 47 is chosen from Kadota et al. (2012) to estimate the size of the emission region. For t_{var} = 1.30 hr and δ = 47, the size of the emission region is found to be R $\sim 4.85 \times 10^{15}$ cm. A less extreme Doppler factor of 10 would imply an emission region of radius R $\sim 1.03 \times 10^{15}$ cm. The size of emission region estimated in this study is very much in agreement with the value calculated by Brown (2013) and Saito et al. (2013), which are $\sim 9.3 \times 10^{15}$ cm and $\sim 1.5 \times 10^{15}$cm, respectively. Such small emission regions are somewhat challenging to accommodate in the standard framework where the emission takes place from a considerable distance from the central engine (see Tavecchio et al. 2010 and references therein for a more detailed discussion).
The histogram of redshift corrected variability time Δt_{var} mentioned in Table 3.7 is shown in Figure 3.16. The distributions of variability time associated with rising and decaying part of the peaks are found to be non-Gaussian. Instead, the data points are distributed with a mean of 1.75±0.02 hr and 1.76±0.02 hr and with standard deviations of 0.35 hr and 0.40 hr, for rising and decaying part of the peaks respectively.

3.4.8 Summary of Temporal Analysis

Detailed temporal studies of PKS 1510-089 during eight years (2018–2016) of continuous observations from *Fermi*-LAT are presented in this chapter. Total five major flares were observed during these eight years and the finer time binning of the light curve in one day and 6

Table 3.7 Details of the fastest variability time scale of PKS 1510-089 for the whole eight years data has been presented here. Data which has a significance of at least 5σ has been considered (see text for details). Here t_{var} represents the observed characteristic time scale and $\Delta t_{var} = t_{var}\ (1+z)^{-1}$. R (rise) and D(decay) represent the behavior of the flux in a particular time interval.

t_1 (MJD)	t_2 (MJD)	F_1	F_2	t_{var} (hr)	Δt_{var} (hr)	Rise/Decay
t_1 (MJD)	t_2 (MJD)	F_1	F_2	t_{var} (hr)	Δt_{var} (hr)	Rise/Decay
		flare-1(A)				
54916.563	54916.688	1.95±0.45	4.25±0.59	2.67±0.32	1.96±0.17	R
54917.188	54917.313	4.55±0.68	1.75±0.43	-2.18±0.22	-1.60±0.12	D
54917.938	54918.063	0.69±0.25	1.40±0.43	2.96±0.23	2.17±0.12	R
		flare-1(B)				
54945.438	54945.563	0.72±0.29	3.09±0.53	1.43±0.22	1.05±0.12	R
54948.938	54949.063	2.25±0.68	5.49±1.91	2.34±0.12	1.72±0.07	R
54949.688	54949.813	3.10±0.55	1.37±0.36	-2.56±0.26	-1.88±0.14	D
		flare-2(A)				
55739.313	55739.438	0.89±0.36	2.31±0.52	2.17±0.42	1.59±0.22	R
55745.563	55745.688	3.03±0.63	0.95±0.32	-1.79±0.20	-1.32±0.11	D
55745.688	55745.813	0.95±0.32	1.87±0.70	3.07±0.15	2.26±0.08	R
55746.063	55746.188	6.10±1.50	2.95±0.66	-2.88±0.09	-2.12±0.05	D
55746.438	55746.563	7.01±0.95	3.48±0.66	-2.98±0.23	-2.19±0.12	D
55746.563	55746.688	3.48±0.66	1.19±0.43	-1.94±0.31	-1.42±0.17	D
		flare-2(B)				
55767.063	55767.188	1.11±0.45	2.98±0.62	2.11±0.42	1.55±0.23	R
55767.813	55767.938	4.35±1.15	1.94±0.60	-2.59±0.14	-1.90±0.08	D
		flare-2(C)				
55852.063	55852.188	5.80±0.84	1.17±0.43	-1.30±0.18	-0.95±0.10	D
55852.313	55852.438	0.91±0.37	2.57±0.87	2.00±0.13	1.47±0.07	R
55852.438	55852.563	2.57±0.87	5.84±1.75	2.53±0.13	1.86±0.07	R
55853.063	55853.188	3.11±0.65	6.28±0.87	2.97±0.30	2.18±0.16	R
55853.188	55853.313	6.28±0.87	3.00±0.60	-2.81±0.24	-2.07±0.13	D
55853.563	55853.688	3.46±1.43	7.20±2.54	2.84±0.24	2.09±0.13	R
55853.688	55853.813	7.20±2.54	25.50±2.34	1.64±0.34	1.21±0.18	R
55853.938	55854.063	13.35±1.27	4.94±0.76	-2.09±0.12	-1.54±0.07	D
		flare-2(D)				
55867.313	55867.438	3.49±0.70	1.38±0.59	-2.24±0.54	-1.64±0.29	D
55868.438	55868.563	6.92±1.09	2.74±1.15	-2.25±0.64	-1.65±0.35	D
55868.688	55868.813	1.62±0.72	3.55±0.74	2.66±0.81	1.95±0.43	R
55869.063	55869.188	4.78±0.81	2.19±0.52	-2.67±0.24	-1.96±0.13	D
55869.188	55869.313	2.19±0.52	4.50±0.77	2.89±0.27	2.12±0.15	R
55870.313	55870.438	2.05±0.58	4.10±0.90	3.00±0.28	2.20±0.15	R
55872.563	55872.688	2.66±0.87	6.11±0.86	2.50±0.56	1.84±0.30	R
		flare-2(E)				
55989.188	55989.313	3.54±0.59	1.15±0.39	-1.84±0.28	-1.35±0.15	D
55989.313	55989.438	1.15±0.39	2.77±0.56	2.36±0.36	1.74±0.20	R
55990.063	55990.188	1.35±0.38	2.67±0.53	3.06±0.36	2.25±0.20	R
55990.438	55990.563	1.94±0.54	4.33±0.78	2.59±0.32	1.90±0.17	R
55991.313	55991.438	1.01±0.43	2.07±0.50	2.89±0.73	2.12±0.40	R
55991.813	55991.938	1.82±0.43	0.84±0.32	-2.68±0.50	-1.97±0.27	D
55998.938	55999.063	0.78±0.30	1.80±0.54	2.49±0.26	1.83±0.14	R
56000.188	56000.313	1.25±0.41	0.63±0.27	-3.04±0.44	-2.23±0.24	D
56000.688	56000.813	1.35±0.37	2.75±0.52	2.94±0.35	2.16±0.19	R
56001.063	56001.188	2.12±0.45	1.07±0.39	-3.03±0.61	-2.23±0.33	D
		Flare-3				
56556.188	56556.313	1.61±0.49	3.88±0.66	2.37±0.36	1.74±0.19	R
56563.313	56563.438	2.05±0.52	0.93±0.39	-1.98±0.38	-1.45±0.21	D
56568.063	56568.188	2.10±0.49	0.99±0.35	-2.76±0.53	-2.03±0.29	D
		flare-4(A)				
57113.188	57113.313	0.30±0.13	0.93±0.33	1.84±0.15	1.35±0.08	R
57116.938	57117.063	3.65±0.49	1.73±0.42	-2.78±0.40	-2.04±0.22	D
		flare-4(B)				
57164.063	57164.188	1.40±0.38	0.63±0.29	-2.61±0.62	-1.92±0.34	D
57165.688	57165.813	0.97±0.34	2.06±0.47	2.78±0.44	2.04±-0.24	R
57166.188	57166.313	1.30±0.46	2.85±0.61	2.66±0.48	1.95±0.26	R
57166.438	57166.563	2.43±0.51	0.98±0.36	-2.29±0.40	-1.68±0.21	D
57166.688	57166.813	1.27±0.41	3.05±0.67	2.38±0.29	1.75±0.16	R
57169.688	57169.813	1.15±0.40	2.21±0.52	3.19±0.58	2.34±0.31	R
57170.438	57170.563	3.61±0.69	0.81±0.34	-1.39±0.21	-1.02±0.11	D
		flare-4(C)				
57243.438	57243.563	0.57±0.25	1.98±0.60	1.67±0.19	1.23±0.10	R
57245.813	57245.938	4.60±1.55	2.37±0.94	-3.14±0.29	-2.31±0.16	D
57249.563	57249.688	0.78±0.32	1.94±0.66	2.27±0.18	1.67±0.10	R
		Flare-5				
57632.563	57632.688	1.03±0.37	2.09±0.54	2.00±0.33	1.47±0.18	R
57634.938	57635.063	2.30±0.50	1.06±0.35	-2.68±0.39	-1.97±0.21	D
57635.063	57635.188	1.06±0.35	2.13±0.49	2.98±0.43	2.19±0.23	R
57635.188	57635.313	2.13±0.49	0.80±0.30	-2.12±0.31	-1.56±0.17	D

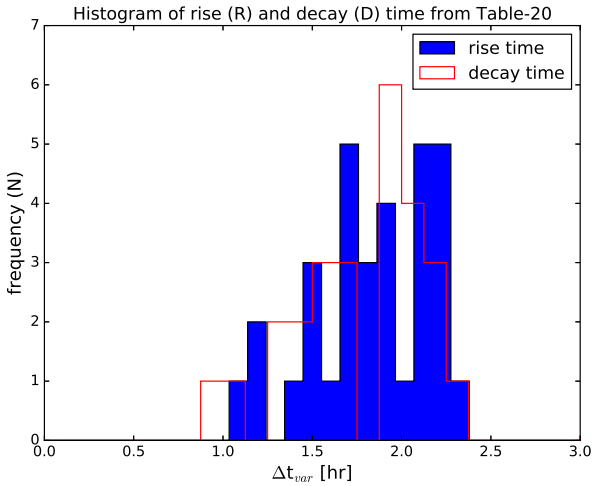

Fig. 3.16 Histogram of the variability time associated with rise and decay part of the peaks, from the Table 3.7 are shown here. They are distributed with mean of 1.75±0.02 hr and 1.76±0.02 hr and standard deviation of 0.35 hr, 0.40 hr respectively.

hr show that the observed five flares can be divided into different sub-flares or substructures. These substructures are generally separated from each other by a months or more than that. In Section 3.4, the light curve study of each substructure is discussed in detail. Few of them have been studied before by several other authors in the context of variability, multiwavelength correlations, SED modeling, and finding the location of the emission region.

A multi-wavelength study has been done before by Abdo et al. (2010a) for Flare-1 (2009 March–April). A good correlation was found between gamma-ray and optical emissions, whereas no strong correlation was seen between gamma-ray and X-ray emissions. A lag of 13 days was observed in optical emission with respect to gamma-ray emission (Abdo et al. 2010a). They have estimated the isotropic luminosity above 100 MeV during the flare (II) of flare-1(A) to be more than 2×10^{48} erg/s. The mass of the black hole in PKS 1510-089 was estimated by using the UV correlation and it was found to be 5.4×10^8 $M_\odot$ (Abdo et al. 2010a).

We have estimated the gravitational radius by using the relation $r_g = GM/c^2$, where M is the mass of compact object, is $r_g = 8.0 \times 10^{13}$ cm, and c = speed of light in vacuum. Now it is

clear that the radius of emission region $R > r_g$, from which we can infer that one possibility is that the central black hole causes the perturbation seen along the jet of PKS 1510-089.

The flare-1(A) has also been observed in very high energy gamma rays by HESS telescope by H.E.S.S. Collaboration et al. (2013). They found that the integral flux in the very high energy (0.15 - 1.0 TeV) band is $1.0\pm 0.2_{stat} \pm 0.2_{sys}) \times 10^{-11}$ cm^{-2} s^{-1} , which is ≈3% of the integral flux from Crab nebula. The steepening in the photon spectrum is also observed with a spectral index of $5.4\pm 0.7_{stat} \pm 0.3_{sys}$ for PL distribution. Foschini et al. (2013) have studied the outburst of October-November 2011, which corresponds to flare-2(C) and flare-2(D) in our study. They estimated the shortest variability time ever detected in MeV-GeV energy regime to be ∼ 20 minutes at MJD 55852, by using the GTI time binning. They have also mentioned about the hour scale variability (see Table-1 of Foschini et al. 2013) by using the 3 hr time binning, which is consistent with our result and the result produced by Brown (2013) and Saito et al. (2013). The shortest variability time found in our analysis of flare-2(C) is ∼1.30 hr between MJD 55852.063 and 55852.188, estimated from 3 hr bin light curve.

A multi-wavelength study of flare-2(E) has also been done previously by the MAGIC collaboration (Aleksić et al. 2014). They have analyzed the *Fermi*-LAT data from January 1 to April 7 in 2012 (MJD 55927–56024). The shortest variability time estimated during time interval MJD 55974 to 55994 is found to be t_{var} = 1.5±0.6 hr, which is in very good agreement with the value estimated in our study t_{var} = 1.84±0.28 hr for almost the same time interval given in Table 3.7 (flare-2E).

Flare-3 has never been studied before. In our study, the maximum flux observed during this flaring period is F_{GeV} = 3.47±0.47 at MJD 56554.1. The fastest variability time is estimated to be t_{var} = 1.98±0.38 hr, shown in Table 3.7, which is comparable to the fastest variability time found for the other flares.

A detailed study of flare-4(A) (MJD 57100–57128) and flare-4(C) (MJD 57235–57259) are

presented as the first time in this chapter. The flare-4(C) is identified as the 3rd brightest flare found in the light curve history of PKS 1510-089. The MAGIC collaboration (Ahnen et al. 2017) has previously performed a multi-wavelength study of flare-4(B) observed in May, 2015 during MJD 57143–57177).

Flare-5 was not studied before and The shortest variability time was calculated as t_{var} = 2.00±0.33 hr (Table 3.7).

Among all the observed flares, the fastest variability time is found to be 1.30 hr during flare-2(C). The variability time is used to estimate the size of the emission region by using equation 3.7 and the size of the emission region is found to be R∼4.85×10^{15} cm.

3.5 Spectral Analysis

The gamma-ray spectral energy distribution (SED) is presented for all the flares observed in PKS 1510-089 during 2008–2016. The spectral data points are produced for all the different phases observed in different flares, and are fitted with three different spectral models PL, LP, and PLEC. The functional form of different spectral models is shown in equations 3.1, 3.2, and 3.3, respectively. Among the three different models, the best fit model can be consider by comparing the log(Likelihood) and Δlog(Likelihood) value provided by the likelihood analysis. The log(Likelihood) and Δlog(Likelihood) values are calculated for each and every phase pattern, where Δlog(Likelihood) is defined as Δlog($\mathcal{L}$) = (log $\mathcal{L}$(log-Parabola / PLEC) - log $\mathcal{L}$(PL)), and $\mathcal{L}$ = Likelihood.

3.5.1 Flare-1

Two substructures flare-1(A) and flare-1(B) are observed in Flare-1. Various phases are identified during flare-1(A) and flare-1(B), and their gamma-rays spectrum are shown in Figure 3.17 and 3.18, respectively. The gamma-ray spectral data points are fitted with the

three different spectral models (PL, LP, and PLEC), which are shown in cyan, black, and red color respectively. The fitted parameters of various models are shown in Table 3.8 and 3.9 for flare-1(A) and flare-1(B) respectively. Tables 3.8 and 3.9 show the progressive spectral hardening during flare-1(A) and flare-1(B) with increasing flux for PL distribution when the source moves from one phase to another phase. During flare-1(A), in pre-flare phase, the flux is 0.45, and corresponding photon spectral index is 2.40. When the source moves to the flare(I) phase the flux increases up to 3.73, and the photon spectral index became harder with a value of 2.30. Similar behavior is also seen in flare-1(B), during the pre-flare phase the flux observed as 1.12 with spectral index 2.50 and flux changes to 5.20 with a corresponding spectral index 2.41 during flare phase. A clear "harder-when-brighter" trend is observed in both flare-1(A) and flare-1(B).

3.5.2 Flare-2

The temporal study suggests that the Flare-2 can be divided into five substructures flare-2(A), 2(B), 2(C), 2(D), and 2(E). The gamma-ray SEDs are produced for all these substructures along with their different phases. The SEDs for flare-2(A), 2(B), 2(C), 2(D) and 2(E) are shown in Figures 3.19, 3.20, 3.21, 3.22, and 3.23, respectively. Three different models PL, LP, and PLEC are used to fit the spectral data points, and their model parameters are tabulated in Table 3.10, 3.11, 3.12, 3.13, and 3.14, respectively. A clear "harder-when-brighter" trends are noticed in all the substructures as the source travel from pre-flare phase to flare phase. A significant spectral hardening was observed in flare-2(B), 2(C), and 2(D) as the source moves from pre-flare to flare phase and the values changes from 2.38 to 2.17, 2.44 to 2.13, and 2.65 to 2.24, when fitted with PL distribution.

3.5.3 Flare-3

A progressive spectral hardening with increasing flux was also noticed during Flare-3. The flux changed from 1.28 to 2.88, and the corresponding spectral index changed from 2.47 to 2.32 respectively, as the source move from the pre-flare to the flare phase. The fitted spectral energy distributions for different phases of Flare-3 are shown in Figure 3.24, and the fitted parameters are mentioned in Table 3.15. A clear "harder-when-brighter" trend is confirmed.

3.5.4 Flare-4

A significant amount of spectral hardening was seen in substructures of Flare-4. Flare-4 was divided into three substructures flare-4(A), flare-4(B), flare-4(C), and these three have different phases. The gamma-ray SEDs are produced for all the different phases and fitted with three different spectral models. A spectral hardening with increasing flux is seen in all the substructures as the source travel from the pre-flare to the flare phase. The SEDs showed in Figure 3.25, 3.26, and 3.27, the model parameters are presented in Table 3.16, 3.17, and 3.18 for flare-4(A), flare-4(B), flare-4(C) respectively. During flare-4(A), flare-4(B), and flare-4(C) the flux changes from 2.21 to 6.41, 1.64 to 4.22, and 1.15 to 4.89 and corresponding photon spectral index decreases from 2.32 to 2.14, 2.40 to 2.19, and 2.42 to 1.96 respectively, which shows a clear "harder-when-brighter" trend.

3.5.5 Flare-5

The last flare in our data set also shows the "harder-when-brighter" trend as shown in Figure 3.28, and the corresponding model parameters are tabulated in Table 3.19. A progressive spectral hardening with increasing flux observed as the source travels from pre-flare to flare phase. The flux increases from 1.64 to 3.01 as the source travels from pre-flare to flare phase, and their corresponding photon spectral index changes from 2.58 to 2.39. A "harder-when-brighter" trend in Flare-5 is observed.

The reduced-χ^2 values for all the models (PL, LP, and PLEC) fit, and the spectral cut-off energies for PLEC fit for different flares are shown in Table 3.20. By comparing the reduced-χ^2 values of different models during flaring episodes, it was found that LP is the best fit among PL, LP, and PLEC for almost all the cases. It was also noticed that in the case of the PLEC fit, the spectral cutoff energy varies from flare to flare. It is interesting to note that in a few cases where the reduced chi-squared values for PLEC are comparable to the values obtained from LP fits, the cut-off energy is well constrained. This has strong physics implications regarding the location of the emission region.

3.5.6 Flux vs Index Plots

In eight years of *Fermi*-LAT observation five major flares were observed in PKS 1510-089. These flares were further divided in various substructures. Various phases like pre-flare, plateau, flare(I), flare(II), and post-flare were observed in different substructures. The gamma-ray spectral points for all the observed phases are produced and fitted with three different spectral models (PL, LP, PLEC). The obtained parameters like integral flux and photon spectral index corresponding to each phase are recorded in Table 3.8–3.19. The photon spectral index as a function of integral flux are plotted in Figure 3.29 for a few of substructures and a clear "harder-when-brighter" trend is seen in all the six cases.

In flare-1(A) and flare-2(A), all the five phases were observed, and the integral flux of all the phases with their spectral index are shown in the top panel of Figure 3.29. The number "1" and "5" represents the pre-flare and post-flare phases respectively, where the flux is low, and the spectral index is greater than 2.30 (3FGL value; Acero et al. 2015). As the flux started rising three different phases like a plateau, flare(I), and flare(II) were observed with a spectrum harder than 2.30. These phases are denoted by number "2", "3", and "4" in the top panel of Figure 3.29.

The middle panel of Figure 3.29 shows the index vs. flux plot for flare-2(B) and flare-2(C).

A similar "harder-when-brighter" trend is seen in both the cases as the source moves from the pre-flare to the flare state. The numbers "1", and "3" represent the pre-flare, and post-flare phase, whereas flare is represented by number "2". The spectral index corresponding to the pre-flare and post-flare phase is above 2.30 (3FGL value), and the flare phase shows the harder spectrum than 3FGL value.

The lower panel of Figure 3.29, represent the index vs. flux plot for four phases substructures (e.g., flare-3 & flare-4(B)). The number "1" and "4" represents the pre-flare and post-flare phases and number "2" & "3", corresponds to the flare(I) & flare(II) phases. A clear "harder-when-brighter" trend is seen in both the substructures.

A simple power law model is used to fit the data points to confirm the "harder-when-brighter" trends, and corresponding reduced-χ^2 value is also shown in Figure 3.29. These plots reveal that when the source gets brighter, its photon spectrum becomes harder, a feature which has also been seen in many other blazars. A similar result was also reported earlier by Foschini et al. (2013). A spectral hardening with increasing flux is a common feature of FSRQ types of blazars (e.g., 3C 454.3; Britto et al. 2016).

3.5.7 Summary of Spectral Analysis

1. The gamma-ray SEDs are produced for all the different phases (pre-flare, plateau, flare, and post-flare) and fitted with three different functional forms PL, LP, and PLEC. To obtain the best fit model, the Δlog(Likelihood) and reduced χ^2 values are calculated for each phase.

2. The reduced-χ^2 values for all the models (PL, LP, and PLEC) fit presented in Table 3.20 suggest that LP is the best model to describe the gamma-ray spectrum.

3. It has been seen that, if the gamma-ray emission region is close to the core of the source, pair production optical depth will prevent the escape of very high energy

gamma rays. As a result, the highest energy gamma-ray photons are expected from zones outside the BLR region, in the optically thin outer jet region (see Aleksić et al. 2014, MAGIC Collaboration).

4. The variations in spectral fittings and spectral cut-off energies of the flares indicate that different flares might have originated from different zones along the length of the jet of PKS 1510-089. Earlier studies on blazar flares also indicate the possibility of multiple emission zones during flares (Brown 2013, Dotson et al. 2012, Dotson et al. 2015). Detailed broadband spectral modeling with photon data ranging from radio to TeV energy would be more useful in exploring the complex nature of flares of this highly variable source.

Table 3.8 Results of SEDs fitted with different spectral types like PL, LP, PLEC. Different periods of activity of the flares (here flare-1(A)) are mentioned in the 1st column. The fitted fluxes and the spectral index are shown in the columns 2 & 3. The goodness of unbinned fits is presented by log(Likelihood) in column 5 and the Δlog(Likelihood) is calculated with respect to the log(Likelihood) of the PL fit (see text for more detail).

		PowerLaw (PL)			
Activity	$F_{0.1-300\ GeV}$ (10^{-6} ph cm^{-2} s^{-1})	Γ		-log(Likelihood)	
pre-flare	0.45±0.06	2.41±0.11	-	24496.5	-
flare(I)	3.73±0.15	2.30±0.04	-	20608.5	-
plateau	3.26±0.14	2.29±0.04	-	20170.3	-
flare(II)	4.57±0.12	2.24±0.02	-	38286.7	-
post-flare	2.27±0.10	2.52±0.05	-	24715.6	-
		LogParabola (LP)			
Activity	$F_{0.1-300\ GeV}$ (10^{-6} ph cm^{-2} s^{-1})	α	β	-log(Likelihood)	Δlog(Likelihood)
pre-flare	0.44±0.06	2.40±0.15	0.00±0.00	24496.5	0.0
flare(I)	3.72±0.15	2.28±0.05	0.00±0.00	20608.5	0.0
plateau	3.18±0.14	2.18±0.06	0.08±0.03	20166.4	-3.9
flare(II)	4.45±0.12	2.14±0.04	0.07±0.02	38279.2	-7.5
post-flare	2.24±0.10	2.46±0.06	0.06±0.04	24714.2	-1.4
		PLExpCutoff (PLEC)			
Activity	$F_{0.1-300\ GeV}$ (10^{-6} ph cm^{-2} s^{-1})	Γ_{PLEC}	E_{cutoff} [GeV]	-log(Likelihood)	Δlog(Likelihood)
pre-flare	0.44±0.06	2.32±0.15	9.359±7.506	24496.3	-0.2
flare(I)	3.71±0.15	2.26±0.04	30.000±0.253	20610.0	1.5
plateau	3.18±0.14	2.11±0.08	5.185 ±2.394	20164.8	-5.5
flare(II)	4.50±0.12	2.16±0.04	15.980±6.358	38281.0	-5.7
post-flare	2.24±0.10	2.40±0.08	6.081±3.856	24713.4	-2.2

Table 3.9 All the columns represent the same parameters as mentioned in Table 3.8, here results are shown for flare-1(B).

		PowerLaw (PL)			
Activity	$F_{0.1-300\ GeV}$ (10^{-6} ph cm^{-2} s^{-1})	Γ		-log(Likelihood)	
pre-flare	1.12 ± 0.07	2.50 ± 0.06	-	33110.1	-
flare	5.20 ± 0.15	2.41 ± 0.03	-	36271.2	-
post-flare	2.56 ± 0.09	2.33 ± 0.03	-	49194.4	-
		LogParabola (LP)			
Activity	$F_{0.1-300\ GeV}$ (10^{-6} ph cm^{-2} s^{-1})	α	β	-log(Likelihood)	Δlog(Likelihood)
pre-flare	1.10 ± 0.07	2.42 ± 0.08	0.08 ±0.05	33108.8	-1.3
flare	5.05 ± 0.15	2.30 ± 0.04	0.11 ±0.03	36260.6	-10.6
post-flare	2.48 ± 0.09	2.21 ± 0.05	0.09 ±0.03	49187.9	-6.5
		PLExpCutoff (PLEC)			
Activity	$F_{0.1-300\ GeV}$ (10^{-6} ph cm^{-2} s^{-1})	Γ_{PLEC}	E_{cutoff} [GeV]	-log(Likelihood)	Δlog(Likelihood)
pre-flare	1.10 ± 0.07	2.37 ± 0.10	5.948 ± 4.510	33108.5	-1.6
flare	5.10 ± 0.15	2.27 ± 0.05	5.740 ± 1.830	36262.9	-8.3
post-flare	2.52 ± 0.09	2.24 ± 0.05	11.670± 5.692	49191.0	-3.4

Table 3.10 All the columns represent the same parameters as mentioned in Table 3.8, here results are shown for flare-2(A).

Activity	$F_{0.1-300\ GeV}$ (10^{-6} ph cm^{-2} s^{-1})	PowerLaw (PL) Γ		-log(Likelihood)	
pre-flare	0.40 ±0.07	2.22±0.13	-	14835.3	-
flare(I)	2.80 ±0.20	2.19±0.06	-	9462.8	-
plateau	2.12 ±0.21	2.32±0.09	-	6705.2	-
flare(II)	2.89 ±0.14	2.21±0.04	-	21374.7	-
post-flare	0.56 ±0.08	2.23±0.10	-	15417.3	-
Activity	$F_{0.1-300\ GeV}$ (10^{-6} ph cm^{-2} s^{-1})	LogParabola (LP) α	β	log(Likelihood)	Δlog(Likelihood)
pre-flare	0.39 ±0.07	2.13±0.21	0.04±0.08	14835.1	-0.2
flare(I)	2.68 ±0.21	2.06±0.10	0.07±0.05	9461.2	-1.6
plateau	1.79 ±0.21	2.07±0.15	0.10±0.07	6697.8	-7.4
flare(II)	2.65 ±0.14	1.95±0.07	0.17±0.04	21362.3	-12.4
post-flare	0.50 ±0.08	1.97±0.21	0.14±0.10	15416.0	-1.3
Activity	$F_{0.1-300\ GeV}$ (10^{-6} ph cm^{-2} s^{-1})	PLExpCutoff (PLEC) Γ_{PLEC}	E_{cutoff} [GeV]	-log(Likelihood)	Δlog(Likelihood)
pre-flare	0.38 ±0.07	2.08±0.22	9.546±12.560	14834.6	-0.7
flare(I)	2.71 ±0.20	2.07±0.10	11.270±8.127	9461.0	-1.8
plateau	1.80 ±0.21	2.03±0.16	5.316±4.204	6697.3	-7.9
flare(II)	2.69 ±0.14	1.86±0.09	2.699±0.733	21359.9	-14.8
post-flare	0.51 ±0.08	1.94±0.21	4.121±3.184	15415.7	-1.6

Table 3.11 All the columns represent the same parameters as mentioned in Table 3.8, here results are shown for flare-2(B).

Activity	$F_{0.1-300\ GeV}$ (10^{-6} ph cm^{-2} s^{-1})	PowerLaw (PL) Γ		-log(Likelihood)	
pre-flare	1.07 ±0.10	2.38±0.08	-	17894.3	-
flare	2.15 ±0.11	2.17±0.04	-	21202.8	-
post-flare	0.71 ±0.07	2.57±0.10	-	20681.9	-
Activity	$F_{0.1-300\ GeV}$ (10^{-6} ph cm^{-2} s^{-1})	LogParabola (LP) α	β	-log(Likelihood)	Δlog(Likelihood)
pre-flare	1.02 ±0.11	2.26±0.13	0.09±0.07	17893.1	-1.2
flare	2.03 ±0.11	1.97±0.07	0.13±0.04	21196.0	-6.8
post-flare	0.70 ±0.07	2.48±0.13	0.11±0.10	20681.2	-0.7
Activity	$F_{0.1-300\ GeV}$ (10^{-6} ph cm^{-2} s^{-1})	PLExpCutoff (PLEC) Γ_{PLEC}	E_{cutoff} [GeV]	-log(Likelihood)	Δlog(Likelihood)
pre-flare	1.03 ±0.10	2.23±0.15	6.094±5.426	17893.1	-1.2
flare	2.06 ±0.11	1.98±0.08	5.818±2.364	21196.6	-6.2
post-flare	0.70 ±0.07	2.46±0.17	6.339±8.688	20681.5	-0.4

Table 3.12 All the columns represent the same parameters as mentioned in Table 3.8, here results are shown for flare-2(C).

Activity	$F_{0.1-300\ GeV}$ (10^{-6} ph cm^{-2} s^{-1})	PowerLaw (PL) Γ		-log(Likelihood)	
pre-flare	2.55 ±0.17	2.44±0.06	-	13635.9	-
flare	9.16 ±0.30	2.13±0.03	-	17028.5	-
post-flare	2.25 ±0.17	2.30±0.07	-	11397.9	-
Activity	$F_{0.1-300\ GeV}$ (10^{-6} ph cm^{-2} s^{-1})	LogParabola (LP) α	β	-log(Likelihood)	Δlog(Likelihood)
pre-flare	2.70 ±0.17	2.45±0.08	0.051±0.050	13642.8	6.9
flare	8.92 ±0.30	2.03±0.04	0.06±0.02	17023.4	-5.1
post-flare	2.25 ±0.17	2.30±0.07	0.00±0.00	11397.9	0.0
Activity	$F_{0.1-300\ GeV}$ (10^{-6} ph cm^{-2} s^{-1})	PLExpCutoff (PLEC) Γ_{PLEC}	E_{cutoff} [GeV]	-log(Likelihood)	Δlog(Likelihood)
pre-flare	2.50 ±0.17	2.34±0.10	9.067±8.024	13634.8	-1.1
flare	9.00 ±0.31	2.05±0.04	18.030±7.530	17023.2	-5.3
post-flare	2.22 ±0.17	2.26±0.07	30.000±0.080	11398.6	0.7

Table 3.13 All the columns represent the same parameters as mentioned in Table 3.8, here results are shown for flare-2(D).

Activity	$F_{0.1-300\ GeV}$ (10^{-6} ph cm^{-2} s^{-1})	PowerLaw (PL) Γ		-log(Likelihood)	
pre-flare	1.45±0.12	2.65±0.10	-	14564.0	-
flare	5.55±0.13	2.24±0.02	-	59688.8	-
post-flare	1.65±0.07	2.48±0.04	-	47148.3	-
Activity	$F_{0.1-300\ GeV}$ (10^{-6} ph cm^{-2} s^{-1})	LogParabola (LP) α	β	-log(Likelihood)	Δlog(Likelihood)
pre-flare	1.41±0.13	2.55±0.12	0.14±0.10	14562.7	-1.3
flare	5.35±0.13	2.11±0.03	0.09±0.02	59672.5	-16.3
post-flare	1.63±0.07	2.42±0.05	0.05±0.03	47147.0	-1.3
Activity	$F_{0.1-300\ GeV}$ (10^{-6} ph cm^{-2} s^{-1})	PLExpCutoff (PLEC) Γ_{PLEC}	E_{cutoff} [GeV]	-log(Likelihood)	Δlog(Likelihood)
pre-flare	1.42±0.13	2.44±0.18	3.140±2.743	14562.9	-1.9
flare	5.44±0.13	2.14±0.03	12.310±3.515	59677.4	-11.4
post-flare	1.63±0.07	2.38±0.07	8.401±5.696	47146.2	-2.1

Table 3.14 All the columns represent the same parameters as mentioned in Table 3.8, here results are shown for flare-2(E).

Activity	PowerLaw (PL) $F_{0.1-300\ GeV}$ (10^{-6} ph cm^{-2} s^{-1})	Γ		-log(Likelihood)	
pre-flare	2.91±0.09	2.40±0.03	-	49012.7	-
flare(I)	4.94±0.09	2.29±0.02	-	70122.5	-
flare(II)	4.13±0.13	2.49±0.03	-	26676.5	-
post-flare	1.26±1.05	2.64±0.08	-	13838.9	-
Activity	LogParabola (LP) $F_{0.1-300\ GeV}$ (10^{-6} ph cm^{-2} s^{-1})	α	β	-log(Likelihood)	Δlog(Likelihood)
pre-flare	2.87±0.10	2.36±0.04	0.03±0.02	49011.6	-1.1
flare(I)	4.78±0.09	2.17±0.02	0.09±0.01	70096.3	-26.2
flare(II)	4.06±0.14	2.44±0.04	0.06±0.03	26674.2	-2.3
post-flare	1.24±0.11	2.58±0.11	0.07±0.06	13838.4	-0.5
Activity	PLExpCutoff (PLEC) $F_{0.1-300\ GeV}$ (10^{-6} ph cm^{-2} s^{-1})	Γ_{PLEC}	E_{cutoff} [GeV]	-log(Likelihood)	Δlog(Likelihood)
pre-flare	2.89±0.09	2.37±0.03	29.970±3.615	49011.7	-1.0
flare(I)	4.83±0.09	2.16±0.03	7.612±1.533	70099.0	-23.5
flare(II)	4.08±0.14	2.41±0.05	9.709±5.118	26673.7	-2.8
post-flare	1.24±0.11	2.54±0.14	7.244±8.785	13838.4	-0.5

Table 3.15 All the columns represent the same parameters as mentioned in Table 3.8, here results are shown for Flare-3.

Activity	PowerLaw (PL) $F_{0.1-300\ GeV}$ (10^{-6} ph cm^{-2} s^{-1})	Γ		-log(Likelihood)	
pre-flare	1.28±0.02	2.47±0.01	-	15158.0	-
flare(I)	2.88±0.06	2.32±0.01	-	24129.8	-
flare(II)	2.22±0.01	2.35±0.02	-	29884.4	-
post-flare	1.78±0.02	2.40±0.01	-	30937.3	-
Activity	LogParabola (LP) $F_{0.1-300\ GeV}$ (10^{-6} ph cm^{-2} s^{-1})	α	β	-log(Likelihood)	Δlog(Likelihood)
pre-flare	1.29±0.11	2.45±0.09	0.02±0.00	15158.0	0.0
flare(I)	2.74±0.08	2.19±0.05	0.10±0.04	24123.9	-5.9
flare(II)	2.17±0.06	2.27±0.03	0.06±0.03	29883.2	-1.2
post-flare	1.76±0.08	2.36±0.04	0.04±0.01	30936.7	-0.6
Activity	PLExpCutoff (PLEC) $F_{0.1-300\ GeV}$ (10^{-6} ph cm^{-2} s^{-1})	Γ_{PLEC}	E_{cutoff} [GeV]	log(Likelihood)	Δlog(Likelihood)
pre-flare	1.27±0.10	2.41±0.08	16.580±2.897	15157.1	-0.7
flare(I)	2.78±0.10	2.15±0.05	5.022±0.180	24123.7	-6.1
flare(II)	2.17±0.05	2.24±0.03	9.043±0.223	29881.6	-2.8
post-flare	1.76±0.06	2.35±0.05	18.030±1.724	30936.5	-0.8

Table 3.16 All the columns represent the same parameters as mentioned in Table 3.8, here results are shown for flare-4(A).

		PowerLaw (PL)			
Activity	$F_{0.1-300\ GeV}$ (10^{-6} ph cm^{-2} s^{-1})	Γ		-log(Likelihood)	
pre-flare	2.21±0.07	2.32±0.03	-	50195.9	-
flare	6.41±0.17	2.14±0.04	-	30084.0	-
post-flare	2.92±0.12	2.42±0.04	-	34033.0	-
		LogParabola (LP)			
Activity	$F_{0.1-300\ GeV}$ (10^{-6} ph cm^{-2} s^{-1})	α	β	-log(Likelihood)	Δlog(Likelihood)
pre-flare	2.14±0.07	2.20±0.04	0.09±0.03	50188.6	-7.3
flare	6.03±0.18	2.03±0.06	0.06±0.03	30067.9	-16.1
post-flare	2.83±0.12	2.33±0.05	0.08±0.03	34029.4	-3.6
		PLExpCutoff (PLEC)			
Activity	$F_{0.1-300\ GeV}$ (10^{-6} ph cm^{-2} s^{-1})	Γ_{PLEC}	E_{cutoff} [GeV]	-log(Likelihood)	Δlog(Likelihood)
pre-flare	2.17±0.07	2.21±0.05	9.657±3.964	50191.3	-4.6
flare	6.35±0.17	2.04±0.07	12.785±8.115	30080.7	-3.3
post-flare	2.86±0.12	2.32±0.06	9.118±5.157	34030.2	-2.8

Table 3.17 All the column represents the same parameters as mentioned in Table 3.8, here results are shown for flare-4(B).

		PowerLaw (PL)			
Activity	$F_{0.1-300\ GeV}$ (10^{-6} ph cm^{-2} s^{-1})	Γ		-log(Likelihood)	
pre-flare	1.64±0.08	2.40±0.05	-	38092.3	-
flare(I)	4.22±0.11	2.19±0.04	-	39757.9	-
flare(II)	3.75±0.11	2.20±0.04	-	36387.9	-
post-flare	1.59±0.12	2.39±0.07	-	16506.6	-
		LogParabola (LP)			
Activity	$F_{0.1-300\ GeV}$ (10^{-6} ph cm^{-2} s^{-1})	α	β	-log(Likelihood)	Δlog(Likelihood)
pre-flare	1.62±0.08	2.37±0.06	0.02±0.03	38092.0	-0.3
flare(I)	4.12±0.11	2.09±0.05	0.07±0.00	39749.7	-8.2
flare(II)	3.61±0.11	2.06±0.04	0.10±0.02	36375.6	-12.3
post-flare	1.49±0.12	2.21±0.11	0.15±0.07	16503.3	-3.3
		PLExpCutoff (PLEC)			
Activity	$F_{0.1-300\ GeV}$ (10^{-6} ph cm^{-2} s^{-1})	Γ_{PLEC}	E_{cutoff} [GeV]	-log(Likelihood)	Δlog(Likelihood)
pre-flare	1.62±0.08	2.36±0.05	30.000±0.050	38093.6	1.3
flare(I)	4.14±0.11	2.06±0.05	9.073±0.308	39747.0	-10.9
flare(II)	3.67±0.11	2.08±0.04	9.743±3.159	36378.8	-9.1
post-flare	1.51±0.12	2.12±0.14	3.060±1.610	16503.0	-3.6

Table 3.18 All the columns represent the same parameters as mentioned in Table 3.8, here results are shown for flare-4(C).

Activity	$F_{0.1-300\ GeV}$ (10^{-6} ph cm^{-2} s^{-1})	PowerLaw (PL) Γ		-log(Likelihood)	
pre-flare	1.15±0.11	2.42±0.09	-	15800.4	-
flare	4.89±0.15	1.96±0.02	-	30002.9	-
post-flare	1.22±0.08	2.42±0.06	-	27063.2	-
Activity	$F_{0.1-300\ GeV}$ (10^{-6} ph cm^{-2} s^{-1})	LogParabola (LP) α	β	-log(Likelihood)	Δlog(Likelihood)
pre-flare	1.35±0.11	2.55±0.09	0.00±0.00	15817.6	17.2
flare	4.64±0.16	1.81±0.04	0.06±0.01	29993.2	-9.7
post-flare	1.16±0.09	2.29±0.10	0.11±0.06	27061.0	-2.2
Activity	$F_{0.1-300\ GeV}$ (10^{-6} ph cm^{-2} s^{-1})	PLExpCutoff (PLEC) Γ_{PLEC}	E_{cutoff} [GeV]	-log(Likelihood)	Δlog(Likelihood)
pre-flare	1.12±0.11	2.31±0.13	8.931±9.809	15799.8	-0.6
flare	4.75±0.16	1.88±0.03	29.710±8.166	29994.5	-8.4
post-flare	1.19±0.09	2.29±0.11	7.354±5.857	27061.7	-1.5

Table 3.19 All the columns represent the same parameters as mentioned in Table 3.8, here results are shown for Flare-5.

Activity	$F_{0.1-300\ GeV}$ (10^{-6} ph cm^{-2} s^{-1})	PowerLaw (PL) Γ		-log(Likelihood)	
pre-flare	1.64±0.12	2.58±0.08	-	14412.7	-
flare	3.01±0.11	2.39±0.04	-	28013.0	-
post-flare	1.85±0.09	2.38±0.04	-	29145.4	-
Activity	$F_{0.1-300\ GeV}$ (10^{-6} ph cm^{-2} s^{-1})	LogParabola (LP) α	β	-log(Likelihood)	Δlog(Likelihood)
pre-flare	1.63±0.12	2.55±0.10	0.04±0.06	14412.5	-0.2
flare	2.93±0.11	2.28±0.05	0.10±0.03	28007.3	-5.7
post-flare	1.82±0.09	2.31±0.06	0.06±0.04	29143.9	-1.5
Activity	$F_{0.1-300\ GeV}$ (10^{-6} ph cm^{-2} s^{-1})	PLExpCutoff (PLEC) Γ_{PLEC}	E_{cutoff} [GeV]	-log(Likelihood)	Δlog(Likelihood)
pre-flare	1.62±0.12	2.44±0.14	4.640±4.235	14411.7	-1.0
flare	2.95±0.11	2.23±0.07	5.016±2.001	28007.2	-5.8
post-flare	1.83±0.09	2.33±0.06	19.040±17.200	29144.5	-0.9

Table 3.20 The reduced-χ^2 for SEDs fitted by PowerLaw (PL), LogParabola (LP) and PowerLaw ExpCutoff (PLEC) for the flaring episodes are displayed below. In most cases, LP and in a few cases, PLEC provide the best fit to the data. Cutoff energies found with PLEC vary from one flare to another, which could be due to different emission regions of these flares.

Activity	Reduced-χ^2			E_{cutoff} for PLEC (GeV)
flare-1(A)	PL	LP	PLEC	
flare(I)	2.28	2.31	1.98	30.00±0.25
flare(II)	2.90	0.12	1.09	15.98±6.36
flare-1(B)				
flare	5.06	0.58	1.03	5.74±1.83
flare-2(A)				
flare(I)	3.66	1.91	2.40	11.27±8.13
flare(II)	2.84	0.92	0.48	2.70±0.73
flare-2(B)				
flare	2.15	0.23	0.43	5.82±2.36
flare-2(C)				
flare	1.73	0.41	0.83	18.03±7.53
flare-2(D)				
flare	8.14	0.43	2.83	12.31±3.51
flare-2(E)				
flare(I)	10.23	1.63	2.41	7.61±1.53
flare(II)	0.43	0.15	0.06	9.71±5.12
Flare-3				
flare(I)	2.73	0.91	1.19	5.02±0.18
flare(II)	0.41	0.42	0.34	9.04±0.22
flare-4(A)				
flare	11.93	3.25	5.82	12.78±8.11
flare-4(B)				
flare(I)	2.41	2.95	1.78	9.07±0.31
flare(II)	8.60	0.50	3.30	9.74±3.16
flare-4(C)				
flare	4.41	1.00	1.84	29.71±8.16
Flare-5				
flare	1.55	0.43	0.50	5.01±2.00

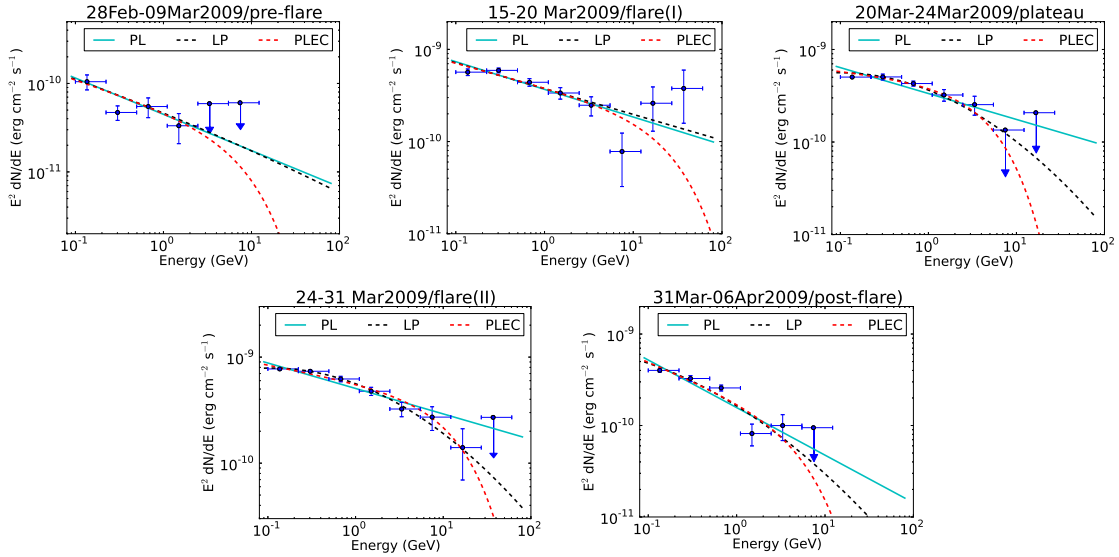

Fig. 3.17 Fermi-LAT SEDs during different activity states of flare-1(A) as defined in Figure 3.2, respective parameters are given in the Table 3.8.

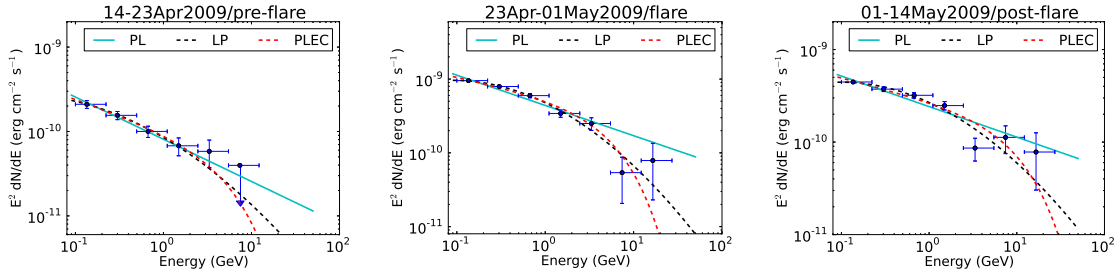

Fig. 3.18 Fermi-LAT SEDs during different activity states of flare-1(B) as defined in Figure 3.3, respective parameters are given in the Table 3.9.

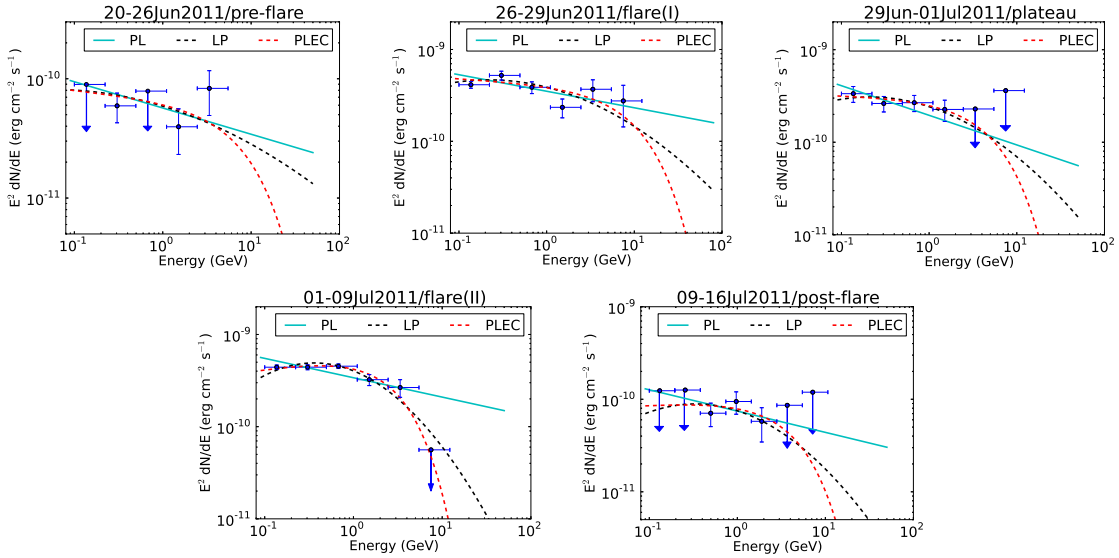

Fig. 3.19 Fermi-LAT SEDs during different activity states of flare-2(A) as defined in Figure 3.4, respective parameters are given in the Table 3.10. PL, LP, PLEC models are shown in cyan, black and red color respectively.

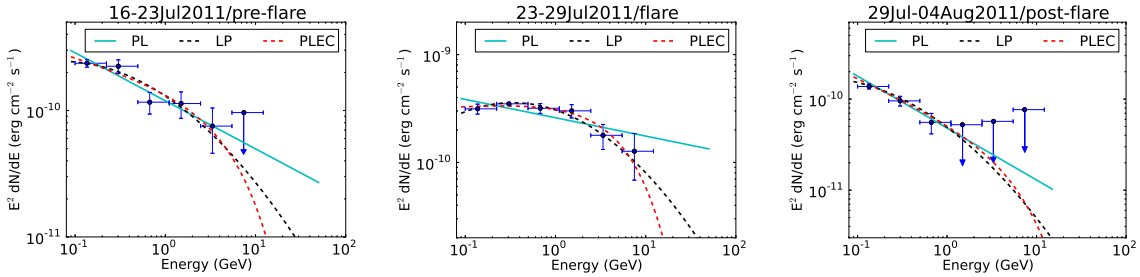

Fig. 3.20 Fermi-LAT SEDs during different activity states of flare-2(B) as defined in Figure 3.5, respective parameters are given in the Table 3.11.

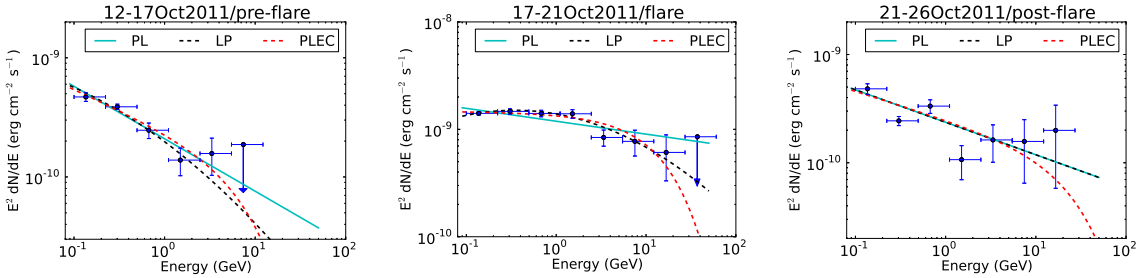

Fig. 3.21 Fermi-LAT SEDs during different activity states of flare-2(C) as defined in Figure 3.6, respective parameters are given in the Table 3.12.

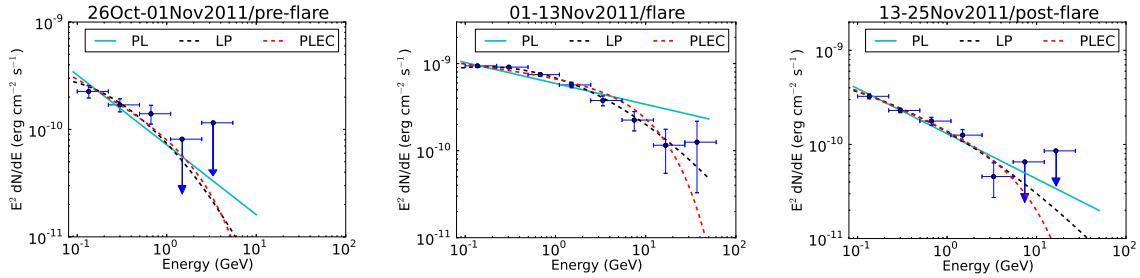

Fig. 3.22 Fermi-LAT SEDs during different activity states of flare-2(D) as defined in Figure 3.7, respective parameters are given in the Table 3.13.

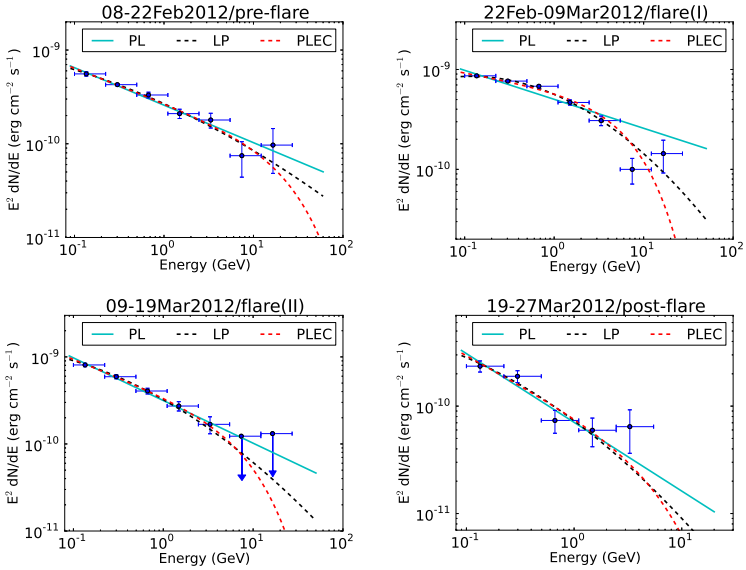

Fig. 3.23 Fermi-LAT SEDs during different activity states of flare-2(E) as defined in Figure 3.8, respective parameters are given in the Table 3.14. PL, LP, PLEC models are shown in cyan, black and red color.

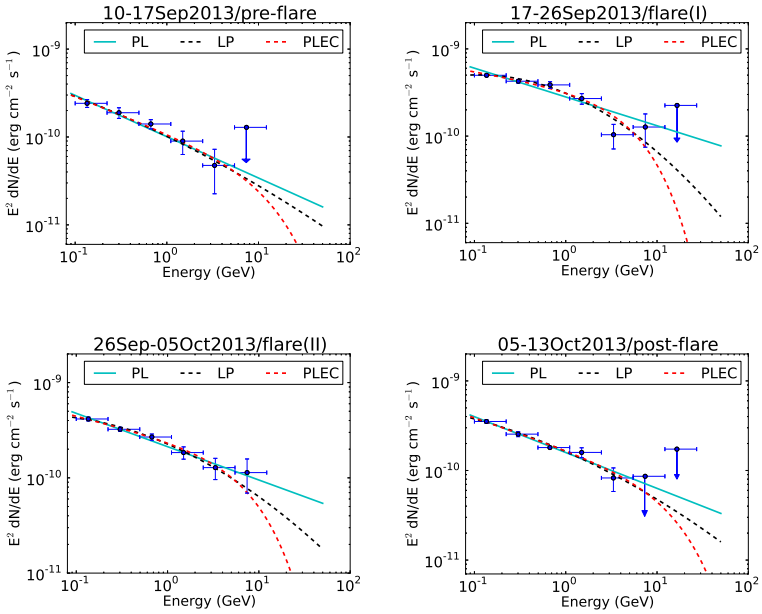

Fig. 3.24 Fermi-LAT SEDs during different activity states of Flare-3 as defined in Figure 3.9, respective parameters are given in the Table 3.15.

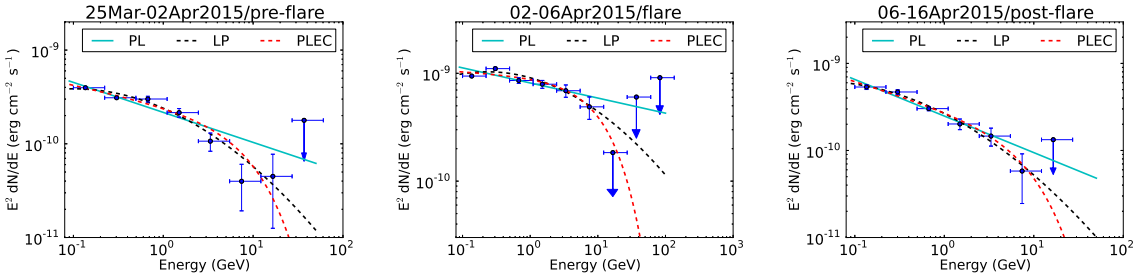

Fig. 3.25 Fermi-LAT SEDs during different activity states of flare-4(A) as defined in Figure 3.10, respective parameters are given in the Table 3.16.

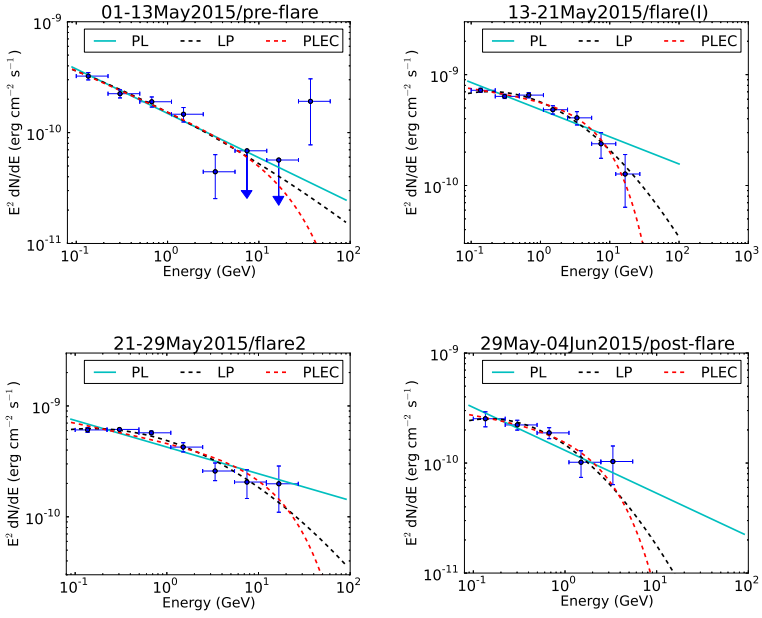

Fig. 3.26 Fermi-LAT SEDs during different activity states of flare-4(B) as defined in Figure 3.11 . PL, LP, PLEC models are shown in cyan, black and red color and there respective parameters are given in the Table 3.17.

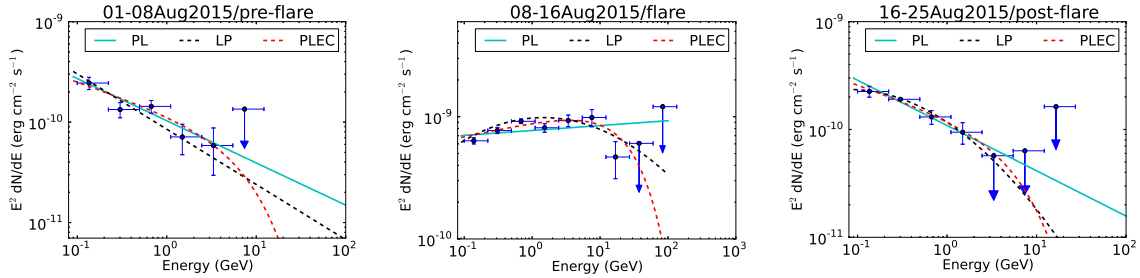

Fig. 3.27 Fermi-LAT SEDs during different activity states of flare-4(C) as defined in Figure 3.12 . PL, LP, PLEC models are shown in cyan, black and red color and there respective parameters are given in the Table 3.18.

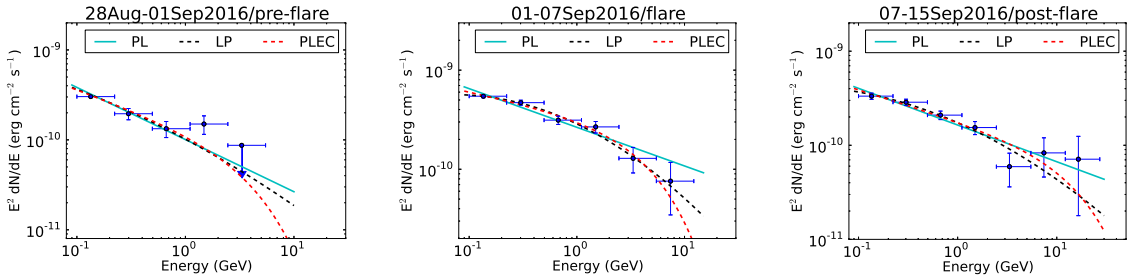

Fig. 3.28 Fermi-LAT SEDs during different activity states of Flare-5 as defined in Figure 3.13 . PL, LP, PLEC models are shown in cyan, black and red color and there respective parameters are given in the Table 3.20.

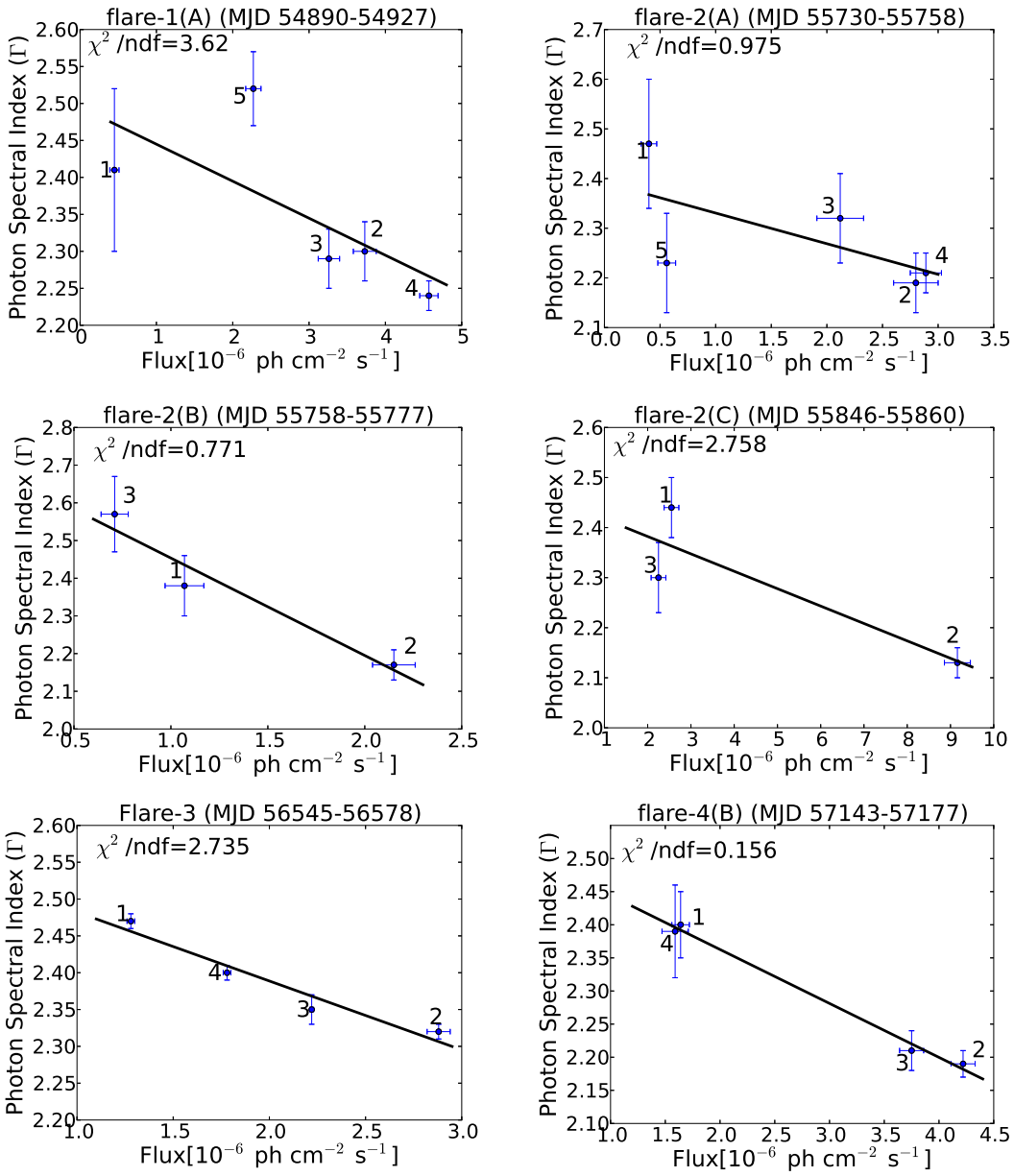

Fig. 3.29 Photon index vs flux are plotted for few sub-flares. And the numbers 1, 2, 3, 4, 5 represent the different time periods. Top panel: 1, 2, 3, 4 and 5 represents the pre-flare, flare(I), plateau, flare(II) and post-flare states respectively. Middle panel: 1, 2 and 3 represents the pre-flare, flare and post-flare respectively. Bottom panel: 1, 2, 3, and 4 represents the pre-flare, flare(I), flare(II) and post-flare respectively. All the points have been fitted by the PL spectral type and the corresponding reduced χ^2 have been mention in the plots. Errors, associated with each data points, are statistical only.

3.6 Two-zone Emission Modeling of PKS 1510-089 During Flare of 2015

3.6.1 Introduction

A long-term analysis of the light curve of PKS 1510-089 with eight years of *Fermi*-LAT data showed several flares. Their temporal and spectral features are discussed in Section 3.4 & 3.5 and also in Prince et al. (2017). A multiwavelength approach is employed here to explain the emission observed in different wavebands during the flare of 2015.

A multiwavelength study has been done by the Abdo et al. (2010a) for the flare observed between September 2008 and June 2009. Their correlation study between different wavelengths reveals that the gamma-ray emission is in weak correlation with UV, strong correlation with optical, and has no correlation with the X-ray emission.

In modeling the SEDs of PKS 1510-0089, it is believed that the low energy emission (radio, optical) can be explained by the synchrotron radiation of the relativistic electrons and the high energy emission (X-ray, gamma-ray) can be seen as the product of inverse Compton scattering of the seed photons in broad line region (BLR) and dusty torus region (Kataoka et al. 2008; Abdo et al. 2010a; Brown 2013; Barnacka, Anna et al. 2014).

Detailed multiwavelength modeling of the flare observed during 2012 January–April covering radio to very high energy gamma rays, is done by Aleksić et al. (2014). They explained the multiwavelength emission as the result of turbulent plasma flowing at relativistic speeds down the jet and crossing a standing conical shock.

Two-zone multiwavelength modeling of high activities seen in PKS 1510-089 during 2011 was studied before by Nalewajko et al. (2012). They have collected the multiwavelength data from the different telescope, which includes Herschel observations, *Fermi*-LAT, Swift, SMARTS, and Sub-millimeter Array (SMA) data, for explaining the spectral and temporal features observed in PKS 1510-089 during 2011.

From March to August, 2015, this source was again very active and very high energy gamma-rays were observed with H.E.S.S telescope. Optical R-band monitoring with ATOM, supporting H.E.S.S. observations, detected a very high flux of optical photons (Zacharias et al. 2017a) during the flare of May 2015. Its enhanced activity in high energy gamma rays was also observed by the MAGIC telescope (Ahnen et al. 2017). The complex nature of multiwavelength emission indicated that a single zone model is not suitable for explaining the flares of PKS 1510-089. In this particular study, several months of observational data have been considered for the multiwavelength modeling of the high state of PKS 1510-089 in 2015. The temporal and spectral features of the optical, UV, X-ray and gamma-ray data have been included to infer the emission regions and model the spectral energy distributions with the time-dependent code GAMERA[2].

3.6.2 Multiwavelength Data Analysis

The *Fermi*-LAT and Swift-XRT/UVOT observations together cover more than ten orders of magnitude in photon energy, hence immensely useful in modeling blazar flares.

Fermi-LAT

The third *Fermi* source catalog (3FGL; Acero et al. 2015) shows that the extragalactic sky is dominated by the active galactic nuclei (AGN) emitting high energy gamma rays. Thousands of sources have been observed in the gamma-ray sky by the Large Area Telescope (LAT) on-board Fermi satellite. *Fermi*-LAT has continuously monitored the FSRQ PKS 1510-089 since August, 2008. The standard data reduction and analysis procedure[3] is used to analyze the *Fermi*-LAT data. LAT covers 20% of the sky at any time because of its large field of view (2.4 sr; Atwood et al. 2009) and it can scan the whole sky every three hours. Its working energy range is between 20 MeV to 500 GeV.

[2]https://github.com/libgamera/GAMERA
[3]https://fermi.gsfc.nasa.gov/ssc/data/analysis/documentation/

In this study, we have analyzed the *Fermi*-LAT data of year 2015. Our analysis considered the energy range between 100 MeV to 300 GeV. A circular region of radius 10° was chosen around the source also known as region of interest (ROI). The detailed description of analysis procedure is mentioned in section 3.2. The data analysis procedure rejected the events having zenith angle higher than 90° just to reduce the contamination from the earth limb. In this analysis, we have used the latest instrument Response Function "P8R2_SOURCE_V6" provided by the *Fermi* Science Tools.

The gamma-ray SEDs are produced in the energy range 0.1–300 GeV by using the unbinned likelihood analysis. The observed gamma-ray spectrum are fitted with four different spectral models, Power Law (PL), Log Parabola (LP), Power Law with Exponential cut-off (PLEC), and Broken Power Law (BPL) as discussed in Section 3.2. Further details procedure of *Fermi*-LAT data analysis are presented in section 2.1.1 of chapter 2.

Swift-XRT/UVOT

PKS 1510-089 is also observed by Swift-XRT/UVOT during the flares of 2015. Swift data for PKS 1510-089 has been collected from *HEASARC* webpage[4] for a period of one year during 2015. In total, 44 observations are reported during the year 2015. A 20 arc second source and the background region are chosen around the source and away from the source respectively. A task "*xrtpipeline*" is used to get the cleaned events file. The X-ray spectrum is obtained and fitted in "xspec" by using a simple power law model with the galactic absorption column density $n_H = 6.89 \times 10^{20}$ cm^{-2} (Kalberla et al. 2005).

The *Swift* Ultraviolet/Optical Telescope (UVOT) also observed the PKS 1510-089 in all the available six filters *U*, *V*, *B*, *W1*, *M2*, and *W2*. The source image has been extracted by choosing a circular region of 5 arcsecond around the source. Similarly, the background region is also selected with a radius of 10 arcsecond away from the source. The task 'uvotsource' has been used to extract the source magnitudes and fluxes. Magnitudes are corrected for

[4]https://heasarc.gsfc.nasa.gov/cgi-bin/W3Browse/w3browse.pl

galactic extinction (E(B-V) = 0.087 mag; Schlafly and Finkbeiner 2011) and converted into a flux using the zero points (Breeveld et al. 2011) and conversion factors (Larionov et al. 2016). Other details about the Swift-XRT and UVOT data analysis procedure are provided in Section 2.1.2 of Chapter 2.

Radio data at 15 and 230 GHz

The flare of PKS 1510-089 during 2015 is also observed in radio at 15 GHz and 230 GHz by OVRO (Richards et al. 2011) and Sub-millimeter array (SMA; Gurwell et al. 2007) telescope. These two observatories are part of the *Fermi* monitoring program, and the archival data from both the observatories are collected for the year of 2015.

3.6.3 Multiwavelength Light Curves

Multiwavelength light curve for PKS 1510-089 during the year 2015 are shown in Figure 3.30. A number of flaring episodes are observed in all the wavebands followed by the few quiescent states. In Figure 3.30, the top panel represents the gamma-ray light curve in energy range 0.1–300 GeV from the *Fermi*-LAT, second top panel shows the X-ray light curve for 0.3–10 keV energy range from Swift-XRT, and the bottom two panels represent the optical and UV light curves from UVOT. The identification of flares are done based on the observed gamma-ray flux during different time periods. We have used the fractional variability amplitude (Fossati et al. 2000; Vaughan et al. 2003) to define the variable and quiescent state. Detailed description of fractional variability is presented in Chapter 4. We have set a criteria that, If the fractional variability for a particular time period is observed above 50% and the average flux is significantly high, then this period will consider as flaring period. The fractional variability and the average flux was estimated for various time periods shown in Figure 3.30. The fractional variability amplitude is found to be 0.50±0.04 for a time period of MJD 57023–57100. The average flux observed during this period is 2.49±0.10 ($\times 10^{-7}$

ph cm^{-2} s^{-1}) and is constant over the time period. We define this period as quiescent state Q1.

The source has gone to a higher state for a period of 50 days from MJD 57100-57150 and the average flux measured during this period is 10.06±0.19 ($\times 10^{-7}$ ph cm^{-2} s^{-1}) which is five times higher than the quiescent state Q1 flux value. The fractional variability recorded for this period is 0.67±0.02 which reveals that the source is more variable than the state Q1. This period of high flux and large fractional variability is defined as flare A as shown in Figure 3.30.

As soon as the flare A ended in within 2-3 days the flux again started rising and lasted for a month. The period is noted between MJD 57150–57180. The average flux found during this higher state is 12.17±0.26 ($\times 10^{-7}$ ph cm^{-2} s^{-1}) and the fractional variability estimated as 0.57±0.02. This period of higher fractional variability and high flux state is defined as flare B and shown in Figure 3.30.

After flare B, the source flux reduced to a very low value compared to flare A and flare B and continued for a month in the low flux state. The time period is defined as MJD 57180–57208 and the average flux obtained was 5.37±0.21 ($\times 10^{-7}$ ph cm^{-2} s^{-1}). The fractional variability noticed during this period is 0.28±0.04 which is not significant as it is below 30%. This period is named as quiescent state Q2 because of the low flux value and fractional variability.

After spending a month in low flux state Q2, the source again started showing high activity. The period of high activity state was considered between MJD 57208–57235. The average flux measured during this high activity was 7.20±0.23 ($\times 10^{-7}$ ph cm^{-2} s^{-1} which is higher than the average flux observed during state Q1 and Q2. The fractional variability found during this period is 0.51±0.03, which is just above the limit we have set (50%). This period is defined as flare C which is more like an orphan optical/UV flare (Figure 3.30).

A higher flux state surpassing all the observed flares and quiescent states are observed dur-

ing MJD 57235–57260. The average flux found during this period is much higher than the average flux noticed during any of the other states. The average flux value is estimated to be 12.67±0.36 ($\times 10^{-7}$ ph cm^{-2} s^{-1}). Huge flux variation was observed during this period and can be confirmed from Figure 3.30. The fractional variability is estimated to be 1.16±0.03 which is more than 100%. This period of high flux states and large fractional variability is defined as flare D.

The flux reduced sharply after flare D and achieved an average flux value of 2.93±0.12 ($\times 10^{-7}$ ph cm^{-2} s^{-1}). The source continued to be in this low flux states between MJD 57260–57320. The fractional variability is estimated to be 0.50±0.05 and the observed flux is very low. This period is defined as quiescent state Q3. The source finally settled down to a low flux state till the end of the year 2015.

The maximum flux achieved during flare A, B, C, and D are 38.4, 27.9, 15.78, and 55.05 in units of $\times 10^{-7}$ ph cm^{-2} s^{-1} and the corresponding times are MJD 57115.5, 57167.5, 57220.5, and 57244.5 respectively. Among all four flares, flare D is observed to be the brightest gamma-ray flare of the year 2015.

No X-rays or UVOT observations were found for quiescence state Q1 and Q2. However, The number of observations are available for all the flares and quiescence state Q2. Different flares and quiescence state Q2 are separated by each other by vertical green lines, as shown in Figure 3.30. From the visual inspection to the light curve of X-ray, UV, and Optical, it is very much clear that the flux is indeed high in these wavebands corresponding to the different flaring state observed in the gamma-ray light curve.

In Figure 3.30, the gamma-ray light curve is binned in one day time bin and other light curves do not have equally spaced binning as different observations were carried out at different times. The average time bin for X-ray and optical/UV light curves are estimated and it is found to be 3.4 days in X-rays, and in optical/UV band it is found to be 4.1, 4.3, 3.8, 3.8, 4.4, and 3.5 days for filters U, B, V, W1, M2, W2 respectively.

3.6.4 Variability Time Scale

The variability time is a measure of how fast the flux changes between two consecutive time intervals. The variability time measured in different wavebands can tell us about the size and locations of different emission regions involved in multiwavelength emission. This section focuses on the variability study in various emission bands.

γ-ray variability

The multiwavelength light curve of PKS 1510-089 during the flare of 2015 is shown in the Figure 3.30. The uppermost panel represents the *Fermi*-LAT data in the energy range of 0.1-300 GeV. A high activity state is observed during year 2015, as it had also been seen earlier. The maximum flux achieved during the year 2015 is 5.50±0.34 ($\times 10^{-6}$ ph cm^{-2} s^{-1}) with photon spectral index 1.86 at MJD 57244.5. The gamma-ray light curve during year 2015 is shown separately in Figure 3.31 along with the corresponding photon spectral index. A clear flux variability is seen in the upper panel of Figure 3.31 and the lower panel represent the photon spectral index corresponding to each gamma-ray flux point. All the flares observed during year 2015 show that as the flux increases in the gamma-ray the corresponding photon spectral index becomes harder.

The flux doubling/halving time is estimated during the flaring episodes by using the following expression,

$$F_2 = F_1 . 2^{(t_2 - t_1)/\tau_d} \tag{3.8}$$

where, F_1 and F_2 are the fluxes observed at two consecutive times t_1 and t_2 and the τ_d is the flux doubling/halving time scale. One day binned gamma-ray light curve, shown in Figure 3.31, exhibit the variability time of 10.6 hr. This is found to be one of the fastest variability time during year 2015, when the source flux is changing from 1.15×10^{-6} to 5.50×10^{-6} between MJD 57243.5 to MJD 57244.5.

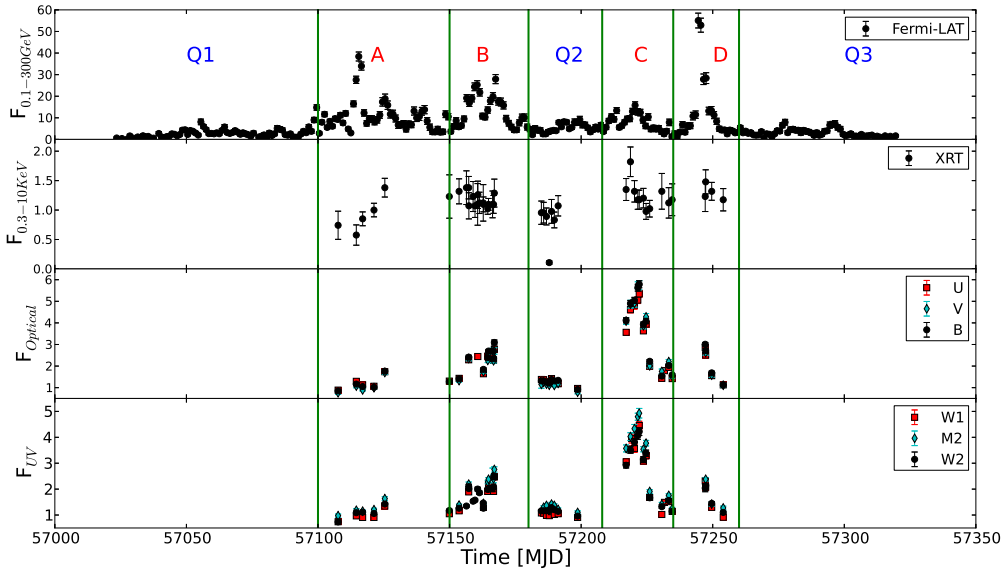

Fig. 3.30 Light curve of PKS 1510-089 during 2015. Four major flares A, B, C, and D have been detected with three quiescent states Q1, Q2, and Q3. Vertical green lines separate the different states of the source. Top panel represents the Fermi-LAT data for 1 day binning, second top panel represents the Swift-XRT data in the energy range of 0.2-10 KeV, and the last two panels show the data in different filters of the Swift-UVOT telescope.

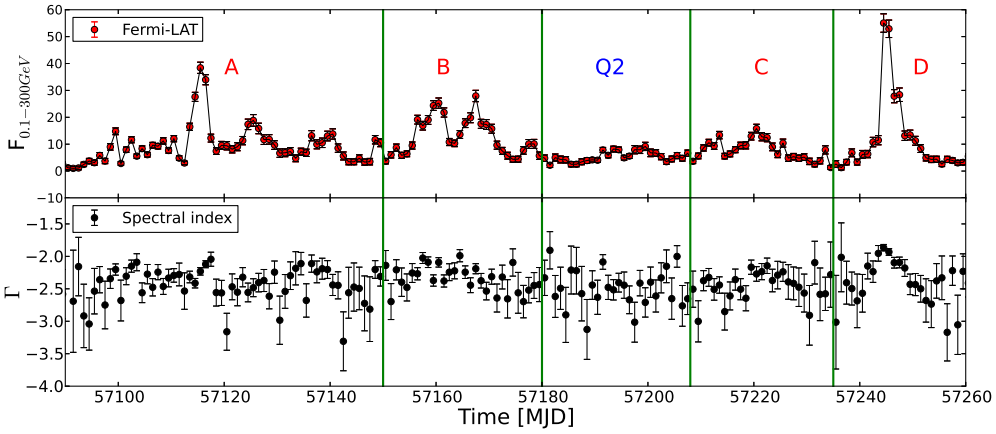

Fig. 3.31 One day binned gamma-ray light curve with corresponding spectral index.

X-ray variability

The X-ray and UV/optical emission during year 2015 are also captured by the Swift-XRT/UVOT telescope to unveil the behavior in X-ray, UV, and Optical. The second panel of Figure 3.30 represents the X-ray light curve in the energy range of 0.3–10 keV. The source is observed to be less variable in X-rays and the flaring states cannot be clearly identified. The flux doubling time is estimated by using equation 3.8 from X-ray light curve and it is found to be 2.5 days for $F_1 = 1.38\times10^{-11}$ erg cm^{-2} s^{-1} at t_1 = MJD 57156.41 and $F_2 = 1.07\times10^{-11}$ erg cm^{-2} s^{-1} at t_2 = MJD 57157.34.

Optical and UV variability

The Optical and UV light curve for all the available filters in *Swift*-UVOT are plotted in the last two panels of Figure 3.30 respectively. A significant amount of flux variability is noticed during flare C, whereas flare A, B, and D are found to be less variable. In these three flares (A, B &D) the variability of the source is constrained by the number of observations. The variability times estimated from *U*, *B*, and *V* band light curves are 1.0, 0.7, and 1.1 days respectively. In UV bands filters (*W1*, *M2*, *W2*), the variability times are found to be 0.8, 1.4, and 1.1 days.

The details about the variability time and other parameters are shown in Table 3.21.

Radio Light curves

The radio light curve of PKS 150-089 in two different frequencies are shown in Figure 3.32, for year 2015. Owens Valley Radio Observatory (OVRO) and Sub-millimeter array (SMA) telescope radio data at 15 GHz and 230 GHz are plotted in top and bottom panel of Figure 3.32 respectively. The radio light curves during 2015 clearly show that the radio flux in both the band is increasing towards the end of the year. The maximum radio flux in 2015 has been recored as 4.77 Jy and 4.55 Jy at 15 GHz and 230 GHz respectively. The variability

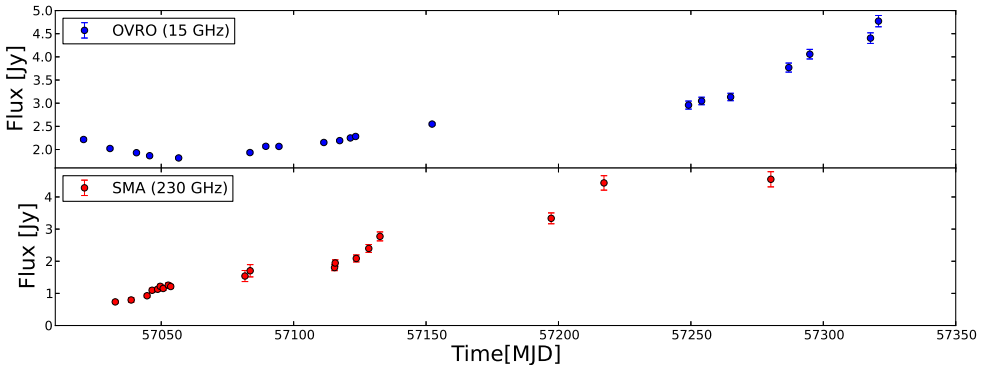

Fig. 3.32 OVRO (15 GHz) and SMA (230 GHz) radio light curve for PKS 1510-089 during flares of 2015.

time for both the radio light curve is not estimated because of the poorly sparse radio flux data points.

3.6.5 Fractional Variability (F_{var})

In order to compare and quantify the total variability in various wavebands, the fractional variability was estimated following the Vaughan et al. (2003). The detailed description of the fractional variability are presented in the chapter 4. It is used to find out the variability across the entire electromagnetic spectrum. The fractional variability of the multiwavelength light curve shown in Figure 3.30 and Figure 3.32 are estimated and mentioned in Table 3.22. The estimated F_{var} is plotted in Figure 3.33 along with the frequency. An increasing trend was observed in the radio frequency. In optical/UV frequency range it showed a peak which is followed by a dip in X-ray waveband. Again an increasing trend of F_{var} was observed between X-rays and gamaa-rays. The Figure 3.33 resembles a double-hump structure, similar to the multiwavelength SED of FSRQ type of blazar. The double peak in F_{var} was also noticed by several authors for different blazars (Soldi et al. 2008; Aleksić et al. 2015; Chidiac et al. 2016).

Table 3.21 Table shows the variability time estimated from equation 3.8 for all the different bands. The units of gamma-ray fluxes (F_1 & F_2) are in 10^{-7} ph cm^{-2} s^{-1} and X-rays/Optical/UV are is units of 10^{-11} erg cm^{-2} s^{-1}.

Telescope/Bands	F_1	F_2	t_1	t_2	t_{var}
Fermi-LAT					(hr)
γ-rays	1.15	5.50	57243.5	57244.5	10.6
Swift-XRT/UVOT					(days)
X-rays	1.38	1.07	57156.41	57157.34	2.5
U	2.27	2.78	57166.72	57167.01	1.0
B	2.35	3.09	57166.72	57167.01	0.7
V	2.24	2.70	57166.72	57167.01	1.1
W1	1.91	2.47	57166.72	57167.01	0.8
M2	2.40	2.76	57166.72	57167.01	1.4
W2	2.07	2.47	57166.72	57167.01	1.1

Table 3.22 The fractional variability amplitude estimated across the entire electromagnetic spectrum.

Telescope/Bands	F_{var}	err(F_{var})
Fermi-LAT		
γ-ray	1.04	0.01
Swift-XRT/UVOT		
X-rays	0.14	0.04
U	0.55	0.01
B	0.59	0.01
V	0.64	0.01
W1	0.57	0.01
M2	0.53	0.01
W2	0.48	0.01
OVRO (15 GHz)	0.34	0.01
SMA (230 GHz)	0.60	0.02

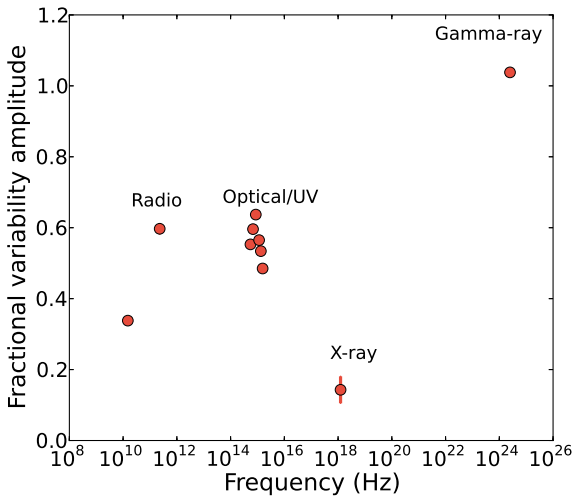

Fig. 3.33 The fractional variability amplitude of PKS 1510-089 from radio to gamma-ray frequencies.

3.6.6 Cross-correlation Studies

A cross-correlation study between various waveband emissions are done to probe the location of different emission regions responsible for multiwavelength emission along the jet axis. The Discrete Correlation Function (DCF) formulated by Edelson and Krolik (1988) are used to estimate the cross and auto-correlations of the unevenly sampled light curves. In this study, the DCF is estimated for a few different waveband combinations and the combinations are: γ-ray vs. Swift B band, γ-ray vs. X-rays, γ-ray vs. OVRO, γ-ray vs. SMA, and OVRO vs. SMA. The DCF for all the combinations are plotted in Figure 3.34. When the two light curves LC1 and LC2 are cross-correlated, there are three possibility that could happen; positive lag, zero lag, and negative lag. A positive time lag between LC1 and LC2 implies that the light curve LC1 is leading with respect to LC2, and a negative time lag implies the opposite. A zero time lag suggest the simultaneous emission.

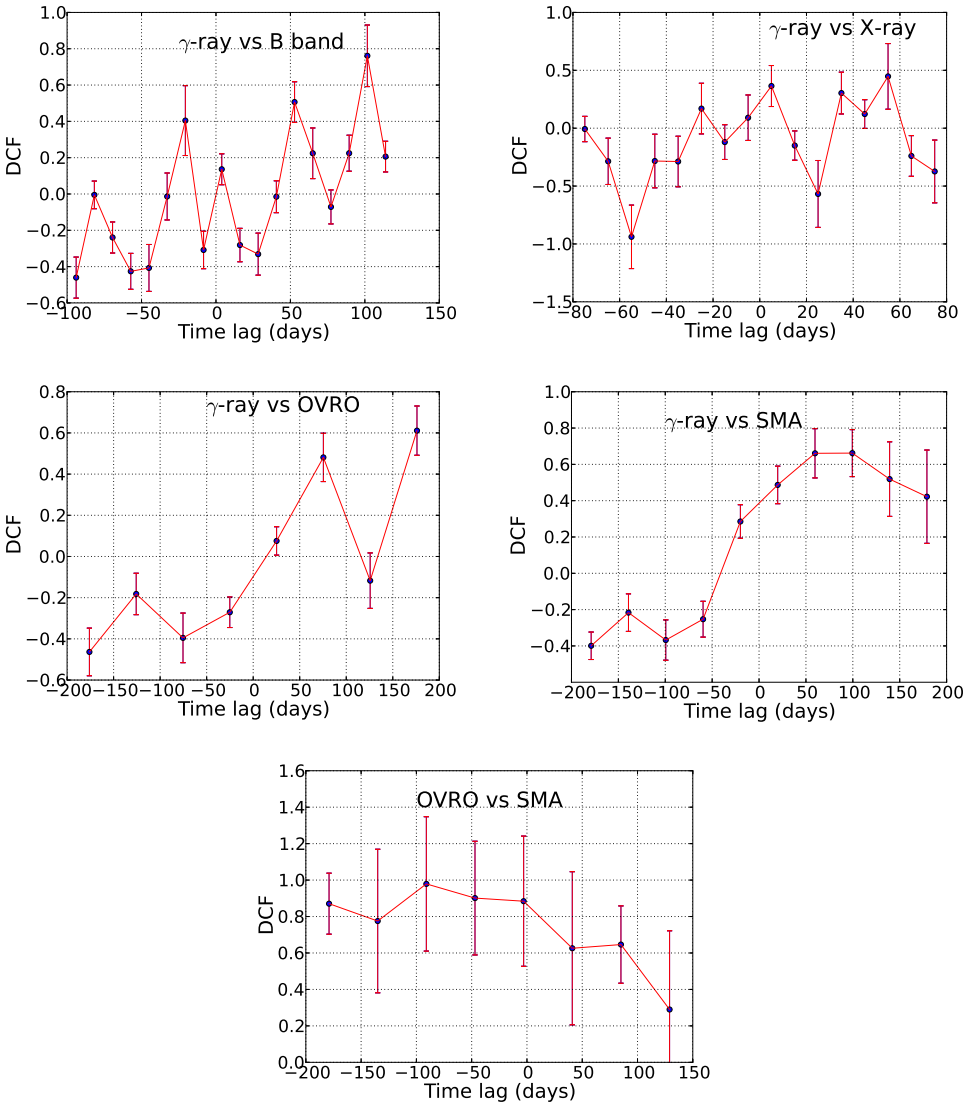

Fig. 3.34 DCFs for different combinations are plotted from top to bottom. The meaning of positive and negative time lags are described in section 3.6.6.

γ-ray vs optical B-band DCF:

DCF for all the combinations are shown in Figure 3.34 and the left plot of upper panel shows the DCF between γ-ray and Swift optical B-band. Various peaks at different time lags are observed but the peak close to zero time lag was selected to constrain the location of the emission region. The peaks observed at +52 days and -20 days and beyond that could be due to a strong gamma-ray flare correlating with the strong optical flare within the total period used for the DCF analysis. A peak with low correlation coefficient is observed at a time lag of 3.9 days. The average time resolution of the worst light curve is estimated. To produce the good DCF, the time bin was chosen to be at-least three times of the average time resolution of the worst light curve (Edelson and Krolik 1988; Castignani, G. et al. 2014). In case of gamma-ray vs. optical B-band the DCF time bin was chosen to be 12.2 days and the peak found within the DCF time bin was not considered to be a time lag. Multiple peaks in DCF was also observed by Kushwaha et al. (2017) for 3C 454.3 during segment 4 as mentioned in their paper. The zero time lag was observed in PKS 1510-089 by Castignani et al. (2017) and the small time lag was observed in our case is consistent with the results obtained by Abdo et al. (2010a) and Nalewajko et al. (2012) for other epochs. A zero or small time lag between two different waveband emissions suggest their co-spatial origin. Similar results were also observed for different sources (Prince 2019, Kaur and Baliyan 2018). A small time lag seen between gamma-ray and optical B band emission suggest that the gamma-ray and optical photons are produced in the same region by the inverse Compton and synchrotron emission of the same population of electrons respectively.

γ-ray vs X-ray DCF:

The gamma-ray vs. X-ray DCF is shown in the right side of the upper panel in Figure 3.34. A DCF peak with a correlation coefficient 0.36 ± 0.17 was observed at a time lag of 4.99 days. The DCF time bin is chosen to be 10.2 days based on the average time resolution of

the X-ray light curve. The observed peak is within the DCF time bin and hence was not considered as the time lag between gamma-ray and X-ray emission. The peak observed at the boundary of the DCF plot can be discarded. The DCF produced by Castignani et al. (2017) for PKS 1510-089 between gamma-rays and X-rays shows a time lag of 50 days. The time lag between gamma-rays and X-rays suggests that the X-rays might have been produced far away from the gamma-ray emission region. However, our DCF study does not show any such behavior. A small correlation coefficient observed in our case makes our results consistent with the result obtained by Abdo et al. (2010a), where they have also been unable to find any robust evidence of cross-correlation between gamma-ray and X-ray emission at zero time lag.

γ-ray vs OVRO and SMA DCF:

The middle panel of Figure 3.34 represent the gamma-ray vs. OVRO (15 GHz) and gamma-ray vs. SMA (230 GHz) DCFs in left and right side respectively. A DCF peak at time lag of 75 days was observed in gamma-ray vs. OVRO, which is almost equal to one third of the length of the OVRO light curve. Hence, it cannot be considered to be a DCF peak. Similar behavior is also seen in gamma-ray vs. SMA DCF, where a peak is observed at a time lag between 60–100 days. This peak also lies at one third of the length of the SMA light curve and hence cannot be considered as DCF peak.

OVRO vs SMA DCF:

The DCF between OVRO and SMA light curve was also estimated and the result is plotted in the lower panel of Figure 3.34. No significant DCF peak was observed in their correlation. Therefore, it is unfair to comment anything about the correlation between these two emissions.

The DCF plot presented in Figure 3.34 shows that no good correlation was observed in any

of the pairs. One of the reasons behind this could be non-availability of good quality data or a small number of observations in X-ray, optical, and radio wavebands for this particular period of time. Therefore, we cannot justifiably conclude anything about the locations of the different emission regions from this analysis.

3.6.7 Multiwavelength SEDs

The observations shows that the year 2015 was a very active period for PKS 1510-089 in gamma-ray energy band. The detailed analysis reveals that the source went through a long and bright flaring episodes during this period. During one year of time span, four major bright flaring episodes was identified as Flare-A, Flare-B, Flare-C, and Flare-D along with three quiescence state Q1, Q2, and Q3. The gamma-ray spectral energy distributions (SEDs) are produced for all the four gamma-ray flares along with one of the quiescent state Q2. The gamma-ray SEDs points are fitted with four different spectral models presented in section 3.2 as equation 3.1, 3.2, 3.3, and 3.4, the spectral models are LP, LP, PLEC, and BPL. Figure 3.35 shows the gamma-ray SED fitting and the corresponding model parameters are tabulated in Table 3.23. The log(Likelihood) value of different fits, which tells us about the quality of the unbinned fit, are compared to each other and found that gamma-ray SEDs are well described by the LP distribution function. It has been discussed in literature that a LP photon spectrum can be produced by radiative losses of an LP electron distribution (Massaro et al. 2004). The LP is used as a input electron distribution while modeling the multiwavelength SEDs after including the spectrum from other wavebands.

The X-rays and Optical/UV spectrum was also produced from Swift-XRT and UVOT data sets. The X-ray spectral points are estimated from *Xspec* by fitting the spectrum with single powerlaw model. The UVOT spectral points are estimated from “uvotsource” task.

Table 3.23 Results of SEDs fitted with different spectral distributions PL, LP, PLEC, and BPL. The different states during the observations are mentioned in the 1st column. The values of the fitted fluxes and spectral indices are presented in columns 2 & 3. TS_{curve} = 2(log $\mathcal{L}$(LP/PLEC/BPL) – log $\mathcal{L}$(PL)).

PowerLaw (PL)						
Activity	$F_{0.1-300\ GeV}$	Γ			log(Likelihood)	Δlog(Likelihood)
	(10^{-6} ph cm^{-2} s^{-1})					
flare A	2.56±0.04	2.28±0.01	-		214907.50	-
flare B	3.12±0.06	2.25±0.02	-		117287.47	-
flare C	2.10±0.05	2.38±0.02	-		94461.22	-
flare D	2.23±0.07	2.07±0.02	-		76861.60	-
Q2 state	1.46±0.05	2.43±0.03	-		91513.24	-
LogParabola (LP)						
Activity	$F_{0.1-300\ GeV}$ (10^{-6} ph cm^{-2} s^{-1})	α	β		log(Likelihood)	Δlog(Likelihood)
flare A	2.49±0.04	2.24±0.02	0.06±0.01		214889.23	-18.27
flare B	3.02±0.06	2.19±0.02	0.07±0.01		117267.38	-20.09
flare C	2.05±0.05	2.36±0.03	0.06±0.02		94455.98	-5.24
flare D	2.15±0.07	2.01±0.03	0.05±0.02		76855.64	-5.96
Q2 state	1.44±0.05	2.41±0.03	0.04±0.02		91511.21	-2.03
PLExpCutoff (PLEC)						
Activity	$F_{0.1-300\ GeV}$ (10^{-6} ph cm^{-2} s^{-1})	Γ_{PLEC}	E_{cutoff} [GeV]		TS	TS_{curve}
flare A	-	-	-		-	-
flare B	-	-	-		-	-
flare C	2.06±0.05	2.26±0.04	7.723±2.388		94451.69	-10.53
flare D	2.18±0.06	2.00±0.02	30.000±0.085		76855.68	-5.92
Q2 state	1.44±0.05	2.36±0.05	12.900±6.586		91510.01	-3.23
Broken PowerLaw (BPL)						
Activity	$F_{0.1-300\ GeV}$ (10^{-6} ph cm^{-2} s^{-1})	Γ_1	Γ_2	E_{break} [GeV]	TS	TS_{curve}
flare A	2.50±0.04	2.19±0.0.02	2.50±0.04	0.985±0.022	214891.50	-16.00
flare B	3.04±0.06	2.13±0.03	2.54±0.06	1.008±0.117	117268.06	-19.41
flare C	-	-	-		-	-
flare D	2.17±0.09	1.97±0.07	2.19±0.06	0.850±0.130	76857.19	-4.41
Q2 state	-	-	-	-	-	-

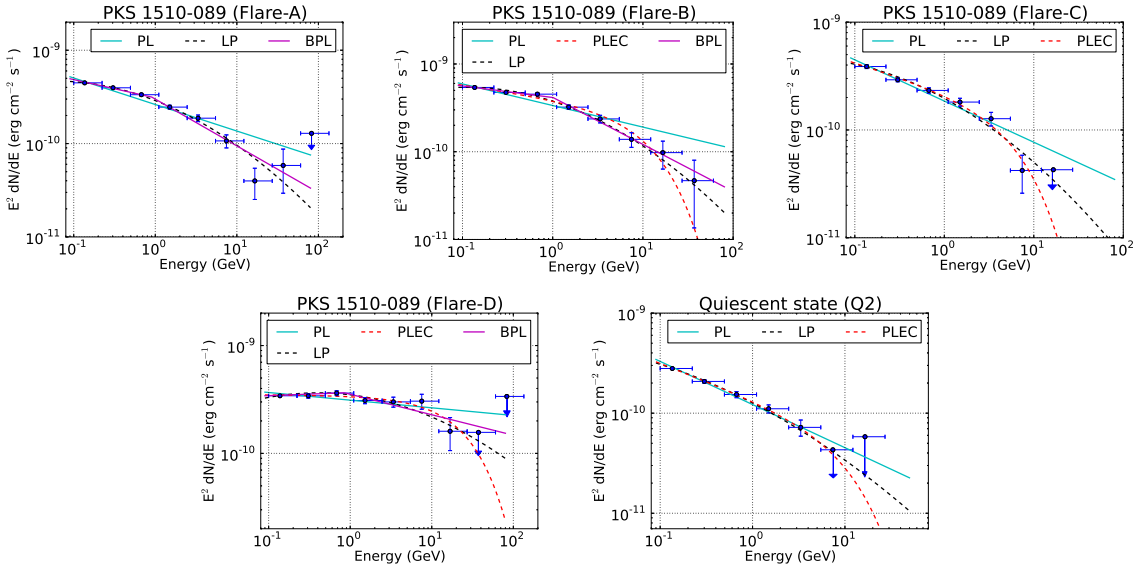

Fig. 3.35 The gamma-ray SEDs of different flares. The SEDs data points are fitted with different models.

3.6.8 Multiwavelength SED Modeling

GAMERA

To model the multiwavelength SEDs of PKS 1510-089 during flare of 2015, the publicly available time dependent code GAMERA[5] (Hahn 2015; Prince et al. 2018) is used. GAMERA solves the time dependent transport equation for an input injected electron distribution and estimate the propagated electron spectrum. The propagated electron spectrum used as a input for estimating the non-thermal synchrotron and inverse Compton (IC) processes. As discussed in section 3.6.7, a LP electron distribution can be used as a input injected electron spectrum in GAMERA. The continuity equation used by GAMERA is as follows,

$$\frac{\partial N(E,t)}{\partial t} = Q(E,t) - \frac{\partial}{\partial E}\Big(b(E,t)N(E,t)\Big) \tag{3.9}$$

[5]http://joachimhahn.github.io/GAMERA

where $Q(E,t)$ represents the injected electron spectrum, the propagated electron spectrum after the radiative loss is denoted by $N(E,t)$, and all the radiative loss due to synchrotron, synchrotron self-Compton (SSC) and external Compton (EC) are covered in $b(E,t)$. The inverse Compton emission in GAMERA was estimated by using the full Klein-Nishina cross-section from Blumenthal and Gould (1970).

3.6.9 Modeling the SEDs

The variability time estimated in various wavebands are found to be different, suggest the possibility of different emission zones (Table 3.21). The variability time found in gamma-ray and optical/UV bands are very close to each other which suggests they might have originated in the same region. On the other hand, the variability time found in X-ray waveband is far away from the gamma-ray and optical waveband variability time. In multiwavelength SEDs modeling two emission zones are considered , one is responsible for optical/UV and gamma-ray emission and the second zone is responsible for the X-ray emission.

The variability time also plays an important role in estimating the location of the emitting blobs along the jet axis. To locate the emission region following relation was used,

$$d = \frac{ct_{var}\delta}{(1+z)\theta_{jet}} \tag{3.10}$$

where t_{var} is the observed variability time and θ_{jet} is the half opening angle of the jet (Kaur and Baliyan 2018), d is the distance of the the emitting region from the central super massive black hole (SMBH), c is the speed of light in vacuum, z=0.361 is the redshift of the PKS 1510-089, and δ=25 (Aleksić et al. 2014) is the Doppler boosting. The jet opening angle was estimated from the radio observations by using the equation $\theta_{jet} = \theta_p sin\langle\Theta_0\rangle$, where θ_p = 4.8° is the projected half opening angle, and $\langle\Theta_0\rangle$ is the angle between jet axis and the line of sight. With the values of θ_p and $\langle\Theta_0\rangle$ from Jorstad et al. (2005) the jet opening angle

was estimated to be 0.12°. The variability time observed from gamma-ray and X-ray light curves are 10.6 hr and 2.5 days respectively. These times are used as t_{var} in equation 3.10 to estimate the distances of the gamma-ray and X-ray emission regions from the SMBH. The location of gamma-ray emitting blob along the jet axis was estimated to be 1.76×10^{17} cm, whereas X-ray emitting blob is located further down in the jet from the central SMBH at distance of 1.0×10^{18} cm. The boundary of the broad line region (BLR) and dusty torus (DT) are not well known, but people have some idea about their sizes. To estimate the radius of BLR and DT, a simple scaling law was introduced by Ghisellini and Tavecchio (2009). According to the scaling law, the size of BLR and DT only depends on the disk luminosity (L_{disk}). These are the following relations, $R_{BLR} = 10^{17}L_{d,45}^{1/2}$ and $R_{DT} = 2.5\times10^{18}L_{d,45}^{1/2}$, where $L_{d,45}$ is the disk luminosity in units of 10^{45} erg/s. The disk luminosity of PKS 1510-089 was earlier estimated by several authors (Celotti et al. 1997; Nalewajko et al. 2012) in the range of $3–7\times10^{45}$ erg s^{-1}. The typical value of disk luminosity ($L_{disk} = 6.7\times10^{45}$ erg s^{-1}) is used. The radius of BLR and DT are found to be (R_{BLR}) = 2.6×10^{17} cm and (R_{DT}) = 6.47×10^{18} cm respectively. Comparing the value of R_{BLR} and R_{DT} with the location of gamma-ray and X-ray emission region suggest that the gamma-ray emitting blob is located near the outer edge of the BLR, whereas the X-ray emitting blob is found to be outside the BLR, in the DT region. These inferences are used while modeling the SED with the time dependent code GAMERA.

Model set-up

All the non-thermal emissions produced in the jets of the blazar are boosted along the jet axis due to relativistic effects. As a result multiwavelength emissions are observed simultaneously or non-simultaneously in different telescope on the earth or in space. It is believed that jets is made up of mixture of plasma of electron-positron or electron-proton (still under debate) and it also has an intrinsic magnetic field embedded in it. It is conceptualized

that a spherical blob of charged particles produced at the base of the jets, travels along the jet axis with Lorentz factor, Γ. According to the synchrotron process the charged particles inside the blob interact on the way with the embedded magnetic field in the jet and produced synchrotron emission. Sometimes, these synchrotron photons can also interact with the same distribution of electrons and since electrons are moving relativistically, so they upscattered the low energy synchrotron photon to high energy gamma-ray by inverse Compton (IC) scattering, this process is called synchrotron self-Compton (SSC). In blazar, BLR, disk, and DT also act as sources of low energy seed photons for the IC scattering inside the jet. So, when these seed photons from outside the jets i.e. BLR, disk, and DT enter in to the jets, they interact with the charged particles moving relativistically along the jets and do the inverse Compton scatterings. As a result X-rays and gamma-ray emissions are observed at the different telescope. This process is called external Compton. Since we are dealing with number of photons and charged particle, so a distribution of photons (energy density of photons) and charged particles are used for further investigation.

The energy density of the external radiation field in the comoving jet frame is given as,

$$U'_{ext} = \frac{\Gamma^2 \xi_{ext} L_{disk}}{4\pi c R_{ext}^2} \tag{3.11}$$

where “ext" represents the BLR or DT. ξ_{BLR} represent the fraction of disk radiation reprocessed by BLR and ξ_{DT} is the fraction of the disk radiation reprocessed by DT. The R_{ext} is the size of the external radiation field. The values of $\xi_{BLR} = 0.06$, and $\xi_{DT} = 0.12$ are used from Barnacka, Anna et al. (2014) and the jet Lorentz factor $\Gamma = 20$ is taken from Aleksić et al. (2014). The BLR and DT energy density in jet comoving frame is estimated from equation 3.11 by using the above parameters along with $L_{disk} = 6.7\times10^{46}$ erg s^{-1}, $R_{BLR} = 2.6\times10^{17}$ cm, and $R_{DT} = 6.47\times10^{18}$ cm. The BLR and DT energy density in the jet comoving frame is estimated as $U'_{BLR} = 6.41$ erg cm^{-3} and $U'_{DT} = 2\times10^{-3}$ erg cm^{-3} respectively. GAMERA uses the energy density and temperature of external photon field

as a input parameters along with electron distribution. A LP distribution is used as input injected electron spectrum and the temperature of BLR and DT are $T_{BLR} = 10^4$K and $T_{DT} = 10^3$K, taken from Peterson (2006) and Ahnen et al. (2017) respectively. The Doppler factor (δ=25) and the jet Lorentz factor (Γ=20) are taken from earlier study on PKS 1510-089 by Aleksić et al. (2014). The size of the emitting blob also used as a input parameters in GAMERA and it can be estimated by the relation $R < ct_{var}\ \delta/(1+z)$, where t_{var} is the observed variability time, c is the speed of light in vacuum, and z is the redshift of the PKS 1510-089. The size of the gamma-ray and X-ray emitting blob is estimated separately and it is found to be 2.1×10^{16} cm and 1.2×10^{17}cm respectively.

Modeling Results

Various flares and quiescent state Q2 observed during high activity of PKS 1510-089 in 2015 are modeled with GAMERA. The modeling results are shown in Figure 3.36. The parameters like injected electron spectrum, blob magnetic field, injected electron luminosity, and minimum and maximum energy of electrons are optimized to fit the multiwavelength SEDs. The derived and optimized model parameters in SED modeling are presented in Table 3.24. The input injected electron spectra evolves with time as the electron loses its energy radiatively by synchrotron and IC processes. The time periods of individual flares and the quiescence state Q2 are significantly longer than the cooling time scale of electrons, as a result the electron spectra become steady in a short time period. The synchrotron emission produced in the jets, depends on the strength of the magnetic field and the luminosity of the relativistic electrons. The EC emission depends on the energy density and temperature of the external photon fields and also the luminosity of the relativistic electrons. The synchrotron self Compton (SSC) emission depends on the energy density of the synchrotron photons, which depends on the size of the blob, magnetic field and luminosity of the relativistic electrons. The SSC emission is found to be very low in our modeling compared to the

external Compton emission, which is true for FSRQ type of blazar. For the given magnetic field in DT region the synchrotron emission is found to be very low and it is below 10^{-13} erg/cm^2/s and that's the reason it can not be seen in Figure 3.36.

The optical depth correction due to the absorption of gamma-rays by the EBL (extragalactic background light) is not important for the Fermi-LAT observed gamma-ray flux from PKS 1510-089. The optical depth correction on the observed data points by MAGIC from Ahnen et al. (2017) are included. The de-absorbed data points are used in the the SED modeling. To obtain the best model fit to the data points, the following parameters e.g. the magnetic field in the blob, luminosity and spectral index of injected relativistic electrons, and also their minimum and maximum energies (γ_{min}, γ_{max}) are optimized. The ratio of of leptons to cold protons in the jets are assumed to be 10:1. The jet power in the relativistic electrons and positrons, or the cold protons, or the magnetic field are also calculated with the expression $P_{e,p,B} = \pi r^2_{blob} \Gamma^2 c U_{e,p,B}$, where $U_{e,p,B}$ denotes the energy density in electrons and positrons, or in protons, or in the magnetic field. The total jet power required in each state is much lower than the Eddington's luminosity of this source 6.86×10^{46} erg/sec, calculated with the black hole mass given in Abdo et al. (2010a). The parameter values which can explain the SEDs of the flares A, B, C, D and the quiescent state Q2 are listed in Table 3.24.

3.7 Discussion

The results are discussed in this section and compared with previous works.

3.7.1 Multiwavelength Studies with SED Modeling

In the year 2015, PKS 1510-089 is observed in high flux state. Four flaring states and three quiescent states are identified during the year 2015. The flaring states A, B, C, D and the quiescent states Q1, Q2 and Q3 are shown in the gamma-ray light curve in Figure 3.30 along

with the X-ray and Optical/UV light curves. The variability times in different wavelengths are found to be different, which motivated us to fit the multiwavelength SED with two-zone emission model. The fitted parameters found in two zone modeling are presented in the Table 3.24. The emission zone located at the outer boundary of the BLR region required a range of magnetic field from 2.8 to 5.1 Gauss to fit the optical/UV data points. However, the magnetic field in the second zone located in the DT region is not constrained by optical or UV data in our model. It was assumed to be very low to minimize the jet power. However, in principle, it could be higher. The jet power in electrons and positrons in the second zone are constrained by the X-ray flux (Figure 3.36). It is found that in the first zone the magnetic field has more jet power than that in electrons and positrons. In this zone the electrons and positrons carry more energy during the flaring states. MAGIC detected very high energy gamma-rays (Ahnen et al. 2017) during the Flare B. The maximum energy of the relativistic electrons and positrons in our model is the highest during this flare. In the second zone also this jet power is expected to be higher during the flaring states if the X-ray flux is higher than that in the quiescent states.

A correlation study done by Abdo et al. (2010a) for the flaring activity of PKS 1510-089 between September 2008 and June 2009 has revealed a complex correlation between fluxes of different wavebands. Flare of PKS 1510-089 during year 2009 was also studied by Marscher et al. (2010). They observed a good correlation in optical and gamma-ray flux.

The 2009 GeV flares of PKS 1510-089 was also studied by Dotson et al. (2015). They have identified the four bright gamma-ray flare during 2009 and discussed about the location of the emission region of these GeV flares. For two flares they have suggested that the emission region could be in the DT region and for the other two at the vicinity of VLBI radio core. Flare detected in March 2009 from PKS 1510-089 was studied by Barnacka, Anna et al. (2014). They have modeled the 2009 flare by considering the seed photons from both the BLR and DT regions for the EC emission. They have located the emission region at the

distance of 7×10^{17} cm from the black hole. The SSC emission observed was very insignificant compared to the EC emission.

Recently, a detailed study was done by using the MAGIC data (MAGIC Collaboration et al. 2018) between 2012 to 2017, when the PKS 1510-089 was in low flux state. The study revealed that the location of the gamma-ray emission region is beyond the BLR region. To model the broadband emission using an EC process, They have chosen two scenarios with the emission regions located at 7×10^{17} cm and 3×10^{18} cm away from the black hole respectively. A high state of PKS 1510-089 during year 2015 was studied by Ahnen et al. (2017), where they have located the emission region at distance of 6×10^{17} cm away from the black hole. All the above estimates are comparable to our results. Ahnen et al. (2017) estimated the size of the gamma-ray emission region and found to be 2.8×10^{16} cm, which is also comparable to the size of the gamma-ray emission region found in our study 2.1×10^{16} cm. The values of Lorentz factor and Doppler factor used in our modeling are similar to Aleksić et al. (2014).

Tavecchio et al. (2010) have studied the light curves of PKS 1510-089 and 3C 454.3 during the period between August 4, 2008 to January 31, 2010. They have constrained the location of the gamma-ray emission region through rapid variability seen in the Fermi-LAT data. An hour scale of variability was observed in the gamma-ray flux for both the sources PKS 1510-089 and 3C 454.3. Using the variability time and $\delta = 10$, they have constrained the size of the emission region to be less than 4.8×10^{15} cm and 3.5×10^{15} cm for PKS 1510-089 and 3C 454.3 respectively. Extreme value of Doppler factor $\delta = 50$ can also constrains the size of the emission region to be less than 0.01 pc. They suggested that such a small emission regions are likely to be located near the black hole. So finally, they concluded that the far dissipation scenario, where the gamma-ray emission region is located 10-20 pc away from the black hole is disfavored.

A time dependent modeling of gamma-ray flares of PKS 1510-089 were done by Saito et al.

(2015) within the framework of the internal shock scenario. They have shown that the emission region is located between 0.3 pc to 3 pc from the black hole depending on whether the jet is freely expanding or collimated. They have also discussed about the non-uniformity of Doppler factor across the jet due to the radial expansion of the outflow. This may result in time distortion in the observed gamma-ray light curve and asymmetric flux profiles with extended decay time could be seen.

A multiwavelength temporal variability in 3C 454.3 during its active state in 2014 was studied by Kushwaha et al. (2017). They have observed that in some of the epochs IR/optical and gamma-ray fluxes show nearly simultaneous variation. A significant correlation in Optical and gamma-ray frequencies was observed in June, 2016 outburst of 3C 454.3 (Weaver et al. 2019). Recently, Rajput et al. (2019) have analyzed quasi-simultaneous data at optical, UV, X-ray and gamma-ray energies collected over a period of 9 years between August 2008 to February 2017. They have identified four epochs when the source showed large optical flares. A significant correlation was observed in two epochs between optical and gamma-ray emission. In other two epochs the flare in gamma-rays are weak or absent.

A correlation in optical and gamma-ray photons from flares of PKS 1510-089 during Jan 2009 to Jan 2010 has been suggested by Castignani et al. (2017), which could be a common feature among these blazars. This inference has also been used in our analysis to model the SED. We also note that in some FSRQs like 3C 279 the time lag between optical and gamma-ray emission could be due to the variations in the ratio of energy densities in external photon field and magnetic field with distance across the length of the jet (Janiak et al. 2012).

3.7.2 Gamma-Radio Correlation

An interesting feature was observed in the radio frequencies where the gradual increase was noticed in the radio flux over a long period of time. In Figure 3.32, the light curves at 15 GHz

from OVRO observations and 230 GHz from SMA observations are shown. DCF estimated between these two light curves does not show any clear peak or lag as shown in Figure 3.34. Even at the end of the high state when the gamma-ray flux reached the quiescent state Q3 the radio flux continued to increase. The OVRO flux reached the maximum level in October, 2016 and subsequently, decreased slowly.

Ahnen et al. (2017) also reported gradual increase in radio flux in the second half of 2015. They have shown the light curve of the radio core at 43 GHz. A bright and slow radio knot K15 was ejected on MJD 57230±52. They associated the increase in radio flux with the ejection of the radio knot K15. Due to the large uncertainty in the ejection time of K15 it could not be associated with any particular GeV flare.

A similar feature was also observed with the gamma-ray high state in Feb-April 2012 when a radio knot K12 emerged from the core (Aleksić et al. 2014). In the second half of 2011 PKS 1510-089 had a major outburst in radio flux. The outburst first peaked at higher frequency. The peak at 37 GHz was reached around 21 Oct, 2011 and later at 15 GHz around 15 Dec, 2011. After attaining the peaks the light curves gradually decayed. Small outbursts continued to happen after this. VLBA 43 GHz images show a new component (knot K11) in December 2011. This was also observed at 15 GHz in MOJAVE as reported by Orienti et al. (2013). The temporal evolution of gamma-ray and radio flux suggests they are produced by different populations of electrons, located at different regions along the length of the jet.

3.7.3 Summary

1. For PKS 1510-089, year 2015 is considered as a very long flaring period in gamma-ray and this long period is divided in to four major flares identified as flare A, B, C, and D and three quiescent state Q1, Q2, and Q3.

Table 3.24 Parameters of two zone modeling, injection spectrum of electrons dQ(E)/dE = Q_p $(E/E_p)^{-\alpha-\beta\log(E/E_p)}$, E_p=90 MeV.

Model parameters	BLR	DT
Energy density in BLR/DT (erg/cm^3)	6.41	0.002
Temperature in BLR/DT (K)	1e4	1e3
Doppler factor (δ)	25	25
Lorentz factor (Γ)	20	20
Size of blob (r_{blob} cm)	2.1×10^{16}	1.2×10^{17}
Flare-A		
jet power in electrons (P_e erg/sec)	1.15×10^{45}	8.79×10^{44}
jet power in magnetic field (P_B erg/sec)	5.18×10^{45}	2.16×10^{42}
Injected electron spectrum (α)	2.0	3.1
β	0.08	0.08
γ_{min}	100	25
γ_{max}	9×10^3	2.2×10^3
Magnetic field (B Gauss)	2.8	0.01
Flare-B		
jet power in electrons (P_e erg/sec)	1.08×10^{45}	1.67×10^{45}
jet power in magnetic field (P_B erg/sec)	8.10×10^{45}	2.16×10^{42}
Injected electron spectrum (α)	2.1	3.3
β	0.16	0.08
γ_{min}	250	30
γ_{max}	2.7×10^4	4×10^3
Magnetic field (B Gauss)	3.5	0.01
Flare-C		
jet power in electrons (P_e erg/sec)	9.38×10^{44}	1.30×10^{45}
jet power in magnetic field (P_B erg/sec)	1.72×10^{46}	2.16×10^{42}
Injected electron spectrum (α)	2.1	3.5
β	0.17	0.10
γ_{min}	190	24
γ_{max}	8×10^3	9×10^2
Magnetic field (B Gauss)	5.1	0.01
Flare-D		
jet power in electrons (P_e erg/sec)	8.27×10^{44}	2.51×10^{44}
jet power in magnetic field (P_B erg/sec)	7.65×10^{45}	2.16×10^{42}
Injected electron spectrum (α)	1.7	3.0
β	0.07	0.07
γ_{min}	170	25
γ_{max}	1.2×10^4	1.3×10^3
Magnetic field (B Gauss)	3.4	0.01
Quiescent State (Q2)		
jet power in electrons (P_e erg/sec)	7.80×10^{44}	1.63×10^{45}
jet power in magnetic field (P_B erg/sec)	9.55×10^{45}	2.16×10^{42}
Injected electron spectrum (α)	2.2	3.3
β	0.08	0.08
γ_{min}	200	27
γ_{max}	6×10^3	8×10^2
Magnetic field (B Gauss)	3.8	0.01

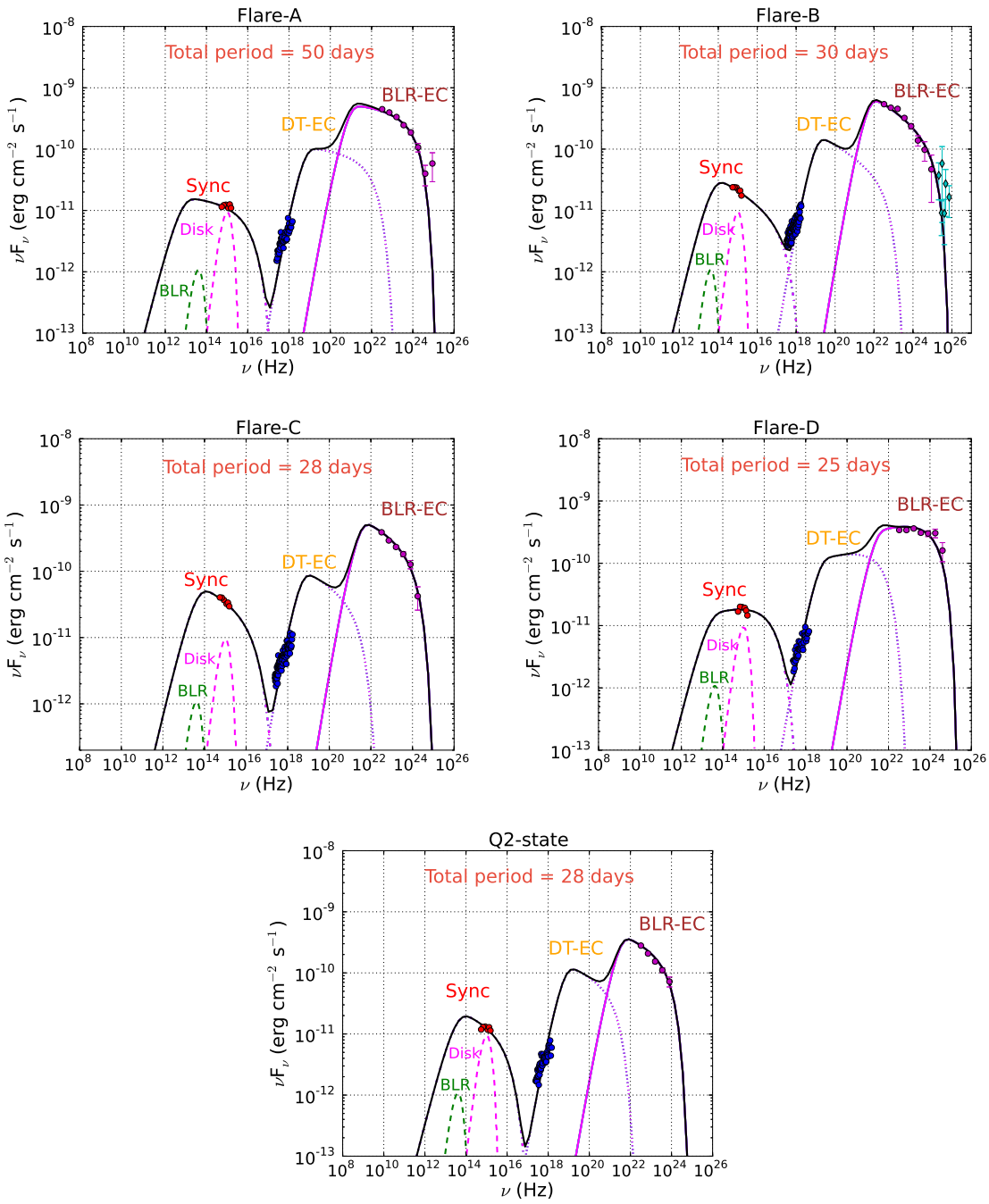

Fig. 3.36 Multi-wavelength SED modeling for four flares and quiescent state Q2. Swift XRT/UVOT data points shown in blue/red solid circles. Fermi LAT data points shown in pink solid circles, for Flare B the de-absorbed MAGIC data points shown with teal diamonds. The SEDs of the four time intervals measured in days during each state overlap with each other.

2. The multiwavelength data from Swift-XRT and UVOT are collected for year 2015. All the four flares and quiescent state Q2 is found to have simultaneous X-ray, UV, and Optical data with respect to gamma-ray from *Fermi*-LAT.

3. The temporal studies reveals that the different flux variability time is observed in different wavebands, which suggests an involvement of multiple emission zones for different waveband emissions. The variability times for gamma-ray and Optical/UV are very close to each other whereas variability time in X-ray is found to be large compare to gamma-ray and Optical/UV. These results suggested a co-spatial origin of gamma-ray and Optical/UV emission and a separate emission zone for X-ray emission.

4. A cross correlation study between different energy bands are done. No significant correlation is observed in any of the combinations.

5. Two-zone emission model are considered in GAMERA to explain the multiwavelength SEDs of PKS 1510-089.

6. The modeling of multiwavelength SEDs with GAMERA shows a two-zone model can be applied to explain the multiwavelength SED data points. First zone which explains the gamma-ray and UV/Optical emission is kept inside the BLR, whereas the second zone is kept outside the BLR or inside the DT to explain the X-ray emission.

7. Parameters like spectral index, minimum and maximum energy of input injected electron spectrum, blob magnetic field, and injected electron luminosity are optimized to its best value to fit the multiwavelength SED of different flares and quiescent state Q2.

3.8 Summary of the Chapter

Summary of the whole Chapter 3 is provided in this Section.

1. A long-term temporal and spectral analysis of PKS 1510-089, in gamma-ray, is carried on for a period of eight years from 2018–2016. Five major flares are identified based on the flux value.

2. A finer time binning of light curve in 1 day and 6 hr bin exhibit the several sub-structures corresponding to each identified flare. All the substructures are divided in different phases like pre-flare, plateau, flare, and post-flare.

3. The brightest flare of PKS 1510-089 is observed during flare-2(C) with flux value F_{GeV} = 17.56$\pm$1.15 ph cm^{-2} s^{-1} at MJD 55853.9 and the fastest variability time is estimated to be 1.30$\pm$0.18 hr between MJD 55852.063–55852.188, which locates a small emission region of size 4.85×10^{15} cm at the base of the jet.

4. The gamma-ray SEDs are produced for all the phases separately and are fitted by three different model PL, LP ad PLEC. A LP spectral model appears to be the best model to describe the gamma-ray spectrum.

5. PKS 1510-089 has shown a typical behavior of FSRQ by exhibiting the “harder-when-brighter" trend during all the flares.

6. Among five major flares, the flare observed during year 2015 is considered for multi-wavelength SED modeling. To model the source, a publicly available code GAMERA is used. We have revised our definition of flare and the high state of year 2015 is divided in to four flare along with a few quiescent states. The multiwavelength data for all the flares and quiescent state Q2 are collected and analyzed.

7. Temporal analysis of multiwavelength light curve exhibits different time variability in different wavebands, which suggests the presence of multiple emission zone. To

investigate the possibility of multi-zone emission a cross-correlation study between different wavebands light curve are done. The variability times suggest gamma-ray and optical emissions are produced from the same emission region whereas X-rays are produced from another emission region.

8. To model the multiwavelength SEDs with GAMERA, we have considered one emission zone inside the BLR and another in DT.

Chapter 4

The Brightest Gamma-ray Flare Ever Detected from CTA 102

4.1 Introduction

CTA 102 is a FSRQ type of blazar, and it is one of the most variable sources, in 3FGL catalog, observed by *Fermi*-LAT. As a quasar, CTA 102 was first identified by Sandage and Wyndham (1965) and classified as a highly polarized quasar by Moore and Stockman (1981). It is considered as the most luminous and well-studied quasar located at a redshift of z = 1.037 (Schmidt 1965). All the non-thermal emission in blazar is boosted along the jet axis and as a result violent variability are observed at all wavelengths. Its variability has been investigated in the past by Osterman Meyer et al. (2009), and they have revealed that it is a highly variable source in the optical waveband. They have also reported that the fastest variability is associated with the higher flux states. Variability during flare in centimeter and millimeter wavelengths as well as in the X-rays (RXTE observation) was also observed in CTA 102, as reported by Osterman Meyer et al. (2009).

CTA 102 was observed in gamma-ray energy by CGRO/EGRET telescopes as well as by *Fermi*-LAT telescopes. The source luminosity in gamma-ray was noted as $L_\gamma = 5 \times 10^{47}$

erg/s, and got recognized in the list of gamma-ray bright sources (Nolan et al. 1993; Abdo et al. (2009). The source CTA 102 was also observed in radio by Very Large Array (VLA). It showed the kpc-scale radio morphology of the source, which includes a strong central core and two less luminous radio lobes on opposite sides of the central object (Spencer et al. 1989; Stanghellini et al. 1998). Other radio telescopes like Very Long Baseline Array (VLBA) 2 cm survey and its successor, the MOJAVE (Monitoring of Jets in Active galactic nuclei with VLBA Experiments) program have been regularly monitoring the CTA 102 since mid-1995. A radio flare observed in CTA 102 during 2006 was studied in many papers (Fromm et al. 2011, Fromm et al. 2013a, Fromm et al. 2013b), where they have found that the variations in the physical properties during radio flare is connected to a new traveling feature and the interaction between the shock wave and a stationary structure (Fromm et al. 2013b).

A gamma-ray flare with flux $F_{>100MeV} = 5.2 \pm 0.4 \times 10^{-6}$ ph cm^{-2} s^{-1} (Casadio et al. 2015) was observed by *Fermi*-LAT during 2012 September-October along with the simultaneous outburst in optical and near-infrared (NIR) wavebands. Intra-night variability in optical fluxes was observed in CTA 102 during the flare of 2016–2017.

In this chapter, we have studied the high state of CTA 102 between September 2016 to March 2017 using γ-ray and X-ray/UVOT data to explore the fast variability and time-dependent multi-frequency spectral energy distributions (SEDs).

Throughout the chapter, the γ-ray flux is in units of 10^{-6} ph cm^{-2} s^{-1} unless otherwise mentioned. The standard flat cosmology model with $H_0 = 69.6$ km s^{-1} Mpc^{-1}, and $\Omega_M = 0.27$ has been used to estimate the luminosity distance ($d_L = 7.08 \times 10^9$ pc).

4.2 Observations and Data Reduction

Fermi-LAT continuously monitors the CTA 102 in gamma-ray energy band and Swift-XRT/UVOT in X-ray and Optical/UV bands. In gamma-ray, the first flare of CTA 102 was observed in

2012 September-October with the highest flux value of 5.2 ± 0.4 (Casadio et al. 2015). The recent flare observed in gamma-ray during 2016 September– 2017 March is brighter than the first gamma-ray flare. The gamma-ray, X-ray, and optical/UV data were collected from both the above instruments during September, 2016 to March, 2017 to study this flare.

The standard data reduction and analysis procedure are followed to analyze the *Fermi*-LAT data and details of which were shown in chapter 2. The gamma-ray photon spectra is fitted with four different spectral models shown in equation 3.1, 3.2, 3.3, and 3.4. The reference energy of various spectral models are different for CTA 102 , and its values are mentioned in Prince et al. (2018).

Swift-XRT/UVOT data from *HEASARC ARCHIVE*[1] are also collected for gamma-ray flaring period between September, 2016 to March, 2017. A total 35, number of observation are found between September, 2016 to January, 2017 January, whereas no observation were found during February to March, 2017. The task *xrtpipeline*, *xselect*, *xrtmkarf*, and *grppha* are used to analyze the X-ray data. The details about each task are mentioned in chapter 3. The task *XSPEC* is used for spectral fitting, and all the X-ray spectra were fitted with an absorbed BPL model with a galactic absorption column density $n_H = 5.0 \times 10^{20}$ cm^{-2} estimated from Kalberla et al. (2005).

CTA 102 is observed in all the six filters of UVOT during the gamma-ray flaring period. The source and background regions are chosen of sizes 10 and 30 arcsec centered at the source and away from the source, respectively. The task *uvotsource* is used to extract the source magnitudes. A galactic extinction correction is done for the magnitudes before converting into flux. The details about the zero points and conversion factors are given in chapter 2.

[1] https://heasarc.gsfc.nasa.gov/cgi-bin/W3Browse/w3browse.pl

4.3 Multiwavelength Light Curves

The multiwavelength light curve shown in Figure 4.1, represents the total flaring period of CTA 102 during September, 2016 to March, 2017. The top panel of Figure 4.1 shows the gamma-ray light curve for energy 0.1–300 GeV from *Fermi*-LAT and all the lower panel have X-ray, UV, and Optical light curve produced from Swift-XRT (0.3–10 keV) and UVOT telescope. Based on the observed flux values, in gamma-ray, by *Fermi*-LAT, the whole period is divided into four different states. All these states are named as Pre-flare, Rising Segment, Flares, and Decaying segment which are separated by a green dotted vertical lines (Figure 4.1). Various states are also distinguished by fractional variability estimated in section 4.3.4. From eye inspection to Figure 4.1, a good temporal correlation can be seen in all wavebands. The detail about each light curves are discussed below in a separate section.

4.3.1 Gamma-ray Light Curve

The flaring state detected in CTA 102 during Septembe, 2016 to March, 2017 (Figure 4.1) has been studied in detail in this section. A finer time binning is done for the flaring state. A 12 hr, 6 hr, and 3 hr light curves are produced and presented in Figure 4.2 along with one-day bin light curve. The γ-ray variability of the source can be seen by generating the finer time bin light curves (Figure 4.2) with various time bins (1 day, 12 hr, 6 hr, and 3 hr). CTA 102 started showing the high activity from December 13, 2016 (MJD 57735) and continued for almost a month till January 10, 2017 (MJD 57763), which manifested in Figure 4.2. The flaring state lasted for 28 days and which can be divided into four different flares. The observed four flares are separated by a red dotted vertical lines. The flares were named as flare-1, flare-2, flare-3, and flare-4 and their corresponding time periods are found to be MJD 57735–57740, MJD 57740–57748, MJD 57748–57756, and MJD 57756–57763, respectively. The light curves for different time bins are shown in separate panels of Figure 4.2. The top panel represents 1 day time binning, which reveals the four flares. The 12 hr,

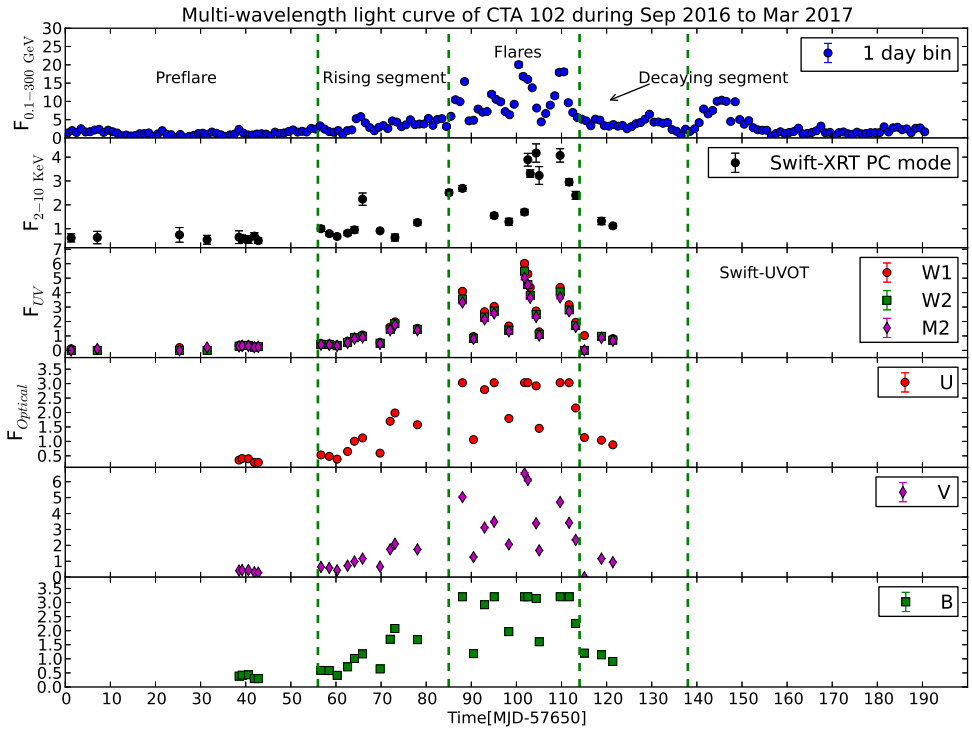

Fig. 4.1 Light curve of the CTA 102 during the September, 2016 to March, 2017 outburst. Four major flaring episodes have been identified and further studied. Pre-flare, rising and decaying segments are also present before and after the flaring events, separated by a green dashed line. XRT flux is in unit of 10^{-11}, F_{UV} and $F_{optical}$ flux is in unit of 10^{-10} erg cm^{-2} s^{-1}. γ-ray flux shown in the top panel is in unit of 10^{-6} ph cm^{-2} s^{-1}.

6 hr, and 3 hr time bin light curve reveal the substructures in each flare. Variations in the flux values during the flare can be identified as different peaks. The heights and the width of peaks were found to be different in each case. The 6 hr and 3 hr light curve are used to understand temporal behavior and the variability time scale, of CTA 102, respectively. The data points below the detection limit of 3σ (TS < 9; Mattox et al. 1996) have been rejected from both the temporal and variability study.

The temporal evolution of each flare has been done separately, and the peaks found in 6 hr binning of different flares are fitted with a function called the sum of exponentials. Two exponentials function together can defined a peak one for rising part of the peak and the second is for decaying part of the peak. So, fitting the peaks with the sum of exponentials can tell us about the rise and decay time of the peaks. The functional form of the sum of exponentials is as follows:

$$F(t) = 2F_0 \left[\exp\left(\frac{t_0 - t}{T_r}\right) + \exp\left(\frac{t - t_0}{T_d}\right) \right]^{-1}, \tag{4.1}$$

where F_0 is the flux at time t_0 representing the approximate flare amplitude, T_r and T_d are the rise and decay times of the flare respectively (Abdo et al. 2010c). All the fitted peaks of different flares are shown in Figure 4.3, and the fitted parameters are presented in Table 4.1. Any physical process faster than the light travel time or the duration of the event will not be detectable from the light curve (Chiaberge and Ghisellini 1999; Chatterjee et al. 2012). Symmetric temporal evolution, having equal rise and decay times, may occur when a perturbation in the jet flow or a blob of denser plasma passes through a standing shock present in the jet (Blandford and Königl 1979). In flare-1, the peak P1 has nearly equal rise and decay times whereas the second peak P2 has shown a fast decay and slow rise time. The slow rising time can be seen as a slow injection of electrons into the emission region. Similar behavior is also seen in flare-2 for peak P1 and P4. The peak P2 of the flare-2 and P4 of flare-3 have shown a significantly longer decay time than rising time. The observed

longer decay time can be seen as a longer cooling time of electrons. Among the 14 peaks observed during the total flaring period, as shown in Table 4.1, five peaks have nearly equal rise and decay times. Five peaks have a slower rise and fast decay time, and the rest of the four have slow decay and fast rise time. Hence, all the three scenario observed in CTA 102 are equally probable.

The details about the different states identified in Figure 4.1 are presented below.

Table 4.1 Results of temporal fitting with the sum of exponentials (Equation 4.1 in the text) for different peaks of the flares. Column 2 represents the time (in MJD) at which the peaks observed, and the peak fluxes given in column 3. The fitted rise (T_r) and decay (T_d) times are mentioned in columns 4 & 5

Peak	t_0 (MJD)	F_0 (10^{-6} ph cm^{-2} s^{-1})	T_r (hr)	T_d (hr)
		flare-1		
P1	57736.4	12.81±1.42	7.66±1.35	7.76±1.36
P2	57738.4	19.45±0.68	10.01±0.92	6.51±0.59
		flare-2		
P1	57741.6	9.12±0.55	13.21±2.45	6.31±1.70
P2	57742.6	8.70±0.56	4.01±1.15	9.48±2.11
P3	57744.6	14.38±1.24	12.50±1.84	15.30±3.35
P4	57746.6	10.84±1.46	14.53±4.37	9.83±2.09
		flare-3		
P1	57750.1	20.93±1.24	7.20±1.00	7.45±1.91
P2	57750.9	21.17±1.67	5.61±1.62	6.06±1.84
P3	57751.6	20.09±1.60	4.64±1.61	4.56±0.95
P4	57752.6	20.82±1.08	5.05±0.85	11.41±1.50
P5	57753.6	14.79±1.01	4.94±1.41	4.49±1.17
		flare-4		
P1	57758.1	13.01±1.20	7.21±1.66	4.89±1.41
P2	57759.6	22.50±1.73	10.07±1.36	1.74±0.99
P3	57760.4	21.36±1.52	8.97±1.21	8.72±0.82

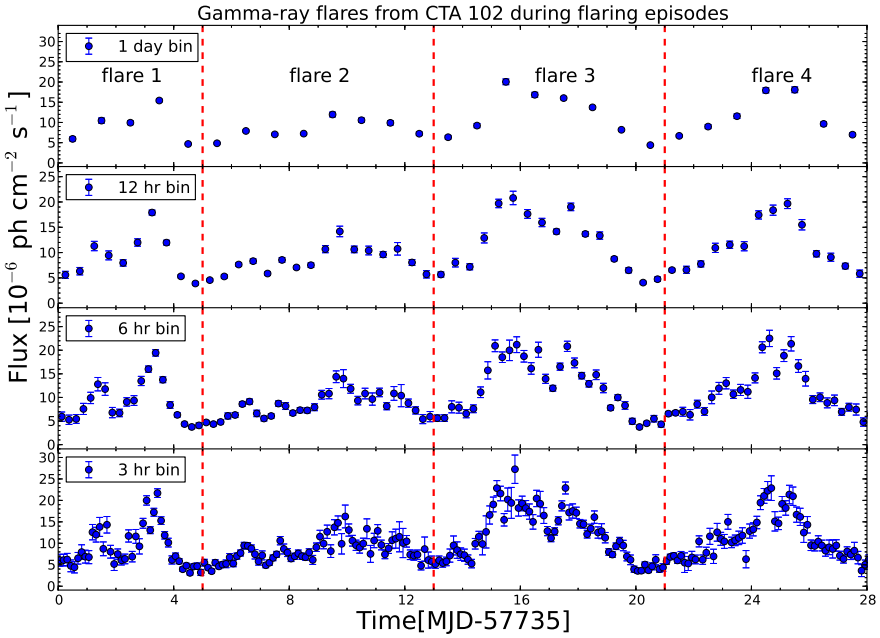

Fig. 4.2 Zoomed version of flaring episodes. The flares are separated by red dashed lines and their time durations are as follows: MJD 57735–57740, MJD 57740–57748, MJD 57748–57756, and MJD 57756-57763. Substructures are seen from 6 hr and 3 hr binning, which also gives a hint about the flux variability shorter than day scale.

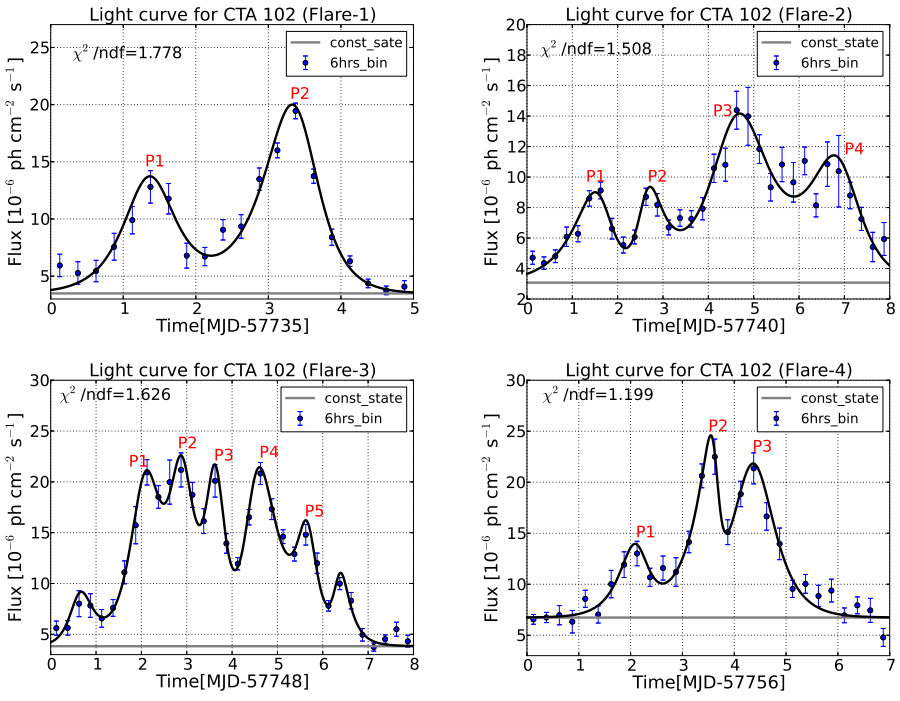

Fig. 4.3 The sum of exponentials fits the peaks of all the four flares, and the fitted parameters are mentioned in Table 4.1. The light gray line represents the constant flux or baseline.

Pre-flare, Rising and Decaying Segment

Before showing the flaring activity on December 13, 2016 (MJD 57735), the blazar CTA 102 was in a long low flux or quiescence state. In this study, the time period between September 19, 2016 to November 11, 2016 (MJD 57650 – MJD 57706) is considered as low flux state. As shown in Figure 4.1, this low flux state is defined as a pre-flare phase. The average flux observed during pre-flare phase is F_{GeV} = 1.40±0.10 ph cm^{-2} s^{-1}. Just after the pre-flare phase the flux started rising very slowly and lasted for almost one month from MJD 57706 – MJD 57735, this period is defined as rising segment. The average flux observed during rising segment is F_{GeV} = 3.83±0.08 ph cm^{-2} s^{-1}, which is higher than the average flux value of pre-flare phase . The slow rise in flux during rising segments suddenly changed to higher flux value and continued to be in the higher state for almost a month. This period of high flux state from MJD 57735–MJD 57763 was defined as flares. After spending one months in the flaring state the flux started decreasing but very slowly. The period of slow decay is defined as decaying segment in this study. The average flux noticed during decaying segment is almost similar to the rising segment flux value. The total flaring period observed in Figure 4.1 can be divided into four separate flares as shown in Figure 4.2. These flares are named as flare-1, flare-2, flare-3, and flare-4. Details about all the flares are presented separately in the coming section.

Flare-1

Various time bins light curve for all the four flares are shown in Figure 4.2 , which help us to distinguished one flare from the others. Different time binning also help us to understand the clear structures of each flare. As a result, a flare can be seen as a combination of several peaks. Flare-1 is observed during MJD 57735–57740, as shown in Figure 4.2. Two major peaks, P1 and P2, are observed during flare-1 and are fitted with the function given in equation 4.1. The rise and decay times estimated from the fitting are mentioned in Table

4.1, and their peak fluxes are observed to be F_{GeV} = 12.81±1.42 and 19.45±0.68 at MJD 57736.375 and MJD 57738.375, respectively. Along with the peaks, the baseline flux is also fitted, as shown in Figure 4.3 (gray line), which is found to be very close to the quiescent state flux value mentioned in Section 4.3.1.

Flare-2

Flare-2 is observed during MJD 57740–57748. The temporal evolution of flare-2 is shown in Figure 4.3. At MJD 55740, flare-2 started rising and lasted up to eight days till MJD 57748. Four major peaks P1, P2, P3, and P4 are observed during flare-2 and fitted with the function sum of exponentials. The fitted parameters like the rise and decay times are tabulated in Table 4.3 along with the peak fluxes F_{GeV} = 9.12±0.55, 8.70±0.56, 14.38±1.24 and 10.84±1.46 measured at MJD 57741.625, 57742.625, 57744.625 and 57746.625 respectively. The baseline flux observed in flare-2 (gray line) is close to the quiescent state flux value.

Flare-3

A 6 hr binning of flare-3 is performed similar to flare-1 and flare-2, to study the temporal evolution, as shown in Figure 4.3. Flare-3 is observed during MJD 57748–57756, and identified as one of the brightest flares ever detected from CTA 102. The flux measured to be F_{GeV} = 27.26±3.30 at MJD 57750.813 (from 3 hr binning). It is far brighter than the previous flare observed in September-October, 2012 (Casadio et al. 2015) with a flux of F_{GeV} = 5.2±0.4. The source spent almost a week in its flaring state and subsequently its flux reduced to the quiescent state flux value. Four major peaks, P1, P2, P3, and P4, are observed during flare-4. The fitted parameters of peaks P1, P2, P3, P4, and P5 are mentioned in Table 4.1 along with the peak fluxes F_{GeV} = 20.93±1.24, 21.17±1.67, 20.09±1.60, 20.82±1.08

and 14.79±1.01 observed at MJD 57750.125, 57750.875, 57751.625, 57752.625 and MJD 57753.625, respectively.

Flare-4

Flare-4 is observed during MJD 57756–57763 as shown in Figure 4.3. The temporal evolution of flare-4 revealed three major peaks classified as P1, P2, and P3. The rise and decay time of all the peaks are mentioned in Table 4.1 along with the observed fluxes F_{GeV} = 13.01±1.20, 22.50±1.73, and 21.36±1.52 measured at MJD 57758.125, 57759.625, 57760.375 respectively.

4.3.2 γ-ray Variability

The variability time plays a crucial role when the source flux between two consecutive time intervals changes very rapidly during flare. The shortest variability time or fast flux change suggest a compact emission region located close to the SMBH. The size of the emission region for a given value of Doppler factor (δ) and redshift (z) of the source can be estimated by the variability time. The search for the fastest variability time was carried on from 90 minutes time bin light curve. To estimate the fastest variability time following equation was used:

$$F(t_2) = F(t_1).2^{(t_2-t_1)/t_d}, \tag{4.2}$$

where $F(t_1)$ and $F(t_2)$ are the fluxes measured at two consecutive instants of time t_1 and t_2 respectively, and t_d represents the flux doubling/halving timescale. The whole flaring period is scanned with the above function with some conditions, and the conditions are: the variability time should be considered only for those time periods which have at least 5σ detection (TS $>$ 25) and the flux should changed by more than two for rising part or less than half for decaying part of the flare. The time intervals which satisfied only one condition are not considered for the fast variability calculations. The shortest variability time is found

to be t_{var} = 1.08±0.01 hr between MJD 57761.47 – 57761.53. The variability time found in this study is consistent with the hour scale variability found for other FSRQ like PKS 1510-089 (Prince et al. 2017; Brown 2013; Saito et al. 2013). It is also noticed that the variability time was not a constant value. The analysis showed a range of variability time from 1 hr to several days during flaring period of CTA 102.

4.3.3 X-ray Light Curve

The simultaneous X-ray (2 – 10 keV) and UVOT (six filters) light curves are shown in the lower panel of Figure 4.1. Swift observations for flaring episode was carried out along with *Fermi*-LAT till MJD 57771 (Mar 18, 2017). The 2-10 keV X-ray fluxes, obtained using the CFLUX convolution model, are used in the X-ray light curve shown in Figure 4.1. The UVOT light curves show the fluxes in all the available six filter during each of the observations. The light curves, though sparsely populated as compared to the γ-ray light curves, do show correlated increased intensities during the flaring episodes.

4.3.4 Fractional Variability (F_{var})

Generally, the fractional variability is used across the whole electromagnetic spectrum (Vaughan et al. 2003) to find out the flux variability amplitude in the different part of the spectrum. Here, the fractional variability is estimated to distinguished the different activity states, like pre-flare, rising segment, flare, and decaying segment, observed in gamma-ray light curve. The fractional variability amplitude was first formulated by (Edelson and Malkan 1987; Edelson et al. 1990), and it can be estimated by using the following relation given in Vaughan et al. (2003),

$$F_{var} = \sqrt{\frac{S^2 - \sigma^2}{r^2}} \tag{4.3}$$

Table 4.2 Fractional variability amplitudes for all the different activity states.

Activity	σ^2_{NXS}	err(σ^2_{NXS})	F_{var}	err(F_{var})
Pre-flare	0.0626	0.0192	0.2502	0.0384
Rising segment	0.1295	0.0147	0.3598	0.0205
Decaying segment	0.1189	0.0129	0.3449	0.0188
Flare-(1-4)	0.1899	0.0076	0.4358	0.0087

$$err(F_{var}) = \sqrt{\left(\sqrt{\frac{1}{2N}}.\frac{\sigma^2}{r^2 F_{var}}\right)^2 + \left(\sqrt{\frac{\sigma^2}{N}}.\frac{1}{r}\right)^2} \tag{4.4}$$

where, $\sigma^2_{XS} = S^2 - \sigma^2$, is called excess variance, S^2 is the sample variance, σ^2 is the mean square uncertainties of each observations, and r is the sample mean. The normalized excess variance was also estimated, $\sigma^2_{NXS} = \sigma^2_{XS}/r^2$. The increase in the value of the fractional variability and excess variance is noticed when flux changed from pre-flare to flaring state and subsequently decreased when flux changed from flaring state to decaying state. The fractional variabilities for different states are mentioned in Table 4.2. The fractional variability reveal that the source is more variable during flare compare to the rising and decaying segment. As expected, the fractional variability is observed to be less during the pre-flare phase compared to the flaring phase because of the steady state of the source. The F_{var} was also estimated for multiwavelength data by Kaur and Baliyan (2018) for CTA 102. They have observed a higher fractional variability at higher energy, e.g., 0.87 in γ-rays, 0.45 in X-rays, 0.082 in UVW2-band and 0.059 in optical B-band. Similar result was also reported by Patel et al. (2018) for 1ES 1959+650. They found that fractional variability increases with increasing energy. The opposite scenario was observed by Bonning et al. (2009) for 3C 454.3, where fractional variability decreases with increasing energy (IR, Optical, UV) due to the presence of steady thermal emission from the accretion disk.

4.4 Detection of High Energy Photon

Detection of high energy photons with, energy greater than 15 GeV, respect to the arrival time on the x-axis are plotted in Figure 4.4 for all the observed flares (flare-1 to flare-4). To find out the high energy photons and its probability of being coincide with a particular source, a tool called *gtsrcprob*, provided by the *Fermi* Science Tools, is used. The *Fermi*-analysis is done with the "ULTRACLEAN" class of events and 0.5° of ROI to detect the high energy photons. The analysis is restricted to photon energy E $>$ 15 GeV and also the probability of being from a source to 99.5%. The photons who satisfy the above conditions are only considered in our result and shown in Figure 4.4. A photon of energy E = 73.8 GeV is detected at MJD 57750.06 with a probability of being from the CTA 102 was 99.99%. Incidentally, this high energy photon is a part of the brightest flare of CTA 102 i.e. flare-3. This photon is found to be the highest energy photon ever detected from CTA 102. One 17 GeV photon is observed during flare-1 and during flare-2, 3, and 4 a large number of high energy photons are observed (Figure 4.4). The highest energy photons observed during flare-1, 2 and 4 are 17, 30 and 58 GeV respectively at MJD 57740.79, 57745.56 and 57762.23. Such observed high energy photons can be produced in external Compton scattering of the BLR, disk or dusty torus photons by the relativistic electrons in the jet and also by synchrotron self Compton emission.

4.5 SEDs of gamma-ray flares

The gamma-ray SEDs are produced for all the different states observed during the high state of September, 2016 to March, 2017 . The various observed states are recognized as pre-flare, rising segment, flare, and decaying segment. Further, the flaring period is divided into four different flares (flare-1, 2, 3, and 4). The gamma-ray spectral data points for each state are produced separately by likelihood analysis, and further, the data points are fitted with

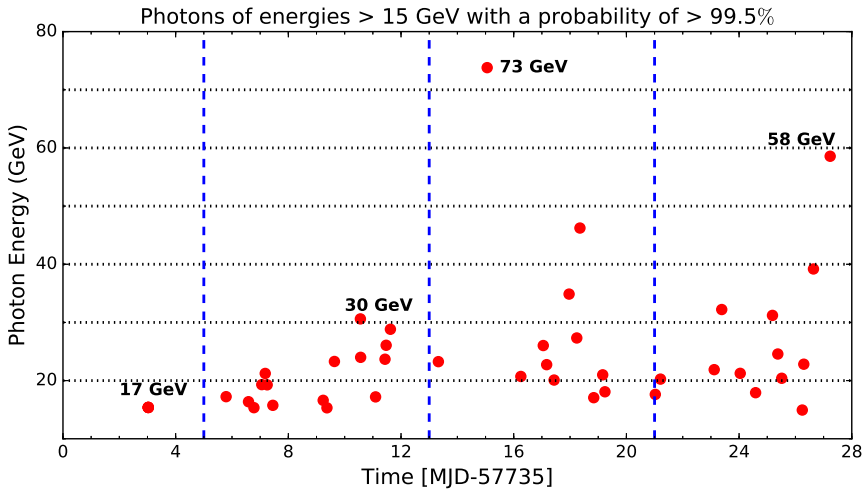

Fig. 4.4 Arrival time and energy of (E $>$ 15 GeV) photons, with a probability higher than 99.5%, plotted for all the flares. Vertical dashed blue lines are separating the flares.

four different spectral models (PL, LP, PLEC, and BPL) defined by Equations 3.1, 3.2, 3.3, and 3.4. The selection of these functional form are motivated by earlier studies on spectral analysis of blazar flares (Ackermann et al. 2010). The spectral fitting of all the different states are shown in Figure 4.5 and the corresponding fitted parameters are mentioned in Table 4.3. The photon flux is increased drastically when the source moved from pre-flare to flaring states, and a significant amount of spectral hardening is observed in the power-law photon spectra. The highest photon flux is observed during flare-3 which is also associated with the maximum hardening in the spectrum. A significant amount of spectral hardening is also seen before from flares of another blazar like 3C 454.4 (Britto et al. 2016).

Presence or absence of curvature in the gamma-ray spectrum are estimated by calculating the TS_{curve} value which is defined as $TS_{curve} = 2(\log \mathcal{L}(\text{LP/PLEC/BPL}) - \log \mathcal{L}(\text{PL}))$ (Nolan et al. 2012). The higher the TS_{curve} value better the fit is. The spectral curvature was considered to be significant if $TS_{curve} > 16$ (Acero et al. 2015). In Table 4.3, the maximum curvature in the gamma-ray spectrum is noticed during rising, flaring, and decaying states. A BPL or an LP function best fits the spectral data points of pre-flare state. The TS_{curve}

values do not differ much in these two cases. Except for SED of flare-1, which can be well described by PLEC, other flares and rising and decaying states are well described by LP distribution. Flare-1 has comparable TS_{curve} values for BPL and PLEC functions. These results suggest that the observed curvature in the gamma-ray spectra during pre-flare, rising, flare, and decaying states could be due to the curvature in the spectrum of the relativistic electrons in the emission region.

4.6 Modeling the SEDs

GAMERA, a publicly available time-dependent code, is used to model the multiwavelength spectral energy distributions for all the flaring and pre-flare, rising, and decaying state. The details about the code are presented in chapter 3. To model the SED, a single emission zone is considered which is moving relativistically along the jet axis of CTA 102. The important input of GAMERA is, injected electron spectrum which is derived from gamma-ray SEDs. Table 4.3 represents the results of gamma-rays spectral fitting for the pre-flare, rising, flare and decaying states, which are fitted with four different spectral models. By comparing the fitted parameters of different models, It is concluded that a log-parabola function well describes the most of the gamma-ray SEDs. In literature, it was found that a log-parabola photon spectrum can be produced by radiative losses of a log-parabola electron spectrum (Massaro et al. 2004). Therefore, In multiwavelength SED modeling a LP distribution is considered to be the input electron spectrum. The injected electron spectrum $Q(E,t)$ in the continuity equation 3.9 could be log-parabola (LP) spectrum if the probability of acceleration decreases with increasing energy. After undergoing radiative losses, this spectrum becomes steeper and denote by $N(E,t)$. In the continuity equation 3.9, the diffusive loss is not included because it is assumed to be less significant compared to the radiative losses by the electrons. According to the jet demography, the photons emitted from the broad line region (BLR) are the target for external Compton emission. The radiation energy density

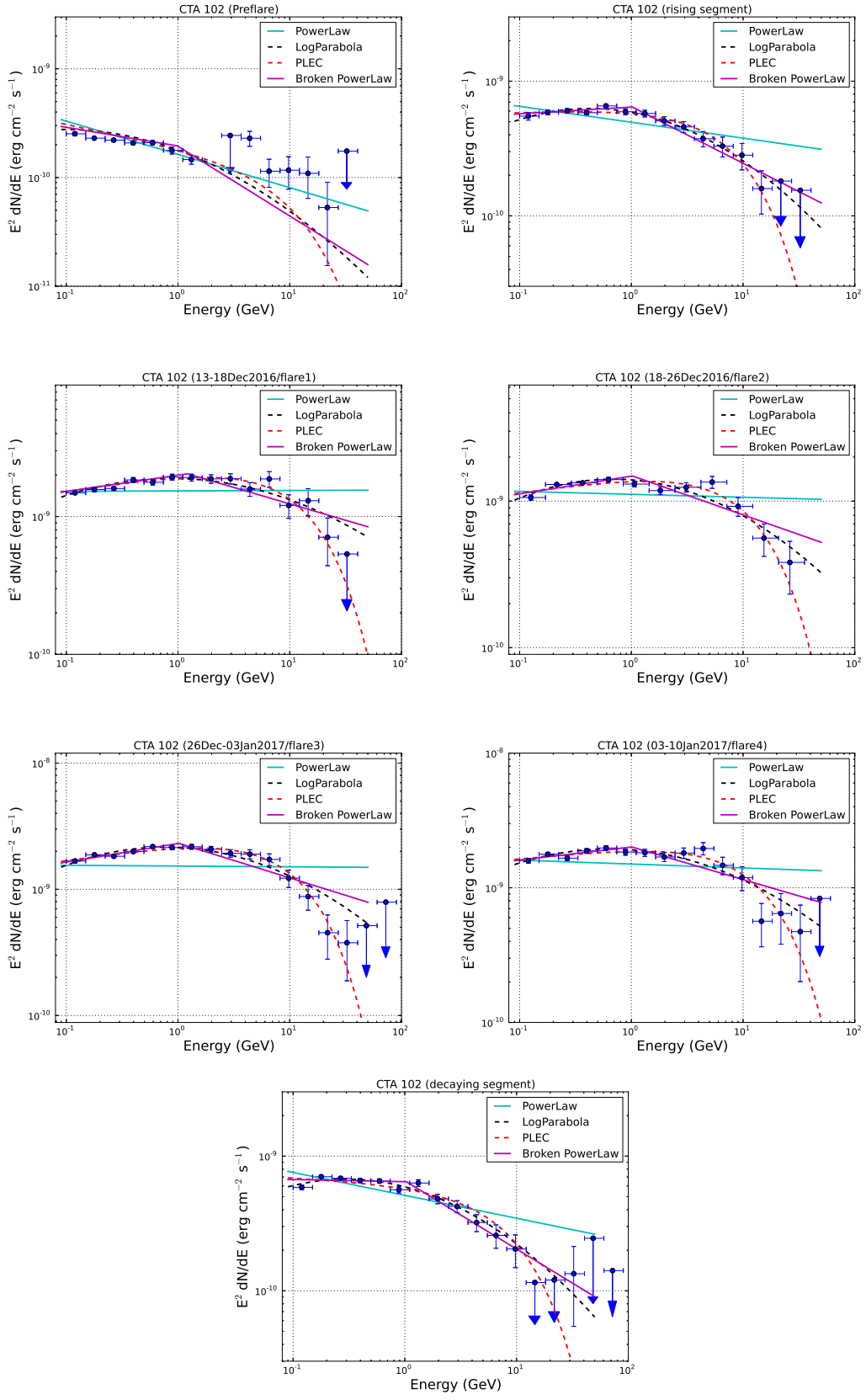

Fig. 4.5 The gamma-ray SEDs for different activity periods identified in Figure 4.1. The SEDs data points were fitted with four different spectral models PL, LP, PLEC, and BPL shown in cyan, black, red, and magenta, respectively. The fitted parameter values are displayed in Table 4.3.

Table 4.3 Results of gamma-ray SEDs fitted with different spectral distributions PL, LP, PLEC, and BPL. The different activity states during the observations are mentioned in the 1st column. The values of the fitted fluxes and spectral index are presented in columns 2 & 3. TS_{curve} = 2(log $\mathcal{L}$(LP/PLEC/BPL) – log $\mathcal{L}$(PL)).

		PowerLaw (PL)				
Activity	$F_{0.1-300\ GeV}$ (10^{-6} ph cm^{-2} s^{-1})	Γ			TS	
pre-flare	1.44±0.04	2.31±0.02	-		6965.29	-
rising segment	3.87±0.07	2.12±0.01	-		18236.04	-
flare-1	10.60±0.17	1.99±0.01	-		26338.38	-
flare-2	7.87±0.12	2.02±0.01	-		30981.15	-
flare-3	11.90±0.14	2.01±0.01	-		46205.62	-
flare-4	11.10±0.18	2.03±0.01	-		24250.71	-
decaying segment	4.17±0.07	2.17±0.01	-		18320.72	-
		LogParabola (LP)				
Activity	$F_{0.1-300\ GeV}$ (10^{-6} ph cm^{-2} s^{-1})	α	β		TS	TS_{curve}
pre-flare	1.38±0.04	2.18±0.03	0.08±0.02		6980.74	15.45
rising segment	3.66±0.07	1.96±0.02	0.09±0.01		18333.51	97.47
flare-1	10.30±0.17	1.87±0.02	0.06±0.01		26408.49	70.11
flare-2	7.60±0.12	1.87±0.02	0.08±0.01		31083.27	102.12
flare-3	11.50±0.14	1.85±0.02	0.08±0.01		46437.84	232.22
flare-4	10.70±0.19	1.89±0.02	0.07±0.01		24332.05	81.34
decaying segment	3.96±0.07	2.01±0.02	0.09±0.01		18412.52	91.80
		PLExpCutoff (PLEC)				
Activity	$F_{0.1-300\ GeV}$ (10^{-6} ph cm^{-2} s^{-1})	Γ_{PLEC}	E_{cutoff} [GeV]		TS	TS_{curve}
pre-flare	1.40±0.04	2.21±0.04	12.39±4.16		6976.88	11.59
rising segment	3.72±0.07	1.97±0.02	9.45±1.46		18326.98	90.94
flare-1	10.40±0.17	1.88±0.02	14.21±2.22		26421.66	83.28
flare-2	7.67±0.12	1.89±0.02	12.71±1.79		31081.92	100.77
flare-3	11.60±0.14	1.87±0.02	11.98±1.33		46414.40	208.78
flare-4	10.80±0.18	1.92±0.02	15.46±2.69		24326.29	75.58
decaying segment	4.05±0.07	2.05±0.02	10.76±2.13		18385.50	64.78
		Broken PowerLaw (BPL)				
Activity	$F_{0.1-300\ GeV}$ (10^{-6} ph cm^{-2} s^{-1})	Γ_1	Γ_2	E_{break} [GeV]	TS	TS_{curve}
pre-flare	1.38±0.06	2.17±0.07	2.64±0.10	0.98±0.12	6984.17	18.88
rising segment	3.69±0.09	1.96±0.03	2.42±0.05	1.02±0.09	18323.99	87.95
flare-1	10.40±0.17	1.88±0.02	2.24±0.04	1.21±0.11	26396.25	57.87
flare-2	7.65±0.12	1.88±0.02	2.27±0.03	1.02±0.04	31060.34	79.19
flare-3	11.60±0.14	1.85±0.02	2.28±0.03	1.01±0.14	46402.10	196.48
flare-4	10.80±0.18	1.90±0.03	2.24±0.04	1.01±0.19	24312.09	61.38
decaying segment	4.00±0.07	2.02±0.03	2.51±0.06	1.03±0.14	18403.22	82.50

of BLR in the comoving jet frame is given in equation 3.11. Here, I have been considered that only 2% ($\xi_{BLR} \sim 0.02$) of the disk radiation reprocessed in BLR. The size of the BLR is important to estimate the BLR energy density as well as absorption of γ-ray from the emission region. The accretion disk luminosity, mass of SMBH, and Eddington luminosity for CTA 102 were estimated by Zamaninasab et al. (2014). The values derived by Zamaninasab et al. (2014) are $L_{disk} = 3.8\times10^{46}$ erg/s, $M_{BH} \sim 8.5\times10^{8}\ M_{\odot}$, and $L_{Edd} = 1.1\times10^{47}$ erg/s respectively. To estimate the radiation energy density of BLR (U'_{BLR}), the disk luminosity $L_{disk} = 3.8\times10^{46}$ erg/s and $\Gamma = 15$ are used. The size of BLR is estimated from the scaling law R_{BLR}=10^{17} $L^{1/2}_{disk,45}$, where $L_{disk,45}$ is the value of disk luminosity in units of 10^{45} erg/s, and it is found to be 6.16×10^{17} cm, which is similar to BLR radius (R_{BLR}=6.7×10^{17} cm) estimated by Pian et al. (2005).

The direct disk emission also plays an important role and considered as an external source of seed photons for external Compton emission by the relativistic electrons. The energy density of disk photon in the comoving frame (Dermer and Menon 2009) is calculated from the following relation,

$$U'_{disk} = \frac{0.207 R_g l_{Edd} L_{Edd}}{\pi c z^3 \Gamma^2} \tag{4.5}$$

where R_g is the gravitational radius, $l_{Edd} = L_{disk}/L_{Edd}$ is called the Eddington ratio, and $z = 6.7\times10^{17}$cm is the distance of the emission region from the super massive black hole. The disk temperature was estimated from Dermer and Menon (2009) by using the l_{Edd} and the mass of the central black hole (M_{BH}). It was noted that the external Compton (EC) emission by different photons (NIR/optical/UV) emitted by the disk and dusty torus-based clouds irradiated by a spine-sheath jet could be important (Finke 2016, Gaur et al. 2018, Breiding et al. 2018) in some cases. The dusty torus (DT) is not included as target photon field in our model, due to the lack of observational evidence. The magnetic field and the Doppler factor of the blob along with the spectral indices of the injected electron spectrum,

and luminosity in injected electrons are the model parameters, whose values are optimized to fit the SEDs in Figure 4.6.

4.7 Multiwavelength SEDs

The SEDs data points are also produced from Swift-XRT and UVOT in X-rays and UV/optical for all the observed flaring and quiescence state, including rising and decaying segment. Along with the gamma-ray SEDs, X-rays, and UV/optical SEDs are also considered for the multiwavelength SED modeling. Time-dependent multiwavelength SED modeling is performed for all the states by using the publicly available code GAMERA. Details about the GAMERA are provided in chapter 3. In each phase or states injected electron spectrum evolves with time as the electrons lose energy radiatively. The time evolved electron spectrum is further used to produced the synchrotron, SSC, and IC emission. The Doppler factor is assumed to be 35, which is quite high compared to the value estimated by Casadio et al. (2015), and the Lorentz factor is used to be 15. The size of the emission region is adjusted to 6.5×10^{16} cm so that SSC emission is not too high. In Figure 4.6, the X-ray data constrains the SSC emission. It must be note that the intra-night variability observed in optical flux suggests an upper limit on the size of the emission region and the value estimated to be 4.5×10^{16} cm for Doppler factor 35 (Zacharias et al. 2017b). The value estimated here is comparable to the size used in our model. In *Fermi*-LAT data, the variability time is observed to vary in the range of one hour to several days. Modeling the multiwavelength SED reveals that a strong magnetic field is needed to produce the synchrotron and SSC emission. The magnetic field also changes as source transits from pre-flare to flaring state because of the increase in the synchrotron peak. The magnetic field found during pre-flare phase is 4.0 Gauss while for flaring periods it is recorded to be 4.2 Gauss. The injected electron luminosity mainly controls the IC peaks, and during the flaring period the IC peak was observed to be much higher compared to the IC peak during pre-flare phase . Hence, a large amount of

luminosity has to put in electron to explain the gamma-ray data in multiwavelength SEDs. Our modeling result show that the luminosity injected in electrons increases nearly by a factor of seventy as the source travels from the pre-flare to the flaring state. The jet power carried by magnetic field and electrons are estimated, and it is found that most of the jet power go to the magnetic field, not the injected electrons. The maximum jet power required in our model is 6.6×10^{46} erg/sec. The photon flux during various phases (pre-flare, rising segment, flare-1, flare-2, flare-3, flare-4, and decaying segment) are calculated and compared with the data in Figure 4.6. The parameter's value found in the model fitting (Table 4.4) is the best model parameters to fit the observed photon flux.

4.8 Results

Light curve

The blazar CTA 102 is found to be very active during September, 2016 to March, 2017 not only in gamma-ray but also in X-ray and optical/UV. The flux in gamma-ray crossed its all previous year flux values and became the brightest one ever detected from this source. The total time period of 190 days are divided into various states like pre-flare, rising segment, flare, and decaying segment. The flaring period observed for 28 days are further divided into four different flaring state, named as flare-1, flare-2, flare-3, and flare-4. The maximum flux achieved during flaring period is $30.12 \pm 4.48 (\times 10^{-6})$ ph cm^{-2} s^{-1} from the 90 minutes time bin light curve. The rise and decay time of the different peaks are observed during all the flares (Figure 4.3) and presented in Table 4.1. A simultaneous observations in X-ray and optical/UV reveals that the source was very bright in these wavebands too.

Variability time

During the flaring period, the gamma-ray variability time from the 90 minutes time bin light curve is found to be in the range of an hour scale to several days. Intra-night variability was observed in the optical flux by Bachev et al. (2017) for CTA 102, where they have studied the outburst of 2012 and 2016. This study used the one day as a variability time to estimate the size of the emission region by using equation 4.6. For Doppler factor 35 intra-night variability time scale gives an upper limit of 4.5×10^{16} cm on the size of the emission region. In modeling the SEDs, the value 6.5×10^{16}cm is used as the size of the blob so that the SSC emission is not too high. The region size is related to the Doppler factor and variability time scale by the following relation,

$$R \leq c\, t_{var}\, \delta\, (1+z)^{-1} \tag{4.6}$$

where z is the redshift of the source and c is the speed of light in vacuum. It is essential to note that the above relation is an approximation and there are other effects also which may introduce significant errors in determining the size of the emission region (Protheroe, 2002).

Days to year scale of variability in blazar emission could be seen because of change in accretion rate as discussed in Sartori et al. (2018). Following the idea addressed by Kelly et al. (2011), and Sartori et al. (2018), the AGN variability can be modeled as a result of variations in the fueling of SMBH. The continuous fueling of black hole may occur due to physical processes of different spatial scales. Disk properties like its structure, viscosity, and the system's response to perturbations could be one of the factors influencing the conversion of gravitational energy to jet luminosity (Shakura and Sunyaev 1973). Possible accretion disk origin of variability in the jet of Mrk 421, which is a BL Lac has been reported by Chatterjee et al. (2018). A strong jet emission and weak disk emission in X-rays exhibit a

break in power spectral density, and which could be connected to variation in accretion rate. This result strengthens the motivation for an accretion-jet scenario of blazar flares.

Different states of the source found during September, 2016 to March, 2017 are classified based on the fractional variability amplitude. The F_{var} show that the source flux is more variable during flares and less variable in pre-flare, rising, and decaying segment. CTA 102 is confirmed as a source of very high energy photon, and a 73 GeV of photon is detected during the flaring period.

SEDs Modeling

The external Compton emission of BLR photons dominates in high energy emission in blazar. Along with BLR, the disk photon and dusty torus (DT) photons also contribute to the external Compton emission in FSRQ type blazars. However, we do not include the dusty torus region as a target photon field because of the lack of observational information, in our study to model the external Compton. The values of the parameters fitted in our multiwavelength modeling are shown in Table 4.4, and the different SEDs are plotted in Figure 4.6. Nearly seventy times of more injected electron luminosity is needed during the flare, to explain the multiwavelength SEDs, compare to the pre-flare state. The rise in the injected luminosity of electrons or jet power during the flaring period can be explained with an increase in accretion rate of the supermassive black hole, which powers the jet. A relationship between jet power and accretion in blazars has been well studied earlier. A large sample of blazars was studied by Sbarrato et al. (2014) in context of jet-disc connection. Their result shows that the BLR luminosity is a tracer of accretion rate while gamma-ray luminosity is a tracer of jet power. It concluded that the two luminosities are linearly connected. Fluctuation in luminosity and variability in AGN was discussed as a stochastic process in Kelly et al. (2011), where they gave a relation between the characteristic time scale of high energy X-ray emission and black hole mass of AGN.

4.9 Discussion

CTA 102 has shown an exceptional outburst during September to October, 2012, studied by Larionov et al. (2016). Multiwavelength SEDs modeling is done by collecting the data from near-infrared (NIR) to gamma-ray wavebands. The SEDs are modeled by assuming a spherical emission region or shock wave moving along a helical path down the jet. The change in the viewing angle because of the motion of the shock wave along the helical path produced a significant change in the value of the Doppler factor from 28 to 16. They have found the co-spatial origin of the optical and gamma-ray emission, which supports SSC emission mechanism.

The gamma-ray flare observed in January, 2016 was studied by a helical jet model by Li et al. (2018). They found that the value of Doppler factor to be 17.5 and the size of the emission region to be 0.11-0.32 pc. They have also estimated the location of gamma-ray emission region which was located at a distance between 5.7 to 16.7 pc from the central SMBH assuming a conical jet geometry. They have estimated the magnetic field at a distance of 1 pc from the SMBH along the jet axis by using the core shift method. The value of the magnetic field was found to be 1.57 Gauss.

The flare of CTA 102 from 2016 to 2017 has also been studied before by Zacharias et al. (2017b), where they have modeled the gamma-ray flares by ablation of a gas cloud by relativistic jets. They have explained the rise of the flare as a result of gradual increase in the number of injected electrons in the jet due to slice by slice ablation of cloud until the center of the cloud is reached. When the cloud moves outside the jet particle injection decreases, which results in decay of the flare. The similar values of Doppler factor and BLR temperature from Zacharias et al. (2017b) are used in our modeling. They have assumed a magnetic field 3.7 Gauss, which is comparable to the value found in our study. They have chosen a smaller region size (2.5×10^{16}) compared to us and have assumed time-dependent luminosity and spectral index of injected electrons. In our modeling, these variables were

constants and adjusted for each state to obtain the best fit to the multiwavelength SED data points. They have also considered EC by BLR photons is the main radiative loss mechanism of relativistic electrons, and SSC emission is found to be always insignificant.

The multiwavelength emission from CTA 102 has also been studied by Gasparyan et al. (2018). The EC component were fitted with both the BLR photons and the DT photons along with the SSC. They have also observed a spectral curvature and hardening in the gamma-ray spectra. In their work, the magnetic field and the luminosity in injected electrons differ significantly from one epoch to another epoch.

Thus the different high activity states of CTA 102 were modeled in various ways to obtain the excellent fit to the observed multiwavelength data. It has been seen that the values of the physical parameters like the magnetic field, luminosity in injected electrons, etc., are model dependent. A study of the time evolution of the physical parameters (e.g., magnetic field, Doppler factor, spectral index and luminosity in electrons, region size) required for SED modeling in pre-flare, flare, and decaying states is necessary as the variations in the values of these parameters could be good indicators of the underlying model. At least some of the models could be excluded in this way. Simulated SEDs could be compared with the parametric fitting of SEDs for this purpose.

4.10 Summary

1. Four bright flares are observed in CTA 102 during high activity period between September, 2016 to March, 2017.

2. The gamma-ray flare is found to be brightest flare ever detected from CTA 102 with flux value $(30.12\pm4.48)\times10^{-6}$ ph cm^{-2} s^{-1}.

3. The shortest variability time in gamma-ray is found to be 1.08 ± 0.01 hr during the flaring period of CTA 102.

4. Bachev et al. (2017) have estimated the intra-night variability in optical band and the size of the emission region has been estimated to be 4.5×10^{16} cm. However, to model the SED we have used 6.5×10^{16} cm as size of emitting region to constrain the SSC emission.

5. The multiwavelength data from Swift-XRT/UVOT were collected along with *Fermi*-LAT to do the broadband SED modeling. A publicly available time dependent code GAMERA has been used to model the SED.

6. The injected electron luminosity has to be seventy times higher during the flaring state compared to the pre-flare state to explain the multiwavelength SED.

7. The other parameters: magnetic field in the blob, injected electron spectrum, minimum and maximum electron energy are optimized to obtain the best model fit.

Table 4.4 Results of Fitting Multi-wavelength SEDs in Figure 4.6. A log-parabola model is used as electron injected spectrum which is defined as dN/dE = $N_0(E/E_0)^{(-\alpha-\beta*log(E/E_0))}$, where E_0 is chosen as 90 MeV.

Activity	Parameters	Symbol	Values	Activity period (days)
	Min Lorentz factor of injected electrons	γ_{min}	3.5	
	Max Lorentz factor of injected electrons	γ_{max}	7.5×10^3	
	BLR temperature	T'_{blr}	5×10^4 K	
	BLR photon density	U'_{blr}	1 erg/cm^3	
	Disk temperature	T'_{disk}	2.6×10^6 K	
	Disk photon density	U'_{disk}	3.7×10^{-7} erg/cm^3	
	Size of the emission region	R	6.5×10^{16} cm	
	Doppler factor of emission region	δ	35	
	Lorentz factor of emission region	Γ	15	
Pre-flare				
	Spectral index of injected electron spectrum (LP)	α	1.9	
	Curvature parameter of LP electron spectrum	β	0.08	
	magnetic field in emission region	B	4.0 G	56
	luminosity in injected electrons	L_e	1.78×10^{42} erg/sec	
Rising				
	Spectral index of injected electron spectrum (LP)	α	1.8	
	Curvature parameter of LP electron spectrum	β	0.08	
	magnetic field in emission region	B	4.1 G	29
	luminosity in injected electrons	L_e	6.94×10^{42} erg/sec	
Decaying				
	Spectral index of injected electron spectrum (LP)	α	1.8	
	Curvature parameter of LP electron spectrum	β	0.08	
	magnetic field in emission region	B	4.1 G	22
	luminosity in injected electrons	L_e	8.76×10^{42} erg/sec	
Flare-1				
	Spectral index of injected electron spectrum (LP)	α	1.7	
	Curvature parameter of LP electron spectrum	β	0.02	
	magnetic field in emission region	B	4.2 G	5
	luminosity in injected electrons	L_e	1.27×10^{44} erg/sec	
Flare-2				
	Spectral index of injected electron spectrum (LP)	α	1.7	
	Curvature parameter of LP electron spectrum	β	0.02	
	magnetic field in emission region	B	4.1 G	8
	luminosity in injected electrons	L_e	5.0×10^{43} erg/sec	
Flare-3				
	Spectral index of injected electron spectrum (LP)	α	1.7	
	Curvature parameter of LP electron spectrum	β	0.02	
	magnetic field in emission region	B	4.2 G	8
	luminosity in injected electrons	L_e	9.04×10^{43} erg/sec	
Flare-4				
	Spectral index of injected electron spectrum (LP)	α	1.7	
	Curvature parameter of LP electron spectrum	β	0.02	
	magnetic field in emission region	B	4.2 G	7
	luminosity in injected electrons	L_e	8.91×10^{43} erg/sec	

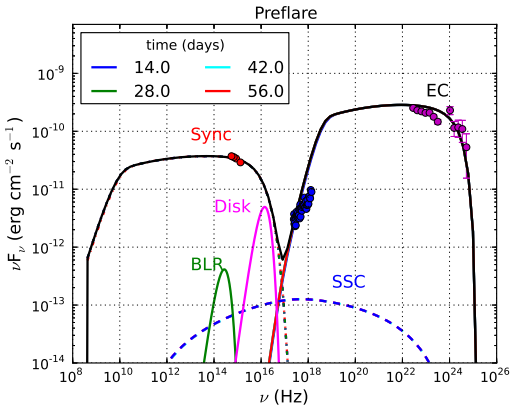
Preflare
time (days)
14.0
28.0
42.0
56.0
Sync
Disk
BLR
EC
SSC
νF_ν (erg cm^{-2} s^{-1})
ν (Hz)

(a)

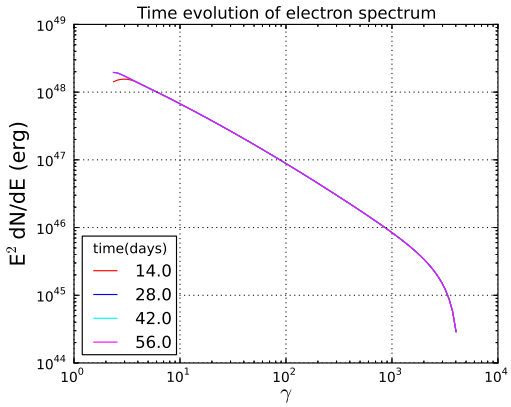
Time evolution of electron spectrum
time(days)
14.0
28.0
42.0
56.0
E^2 dN/dE (erg)
γ

(b)

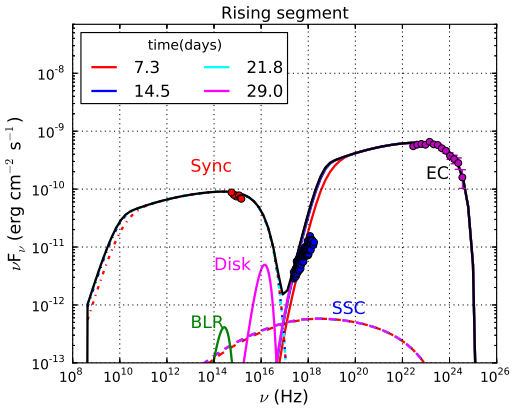
Rising segment
time(days)
7.3
14.5
21.8
29.0
Sync
Disk
BLR
EC
SSC
νF_ν (erg cm^{-2} s^{-1})
ν (Hz)

(c)

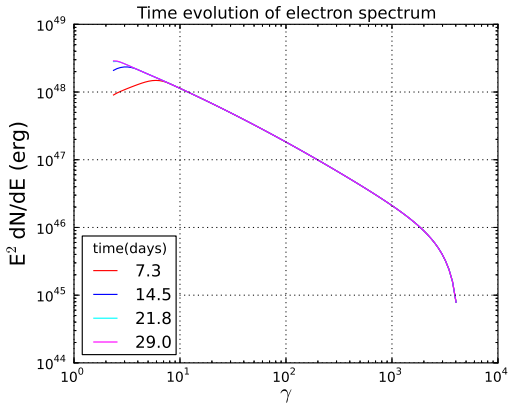
Time evolution of electron spectrum
time(days)
7.3
14.5
21.8
29.0
E^2 dN/dE (erg)
γ

(d)

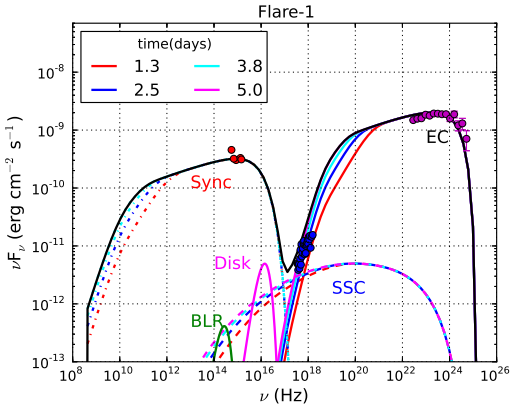
Flare-1
time(days)
1.3
2.5
3.8
5.0
Sync
Disk
BLR
EC
SSC
νF_ν (erg cm^{-2} s^{-1})
ν (Hz)

(e)

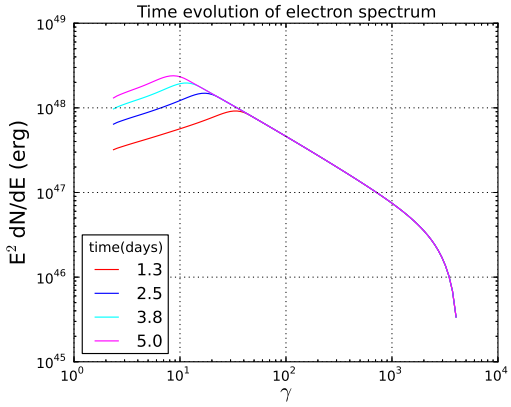
Time evolution of electron spectrum
time(days)
1.3
2.5
3.8
5.0
E^2 dN/dE (erg)
γ

(f)

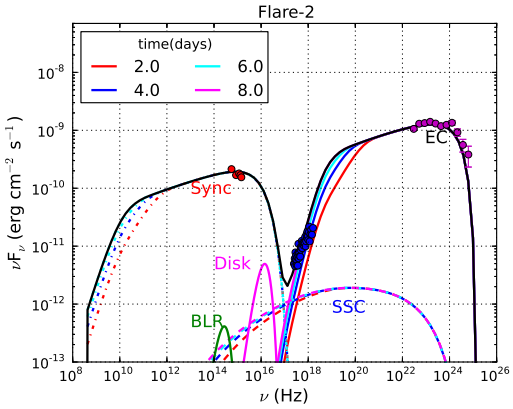
Flare-2
time(days)
2.0
4.0
6.0
8.0
Sync
Disk
BLR
EC
SSC
νF_ν (erg cm^{-2} s^{-1})
ν (Hz)

(g)

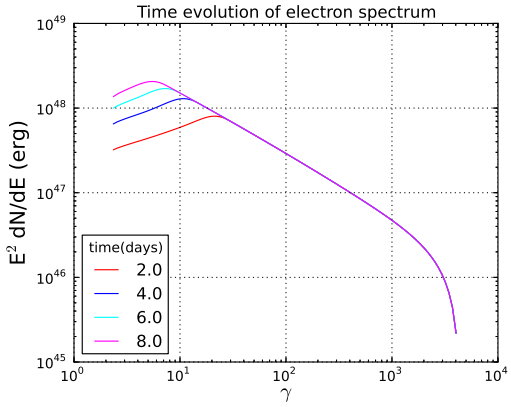
Time evolution of electron spectrum
time(days)
2.0
4.0
6.0
8.0
E^2 dN/dE (erg)
γ

(h)

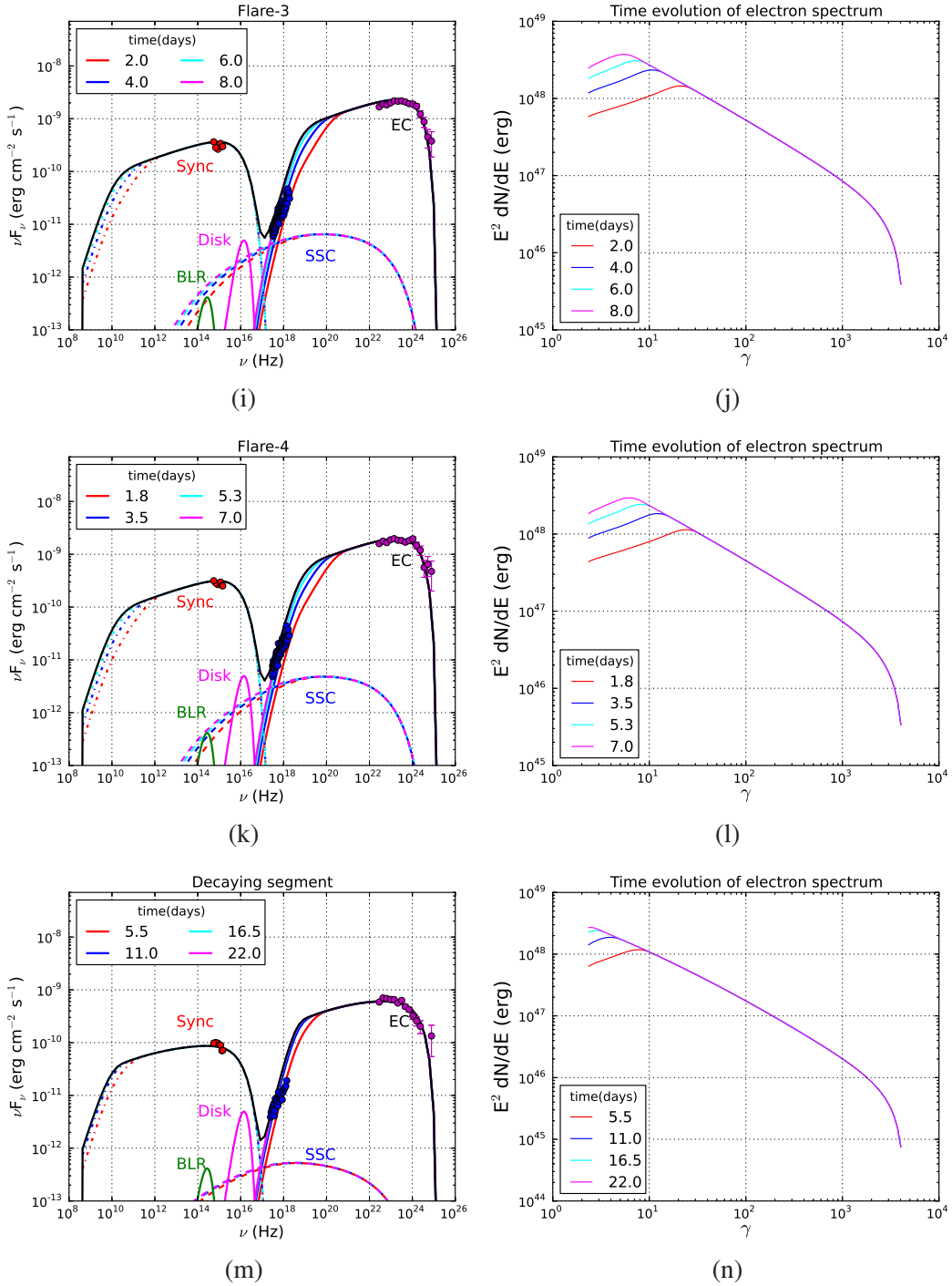

Fig. 4.6 Modeled multiwavelength SEDs during different activity periods shown in the left panel and the time evolution of electron spectra is shown in the right panel. The plots arranged in the following order pre-flare, rising segment, flare-1, flare-2, flare-3, flare-4, and decaying segment. Each activity period was divided into four equal time intervals and shown in different colors. The model parameters are mentioned in Table 4.4.

Chapter 5

Multi-frequency Variability and Correlation Study

5.1 TON 599 during flare of 2017

Ton 599 is an FSRQ type blazar also known as 4C 29.45, and in third *Fermi* catalog it was named as 3FGL J1159.5+2914 (Acero et al. 2015) with RA = 179.8826413 deg, Dec = 29.2455075 deg, and redshift $z = 0.72449$ (Schneider et al. 2010; Hewett and Wild 2010). It shows a significant amount of variability across the entire electromagnetic spectrum ranging from radio to gamma-rays. It has been studied in the past for more than four decades in several energy bands. In gamma-ray band, It was first detected in the second EGRET catalog by Thompson et al. (1995). *Fermi*-LAT detected Ton 599 in the first three months of its operation (Abdo et al. 2010b) because of the good sensitivity of the telescope. It has been a strong flaring source since 1992, EGRET observed it within the four years (1992–1996) of time span, three strong flares were observed with flux $\sim 3.9 \times 10^{-10}$ Jy above 100 MeV by EGRET (Thompson et al. 1995; Mukherjee et al. 1997, Hartman et al. 1999). During the year 2017, the source has gone through a prolonged flaring state across the entire electromagnetic spectrum.

The correlation between different wavebands has been done before for various FSRQ to find out the connection between their emission region. A sample of fourty blazars has been studied by Cohen et al. (2014), where they have estimated the correlation between optical and gamma-ray emission. Their results show that in all the cases, the high energy emission (gamma-ray) leads to low energy emission (optical) with a time lag of almost 1–10 days. A radio and gamma-ray correlation have been done for a sample of 183 blazars by Pushkarev et al. (2010), where they have found that in almost all the cases radio flare lags the gamma-ray flares. It was believed that the time delay observed between two different band emissions depends upon the separation between their emission region (Fuhrmann et al. 2014). The exact location of the gamma-ray emitting zone in blazar is not well known because of the poor angular resolution of high energy telescope. However, the radio emission region can be resolved in the blazar's jet with milliarcsecond angular resolution of the radio telescope. A correlation study was also done for Ton 599 between gamma-ray and radio emission by Ramakrishnan et al. (2014). Their results show that the gamma-ray emission lags behind the radio emission with a time lag of 120 days, which constrains the location of emission region in the parsec-scale jet.

In this part of the chapter, I have studied the correlation between the different energy bands of Ton 599 to understand the multiwavelength emission during the flare of 2017.

5.2 Multiwavelength Observations and Data Analysis

5.2.1 *Fermi*-LAT

Fermi-LAT is a pair conversion γ-ray Telescope sensitive to photon energies between 20 MeV to higher than 500 GeV, with a field of view of about 2.4 sr (Atwood et al. 2009). The instrument was launched by NASA in 2008 June and started taking the data since August, 2008. *Fermi*-LAT is an all-sky monitor, and it is monitoring Ton 599 since August, 2008

. *Fermi* Science Tools has standard data reduction and analysis procedure[1] to analyze the *Fermi*-LAT data. The same procedure is followed to analyze the flaring state of Ton 599. The other details about the analysis procedure is discussed in section 3.2 of chapter 3. *Fermi*-LAT data was collected from January, 2014 to January, 2018 for Ton 599, and analysis reveals that during these four years, most of the time the source is observed in a quiescent state. At the end of the year 2017, Ton 599 started showing the activity in gamma-ray which lasted for around three months (Figure 5.1). A small flare is also observed at the end of the year 2015, but it did not last for a long time. The maximum flux achieved during the flare of 2015 is found to be $\sim 4\times10^{-7}$ ph cm^{-2} s^{-1}.

5.2.2 Swift-XRT/UVOT

Swift-XRT and UVOT have also observed the blazar Ton 599 during flaring state and details about the observations are shown in Table 5.1. The task '*xrtpipeline*' version 0.13.2 is used to produce the cleaned events files, and the latest calibration files are used to reprocess the raw data. The photon counting (PC) mode events files are considered during the analysis. The standard procedure for selecting the source and background regions are followed. A circular region of size 20 arcsecond is chosen for source and background region. The X-ray spectra are fitted in *xspec* using a simple power law model with the galactic absorption column density $n_H = 1.77\times10^{20}$ cm^{-2} (Kalberla et al. 2005). Ton 599 is also seen by all the available filters (U, V, B, W1, M2, and W2) of UVOT. A circular region of size 5 and 10 arc seconds is chosen to extract the image of source and background, respectively. The task 'uvotsource' is used to extract the source magnitudes and fluxes. Magnitudes are corrected for galactic extinction (Schlafly and Finkbeiner 2011) and converted into flux using the zero points (Breeveld et al. 2011) and conversion factors (Larionov et al. 2016).

[1] https://fermi.gsfc.nasa.gov/ssc/data/analysis/documentation/

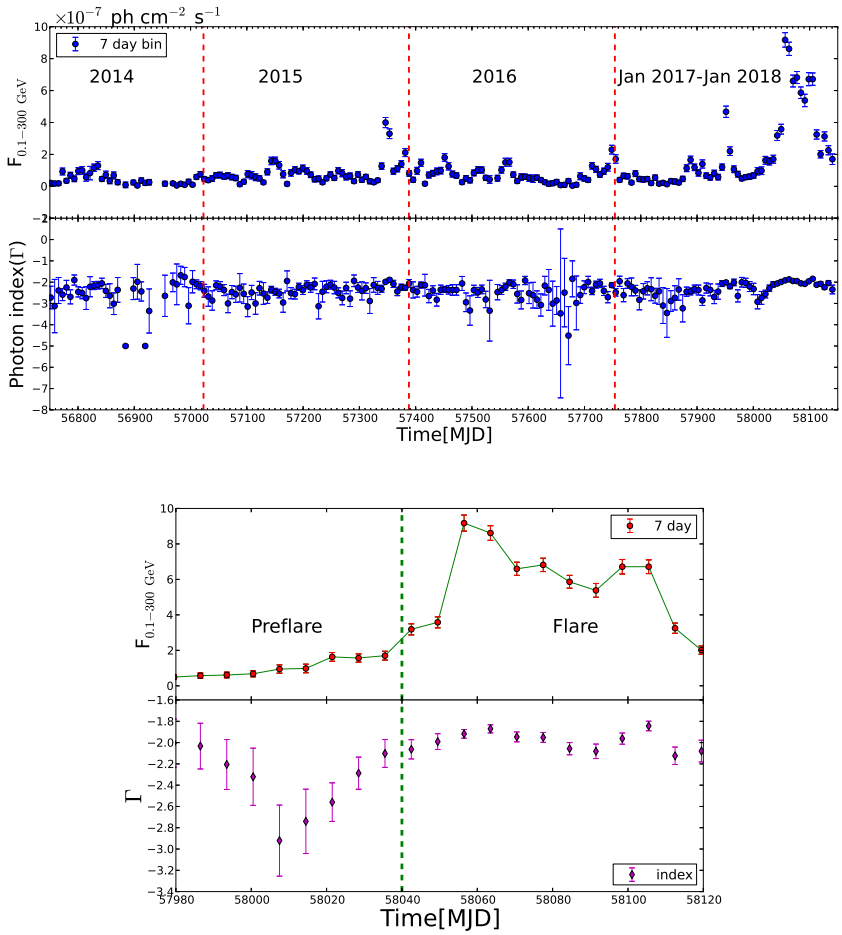

Fig. 5.1 Top panel: Light curve of Ton 599 from January, 2014 to January, 2018 are shown. Bottom panel: Zoomed version of the flares observed at the end of 2017 are shown and the vertical green dashed lines are separating the two state of the source.

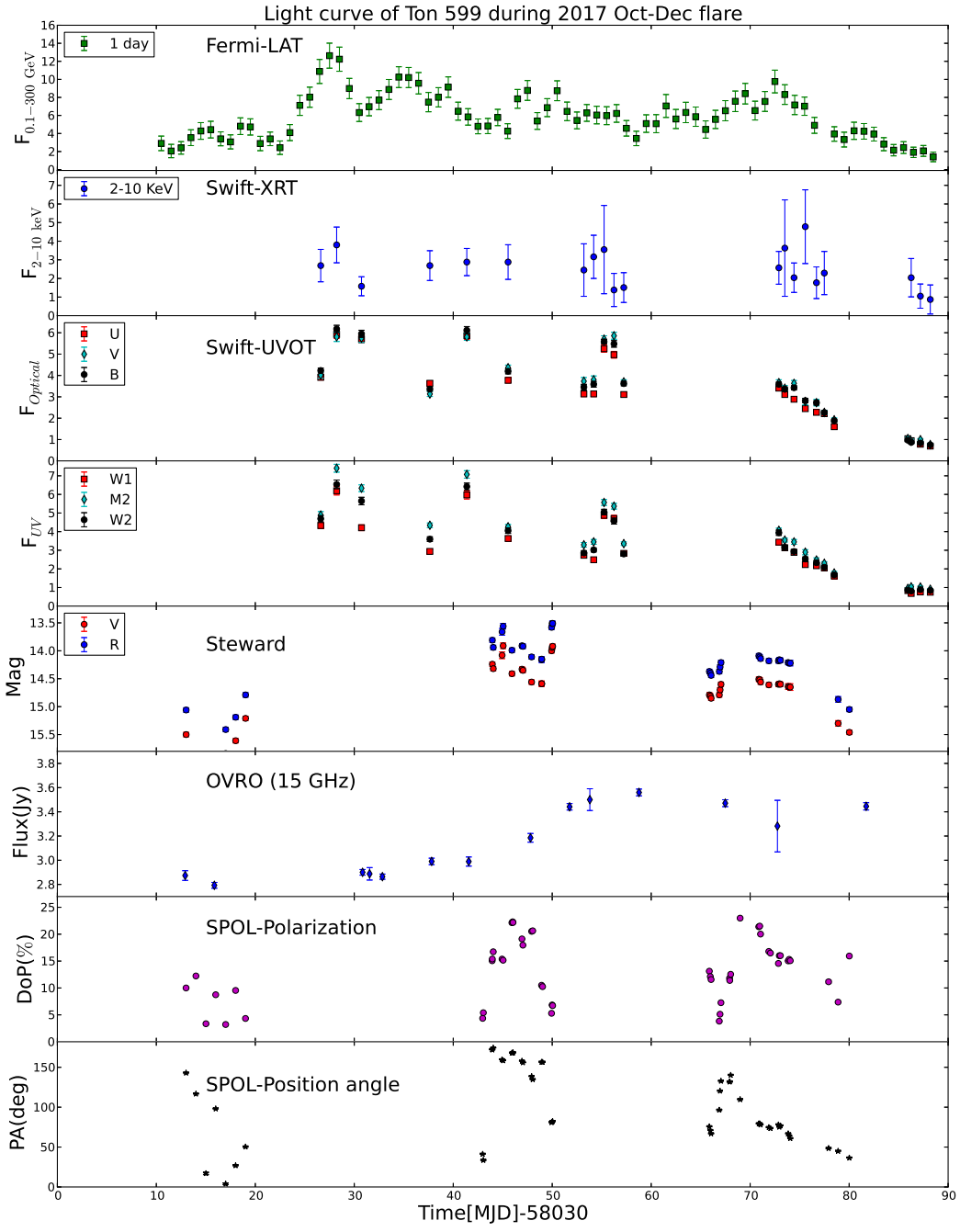

Fig. 5.2 Multi-wavelength light curve of Ton 599 during the end of 2017. *Fermi*-LAT data are in units of 10^{-7} ph cm^{-2} s^{-1}. Swift-XRT and UVOT are in units of 10^{-12} and 10^{-11} erg cm^{-2} s^{-1} respectively.

Table 5.1 Table shows the log of the observations during the flaring period (MJD 58040 – 58120).

Observatory	Obs-ID	Exposure (ks)
Swift-XRT/UVOT	00036381023	2.48
Swift-XRT/UVOT	00036381024	2.53
Swift-XRT/UVOT	00036381025	2.46
Swift-XRT/UVOT	00036381026	2.47
Swift-XRT/UVOT	00036381027	2.40
Swift-XRT/UVOT	00036381028	1.61
Swift-XRT/UVOT	00036381030	2.20
Swift-XRT/UVOT	00036381031	2.27
Swift-XRT/UVOT	00036381032	1.58
Swift-XRT/UVOT	00036381033	1.65
Swift-XRT/UVOT	00036381034	1.67
Swift-XRT/UVOT	00036381035	1.99
Swift-XRT/UVOT	00036381036	0.99
Swift-XRT/UVOT	00036381037	1.94
Swift-XRT/UVOT	00036381038	2.02
Swift-XRT/UVOT	00036381040	1.92
Swift-XRT/UVOT	00036381041	0.90
Swift-XRT/UVOT	00036381042	0.87
Swift-XRT/UVOT	00036381044	1.73
Swift-XRT/UVOT	00036381046	1.84
Swift-XRT/UVOT	00036381047	1.94
Swift-XRT/UVOT	00036381048	1.93

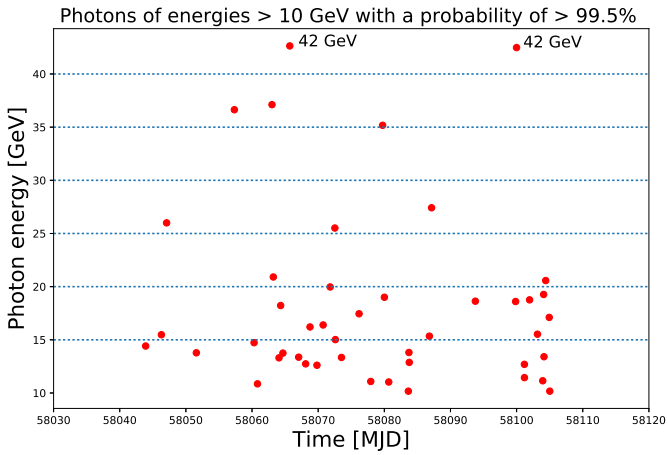

Fig. 5.3 The arrival time of photons of energy > 10 GeV , with probability $> 99.5\%$.

5.2.3 Steward Optical Observatory

The archival data from the Steward optical observatory, Arizona (Smith et al. 2009)[2] is used in this study. The Steward optical observatory is the part of the *Fermi* multiwavelength support program and continuously monitoring the Fermi blazar. Ton 599 is continuously monitored with the SPOL CCD Imaging/Spectrometer. The optical V-band and R-band photometric data along with the Polarimetry (degree of polarization and position angle) data are collected for the whole flaring period during the end of 2017.

5.2.4 OVRO data at 15 GHz

Ton 599 is also observed in radio waveband by Owens Valley Radio Observatory (OVRO; Richards et al. 2011) as a part of *Fermi* monitoring program. The radio data at 15 GHz are collected during MJD 58040 – 58120.

[2]http://james.as.arizona.edu/ psmith/Fermi/

5.3 Results and Discussion

The *Fermi*-LAT data are collected from January, 2014 to January, 2018 or during MJD 56751–58140 for Ton 599. The primary analysis produced the light curve, which is shown in Figure 5.1 along with the photon spectral index. During these four years of observations of Ton 599 it is observed that most of the time source is in quiescence state or steady state. The flux during the steady state is very low ($\sim 1\times10^{-7}$ ph cm^{-2} s^{-1}). Only two times in four years, the source has gone to a higher state, the first one is in the year 2015 and the second one is in the year 2017. A maximum flux $\sim4\times10^{-7}$ ph cm^{-2} s^{-1} is observed during the 2015 flare. In 2016, flux level was below $\sim2\times10^{-7}$ ph cm^{-2} s^{-1} with small occasional fluctuations in the flux value. In the first three months of 2017, the source was almost quiet, and it started showing the major activity at the end of the year 2017. A clear full-fledged flare is observed between October 14, 2017 to January 02, 2018 (MJD 58040–58120). Lower panel of Figure 5.1, shows the zoomed light curve of the flaring period. A period of two months is chosen just before the main flare where the flux is almost constant, and defined as pre-flare. This major flare has been studied in this chapter along with the multi-wavelength observations and performed the fractional variability and correlation studies among different wavelength during the flaring period (MJD 58040 – MJD 58120).

Gamma-ray spectral analysis is also performed, four spectral models mentioned in section 3.2 were used to fit the gamma-ray spectral energy distribution (SED).

5.3.1 Multi-wavelength light curves

The data collected from different telescopes and observatories for Ton 599 in different wavebands are plotted together in Figure 5.2 over the flaring period MJD 58040 – MJD 58120. The first panel of the figure shows the one-day bin gamma-ray light curve from *Fermi*-LAT, which shows that the source started showing the activity at October 14, 2017 (MJD 58040). The source continued to be in the high state for almost two and a half months, and after MJD

58120 the source got settled down in its quiescence state. During this long flaring period few major peaks along with moderate variations in flux are observed. The maximum flux achieved during a major peak at MJD 58057.5 is $\sim 13\times10^{-7}$ ph cm^{-2} s^{-1} from one-day bin light curve. After the major peak, the source was in a higher state for almost two months with the average flux 6.69×10^{-7} ph cm^{-2} s^{-1}.

The second panel of Figure 5.2 shows the X-ray light curve from Swift-XRT in the energy range of 2–10 keV. Different observations and their exposure times are presented in Table 5.1. The observations with Swift were carried on when the source was already flaring in gamma-ray. An X-ray peak is observed in coincidence with gamma-ray peak with a peak flux of 3.80×10^{-12} erg cm^{-2} s^{-1} at MJD 58058. No clear variation is seen in X-ray over a gamma-ray flaring period, but source flux is still high. Similar to gamma-ray flux, the X-ray flux also got settled down in low flux state at the end of the flare. The flux in lower state is found to be 0.87×10^{-12} erg cm^{-2} s^{-1}.

Swift-UVOT also observed the source in all the available six filters (U, B, V, W1, M2, W2). The light curve of optical and UV bands are shown separately in the third and fourth panel of Figure 5.2, respectively. In gamma-ray, the source was already in flaring state when the Swift telescope started looking at it, and hence high flux was observed in both optical and UV bands. A peak is observed in optical and UV bands at MJD 58058 which coincides with the peaks observed in X-ray and gamma-ray light curve. The peak fluxes corresponding to different filters are different at same MJD 58058. In optical filter U, B, and V the fluxes are observed to be 5.92×10^{-11}, 6.17×10^{-11}, 5.81×10^{-11} and in UV filters W1, M2, W2 the fluxes are measured to be 6.19×10^{-11}, 7.41×10^{-11}, 6.54×10^{-11} in units of erg cm^{-2} s^{-1} respectively. Similar to the gamma-ray, after the first peak source was also variable for almost two months in optical and UV bands and got settled down at the end of the flare. The flux in Optical and UV band also follow the last peak of γ-ray flare at MJD 58103. After two months of flaring period optical and UV flux attained its quiescence state with a flux

close to zero at MJD 58118.

The archival data from Steward observatory for V and R band are shown in the fifth panel of Figure 5.2. Ton 599 appears to be more bright in the R band compared to V band throughout the total flaring period. It is observed that the source is in a high state during this period. However, no evident variation in magnitudes are seen. The average magnitude estimated during the total flaring period are 14.9 and 14.5 respectively for V and R bands.

The archival data from OVRO observatory at 15 GHz is plotted in the panel sixth of Figure 5.2. The source appears to be in quiescence state for the first 20 days in radio, while it is flaring in gamma-ray and other wavebands. The radio flux started rising slowly at MJD 58060, and after almost thirty days the source achieved the maximum flux of 3.56 Jy at MJD 58089. The delay in the radio flare is investigated while studying the correlations among the different wave band in section 5.3.6.

Optical degree of polarization (DoP) and position angle (PA) from steward observatory are plotted in panel seven & eight of Figure 5.2. A huge variation is observed in DoP and PA during flaring period. In just 10 days of time interval MJD 58070–58080, DoP is changed from 4%– 22% and PA varied from 30 °–175 °. The variation in the DoP and PA can be explained by the shock-in-jet model (Marscher et al. 2008; Larionov et al. 2013; Casadio et al. 2015), in which a shock wave moving down the jet following magnetic field lines, covering only a portion of the jet's cross section can lead to this variation in DoP and PA during the flare.

5.3.2 High energy photons and temporal evolution

A search of high energy photons are carried on with the help of "ULTRACLEAN" class of events for a 0.5° ROI during the likelihood analysis. Figure 5.3 shows the photon detected energy $>$ 10 GeV, along with their arrival time. All the events shown in Figure 5.3 have 99.5% probability for being from the source. It is found that during the flare most of the

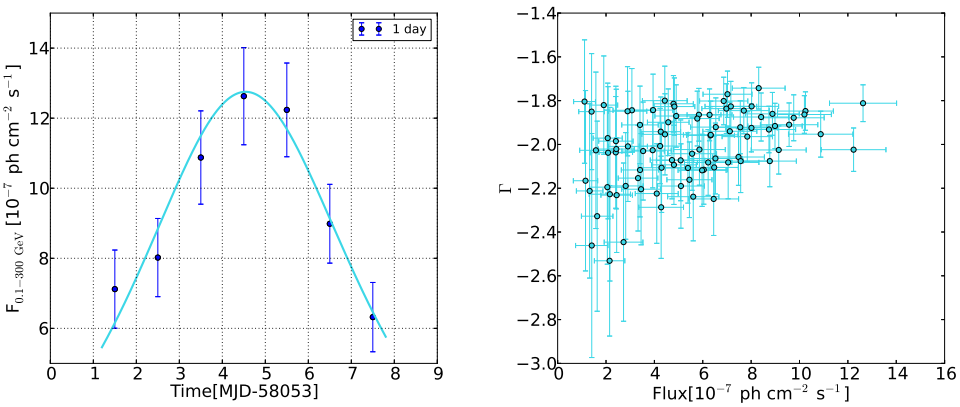

Fig. 5.4 left: Temporal fitting of the first peak of the flare shown in Figure 5.2. Right: Photon index is plotted with photon flux to show the harder-when-brighter trend.

photons are below 20 GeV and only a few were detected above 20 GeV. Two high energy events of 42 GeV are detected at MJD 58065.7 and 58100 respectively. Their probability of being from the Ton 599 is 99.7% and 99.8%. These two photons coincide with the peak flux of the flare, and they do show a harder spectral index. A harder spectral index associated with the detection of high energy photons is a common feature of blazars.

The study of the temporal evolution of gamma-ray flare is done, and the brightest peak of the flare (which is also the first peak in Figure 5.2) is fitted with a function called the sum of exponentials. This fitting provides the rise and decay time of the brightest peak, and it is shown in the left panel of Figure 5.4. The functional form of the sum of exponentials is defined as:

$$F(t) = 2F_0 \left[\exp\left(\frac{t_0 - t}{T_r}\right) + \exp\left(\frac{t - t_0}{T_d}\right) \right]^{-1}, \tag{5.1}$$

where F_0 measures the flare amplitude at time t_0, T_r and T_d are the rise and decay times (Abdo et al. 2010c) respectively. It is found that the peak shown in Figure 5.4 is very much symmetric, which means it has almost equal rise and decay time. From equation 5.1, the rise and decay time are found to be 2.22±0.14 and 2.30±0.13 days, respectively. Equation

5.1, is used to fit the other peak also seen in Figure 5.2, where most of the peaks are found to be symmetric. Symmetric time profile expected when the cooling time of electrons t_{cool} is much smaller than the light crossing time R/c (Chiaberge and Ghisellini 1999), where R is the size of the emission region. This physical scenario seems to be possible for Ton 559 during this flaring period.

The right panel of Figure 5.4 shows the gamma-ray flux vs. photon spectral index plot. A "harder-when-brighter" trend is seen which is also a very common feature of FSRQ. During the flaring period, the spectral index is observed to be harder than those reported in 3FGL catalog (Acero et al. 2015) for Ton 599.

5.3.3 γ-ray emission region

The one-day bin gamma-ray light curve for flaring period along with the photon spectral index is shown in Figure 5.5 separately. Variation in photon spectral index with source flux points is very much clear here and confirms the "harder-when-brighter" trend. Seven days time bin light curve of total studying period of Ton 599 was shown in the lower panel of Figure 5.1. The entire period is divided into pre-flare and flare part based on their flux states. The pre-flare is observed between MJD 57980–58040 and the average flux measured during this period is 9.35×10^{-8} ph cm^{-2} s^{-1} and the average photon spectral index is 2.38. The time duration MJD 58040–58120 is considered as a flaring episode where the source is in higher flux state compared to the pre-flare state. The average photon flux measured during this period is 6.94×10^{-7} ph cm^{-2} s^{-1}, which is more than seven times of average flux value of the pre-flare state. The average spectral index estimated during the flare is 1.96, which is also harder compared to preflare state spectral index value. In the one-day time bin light curve, the maximum flux during the flaring episode was found to be 12.63×10^{-7} ph cm^{-2} s^{-1} at MJD 58057.5 and the corresponding photon spectral index to be 1.81 (Figure 5.5). Figure 5.5 shows a strong variability in flux throughout the total flaring period and the fastest

variability time is estimated here, by using the following expression,

$$F(t_2) = F(t_1).2^{(t_2-t_1)/t_d}, \tag{5.2}$$

where $F(t_1)$ and $F(t_2)$ are the fluxes measured at two consecutive time t_1 and t_2 respectively and t_d represents the flux doubling/halving timescale. The whole flaring period is scanned with equation 5.2. A range of variability time is found, from one day to few days. One day variability time is used to estimate the size of the emission region, by using the following relation,

$$R \leq c\, t_{var}\, \delta\, (1+z)^{-1} \tag{5.3}$$

where, z = 0.72 is the redshift of the source, c is speed of light in vacuum, and δ is the Doppler factor. The size of the emission region is found to be 1.88×10^{16} cm, for δ = 12.5 (Zhang et al. 2002; Liodakis et al. 2017), which is close to value (δ = 15) estimated by Ghisellini et al. (1998).

The high energy photons detected during flare can constrain the location of gamma-ray emission region. According to Liu and Bai (2006), the BLR is opaque for photon above 20GeV/(1+z) energy. They have estimated the optical depth for gamma-ray photons with energies between 10–100 GeV produced within the BLR. They have found that the BLR can absorb the photons above 20 GeV, which means photon detected higher than 20 GeV energy is coming from outside the BLR. In Ton 599, two high energy photons of energy 42 GeV were detected which must have been coming from outside the BLR or from the outer edge of the BLR. The distance of the gamma-ray emitting blob from the central SMBH can be estimated by relation R $\sim$ r/ψ, where r is the size of the emitting blob, and ψ is the semi-aperture angle of the jet (Foschini et al. 2011). For blazar, in general, the ψ

lies between 0.10-0.25 ° (Ghisellini and Tavecchio 2009; Dermer and Menon 2009). The intrinsic opening angle can also be estimated from observations. Pushkarev et al. (2009), have studied a sample of BL Lac and quasars and they have found that the average intrinsic opening angles for a sample of BL Lacs is 2.4±0.6 ° and for quasars is 1.2±0.1 °. Ton 599 was also the part of the sample analyzed by Pushkarev et al. (2009), where it was listed as J1156+295. The intrinsic opening angle for Ton 599 found to be 0.58°. For $\psi = 0.58°$, the location of gamma-ray emitting blob is estimated to be 3.24×10^{16} cm, which is near the boundary of the BLR. The size of the BLR dissipation region found by Wu et al. (2018) and Pian et al. (2005) was 2.4×10^{17} and 2.98×10^{17} cm respectively. Therefore, at the time of 42 GeV of photon emission during the flare, γ-ray emission region must have been located outside or at the edge of the BLR. Pushkarev et al. (2017) have also calculated the intrinsic opening angle for 65 sources from MOJAVE-1 sample. They have found that the intrinsic opening angles for these 65 sources lie between 0.1° to 9.4°, with a median of 1.3°. The range of opening angle suggests that the location of the emission region must lie between 1.88 ± 10^{17} to 2.00 ± 10^{15} cm. The location of the emission region estimated for Ton 599 (3.24×10^{16} cm) was found to be in this range.

5.3.4 Spectral Analysis

The gamma-ray spectral energy distributions are produced and presented in this section for pre-flare and flaring state observed at the end of 2017 in Ton 599. The likelihood analysis performed over all the different states with four different spectral models is presented in Prince et al. (2018) and fitted with PL, LP, PLEC, and BPL. The modeled parameters mentioned in Table 5.2 and the gamma-ray SEDs are shown in Figure 5.6. Fitting the gamma-ray SEDs with these four models is essential to constrain the gamma-ray emission region. Inside the BLR, photon-photon pair production ($\gamma\,\gamma \longrightarrow e^{+}e^{-}$) plays an important role and it can attenuate the gamma-ray flux. As a result, we expect to observe a break in the gamma-ray

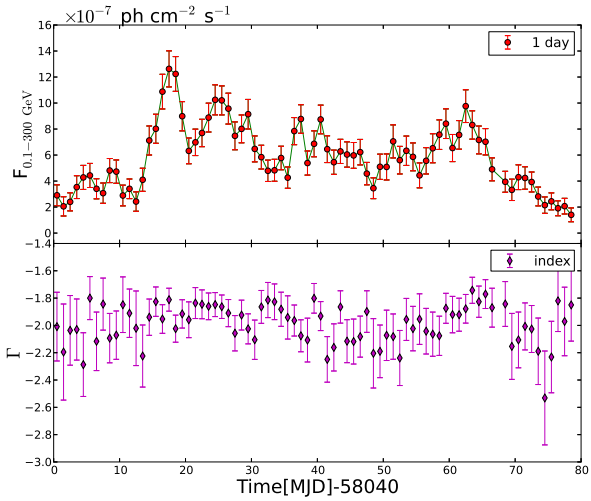

Fig. 5.5 One day bin gamma-ray light curve with corresponding photon spectral index are shown.

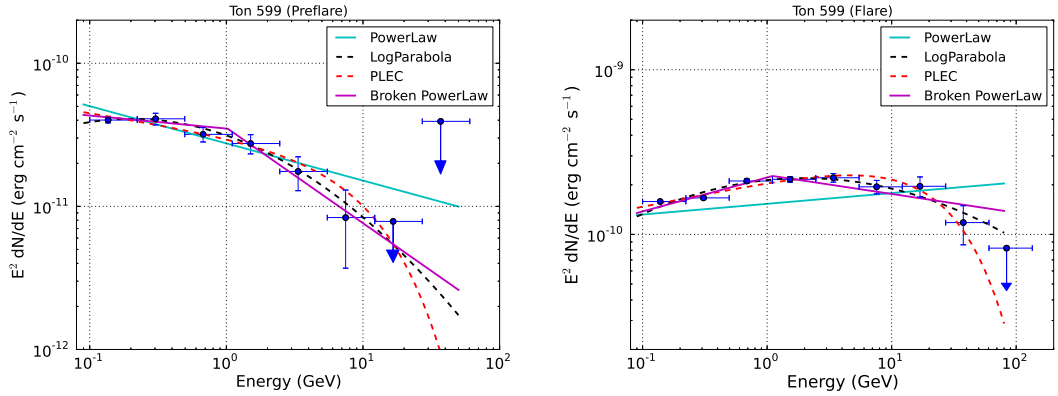

Fig. 5.6 SEDs of pre-flare and flaring period of Ton 599 are plotted here and fitted with different spectral models. The fitted parameters are shown in Table 5.2.

Table 5.2 Parameters obtained from the spectral analysis fit, for the different models PL, LP, PLEC, and BPL, for the pre-flare and flare by using. the Likelihood analysis method. ΔLog(likelihood) estimated with respect to the Log(likelihood) of the PL fit.

Activity	$F_{0.1-300\ GeV}$ (10^{-7} ph cm^{-2} s^{-1})	PowerLaw (PL) Γ			-Log(likelihood)	ΔLog(likelihood)
Pre-flare	2.45±0.15	2.26±0.05			99810.26	
Flare	11.00±0.02	1.94±0.01			183323.43	
		LogParabola (LP) α	β			
Pre-flare	2.27±0.01	2.08±0.09	0.10±0.04		99806.43	-3.83
Flare	10.40±0.02	1.79±0.02	0.06±0.01		183294.99	-28.44
		PLExpCutoff (PLEC) Γ_{PLEC}	E_{cutoff}			
Pre-flare	2.36±0.02	2.15±0.08	12.51±7.60		99808.07	-2.19
Flare	10.60±0.02	1.85±0.01	30.00±0.08		183291.44	-31.99
		Broken PowerLaw (BPL) Γ_1	Γ_2	E_{break}		
Pre-flare	2.30±0.02	2.09±0.08	2.67±0.17	1.10±0.17	99806.06	-4.2
Flare	10.50±0.02	1.79±0.03	2.11±0.04	1.11±0.22	183297.07	-26.36

spectrum. A break in the gamma-ray spectrum can be explained by fitting the gamma-ray SEDs data points with LP/BPL/PLEC models. The scenario is entirely different when the emission region is outside the BLR or within the molecular torus (MT). In this case, a simple PL could be a good fit to the SED data points. The quality of the unbinned fit is presented in Table 5.2 by the Log(likelihood) and ΔLog(likelihood) value. The ΔLog(likelihood) measured with respect to PL and the higher value of ΔLog(likelihood) for a particular model is preferred over the lower value. Comparing ΔLog(likelihood) values for all the models, it is noted that all the three models, LP, PLEC, and BPL, are very much compatible with the SEDs data points. Table 5.2 exhibit a clear spectral hardening with increasing flux as the source moves from pre-flare to flaring state. For PL models, when the source travels from pre-flare to flaring state the flux rises from 2.45±0.15 to 11.00±0.02 ($\times 10^{-7}$ ph cm^{-2} s^{-1}) and the power law spectral index (Γ) changes from 2.26±0.05 to 1.94±0.01. A break is observed in the gamma-ray spectrum during the flaring state for the BPL fitting, and it shows rising and falling spectrum before and after the break and the corresponding photon

index were $\Gamma_1 = 1.79$, $\Gamma_2 = 2.11$ with break energy $E_{break} = 1.11$ GeV. This finding suggests that the peak of the IC mechanism probably lies in the LAT energy band (0.1-300 GeV) and the shape of the γ-ray spectrum likely reflects the distribution of emitting electrons.

5.3.5 Fractional variability (F_{var})

The variability seen at all frequencies and timescales in blazars is completely a random process. It is more prominent during the flare, and the flare profiles depend on the particle acceleration and energy dissipation. The amplitude of variation depends on the jet parameters like magnetic fields, viewing angle, particle density and the efficiency of acceleration (Kaur and Baliyan 2018). To determine the variability amplitude in all energy bands, good quality data is required across the entire electromagnetic spectrum. Observation of Ton 599 across the entire electromagnetic spectrum made it possible to determine the variability amplitude using the fractional root mean square (rms) variability parameter (F_{var}) introduced by Edelson and Malkan (1987); Edelson et al. (1990). Fractional variability is used to compare the variability amplitudes across the entire electromagnetic spectrum and can be estimated by using the relation given in Vaughan et al. (2003),

$$F_{var} = \sqrt{\frac{S^2 - \sigma^2}{r^2}} \tag{5.4}$$

$$err(F_{var}) = \sqrt{\left(\sqrt{\frac{1}{2N}} \cdot \frac{\sigma^2}{r^2 F_{var}}\right)^2 + \left(\sqrt{\frac{\sigma^2}{N}} \cdot \frac{1}{r}\right)^2} \tag{5.5}$$

where, $\sigma_{XS}^2 = S^2 - \sigma^2$, is called excess variance, S^2 is the sample variance, σ^2 is the mean square uncertainties of each observation and r is the sample mean. The fractional variability calculated for all the wavebands is mentioned in Table 5.3. It is found that the source is more variable in γ-ray and then UV, Optical and radio (at 15 GHz). Because of the significant error bar in the X-ray data, the fractional variability could not estimated. The F_{var} is found to be

Table 5.3 Fractional variability is estimated for time interval 57980 to 58120.

Waveband	F_{var}	err(F_{var})
γ-ray	0.730	0.019
U	0.514	0.008
B	0.503	0.007
V	0.485	0.008
W1	0.537	0.009
M2	0.531	0.007
W2	0.536	0.008
OVRO (15 GHz)	0.071	0.004

0.73 in γ-ray, 0.53 in UVW2-band, 0.50 in optical B-band and 0.07 in radio (at 15 GHz). It is noticed that F_{var} is increasing with energy, suggesting that a large number of particles are producing high energy emission. Similar behavior of fractional variability was also seen for other FSRQ like CTA 102 by Kaur and Baliyan (2018), where they found a trend of large fractional variability towards higher energies. Increase in fractional variability was also seen in TeV blazar, Patel et al. (2018) and Sinha et al. (2016) have noted an increase in fractional variability from radio to X-rays and decrease in high energy part from γ-rays to Hard X-rays. An opposite trend was also reported by Bonning et al. (2009), where variability amplitudes decrease towards shorter wavelength (IR, Optical, and UV), which suggests the presence of steady thermal emission from the accretion disk.

5.3.6 Cross-Correlations

In Figure 5.2, it is very much evident that the flares in γ-ray, X-ray, Optical, and UV band are mostly correlated. The radio flare at 15 GHz was noted after few days of γ-ray flare. The detailed study about correlations has been done in this particular section. A cross-correlation study of flux variations in different energy band can give an idea of whether emissions in various bands are coming from the same emission region in the jet and if not, then it indicates a relative distance between the emitting zones. Therefore, the correlation studies

have been done using the z-transformed discrete correlations function (zDCF) formulated by Alexander (1997); Alexander (2013). It provides insight into the emission in different energy bands. Let's suppose there are two discrete data sets a_i and b_j and they have standard deviation σ_a and σ_b, the discrete correlations for all measured pairs (a_i-b_j) is defined as,

$$UDCF_{ij} = \frac{(a_i - \bar{a})(b_j - \bar{b})}{\sqrt{(\sigma_a^2 - e_a^2)(\sigma_b^2 - e_b^2)}} \tag{5.6}$$

where each pairs are associated with a pairwise lag Δt_{ij} = t_j - t_i. The parameters e_a and e_b are the measurement errors associated with data sets a_i and b_j respectively. Binning the $UDCF_{ij}$ in time will directly result in DCF(τ). Averaging the $UDCF_{ij}$ over M number of pairs for which (τ - $\Delta\tau$/2) $\leq \Delta t_{ij} <$ (τ + $\Delta\tau$/2),

$$DCF(\tau) = \frac{1}{M} UDCF_{ij}, \tag{5.7}$$

and the error on DCF is defined as,

$$\sigma_{DCF}(\tau) = \frac{1}{M-1} \left\{ \sum [UDCF_{ij} - DCF(\tau)] \right\}^{1/2} \tag{5.8}$$

The z-transformed Discrete correlations function (zDCF) plotted in Figure 5.7 for different combinations like γ-X-ray, γ-Swift M2, γ-Swift V and γ-OVRO (15 GHz). In γ-X-ray correlations, it is found that there is no time lag between γ-ray and X-ray emission and the maximum DCF found to be 0.55. The strong correlation and zero time lag observed between γ-ray and X-ray suggests that the emissions are originated from the same region or very close-by region.

A significant correlation has been seen between γ-ray and optical (V-band) emission with a small time lag, and the DCF peak is noted to be 0.85. Similar kind of behavior is also seen between γ-ray and UV (M2 filter) emission with DCF peak found to be 0.90. Larionov et al.

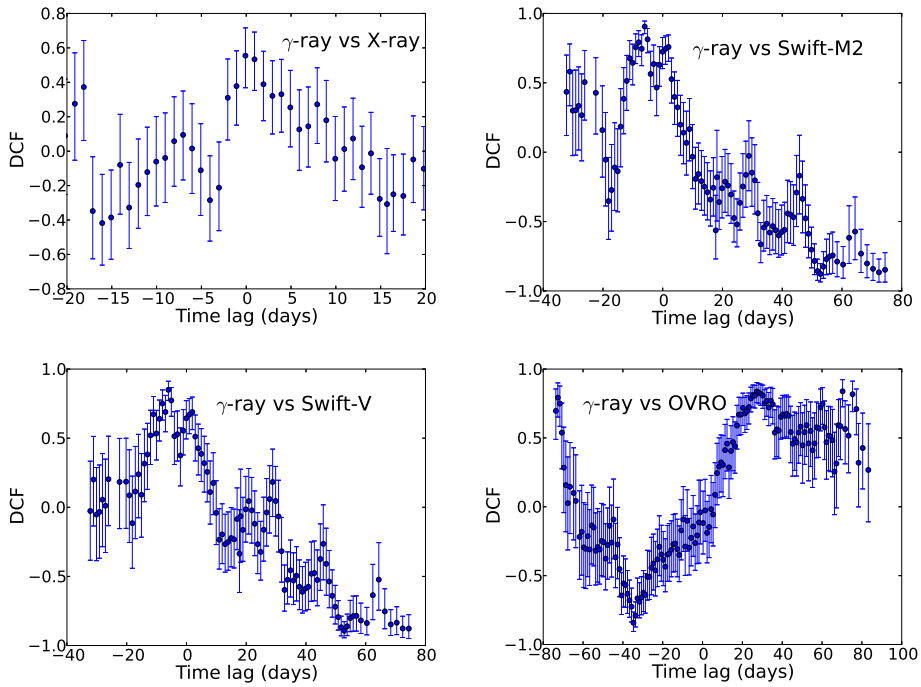

Fig. 5.7 zDCF plotted for all four combinations: γ-X-ray, γ-Swift-M2, γ-Swift-V, γ-OVRO(15 GHz) from left to right, for the flare of Ton 599 during the end of 2017.

(2013) has also observed a small lag between the γ-ray and optical emission for S50716+71 and at the same time they also noted an emergence of radio knot K3. Finally, they have concluded that all these events are co-spatial. Similar results were also noticed for CTA 102 (Larionov et al. 2016; Kaur and Baliyan 2018) during the outburst of 2012 and 2017 with remarkable similarity in two energy emission. Significant correlation and small time lag between γ-ray and optical/UV emission can be explained by leptonic models, where it is assumed that the optical/UV emission is mostly the synchrotron emission from the jets and the γ-ray emission is the product of inverse Compton (IC) scattering of optical/UV photons by the relativistic electrons present in the jets.

It is believed that γ-ray emission is the product of IC scattering of soft photons of the same electrons producing the optical radiation, then its variations are expected to be simultaneous or delayed with respect to the optical radiation, and it can be the result of modeling the non-thermal flares with shocks in a jet model (Sikora et al. 2001; Sokolov et al. 2004; Sokolov

and Marscher 2005). This kind of behavior was already seen in few other blazars like 4C 38.42 (Raiteri et al. 2012), 3C 345 (Schinzel et al. 2012) and in 3C 454.3 (Bonning et al. 2009; Vercellone et al. 2010; Raiteri et al. 2011). Interestingly, the opposite behavior was also seen, where γ-ray was leading the optical radiation, in few blazars, e.g., FSRQ PKS 1510-089 (Abdo et al. 2010a; D'Ammando et al. 2011) and 3C 279 (Hayashida et al. 2012). It can be explained by considering fast decay in the energy density of external seed photon, responsible for the IC emission, along with the jet axis, compared to the decay in magnetic field energy density, which is responsible for the synchrotron emission.

A complex correlation between gamma-ray and optical radiation has also been addressed by Marscher (2014), by considering the effect of turbulence in the jets. Since the magnetic field is embedded in the jets so turbulence in jets can cause turbulent magnetic field which will affect mostly the synchrotron emission and can lead to the optical variability while the turbulent magnetic field cannot affect the γ-ray radiation. In other words, a γ-ray emission region could be better aligned along the line of sight, which can lead to a higher Doppler factor of high-energy flux, as compared to the optical emitting region.

A correlation study between γ-ray and IR/optical/UV has also been done before for other blazars, e.g., Bonning et al. (2009); Vercellone et al. (2009); Raiteri et al. (2011); Jorstad et al. (2013); Larionov et al. (2013) and Cohen et al. (2014), where they suggested the co-spatial origin of γ-ray and IR/optical/UV emission. It is also possible that the nature of the correlation between two emitted fluxes changes with epochs, and it can be seen as the product of different processes and/or different particle population during the high activity.

The right plot of lower panel of Figure 5.7 shows the correlation between γ-ray and radio (OVRO; 15 GHz). A lag of 27 days in the radio emission at 15 GHz is noted with DCF peak of 0.84. Since the γ-ray and optical emission is well correlated with a small time lag which suggests that radio emission also lags with optical by the same amount as with γ-ray.

Time delay uncovered by zDCF analysis can be related to the relative location of the emis-

sion region at different wavebands, which depends on the physics of the jets and high energy radiation mechanisms. The lag of 27 days in the radio emission with γ-ray/optical clearly suggests that these two emissions are from two different locations in the jets. The observed time lag between γ-ray and radio can be used to determine the distance between two emitting regions by using the equation given in Fuhrmann et al. (2014),

$$\Delta r_{\gamma,r} = \frac{\beta_{app} c \Delta t}{sin\theta} \tag{5.9}$$

where θ = viewing angle of the source, β_{app} = apparent jet speed, and Δt = observed time lag. Using Δt = 27 days, and θ = 4.3 °, β_{app} = 16.13 from Liodakis et al. (2017), the distance between two emitting region is found to be $\Delta r_{\gamma,r} \sim 5$ pc. This means the radio emitting region is located far away from the AGN central engine. It is possible that the high energy and radio emission region have different apparent speeds as well as different viewing angles which further implies that they have different Doppler factor. A similar situation was also observed by Raiteri et al. (2013) for BL Lacertae, where they found a lag of 120-150 days between γ-ray/optical to radio and the distance between two emitting regions was estimated to be in a range of 6.5 to 8.2 pc. Rani et al. (2014) have also found a time lag of 82 days between γ-ray and radio emission for S5 0716+714; the distance between two emission region was estimated to be in the range of 2.9 - 4.4 pc (Rani et al. 2015), for β_{app} = 6 - 8 c and viewing angle (θ) = 6 - 9 °).

Alternatively, flares which are delayed and appear late at lower frequencies can be seen as a clear indication of opacity effects, in the context of shock-in-jet model (Marscher and Gear 1985; Valtaoja et al. 1992), due to synchrotron self-absorption. A shock is formed close to the core where the jet is optically thick to radio frequencies but transparent to high energy, and a component at the core of the jet producing an optical/γ-ray flare propagates along with the jets, and after some time jet becomes optically thin to detect the radio flare.

5.4 Summary

1. At the end of 2017 blazar Ton 599 went through a long flaring episode covering the entire electromagnetic spectrum. Flaring was first reported in γ-rays followed by the other wavebands and a long delay in the radio flare was observed by OVRO at 15 GHz as seen from Figure 5.2.

2. Ton 599 is not very much variable in X-ray, but its variability is seen in γ-ray and UV/optical. In γ-ray, during the flaring episode, a maximum flux 12.63×10^{-7} is noticed with photon index 1.81 and a clear "harder-when-brighter" spectral behavior is observed (Figure 5.4).

3. Significant variations in DoP and PA are seen during the flaring period, which can be explained by a shock-in-jet model (Marscher and Gear 1985).

4. Almost all the peaks of the flare showed symmetric profile. The rise and decay time of one of the peaks are found to be 2.22 ± 0.14 and 2.30 ± 0.13 days. Two 42 GeV of photons are detected during the flaring period with a probability of 99.7% and 99.8%.

5. For the γ-rays, the size of the emission region is estimated to be 1.88×10^{16} cm using 1-day as the fastest variability time and the location of the emission region is found to be at the boundary of the BLR.

6. The gamma-ray SED for pre-flare and flare are fitted with four spectral models PL, LP, PLEC, and BPL. For flare, PLEC gives a better fit to the gamma-ray SED over LP and BPL. A break in the γ-ray spectrum at 1.11 GeV is observed, which suggests the peak of the IC mechanism lies in the LAT energy band and the shape of the photon spectrum likely reflects the distribution of emitting electrons.

7. Ton 599 has shown a trend of high fractional variability with increasing energy.

8. A strong correlation is observed between γ-X-ray, γ-UV, γ-Optical, and γ-radio (15 GHz) emissions. A good correlation with the lag of a few days suggests that the γ-ray and optical/UV emissions are co-spatial.

9. A lag of 27 days is observed between γ-ray and radio (15 GHz) emissions, suggesting the presence of two different emission zones. The separation between these two emission zones was estimated to be ~ 5 pc.

10. Detailed gamma-ray and radio observations are needed to probe the two different emission regions and a multiwavelength spectral energy distribution (SED) analysis is also required for better constraints on the different emission mechanisms that are taking place in the jets of blazar Ton 599.

5.5 3C 279 during flare of November, 2017 – July, 2018

The blazar 3C 279 was classified as a FSRQ at redshift (z) of 0.536 by Lynds et al. (1965). It is one of the well-studied blazars in FSRQ class. Its black hole mass was found to be in the range of (3–8)$\times 10^8 M_\odot$ by Woo and Urry (2002), Gu et al. (2001), and Nilsson et al. (2009). Three different methods were used, Woo and Urry (2002) used the luminosity of broad optical emission lines, Gu et al. (2001) measured the width of the H_β lines, and Nilsson et al. (2009) used the luminosity of the host galaxy respectively to estimate the mass of the black hole. 3C 279 was continuously monitored by the *Fermi*-LAT telescope in gamma-ray since 2008. Along with the *Fermi*-LAT it was also monitored by the other facilities in X-ray, optical/UV, and radio wavebands.

A correlation study was performed by Hayashida et al. (2012) for 3C 279, where they have observed a time lag of 10 days between optical and gamma-ray emission. They also have found that the correlation between X-ray and gamma-ray emission is not so strong, and the nature of X-ray emission in blazar is still unclear.

5.6 Multiwavelength Observations and Data Analysis

5.6.1 *Fermi*-LAT and Swift-XRT/UVOT

The *Fermi*-LAT data for 3C 279 was collected for a time period between November, 2017 to July, 2018. It was analyzed by the standard procedure provided by the *Fermi ScienceTools*[3]. The detailed procedure about the *Fermi*-LAT data analysis are discussed in section 5.2.1. During the time period between November, 2017 to July, 2018, three bright flares were observed.

3C 279 was also observed by Swift-XRT/UVOT telescope during November, 2017 to July, 2018. The observation in XRT and UVOT telescope started when it was already flaring

[3] https://fermi.gsfc.nasa.gov/ssc/data/analysis/documentation/

in gamma-ray band. The details about the observation of Swift-XRT/UVOT are present in Table 5.4. The X-ray spectra was modeled by a tool called *Xspec* by using simple power-law model. The galactic absorption column density n_H = 1.77×10^{20} cm^{-2} estimated from Kalberla et al. (2005) is used to model the spectra. The Swift-UVOT telescope also observed the source in all the available six filters U, V, B, W1, M2, and W2. The magnitudes are corrected for galactic extinction using $R_V = A_V/E(B-V)$ = 3.1 and E(B-V) = 0.025 and the other analysis procedure is same as discussed in section 5.2.2.

5.6.2 Steward Optical Observatory

Steward optical observatory is the part of the *Fermi* multiwavelength support program. It provides the optical V and R band data for the LAT-monitored sources and also measures the linear optical polarization. Archival data of the blazar 3C 279 from the Steward Optical Observatory, Arizona (Smith et al., 2009)[4] during November, 2017 to July, 2018 was used.

5.6.3 Radio data at 15 and 230 GHz

Owens Valley Radio Observatory (OVRO; Richards et al. (2011) also monitors the Fermi detected blazars by a 40-meter single disc antenna at a frequency of 15 GHz. The radio data at 15 GHz was collected for 3C 279 for the time period between November, 2017 to July, 2018.

Sub-millimeter Array (SMA) provides the 230 GHz data from observer center database (Gurwell et al., 2007). The data was collected for the time period of 9 months between November, 2017 to July, 2018.

[4]http://james.as.arizona.edu/ psmith/Fermi/

Table 5.4 Details about the observations taken from Swift-XRT/UVOT telescope during the flaring period (MJD 58050 – 58350) are presented in this table.

Observatory	Obs-ID	Exposure (ks)
Swift-XRT/UVOT	00035019201	1.9
Swift-XRT/UVOT	00035019203	1.8
Swift-XRT/UVOT	00035019204	2.0
Swift-XRT/UVOT	00035019206	0.5
Swift-XRT/UVOT	00035019210	0.9
Swift-XRT/UVOT	00035019211	0.9
Swift-XRT/UVOT	00035019213	0.6
Swift-XRT/UVOT	00035019214	0.9
Swift-XRT/UVOT	00035019218	1.1
Swift-XRT/UVOT	00035019219	1.0
Swift-XRT/UVOT	00035019220	1.2
Swift-XRT/UVOT	00035019221	2.1
Swift-XRT/UVOT	00035019222	1.7
Swift-XRT/UVOT	00035019224	1.8
Swift-XRT/UVOT	00035019225	1.6
Swift-XRT/UVOT	00035019227	2.5
Swift-XRT/UVOT	00035019228	0.2
Swift-XRT/UVOT	00035019229	0.7
Swift-XRT/UVOT	00035019230	2.0
Swift-XRT/UVOT	00035019231	2.0
Swift-XRT/UVOT	00035019232	2.0
Swift-XRT/UVOT	00035019233	2.1
Swift-XRT/UVOT	00035019234	1.5
Swift-XRT/UVOT	00035019235	0.8
Swift-XRT/UVOT	00035019236	1.6
Swift-XRT/UVOT	00035019237	0.5
Swift-XRT/UVOT	00035019238	1.5
Swift-XRT/UVOT	00035019239	1.5
Swift-XRT/UVOT	00035019240	1.5
Swift-XRT/UVOT	00035019241	1.1
Swift-XRT/UVOT	00035019242	1.1
Swift-XRT/UVOT	00030867052	1.0
Swift-XRT/UVOT	00030867054	1.4
Swift-XRT/UVOT	00030867055	0.4
Swift-XRT/UVOT	00030867056	1.1
Swift-XRT/UVOT	00030867057	1.0
Swift-XRT/UVOT	00030867058	1.0
Swift-XRT/UVOT	00030867059	1.0
Swift-XRT/UVOT	00030867060	1.1
Swift-XRT/UVOT	00030867061	0.5
Swift-XRT/UVOT	00030867062	1.2
Swift-XRT/UVOT	00030867063	0.6
Swift-XRT/UVOT	00030867064	1.1

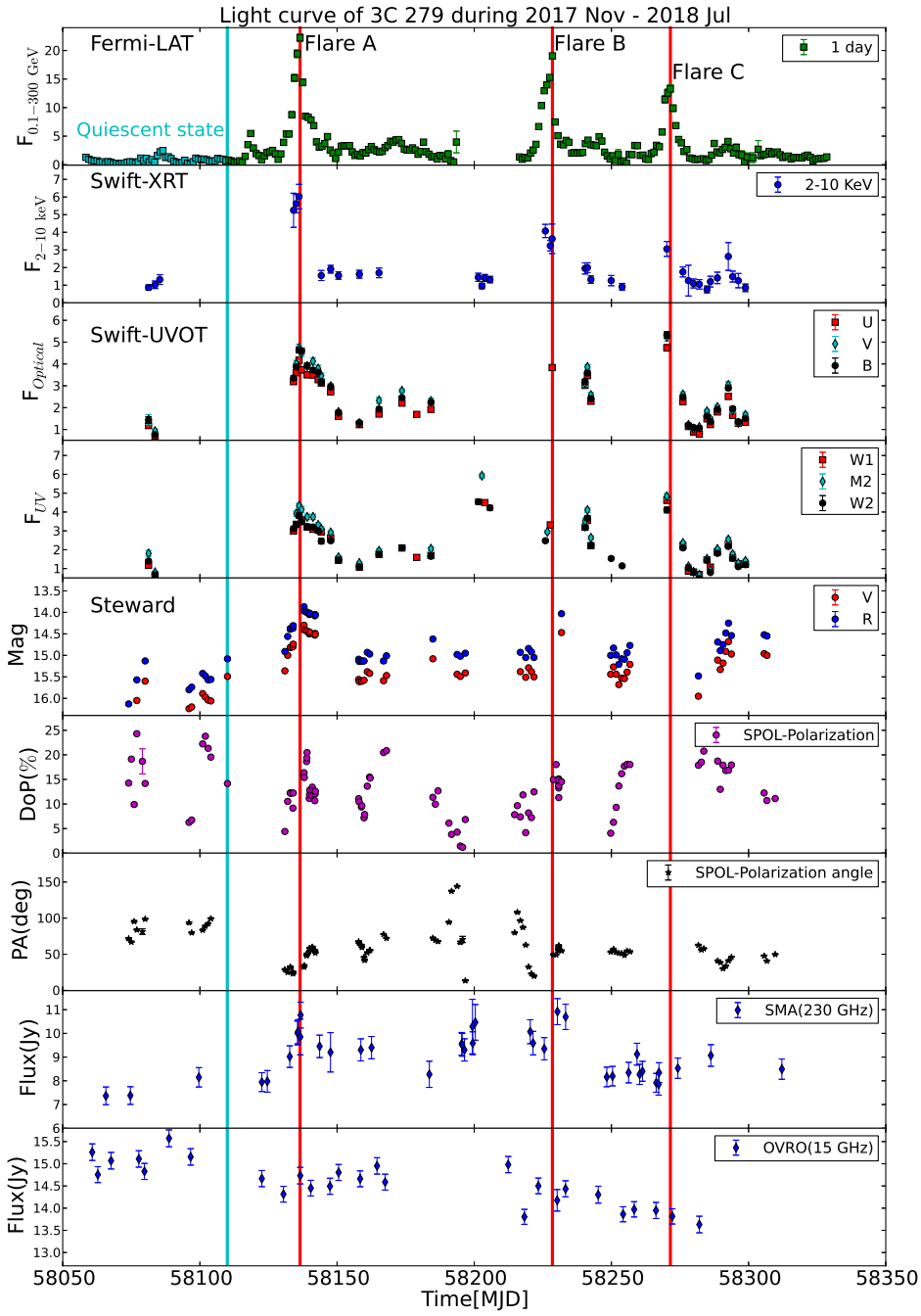

Fig. 5.8 Multiwavelength light curve observed for 3C 279 between November, 2017 to July, 2018. The γ-ray flux are shown in units of 10^{-6} ph cm^{-2} s^{-1}, and X-ray/UV/Optical fluxes are in units of 10^{-11} erg cm^{-2} s^{-1}. The cyan color vertical lines are shown to separate the quiescent state and flaring state.

5.7 Results and Discussions

The multiwavelength data collected from *Fermi*-LAT, Swift-XRT/UVOT are analyzed and the archival data from other telescopes like OVRO, SMA, and Steward observatory are used to study the temporal and spectral behavior of 3C 279 during the flare of November, 2017 to July, 2018. Correlations among different wavebands are also studied in this section. Further, a multiwavelength SED modeling is performed by using a single zone emission model to explain the multiwavelength emission.

5.7.1 Multiwavelength Light Curves

A rapid variability and strong flaring behavior was found to be a common feature of the blazar 3C 279 (Paliya 2015). A long flaring period is observed across the entire electromagnetic spectrum during November, 2017 to July, 2018. The observed multiwavelength light curve is shown in Figure 5.8. The gamma-ray light curve from *Fermi*-LAT for 0.1–300 GeV is presented in first panel of the Figure 5.8. Three flares are identified in gamma-ray during the period of November, 2017 to July, 2018. The gamma-ray light curve shows that the source started flaring at the end of 2017. A bright and strong flare peak is observed at MJD 58136.5 (18 January, 2018) and period between MJD 58110–58150 is defined as "Flare A". After "Flare A", the source stayed for more than two months in low flux states. The flux again started rising and a flare peak is observed at MJD 58228.5 (20 April, 2018) and the time duration chosen between MJD 58215–58250 is recognized as "Flare B". Just after the "Flare B" a period between MJD 58250–58280 is selected and labeled as "Flare C", a peak is observed at MJD 58271.5. The red bold vertical lines shown in Figure 5.8 represent the peak in each gamma-ray flare. In the beginning of the light curve (Figure 5.8) the source was observed to be in a quiescent state for a period of fifty days between MJD 58060–58110. During the quiescent state the gamma-ray flux is very low and constant over a long time period. The quiescent state data points are shown in cyan color and a cyan color

vertical line is also drawn to separate it from flaring state. The average flux measured during quiescent state is found to be 0.73×10^{-6} ph cm^{-2} s^{-1}.

3C 279 is also monitored by Swift-XRT/UVOT telescope. The data are collected from *HEASARC Data Archive*[5] for the period between November, 2017 to July, 2018. The light curves are produced in X-rays, optical, and UV bands and are presented in panels 2, 3, and 4 of Figure 5.8. The X-ray light curve also showed the flaring behavior and three peaks are observed at the same time it is seen in the gamma-ray light curve. The gamma-ray peaks corresponding to "Flare A" and "Flare C" are observed in the optical and UV light curves. The "Flare B" seen in gamma-ray band is missed in optical and UV bands due to unavailability of the Swift-UVOT observations.

The archival data from Steward Observatory in optical V and R bands are also collected for 3C 279. The light curves are shown in the 5th panel of Figure 5.8. The "Flare A" and "Flare B" peaks are reproduced in V and R band while "Flare C" is not seen in Steward light curve. An optical degree of polarization (DoP) and polarization angle (PA) from Steward Observatory is plotted in panel 6th and 7th of Figure 5.8. A huge variation in DoP and PA is observed during the flaring period. Within 12 days from MJD 58130–58142 the DoP changed from 4%–22% and a slow change in polarization angle is noticed from 25°–60°.

The last two panel of Figure 5.8 represent the OVRO and SMA observatory data at 15 GHz and 230 GHHz. It is observed that the radio flux at 15 GHz is not much variable during gamma-ray flaring period. The radio data from SMA observatory at 230 GHz is more variable here compared to OVRO light curve. High radio flux is noticed in SMA light curve corresponding to "Flare A" and "Flare B" observed in gamma-ray light curve.

[5]https://heasarc.gsfc.nasa.gov/cgi-bin/W3Browse/w3browse.pl

5.7.2 Variations in Gamma-ray

The gamma-ray light curve for flare A, B, and C are presented in Figure 5.9 along with the corresponding photon spectral index. The left panel of Figure 5.9 represents the light curve of "Flare A", where the source started showing the activity at MJD 58115 with a small rise in flux value. The fluctuations in the flux was continued for almost 10 days followed by a peak. The flux of the peak is recorded to be 22.24×10^{-6} ph cm^{-2} s^{-1} at MJD 58136.5 and the corresponding photon spectral index is 2.19. Just after the peak the flux started lowering and within 10 days it achieved the quiescent or low flux state at MJD 58149.5. The flux observed at this point is 1.08×10^{-6} ph cm^{-2} s^{-1} and the corresponding photon spectral index is noticed to be 2.31.

After two months of "Flare A", the source was again found in high state and represented by middle panel of Figure 5.9. The time period for higher state was noticed to be between MJD 58215–58250 and defined as "Flare B". During this flaring period the peak flux is observed to be 19.06×10^{-6} ph cm^{-2} s^{-1} at MJD 58228.5. The corresponding photon spectral index is noticed to be 2.04. A fast decrease in the flux is observed within a day and the flux drops from (19.06–7.49)$\times10^{-6}$ ph cm^{-2} s^{-1} to attained the quiescent state. The quiescent state flux value is observed to be 1.00×10^{-6} ph cm^{-2} s^{-1} at MJD 58249.5.

As soon as the "Flare B" ended, the flux again started fluctuating above the quiescent state flux value (0.27×10^{-6} ph cm^{-2} s^{-1}. The fluctuations continued for a week followed by a small peak flux 3.36×10^{-6} ph cm^{-2} s^{-1}). The flux again decreases from the peak and after five days it came back as a full-fledge flaring episode. During this period the flux rose up to 13.31×10^{-6} ph cm^{-2} s^{-1} observed at MJD 58271.5.

The variability time is estimated for all the three flaring periods separately by using the following equation given by Zhang et al. (1999),

$$t_{var} = \frac{F_1 + F_2}{2} \frac{t_2 - t_1}{|F_2 - F_1|} \tag{5.10}$$

Table 5.5 Table shows the variability time estimated from equation 5.10 for all the different flares. The flux F_1 and F_2 are in units of 10^{-6} ph cm^{-2} s^{-1} and t_1 & t_2 are in MJDs.

Flares	F_1	F_2	t_1	t_2	t_{var} (days)
Flare A	1.89	3.91	58129.5	58130.5	1.43±0.16
Flare B	19.06	7.49	58228.5	58229.5	1.14±0.03
Flare C	5.73	11.44	58268.5	58269.5	1.50±0.11

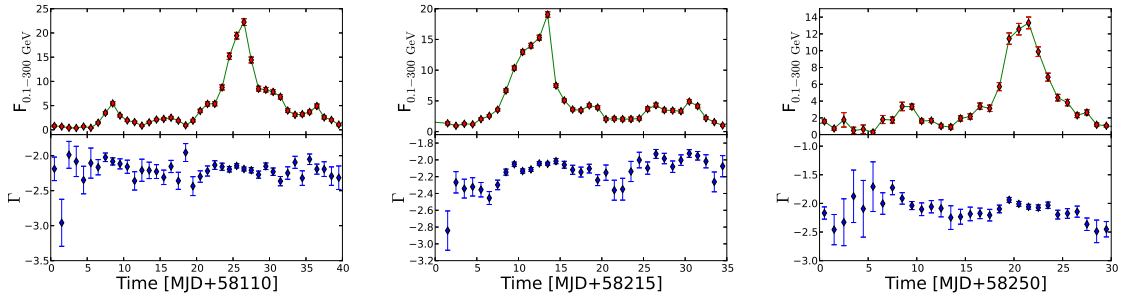

Fig. 5.9 The gamma-ray light curve for all the three flares are plotted with corresponding photon spectral index. The gamma-ray flux are in units of 10^{-6} ph cm^{-2} s^{-1}.

where F_1 and F_2 were the fluxes measure at time t_1 and t_2. The above equation 5.10 is used to scan the whole light curve shown in Figure 5.9 to estimate the variability time. The shortest variability time is found to be an order of the day. The details about the variability time for all the three flares are presented in Table 5.5. The gamma-ray flux and the corresponding photon spectral index for all the flares are plotted together in Figure 5.10. A "harder-when-brighter" trend is noticed. Similar trend has also been seen before for 3C 279 by Hayashida et al. (2012), Hayashida et al. (2015), and Paliya (2015). The spectral hardening during the flaring state can predict the possibility of detection of high energy photons and consequently can shift the IC peak of the SED to higher energy. A strong correlation between spectral hardening during flare and detection of high energy photons are shown by many authors (Britto et al. 2016; Shah et al. 2019).

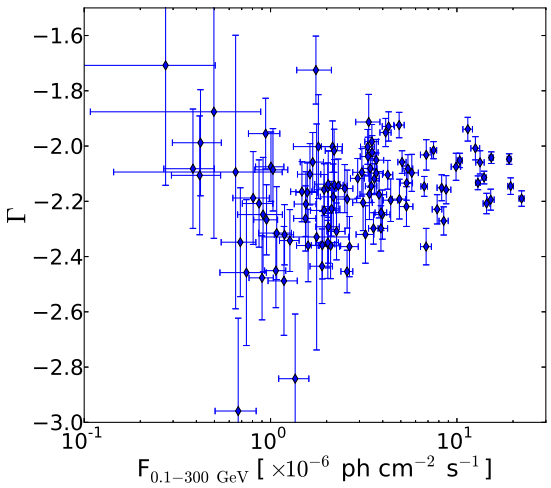

Fig. 5.10 Photon spectral index with respect to observed flux shows a "harder-when-brighter behavior". The gamma-ray flux is in units of ph cm^{-2} s^{-1}.

5.7.3 Variations in X-ray

The X-ray light curve along with the photon spectral index for 2-10 keV are plotted in Figure 5.11. The observations taken by Swift-XRT are poorly sparse and due to that rise and decay part of the flare structures are missed. Flares A, B, and C shown in X-ray light curve (Figure 5.11) are coincides with the gamma-ray flares and the maximum flux observed in X-rays are (6.03, 4.07, and 3.06)$\times 10^{-11}$ erg cm^{-2} s^{-1} respectively. The corresponding photon spectral index is observed to be 1.23$\pm$0.14 for flare A, 1.22$\pm$0.11 for flare B, and 1.35$\pm$0.12 for flare C. The last flare observed in X-ray, i.e. "Flare C", was followed by a small fluctuation at the end of the light curve. Figure 5.11 clearly shows the "harder-when-brighter" trend in X-ray also. The average photon spectral index is estimated as 1.52$\pm$0.03, that is softer than the spectral index observed at highest flux i.e. 1.23$\pm$0.14 during the "Flare-A". Most of the contribution of soft X-ray goes to synchrotron peak and the lower part of the SSC/IC. The "harder-when-brighter" trend in X-ray can be interpreted as the increase in the SSC emission and can also shift the SSC peak towards the higher energy. Increase in the SSC/IC emission

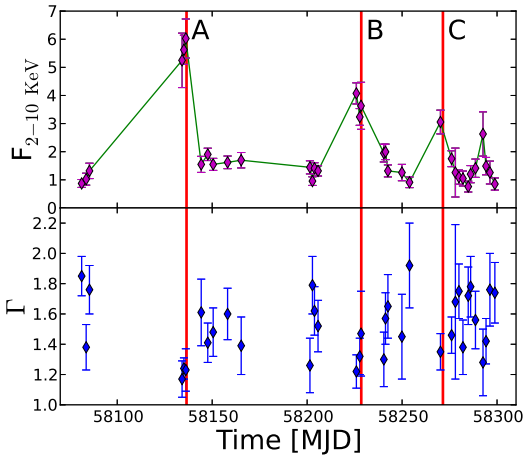

Fig. 5.11 X-ray light curve for all the observed flares are presented here. The fluxes are in units of 1.0×10^{-11} erg cm^{-2} s^{-1}. Lower panel represent the corresponding photon spectral index. A "harder-when-brighter" trend was also observed.

could be probably due to increase in accretion rate. Due to poorly sparse X-ray data points the X-ray variability time is not calculated.

5.7.4 Spectral Ananlysis

The likelihood analysis is used to produce the γ-ray SED for all the three flares and one quiescent state between 0.1 – 300 GeV. The produced gamma-ray spectral points for all the flares and quiescent state are presented in Figure 5.12. Three spectral models are used to fit these spectral points and the spectral models are Power-law (PL), Log-parabola (LP), and simple broken Power-law (BPL). The functional form of all these models are discussed in Prince et al. (2018). An investigation was carried out to find the presence or absence of curvature in the gamma-ray SED, which has been used in the past to constrains the location of the emission region. According to Liu and Bai (2006), BLR region act as an opaque to photons of energy $>$ 20 GeV because of the photon pair production within the BLR. So, a break or curvature in gamma-ray spectrum is expected to observe, when the emission region is within the size of the BLR. The gamma-ray SED modeling with different spectral

models mentioned above will help to identified the curvature in different flares by estimating the TS_{curve}. The TS_{curve} is defined as TS_{curve} = 2(log L(LP/BPL) - log L(PL)), where L represents the likelihood function (Nolan et al. 2012). The fitted model parameters along with the TS_{curve} are mentioned in Table 5.6. The model with large positive value of TS_{curve} is considered to be the best fit to the gamma-ray SEDs and that also suggest the presence of a spectral cut-off. By comparing the values presented in Table 5.6, It is concluded that among all the three models the log-parabola spectral model is a best model to describe the gamma-ray SED. In the Table 5.6, It is also observed that the break energy found in broken power-law fit is constant irrespective of the flaring states. Similar results were also found for the different flares of this source (Paliya 2015) and also in different source (Abdo et al. 2011). There is also an alternative way that has been discussed in literature to explain the curvature in the gamma-ray spectrum, which says that a cut-off in the gamma-ray spectrum can also be identified if the distribution of electron spectrum already has a cut-off.

A strong break is observed in the gamma-ray spectrum while fitting with BPL; similar break has also been noted before for other FSRQ like 3C 454.3 by Abdo et al. (2011) and for 3C 279 during flare of 2014 and 2015 (Paliya 2015; Paliya et al. 2015).

In Table 5.6, during all the flares the BPL photon index before the break (E_{break} = 1 GeV) i.e. Γ_1 was found to be $\leq$ 2, represents an increasing slope. After the break the photon spectral index (Γ_2) is reported to be $\geq$ 2, indicates a falling spectrum. It is known that the gamma-ray spectrum in blazar is governed by the inverse Compton (IC) scattering. It is found that the peak of IC is around 1 GeV, which belongs to the Fermi-LAT energy range between 0.1–300 GeV. Since the break energy is observed to be constant for all the flares, so it might be possible that the observed shape of gamma-ray spectrum is just the reminiscence of the electron energy distribution of the emitting electrons.

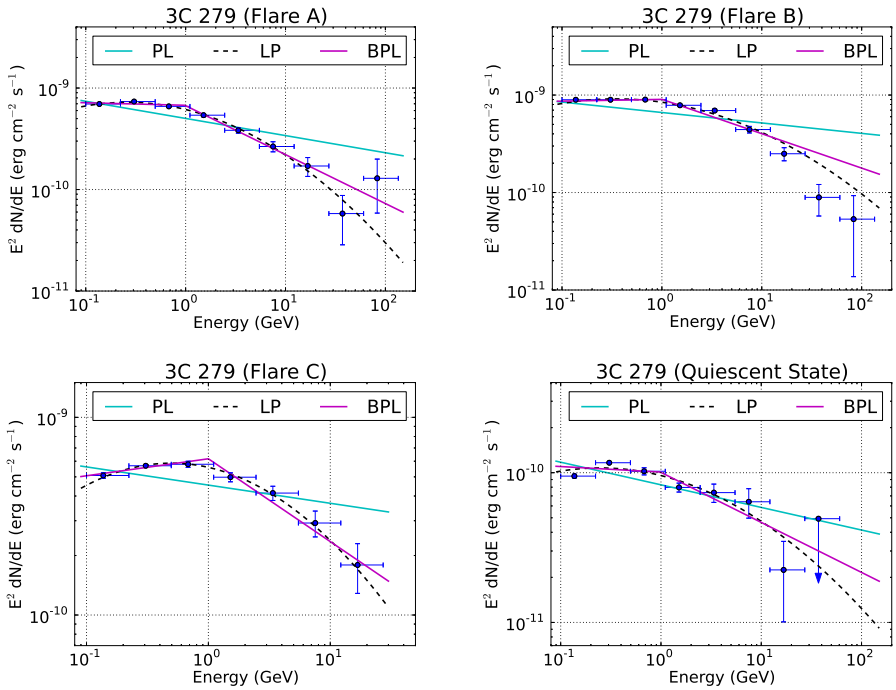

Fig. 5.12 The gamma-ray SEDs produced for all the flares and quiescent state are shown here. The spectral data points are fitted with three different spectral models and the fitted parameters are tabulated in Table 5.6.

Table 5.6 The parameters obtained from the spectral fitting, for the different spectral models PL, LP, and BPL, by using the likelihood analysis method, are presented here. TS_{curve} was estimated with respect to the TS value of the PL fit.

		PowerLaw (PL)					
Activity	$F_{0.1-300\ GeV}$ (10^{-6} ph cm^{-2} s^{-1})	Γ				TS	TS_{curve}
Quiescent state	0.67±0.02	2.15±0.03	-	-		3625.24	
Flare A	4.42±0.05	2.17±0.92	-	-		35533.08	-
Flare B	5.59±0.05	2.11±0.01	-	-		67293.68	-
Flare C	3.47±0.06	2.09±0.02	-	-		15163.31	-
		LogParabola (LP)					
		α	β				
Quiescent state	0.64±0.03	2.04±0.04	0.06±0.02	-		3653.27	28.03
Flare A	4.24±0.05	2.05±0.02	0.090±0.008	-		35759.77	226.69
Flare B	5.39±0.05	1.99±0.01	0.072±0.006	-		67311.92	18.24
Flare C	3.26±0.07	1.93±0.02	0.10±0.01	-		15282.46	119.15
		Broken PowerLaw (BPL)					
		Γ_1	Γ_2	E_{break}			
Quiescent state	0.65±0.03	2.04±0.05	2.33±0.08	0.98±0.17		3633.04	7.8
Flare A	4.27±0.05	2.02±0.02	2.48±0.03	0.98±0.05		35750.45	217.37
Flare B	5.42±0.05	1.98±0.01	2.35±0.02	1.00±0.03		67309.47	15.79
Flare C	3.30±0.07	1.91±0.03	2.42±0.05	1.00±0.06		15263.59	100.28

5.7.5 Fractional variability (F_{var})

Blazars are known for the strong chaotic flux variability across the entire electromagnetic spectrum. The variability in blazars are more prominent during the flaring state, where the flares profile depend on the particle injection spectrum and energy, particle acceleration, and energy loss in the jet of blazars. A good quality of data is required to estimate the variability amplitude across the electromagnetic spectrum. 3C 279 is observed in multiwavelength and provides a good quality of data which makes it possible to estimate the variability amplitude. The variability amplitude is measured by a parameter called fractional root mean square (rms) variability parameter (F_{var}), which was introduced by Edelson and Malkan (1987); Edelson et al. (1990). The expression for the fractional variability (F_{var}) is given in Vaughan et al. (2003) and that is follows as,

$$F_{var} = \sqrt{\frac{S^2 - \sigma^2}{r^2}} \tag{5.11}$$

$$err(F_{var}) = \sqrt{\left(\sqrt{\frac{1}{2N}}.\frac{\sigma^2}{r^2 F_{var}}\right)^2 + \left(\sqrt{\frac{\sigma^2}{N}}.\frac{1}{r}\right)^2} \tag{5.12}$$

where, $\sigma_{XS}^2 = S^2 - \sigma^2$, is called excess variance, S^2 is the sample variance, σ^2 is the mean square uncertainties of each observation and r is the sample mean.

The F_{var} is estimated and shown in Figure 5.13. The values are presented in Table 5.7. The (F_{var}) strongly depends on the frequency as shown in Figure 5.13. It is observed that the source is more than 100% variable in gamma-ray energy band. In X-ray, the source appears to be more than 60% variable and followed by the UV and optical band where the variability was observed to be more than 50%. It is observed that the source is less variable in radio at both the frequency 15 GHz and 230 GHz. The variability found to be less than 10%. Figure 5.13 shows a clear trend of increasing fractional variability towards

Table 5.7 The fractional variability for various wavebands were estimated for the time interval MJD 57980 to 58120 and presented in this table.

Waveband	F_{var}	err(F_{var})
γ-ray	1.201	0.008
X-ray	0.660	0.035
U	0.524	0.008
B	0.520	0.006
V	0.509	0.008
W1	0.548	0.008
M2	0.580	0.007
W2	0.557	0.007
OVRO (15 GHz)	0.032	0.002
SMA (230 GHz)	0.089	0.010

the higher energy, which suggest that the large numbers of particles injected in the jet are producing the high energy flux and consequently higher variability. However, this is not the only scenario, an opposite trend was also observed before, where the variability amplitude decreases towards the lower wavelength (IR, Optical, and UV; Bonning et al. 2009). The decreasing trend of fractional variability in Bonning et al. (2009) suggest the presence of the steady thermal emission from the accretion disk. A double-hump kind of structure of fractional variability was also observed in many cases as discussed in chapter 3, section 3.6.5, which resembles the multiwavelength SED of the blazar.

5.7.6 Correlation Studies

The multiwavelength light curve shown in Figure 5.8 suggest that all the flares observed in different wavebands are mostly correlated. However, the radio light curve at 15 GHz by OVRO does not confirm any flaring behavior within the interested time period, whereas high flux state at 230 GHz radio light curve is observed simultaneous to “Flare A” and “Flare B” observed in gamma-ray band. The cross-correlation between various energy bands are performed and presented here. The important thing about the correlation study is that, it

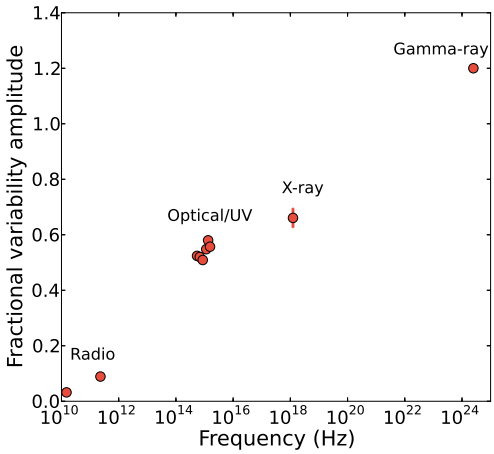

Fig. 5.13 The fractional variability across the entire wavebands are plotted with respect to the frequency.

can provides the insight to the various emission region involved in multiwavelength emissions. A strong and good correlation between two different waveband emissions with zero time lag suggest the co-spatial origin of them. A positive or negative time lag with strong correlation coefficient suggest an involvement of multiple emission region. The time lag (positive or negative) can be used to locate the different emission region along the jet axis and also measure the separation between emission regions. The correlation study is performed by *discrete correlations function (DCF)* formulated by Edelson and Krolik (1988). An observed positive time lag between two light curves LC1 and LC2 implies that LC1 is leading the LC2 and a negative time lag implies the opposite. The *DCF* result obtained between gamma-ray and optical emission for "Flare A" & "Flare C" are presented in Figure 5.14 & Figure 5.15 respectively.

A cross-correlation study between two different energy band light curves by *DCF* needs sufficient data points in each light curve. The "Flare B" does not full-fill this criteria since it has good quality data points only in the gamma-ray light curve. It is Therefore not possible to cross-correlate two different energy band for "Flare B". The gamma-ray and X-ray were cross-correlated separately for "Flare A" & "Flare C". The results of *DCF* between gamma-

rays and X-rays are shown in Figure 5.16.

A strong correlation with zero time lag (within the time bin 2.5 days) is observed between gamma-ray and optical band (U, B, & V) emission for "Flare A" & "Flare C". The value of correlation coefficients for "Flare A" between gamma-ray and optical U, B, & V band is found to be 0.50±0.15, 0.53±0.17, 0.83±0.18. Similarly for "Flare C" the correlation coefficients is noticed to be 0.92±0.44, 0.93±0.44, & 0.91±0.44, respectively, between gamma-ray and optical U, B, & V band. A good correlation with zero time lag (within the time bin 2.5 days) is also observed between gamma-ray and UV (W1, M2, & W2) band emission. The correlation coefficient is found to be 0.45±0.15, 0.83±0.17, & 0.82±0.17 for "Flare A" and 0.92±0.44, 0.90±0.43, & 0.89±0.43 for "Flare C" in W1, M2, & W2 band respectively.

A strong correlation with zero time lag (within the time bin 4.5 days) is observed between gamma-ray and X-ray emission. The correlation coefficient between gamma-ray and X-ray emission is found to be 0.87±0.16 and 0.97±0.36 for "Flare A" & "Flare C". This correlation with zero time lag is found to be the first ever strong correlation detection between gamma-ray and X-ray for 3C 279. The significance of the DCF peaks are also estimated by simulating the 1000 gamma-ray light curves. To simulate the gamma-ray light curves, I have used method mentioned in Emmanoulopoulos et al. (2013). Further, I cross-correlate the simulated gamma-ray light curves with the observed light curves in different wavebands and finally a DCF distribution with time lag is calculated. At each time lag 95% significancewas calculated, which are shown in Figure 5.14, 5.15, 5.16.

5.8 Modeling the Multiwavelength SED

Blazar 3C 279 is simultaneously observed in different energy bands during the flaring period between November, 2017 to July, 2018. The simultaneous observation provides an opportunity to gain further insight on it's multiwavelength properties. This section is dedicated

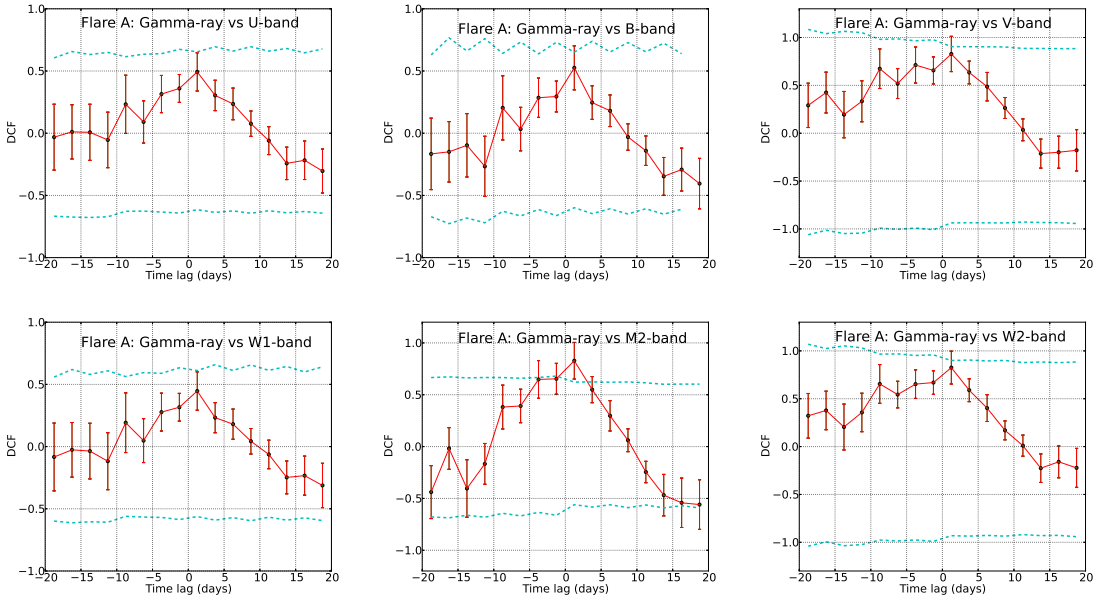

Fig. 5.14 The *DCF* are shown for "Flare A" for all the possible combinations: γ-ray vs. Swift-U, B, V, W1, M2, W2 band. The 95% significance in each time bin are shown in cyan color.

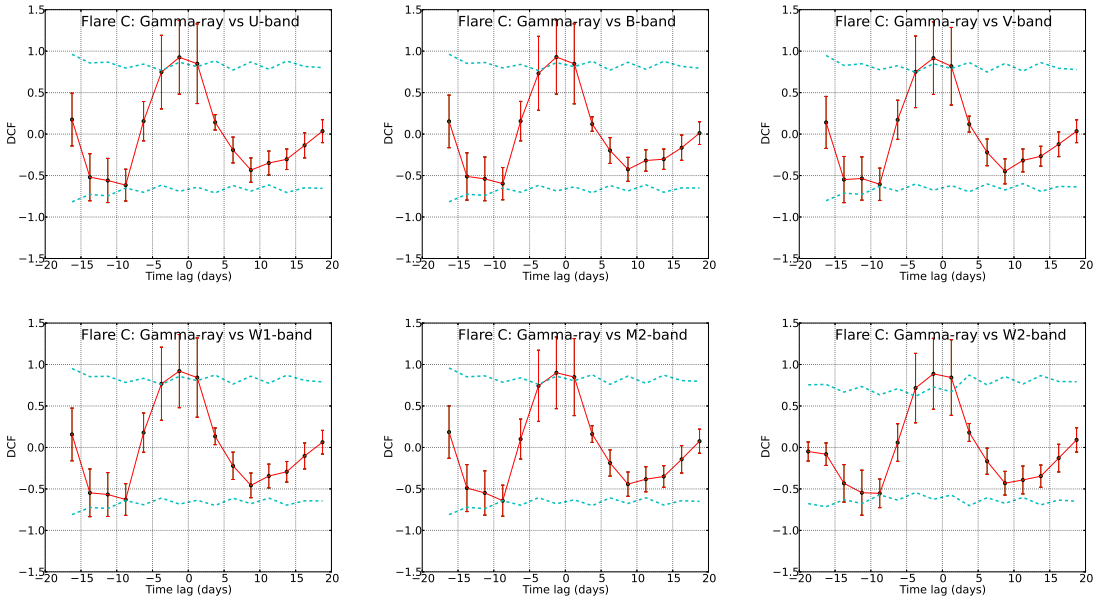

Fig. 5.15 The *DCF* are shown for "Flare C" for all the possible combinations: γ-ray vs. Swift-U, B, V, W1, M2, W2 band. The 95% significance in each time bin are shown in cyan color.

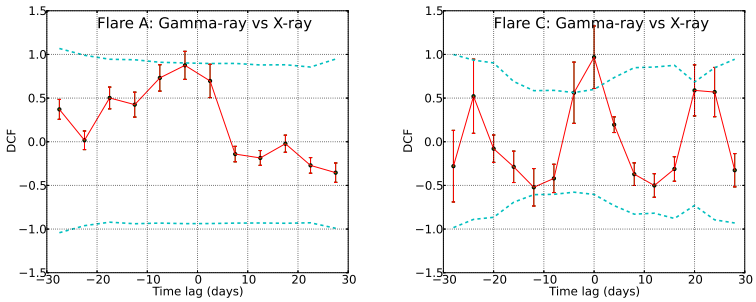

Fig. 5.16 The gamma-ray vs X-ray DCF are presented for "Flare A" and "Flare C".

to the modeling of the observed multiwavelength SED by using the publicly available code GAMERA[6] (Hahn, 2015). Details about the transport equation used by the GAMERA are provided in chapter 3, section 3.6.8.

The gamma-ray spectral analysis presented in section 5.7.4 suggest that the log-parabola (LP) spectral model well describes the gamma-ray photon spectrum. Massaro et al. (2004) suggest that the LP photon spectrum can be produced by an input LP electron distribution. Hence, the LP spectral distribution is considered as the input injected electron spectrum in the transport equation. The correlation study presented in section 5.7.6 suggest that the multiwavelength emissions observed during the flare of 3C 279 are co-spatial. Hence, a single emission zone is considered to model the multiwavelength SED. It is considered that the blob is moving relativistically along the jet axis with Lorentz factor Γ, and Doppler factor, δ. The value of Γ=15.5 and δ=24.1 are adopted from Jorstad et al. (2005).

It was believed that in FSRQ, like 3C 279 the external radiation field required for the external Compton (EC) emission is dominated by the BLR photons. The BLR photon density in the comoving frame is defined as,

$$U'_{BLR} = \frac{\Gamma^2 \eta_{BLR} L_{disk}}{4\pi c R_{BLR}^2} \tag{5.13}$$

[6]http://joachimhahn.github.io/GAMERA

where the η_{BLR} is the fraction of disk emission processed in BLR, and typically it is considered to be only 2% (Pittori et al. 2018), R_{BLR} represents size of the BLR, L_{disk} is the disk luminosity, and the speed of light in vacuum is represented by c. As proposed by Ghisellini and Tavecchio (2009), the size of the BLR is defined as, $R_{BLR} = 10^{17} L_{d,45}^{1/2}$ cm, where $L_{d,45}$ is the accretion disk luminosity in units of 10^{45} erg s^{-1}. Using the value of disk luminosity from Pian et al. (1999) i.e. $L_{disk} = 2\times10^{45}$ erg s^{-1} the size of the BLR was found to be $R_{BLR} = 1.414\times10^{17}$ cm.

The minimum Doppler factor (δ_{min}) during the flare can be estimated from the $\gamma\gamma$ opacity arguments and by estimating the highest energy photon. The minimum Doppler factor can be calculated as (Dondi and Ghisellini 1995; Ackermann et al. 2010),

$$\delta_{min} \cong \left[\frac{\sigma_T d_L^2 (1+z)^2 f_x \varepsilon}{4 t_{var} m_e c^4}\right]^{1/6} \tag{5.14}$$

which assumes that the optical depth of a photon ($\tau_{\gamma\gamma}$) with energy $\varepsilon = E/m_e c^2$ to the $\gamma\gamma$ interaction is 1. The luminosity distance is denoted as d_L (=3.1 Gpc), σ_T is the Thompson scattering cross section, E is the highest photon energy detected during the flare, t_{var} is the variability time, and f_x is the X-ray flux in 0.3-10 keV. Here, the values of E, f_x, and t_{var} are estimated around the same time period and the values are found to be 27 GeV at MJD 58228.45, 3.63×10^{-11} erg cm^{-2} s^{-1} at MJD 58228.38, and 1.14 days at MJD 58228.50 respectively. The minimum Doppler factor is found to be $\delta_{min} = 10.7$. The location of the gamma-ray emission region can be estimated by assuming the bulk Lorentz factor $\Gamma = \delta_{min} = 10.7$, then the location can be defined as $d \sim 2\, c\Gamma^2 t_{var}/(1+z)$. It is found that the gamma-ray emission region is located at distance of 4.40×10^{17} cm from the central SMBH down the jet. This value is comparable to the size of the BLR and hence conculded that during the emission of high energy photon (27 GeV) the gamma-ray emitting region must have been located at the outer boundary of the BLR.

The contribution from the accretion disk photons are also considered in the EC emission. The accretion disk photon energy density in the comoving frame is defined in Dermer and Menon (2009) and the expression is follows as,

$$U'_{disk} = \frac{0.207 R_g l_{Edd} L_{Edd}}{\pi c d^3 \Gamma^2} \tag{5.15}$$

where, R_g represents the gravitational radius, and $l_{Edd} = L_{disk}/L_{Edd}$ is Eddington ratio, and d is distance of the blob from the SMBH and which is estimated to be 4.40×10^{17} cm. For the black hole mass $M_{BH} = 2.51\times10^8$ $M_\odot$ from Wu et al. (2018), the gravitational radius was found to be $R_g = 3.72\times10^{13}$ cm. The dusty torus (DT) lack the observational evidence, and hence, the contribution from DT is not considered in the EC emission.

GAMERA uses number of input parameters to model the SED. The parameters are: the spectral index (α, β) of injected electron distribution, minimum and maximum (γ_{min}, γ_{max}) energy of electrons, magnetic field (B) inside the blob, and injected electron luminosity. These parameters were optimized to obtain the best fit to the SED. The BLR photon density (U'_{BLR}) and BLR Temperature = 10^4K (Peterson, 2006) along with the accretion disk photon density (U'_{disk}) and disk temperature = 2.6×10^6K (Dermer and Menon, 2009), are fixed to the derived value. The size of the emission region can also be estimated by using the variability time and minimum Doppler factor from the relation,

$$R \leq c t_d \delta (1+z)^{-1} \tag{5.16}$$

where t_d=1.14 day, is the observed flux doubling/halving time. The size of the emission region was found to be to be $R = 2.1\times10^{16}$ cm. However, during the SED modeling Doppler factor and the size of the blob are optimized to best fit value.

The SED modeling is performed for all the flaring and quiescent state. The optimized model parameters obtained during the model fitting are presented in Table 5.8 and the multiwave-

length SEDs are shown in Figure 5.17. It is observed that the low energy peak (synchrotron peak) can be constrained by the optical and UV emission whereas the high energy Compton peak can be constrained by the gamma-ray data points obtained from *Fermi-LAT*. The SSC peak in FSRQ type blazar can be constrained by the X-ray emission. The results shows that, during the quiescent state more magnetic filed value is required compared to the flaring state to explain the synchrotron peak, which suggest that the synchrotron process is more dominant during the quiescent state. The maximum energy of electrons found during the different states are almost similar. The total jet power required is also estimated by the following relation,

$$P_{jet} = \pi \, \Gamma^2 \, r^2 \, c \, (U_e + U_B + U_p) \tag{5.17}$$

where Γ is the Lorentz factor, r is the size of the blob. The energy density in electrons, magnetic field, and cold protons are defined by U_e, U_B, and U_p. The jet composition is considered to be mixture of equal number of non-thermal electrons and cold protons. The jet powers estimated in all the components separately are presented in Table 5.8 and it is calculated for Γ=15.5 and $r = 4.64\times10^{16}$ cm. It is observed that the quiescent state has more jet power in magnetic field compared to the flaring state. However, the jet power found in electrons and protons are much higher during the flaring state compare to the quiescent state.

Previous study on flares of 3C 279 done by various people (Dermer et al. 2014; Yan et al. 2015; Vittorini et al. 2017) suggest that most of the time the emission region was found to be outside the BLR. However, in contrast to that the June, 2015 flare of 3C 279 (Paliya 2015) demands a high photon density compact emission region close to the base of the jet. June, 2015 flare was studied by several authors (Hayashida et al. 2015; Ackermann et al. 2016; Pittori et al. 2018) and they suggested that the emission region is located within the boundary or at the outer edge of the BLR. In this study too a similar result is obtained and the emission region is found to be at the boundary of the BLR.

The flare observed during January, 2018 which is denoted as "Flare A" in our study was studied before by Shah et al. (2019). They have considered both the BLR photons and IR photons as a target photon field separately to explain the multiwavelength SED. Their result shows that the photons from both the field can explain the broadband SED. However, they concluded that the parameters used for EC/IR is more acceptable than the parameters found for EC/BLR process. In our case, It is found that a single zone emission model with BLR photons is enough to explain the multiwavelength SED.

December, 2013 flares of 3C 279 was studied by Paliya et al. (2016), where they have used two independent method: a time-dependent lepto-hadronic modeling and a two-zone leptonic modeling, to explain the multiwavelength SED. However, our results show that a single zone leptonic modeling is enough to explain the broadband SED.

A broadband study of 3C 279 from radio to gamma-ray was done by Hayashida et al. (2012) and the data were collected for the first two (2008–2010) of the *Fermi* operation. Their study shows a time lag of 10 days in optical emission with respect to the gamma-ray emission. The X-ray and gamma-ray emission was found to be uncorrelated. However, the DCF analysis done for November, 2017 to July, 2018 flares exhibit a strong correlation between optical, X-ray and gamma-ray emission with zero time lag. Hayashida et al. (2012) reported a huge swing in the optical polarization angle during the gamma-ray flare (Period D). They constrained the location of the emission region based on the observed change in the optical polarization angle. They also argued that a large swing in the polarization angle can be interpreted as the precession in the jet, and which suggest an arbitrary location of the emission region within the BLR. Our study also show a huge variation in polarization angle during the flaring period ("Flare A" and "Flare B"). Assuming the swing in the optical polarization angle was caused by the precession of the jet, a single emission zone was chosen within the BLR to model the broadband SED, which is also consistent with the distance of the emission region estimated in this work.

The observed SED during quiescent and flaring state is compared and it is found that the flux has increased from quiescent state to the flaring state (Figure 5.17, across the entire electromagnetic spectrum. The major flux change is observed in gamma-ray energy band between quiescent and flaring state. However, a small flux change is noticed in gamma-ray energy band between different "Flare A", "B", & "C". A relatively lesser flux change is observed in optical/UV and X-ray band emission among all the observed flares and quiescent state. During the SED modeling a few parameters are varied to explain these changes. It is found that almost ten times more jet power in electrons are required to explain the gamma-ray flares compared to the quiescent state.

5.9 Summary

1. Three bright flares and one long quiescent state are observed by *Fermi*-LAT during November, 2017 – July, 2018.

2. The multiwavelength light curves are shown in Figure 5.8. A huge variation in optical polarization angle and degree of polarization is observed.

3. A day scale of variability is observed in the light curve, which constrains the size of the emission region to 2.1×10^{16} cm and the location of the emission region to 4.40×10^{17} cm, which found to be at the boundary of the BLR (1.414×10^{17} cm).

4. A "harder-when-brighter" trend is observed in gamma-ray and X-ray during the flaring period.

5. The LP spectral model is found to be the best model to describe the gamma-ray photon spectrum over PL and BPL.

6. An increasing trend of fractional variability with frequency is observed and shown in Figure 5.13.

7. The cross-correlation study exhibit a strong correlation between gamma-ray , optical, and X-ray emission with zero time lag, and which suggest a co-spatial origin of them. A strong correlation between optical and gamma-ray emission in 3C 279 was observed before by various authors (Hayashida et al. 2015; Hayashida et al. 2012; Rani et al. 2017). A correlation study between optical and X-ray emission was done by Chatterjee et al. (2008) between year 1996 to 2007. They decomposed the X-ray and optical light curves into thirteen individual flares and found that in six flares X-ray leads the optical emission, in three flares optical leads the X-ray emission, and zero lag in the rest of the four flares.

8. A single zone emission model is chosen to describe the multiwavelength SED.

9. The publicly available code GAMERA is used to model the broadband SED. The parameters like magnetic field, injected electron spectrum, minimum and maximum energy of injected electrons are optimized to obtain a good fit to the SED. It is found that a single-zone emission model is sufficient enough to explain the broadband SED of the brightest *Fermi* blazar called 3C 279.

5.10 Summary of the chapter

1. A detailed correlation study between various wavebands is done on the flares of Ton 599 during 2017 and on 3C 279 during 2017–2018.

2. A strong correlation with zero time is observed between gamma-ray, optical/UV and X-ray emission for both the sources. In Ton 599, the gamma-ray and radio emission is found to be highly correlated with a time lag of 27 days in radio emission with respect to the gamma-ray emission. The correlation between gamma-ray and radio in 3C 279 is unable to estimate due to the poorly sparse radio data.

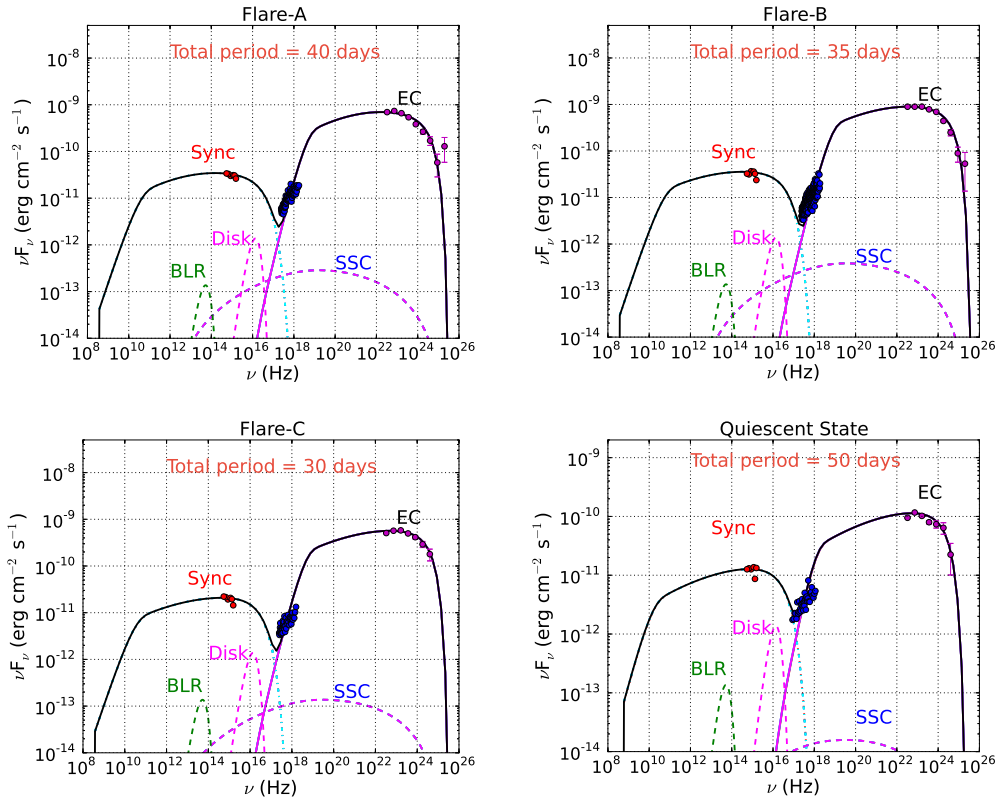

Fig. 5.17 The broadband SEDs of all the flares and one quiescent state are shown here. The optimized model parameters are presented in Table 5.8.

3. In Ton 599, the radio emitting region was found to be at 5 pc away from the gamma-ray emitting zone and in 3C 279 gamma-ray, optical, and X-ray emission is found to be co-spatial.

4. A single zone emission model is used to model the broadband SED in 3C 279.

Table 5.8 The modeling result of broadband SEDs shown in Figure 5.17. A LP model is used as an input electron spectrum which functional form is follows as dN/dE = $N_0(E/E_0)^{(-\alpha-\beta*log(E/E_0))}$, where E_0 is chosen to be 90 MeV.

Activity	Parameters	Symbol	Values	Activity period (days)
	BLR temperature	T'_{blr}	1×10^4 K	
	BLR photon density	U'_{blr}	6.377 erg/cm^3	
	Disk temperature	T'_{disk}	2.6×10^6 K	
	Disk photon density	U'_{disk}	7.9×10^{-7} erg/cm^3	
	Size of the emission region	R	4.64×10^{16} cm	
	Doppler factor of emission region	δ	24.1	
	Lorentz factor of emission region	Γ	15.5	
Flare A				
	Min Lorentz factor of injected electrons	γ_{min}	8.0	
	Max Lorentz factor of injected electrons	γ_{max}	1.5×10^4	
	Spectral index of injected electron spectrum (LP)	α	1.7	
	Curvature parameter of LP electron spectrum	β	0.15	
	magnetic field in emission region	B	2.8 G	40
	jet power in electrons	P_e	1.88×10^{45} erg/sec	
	jet power in magnetic field	P_B	1.52×10^{46} erg/sec	
	jet power in cold protons	P_p	1.87×10^{46} erg/sec	
Flare B				
	Min Lorentz factor of injected electrons	γ_{min}	10.0	
	Max Lorentz factor of injected electrons	γ_{max}	1.7×10^4	
	Spectral index of injected electron spectrum (LP)	α	1.7	
	Curvature parameter of LP electron spectrum	β	0.12	
	magnetic field in emission region	B	2.5 G	35
	jet power in electrons	P_e	2.42×10^{45} erg/sec	
	jet power in magnetic field	P_B	1.21×10^{46} erg/sec	
	jet power in cold protons	P_p	2.24×10^{46} erg/sec	
Flare C				
	Min Lorentz factor of injected electrons	γ_{min}	8.0	
	Max Lorentz factor of injected electrons	γ_{max}	1.5×10^4	
	Spectral index of injected electron spectrum (LP)	α	1.7	
	Curvature parameter of LP electron spectrum	β	0.1	
	magnetic field in emission region	B	2.4 G	30
	jet power in electrons	P_e	1.13×10^{45} erg/sec	
	jet power in magnetic field	P_B	1.12×10^{46} erg/sec	
	jet power in cold protons	P_p	1.56×10^{46} erg/sec	
Quiescent state				
	Min Lorentz factor of injected electrons	γ_{min}	4.0	
	Max Lorentz factor of injected electrons	γ_{max}	1.2×10^4	
	Spectral index of injected electron spectrum (LP)	α	1.7	
	Curvature parameter of LP electron spectrum	β	0.08	
	magnetic field in emission region	B	4.2 G	50
	jet power in electrons	P_e	2.56×10^{44} erg/sec	
	jet power in magnetic field	P_B	3.42×10^{46} erg/sec	
	jet power in cold protons	P_p	7.17×10^{45} erg/sec	

Chapter 6

Conclusions: Summary and Future Perspectives

The high energy non-thermal emission from AGN and particularly from jets of blazars has drawn much attention of the astrophysics community. The launch of *Fermi Gamma-ray Space Telescope* in the year 2008 has opened a new window to observe and study the dynamic high-energy sky. Blazars are the most energetic extragalactic sources ever observed by *Fermi*-LAT. Fourth Fermi source catalog (4FGL; The Fermi-LAT collaboration 2019) has reported more than five thousand sources, which are mostly blazars. Fast variability times observed in many blazars suggest small emission regions of gamma-rays. To investigate the variability time in blazars a temporal analysis approach is generally used and to study the multiwavelength emission spectral modeling is required. Many ground and space based telescopes are used to record the simultaneous or quasi-simultaneous emission in radio to very high energy gamma-rays. The simultaneous data covering radio to gamma-ray frequencies are used to model the spectral energy distributions of blazars and understand the characteristic features of flares in different blazars.

Thesis Summary

In this thesis, I aimed to understand the physical processes behind the fast variability and multiwavelength emission in blazar. I have carried out detailed temporal and spectral analysis of emission during different periods from four FSRQ type blazars, also modeled their spectral energy distributions with a time dependent code.

Spectral analysis of a long term light curve in gamma-ray is done for PKS 1510-089. A minimum flux variability time of the order of one hour (1.30 hr) is observed during one of the flares detected from PKS 1510-089. This constrains the size of the emission region to 4.85×10^{15} cm. The spectral analysis shows that the observed gamma-ray SEDs during different flares are well described by log-parabola spectral distribution. We have selected the gamma-ray high state during the year 2015 for multiwavelength SED modeling. This high state was also observed by MAGIC and HESS gamma-ray detectors. They indicated the possibility of multiple emission zones during this high state. The multiwavelength data from Fermi-LAT, Swift-XRT/UVOT, and radio data from OVRO and SMA observatory have been collected for correlation study as well as for SED modeling. No strong correlation is observed between any two different energy bands. Different variability times have been estimated in different wavebands, and it is found that the variability times in gamma-ray and optical bands are close to each other, whereas X-ray variability time largely deviates from them. This suggests that the gamma-ray and optical emissions are co-spatial and the X-ray emission is produced in another emission zone. The variability times found in gamma-ray and X-ray indicate their emission regions within the BLR and outside the BLR respectively. We have used two zone emission model to explain the multiwavelength SED. The parameters: spectral index of injected relativistic electron population, minimum and maximum energy of electrons, magnetic field in the blob, and jet power in injected electrons are optimized to obtain the best fit to the SED. Detailed results are presented in chapter 3.

To study the blazar CTA 102, we have collected the multiwavelength data from the different

telescope between September, 2016 to March, 2017. A strong correlation in all the wavebands is observed, as shown in Figure 4.1. CTA 102 was found to be in a high state and the brightest flare from this source was observed in gamma-ray. This flare was confirmed as the brightest flare ever detected from CTA 102 in gamma-ray. The fastest variability time was found to be 1.08 hr, which suggests a compact emission region. A 73 GeV photon was detected during the flaring episode with probability of 99.99% for being from the CTA 102. This was probably the first time a photon of such high energy was detected from this source. The multiwavelength SED modeling of the flaring state along with pre-flare state was done. It is found that during flaring state nearly seventy times more jet power in electrons is required compared to the pre-flare state. The sudden increase in the jet power may result from increase in the accretion rate of SMBH that powers the jet. Detailed results from our analysis are provided in chapter 4.

First time in history of Ton 599, a long gamma-ray flaring state was observed during the year 2017. The multiwavelength data from *Fermi*-LAT, Swift-XRT/UVOT Steward and OVRO (15 GHz) observatory show that this source is more variable in gamma-ray and optical/UV band compared to X-ray and radio band. Day scale variability was observed from the one-day bin light curve. Two high energy photons of energy 42 GeV were detected during its flaring episode with a probability of being from Ton 599 of 99.7%. The correlation study between different wavebands suggests the co-spatial origin of gamma-ray, optical/UV and X-ray emission. A lag of 27 days was recorded in radio emission with respect to the gamma-ray emission, which suggests they are coming from two different emission regions located at a distance of $\sim$ 5 pc apart. 3C 279 was observed in a long flaring state during November, 2017 to July, 2018 and multiwavelength data were collected with different telescopes in gamma-ray, X-rays, optical, UV, and radio wavebands. A strong correlation with zero time lag is found between gamma-ray and optical/UV emission from the correlation study. It is also found that the gamma-ray and X-ray emissions are significantly correlated with

zero time lag. This is the first ever correlation observed between gamma-ray and X-ray with zero time lag in 3C 279. Overall the correlation study suggests the co-spatial origin of gamma-ray, optical/UV, and X-ray emission. Paliya et al. (2016) and Hayashida et al. (2012) have studied the flares of 3C 279 and their SED modelings show that a single zone emission model is not adequate to explain the multiwavelength SED. However, in our case a single zone emission model is sufficient to explain the multiwavelength SED. We have performed the SED modeling with single zone emission model for different flaring and quiescent states and it is found that more power in magnetic field is required during the quiescent state compared to the flaring state. Moreover, around ten times more jet power in electrons is needed during the flaring state compared to the quiescent state to explain the high energy gamma-ray emission.

Future Perspectives

This thesis is a tiny effort to understand the physics of multiwavelength emission from blazars. Due to the successful operation of *Fermi*-LAT the wealth of gamma-ray data is available to public to study the physics of blazar flares and their long term light curve. I have utilized this opportunity to learn more about the physics of blazars. The underlying physics of jet launching mechanism, jet compositions, and gamma-ray emission from compact emission zone are still not clear to the community. Studying more and more blazars to find common characteristic features would be helpful to understand these sources. It will also test the validity of some of the fundamental theories such as the blazar sequence. The availability of simultaneous or quasi-simultaneous multiwavelength data will always play an important role in understanding the multiwavelength emission from blazars. Leptonic model and in some cases hadronic model may explain the broadband SEDs. The recent discovery of neutrino from blazar TXS 0506+056 along with the high energy gamma-ray emission supports the hadronic model. Detailed multiwavelength study of large number of blazars is

required to gain further knowledge. The fundamental question about the acceleration mechanism of charge particles to relativistic speed is still an open problem to the gamma-ray and cosmic-ray community. A better understanding is possible by studying the multiwavelength emission from different types of blazars. The *Fermi* support program: Steward, Smarts, OVRO, and SMA observatories along with the Swift-XRT, NuSTAR, XMM-Newton, and ASTROSAT are already helping to collect the multiwavelength data for the *Fermi* detected blazars, which will definitely help to get more insights in blazar physics.

It is important to mention that the next generation ground based high energy gamma-ray array telescope, Cherenkov Telescope Array (CTA) will change this field dramatically. It will have wider energy range from $\sim$30 GeV to $\sim$ 300 TeV and wider field of view of $\sim 6^{\circ}$ to $\sim 8^{\circ}$. Its sensitivity is predicted to be 10 times higher than the existing ground based gamma-ray cherenkov telescopes (e.g. MAGIC, HESS, VERITAS). The observation with CTA will be a crucial step towards understanding of acceleration of charge particles in relativistic jets and revealing the physics of blazars.

References

Abdo, A. A., Ackermann, M., Agudo, I., Ajello, M., Allafort, A., Aller, H. D., Aller, M. F., Antolini, E., Arkharov, A. A., Axelsson, M., and et al. (2010a). Fermi Large Area Telescope and Multi-wavelength Observations of the Flaring Activity of PKS 1510-089 between 2008 September and 2009 June. *ApJ*, 721:1425–1447.

Abdo, A. A., Ackermann, M., Ajello, M., Allafort, A., Antolini, E., Atwood, W. B., Axelsson, M., Baldini, L., Ballet, J., Barbiellini, G., and et al. (2010b). Fermi Large Area Telescope First Source Catalog. *ApJS*, 188:405–436.

Abdo, A. A., Ackermann, M., Ajello, M., Allafort, A., and Baldini, L. (2011). Fermi Gamma-ray Space Telescope Observations of the Gamma-ray Outburst from 3C454.3 in November 2010. *ApJL*, 733:L26.

Abdo, A. A., Ackermann, M., Ajello, M., Antolini, E., Baldini, L., and Ballet, J. (2010c). Gamma-ray Light Curves and Variability of Bright Fermi-detected Blazars. *ApJ*, 722:520–542.

Abdo, A. A., Ackermann, M., Ajello, M., Atwood, W. B., Axelsson, M., Baldini, L., Ballet, J., Band, D. L., Barbiellini, G., Bastieri, D., and et al. (2009). Fermi/Large Area Telescope Bright Gamma-Ray Source List. *ApJS*, 183:46–66.

Acero, F., Ackermann, M., Ajello, M., Albert, A., Atwood, W. B., and Fermi-LAT Collaboration (2015). Fermi Large Area Telescope Third Source Catalog. *ApJS*, 218:23.

Ackermann, M., Anantua, R., Asano, K., Baldini, L., and Barbiellini, G. (2016). Minute-timescale $>$100 MeV γ-Ray Variability during the Giant Outburst of Quasar 3C 279 Observed by Fermi-LAT in 2015 June. *ApJL*, 824:L20.

Ackermann, M., Asano, K., Atwood, W. B., Axelsson, M., Baldini, L., Ballet, J., Barbiellini, G., Baring, M. G., Bastieri, D., Bechtol, K., Bellazzini, R., Berenji, B., Bhat, P. N., Bissaldi, E., Blandford, R. D., Bloom, E. D., Bonamente, E., Borgland, A. W., Bouvier, A., Bregeon, J., Brez, A., Briggs, M. S., Brigida, M., Bruel, P., Buson, S., Caliandro, G. A., Cameron, R. A., Caraveo, P. A., Carrigan, S., Casand jian, J. M., Cecchi, C., and Çelik, Ö. (2010). Fermi Observations of GRB 090510: A Short-Hard Gamma-ray Burst with an Additional, Hard Power-law Component from 10 keV TO GeV Energies. *apj*, 716(2):1178–1190.

Aharonian, F., Akhperjanian, A. G., Bazer-Bachi, A. R., Behera, B., Beilicke, M., Benbow, W., Berge, D., Bernlöhr, K., Boisson, C., Bolz, O., Borrel, V., and Boutelier, T. (2007). An Exceptional Very High Energy Gamma-Ray Flare of PKS 2155-304. *ApJL*, 664:L71–L74.

Ahnen, M. L., Ansoldi, S., Antonelli, L. A., Antoranz, P., Babic, A., Banerjee, B., Bangale, P., Barres de Almeida, U., Barrio, J. A., Bednarek, W., and et al. (2015). Very High Energy γ-Rays from the Universe's Middle Age: Detection of the z = 0.940 Blazar PKS 1441+25 with MAGIC. *ApJL*, 815(2):L23.

Ahnen, M. L., Ansoldi, S., Antonelli, L. A., and Arcaro, C. (2017). Multiwavelength observations of a VHE gamma-ray flare from PKS 1510-089 in 2015. *A&A*, 603:A29.

Aleksić, J., Ansoldi, S., Antonelli, L. A., Antoranz, P., Babic, A., Bangale, P., Barres de Almeida, U., Barrio, J. A., Becerra González, J., Bednarek, W., and et al. (2014). MAGIC gamma-ray and multi-frequency observations of flat spectrum radio quasar PKS 1510-089 in early 2012. *A&A*, 569:A46.

Aleksić, J., Ansoldi, S., Antonelli, L. A., Antoranz, P., Babic, A., Bangale, P., Barres de Almeida, U., Barrio, J. A., Becerra González, J., Bednarek, W., and et al. (2015). The 2009 multiwavelength campaign on Mrk 421: Variability and correlation studies. *A&A*, 576:A126.

Aleksić, J., Antonelli, L. A., Antoranz, P., and Backes, M. (2011). MAGIC Discovery of Very High Energy Emission from the FSRQ PKS 1222+21. *ApJL*, 730(1):L8.

Alexander, T. (1997). Is AGN Variability Correlated with Other AGN Properties? ZDCF Analysis of Small Samples of Sparse Light Curves. In Maoz, D., Sternberg, A., and Leibowitz, E. M., editors, *Astronomical Time Series*, volume 218 of *Astrophysics and Space Science Library*, page 163.

Alexander, T. (2013). Improved AGN light curve analysis with the z-transformed discrete correlation function. *arXiv e-prints*, page arXiv:1302.1508.

Atoyan, A. and Dermer, C. D. (2001). High-energy neutrinos from photomeson processes in blazars. *Phys. Rev. Lett.*, 87:221102.

Atwood, W. B., Abdo, A. A., Ackermann, M., Althouse, W., Anderson, B., Axelsson, M., Baldini, L., Ballet, J., Band, D. L., Barbiellini, G., and et al. (2009). The Large Area Telescope on the Fermi Gamma-Ray Space Telescope Mission. *ApJ*, 697:1071–1102.

Baade, W. and Minkowski, R. (1954). Identification of the Radio Sources in Cassiopeia, Cygnus A, and Puppis A. *ApJ*, 119:206.

Bachev, R., Popov, V., Strigachev, A., Semkov, E., Ibryamov, S., Spassov, B., Latev, G., Muñoz Dimitrova, R. V., and Boeva, S. (2017). Intra-night variability of the blazar CTA 102 during its 2012 and 2016 giant outbursts. *MNRAS*, 471:2216–2223.

Barnacka, Anna, Moderski, Rafal, Behera, Bagmeet, Brun, Pierre, and Wagner, Stefan (2014). Pks 1510-089: a rare example of a flat spectrum radio quasar with a very high-energy emission. *A&A*, 567:A113.

Barthelmy, S. D., Barbier, L. M., Cummings, J. R., Fenimore, E. E., and Gehrels, N. (2005). The Burst Alert Telescope (BAT) on the SWIFT Midex Mission. *SSRv*, 120(3-4):143–164.

Beckmann, V. and Shrader, C. R. (2012). *Active Galactic Nuclei*.

Bednarek, W. and Protheroe, R. J. (1999). The physical parameters of Markarian 501 during flaring activity. *Monthly Notices of the Royal Astronomical Society*, 310(3):577–584.

Begelman, M. C., Sikora, M., Giommi, P., Barr, P., Garilli, B., Gioia, I. M., Maccacaro, T., Maccagni, D., and Schild, R. E. (1987). Inverse Compton scattering of ambient radiation by a cold relativistic jet - A source of beamed, polarized continuum in blazars? *ApJ*, 322:650–661.

Bessell, M. S., Castelli, F., and Plez, B. (1998). Model atmospheres broad-band colors, bolometric corrections and temperature calibrations for O - M stars. *A&A*, 333:231–250.

Blandford, R., Meier, D., and Readhead, A. (2019). Relativistic Jets from Active Galactic Nuclei. *araa*, 57:467–509.

Blandford, R. D. and Königl, A. (1979). Relativistic jets as compact radio sources. *ApJ*, 232:34–48.

Blandford, R. D. and Payne, D. G. (1982). Hydromagnetic flows from accretion discs and the production of radio jets. *MNRAS*, 199:883–903.

Blandford, R. D. and Znajek, R. L. (1977). Electromagnetic extraction of energy from Kerr black holes. *MNRAS*, 179:433–456.

Błażejowski, M., Sikora, M., Moderski, R., and Madejski, G. M. (2000). Comptonization of Infrared Radiation from Hot Dust by Relativistic Jets in Quasars. *ApJ*, 545(1):107–116.

Blumenthal, G. R. and Gould, R. J. (1970). Bremsstrahlung, Synchrotron Radiation, and Compton Scattering of High-Energy Electrons Traversing Dilute Gases. *Reviews of Modern Physics*, 42:237–271.

Boettcher, M., Mause, H., and Schlickeiser, R. (1997). γ-ray emission and spectral evolution of pair plasmas in AGN jets. I. General theory and a prediction for the GeV - TeV emission from ultrarelativistic jets. *A&A*, 324:395–409.

Bonning, E., Urry, C. M., Bailyn, C., Buxton, M., Chatterjee, R., Coppi, P., Fossati, G., Isler, J., and Maraschi, L. (2012). SMARTS Optical and Infrared Monitoring of 12 Gamma-Ray Bright Blazars. *ApJ*, 756(1):13.

Bonning, E. W., Bailyn, C., Urry, C. M., Buxton, M., Fossati, G., Maraschi, L., Coppi, P., Scalzo, R., Isler, J., and Kaptur, A. (2009). Correlated Variability in the Blazar 3C 454.3. *ApJL*, 697:L81–L85.

Böttcher, M., Reimer, A., and Marscher, A. P. (2009). Implications of the very High Energy Gamma-Ray Detection of the Quasar 3C279. *apj*, 703(1):1168–1175.

Bradt, H., Mayer, W., Naranan, S., Rappaport, S., and Spada, G. (1967). Evidence for X-Radiation from the Radio Galaxy M87. *apjl*, 150:L199.

Breeveld, A. A., Landsman, W., Holland, S. T., Roming, P., Kuin, N. P. M., and Page, M. J. (2011). An Updated Ultraviolet Calibration for the Swift/UVOT. In McEnery, J. E., Racusin, J. L., and Gehrels, N., editors, *American Institute of Physics Conference Series*, volume 1358 of *American Institute of Physics Conference Series*, pages 373–376.

Breiding, P., Georganopoulos, M., and Meyer, E. T. (2018). Blazar Sheath Illumination of the Outer Molecular Torus: A Resolution of the Seed Photon Problem for the Far-GeV Blazar Flares. *ApJ*, 853:19.

Britto, R. J., Bottacini, E., Lott, B., Razzaque, S., and Buson, S. (2016). FERMI-LAT OBSERVATIONS OF THE 2014 MAY–JULY OUTBURST FROM 3c 454.3. *The Astrophysical Journal*, 830(2):162.

Brown, A. M. (2013). Locating the γ-ray emission region of the flat spectrum radio quasar PKS 1510-089. *MNRAS*, 431(1):824–835.

Burbidge, E. M. and Kinman, T. D. (1966). Redshifts of Fourteen Quasi-Stellar Radio Sources. *ApJ*, 145:654.

Burrows, D. N., Hill, J. E., Nousek, J. A., and Kennea, J. A. (2005). The Swift X-Ray Telescope. *SSRv*, 120(3-4):165–195.

Byram, E. T., Chubb, T. A., and Friedman, H. (1966). Cosmic X-ray Sources, Galactic and Extragalactic. *Science*, 152(3718):66–71.

Carrasco, L., Porras, A., Recillas, E., Leon-Tavares, J., Chavushyan, V., and Carraminana, A. (2015). NIR Flare if the FSRQ PKS1502+106. *The Astronomer's Telegram*, 7804.

Casadio, C., Gómez, J. L., Jorstad, S. G., and Marscher, A. P. (2015). A Multi-wavelength Polarimetric Study of the Blazar CTA 102 during a Gamma-Ray Flare in 2012. *ApJ*, 813:51.

Castignani, G., Pian, E., Belloni, T. M., D'Ammando, F., Foschini, L., Ghisellini, G., Pursimo, T., Bazzano, A., Beckmann, V., Bianchin, V., Fiocchi, M. T., Impiombato, D., Raiteri, C. M., Soldi, S., Tagliaferri, G., Treves, A., and Türler, M. (2017). Multiwavelength variability study and search for periodicity of PKS 1510-089. *A&A*, 601:A30.

Castignani, G., Guetta, D., Pian, E., Amati, L., Puccetti, S., and Dichiara, S. (2014). Time delays between fermi-lat and gbm light curves of gamma-ray bursts. *A&A*, 565:A60.

Celotti, A., Padovani, P., and Ghisellini, G. (1997). Jets and accretion processes in active galactic nuclei: further clues. *MNRAS*, 286:415–424.

Chatterjee, R., Bailyn, C. D., Bonning, E. W., Buxton, M., Coppi, P., Fossati, G., Isler, J., Maraschi, L., and Urry, C. M. (2012). Similarity of the Optical-Infrared and γ-Ray Time Variability of Fermi Blazars. *ApJ*, 749:191.

Chatterjee, R., Jorstad, S. G., Marscher, A. P., Oh, H., McHardy, I. M., Aller, M. F., Aller, H. D., Balonek, T. J., Miller, H. R., Ryle, W. T., Tosti, G., Kurtanidze, O., Nikolashvili, M., Larionov, V. M., and Hagen-Thorn, V. A. (2008). Correlated Multi-Wave Band Variability in the Blazar 3C 279 from 1996 to 2007. *ApJ*, 689:79–94.

Chatterjee, R., Roychowdhury, A., Chandra, S., and Sinha, A. (2018). Possible Accretion Disk Origin of the Emission Variability of a Blazar Jet. *ApJL*, 859:L21.

Chiaberge, M. and Ghisellini, G. (1999). Rapid variability in the synchrotron self-Compton model for blazars. *MNRAS*, 306:551–560.

Chidiac, C., Rani, B., Krichbaum, T. P., Angelakis, E., Fuhrmann, L., Nestoras, I., Zensus, J. A., Sievers, A., Ungerechts, H., Itoh, R., Fukazawa, Y., Uemura, M., Sasada, M., Gurwell, M., and Fedorova, E. (2016). Exploring the nature of the broadband variability in the flat spectrum radio quasar 3C 273. *A&A*, 590:A61.

Cohen, D. P., Romani, R. W., Filippenko, A. V., Cenko, S. B., Lott, B., Zheng, W., and Li, W. (2014). Temporal Correlations between Optical and Gamma-Ray Activity in Blazars. *ApJ*, 797:137.

Curtis, H. D. (1918). Descriptions of 762 Nebulae and Clusters Photographed with the Crossley Reflector. *Publications of Lick Observatory*, 13:9–42.

D'Ammando, F., Raiteri, C. M., Villata, M., Romano, P., and Pucella, G. (2011). AGILE detection of extreme γ-ray activity from the blazar PKS 1510-089 during March 2009. Multifrequency analysis. *A&A*, 529:A145.

Dermer, C. D., Cerruti, M., Lott, B., Boisson, C., and Zech, A. (2014). Equipartition Gamma-Ray Blazars and the Location of the Gamma-Ray Emission Site in 3C 279. *ApJ*, 782(2):82.

Dermer, C. D. and Menon, G. (2009). *High Energy Radiation from Black Holes: Gamma Rays, Cosmic Rays, and Neutrinos*.

Dermer, C. D. and Schlickeiser, R. (1993). Model for the High-Energy Emission from Blazars. *ApJ*, 416:458.

Dermer, C. D., Schlickeiser, R., and Mastichiadis, A. (1992). High-energy gamma radiation from extragalactic radio sources. *A&A*, 256:L27–L30.

Donato, D., Ghisellini, G., Tagliaferri, G., and Fossati, G. (2001). Hard X-ray properties of blazars. *A&A*, 375:739–751.

Dondi, L. and Ghisellini, G. (1995). Gamma-ray-loud blazars and beaming. *Monthly Notices of the Royal Astronomical Society*, 273(3):583–595.

Dotson, A., Georganopoulos, M., Kazanas, D., and Perlman, E. S. (2012). A Method for Localizing Energy Dissipation in Blazars Using Fermi Variability. *ApJL*, 758:L15.

Dotson, A., Georganopoulos, M., Meyer, E. T., and McCann, K. (2015). On the Location of the 2009 GeV Flares of Blazar PKS 1510-089. *ApJ*, 809:164.

Edelson, R. A. and Krolik, J. H. (1988). The Discrete Correlation Function: A New Method for Analyzing Unevenly Sampled Variability Data. *apj*, 333:646.

Edelson, R. A., Krolik, J. H., and Pike, G. F. (1990). Broad-band properties of the CfA Seyfert galaxies. III - Ultraviolet variability. *ApJ*, 359:86–97.

Edelson, R. A. and Malkan, M. A. (1987). Far-infrared variability in active galactic nuclei. *ApJ*, 323:516–535.

EHT Collaboration, Akiyama, K., Alberdi, A., Alef, W., Asada, K., Azulay, R., Baczko, A.-K., Ball, D., Baloković, M., Barrett, J., and et al. (2019). First M87 Event Horizon Telescope Results. I. The Shadow of the Supermassive Black Hole. *ApJL*, 875:L1.

Emmanoulopoulos, D., McHardy, I. M., and Papadakis, I. E. (2013). Generating artificial light curves: revisited and updated. *mnras*, 433(2):907–927.

Fan, J. H., Cheng, K. S., Zhang, L., and Liu, C. H. (1997). Polarization and beaming effect for BL Lacertae objects. *A&A*, 327:947–951.

Fath, E. A. (1909). The spectra of some spiral nebulae and globular star clusters. *Lick Observatory Bulletin*, 5:71–77.

Finke, J. D. (2016). External Compton Scattering in Blazar Jets and the Location of the Gamma-Ray Emitting Region. *ApJ*, 830:94.

Fitch, W. S., Pacholczyk, A. G., and Weymann, R. J. (1967). Light Variations of the Seyfert Galaxy NGC 4151. *ApJL*, 150:L67.

Foschini, L., Bonnoli, G., Ghisellini, G., Tagliaferri, G., Tavecchio, F., and Stamerra, A. (2013). Fermi/LAT detection of extraordinary variability in the gamma-ray emission of the blazar PKS 1510-089. *A&A*, 555:A138.

Foschini, L., Ghisellini, G., Tavecchio, F., Bonnoli, G., and Stamerra, A. (2011). Search for the shortest variability at gamma rays in flat-spectrum radio quasars. *A&A*, 530:A77.

Fossati, G., Celotti, A., Chiaberge, M., Zhang, Y. H., Chiappetti, L., Ghisellini, G., Maraschi, L., Tavecchio, F., Pian, E., and Treves, A. (2000). X-Ray Emission of Markarian 421: New Clues from Its Spectral Evolution. I. Temporal Analysis. *ApJ*, 541:153–165.

Fossati, G., Maraschi, L., Celotti, A., Comastri, A., and Ghisellini, G. (1998). A unifying view of the spectral energy distributions of blazars. *MNRAS*, 299:433–448.

Fromm, C. M., Perucho, M., Ros, E., Savolainen, T., Lobanov, A. P., Zensus, J. A., Aller, M. F., Aller, H. D., Gurwell, M. A., and Lähteenmäki, A. (2011). Catching the radio flare in CTA 102. I. Light curve analysis. *A&A*, 531:A95.

Fromm, C. M., Ros, E., Perucho, M., Savolainen, T., Mimica, P., Kadler, M., Lobanov, A. P., Lister, M. L., Kovalev, Y. Y., and Zensus, J. A. (2013a). Catching the radio flare in CTA 102. II. VLBI kinematic analysis. *A&A*, 551:A32.

Fromm, C. M., Ros, E., Perucho, M., Savolainen, T., Mimica, P., Kadler, M., Lobanov, A. P., and Zensus, J. A. (2013b). Catching the radio flare in CTA 102. III. Core-shift and spectral analysis. *A&A*, 557:A105.

Fuhrmann, L., Larsson, S., Chiang, J., Angelakis, E., Zensus, J. A., Nestoras, I., Krichbaum, T. Â. P., Ungerechts, H., Sievers, A., Pavlidou, V., Readhead, A. C. S., Max-Moerbeck, W., and Pearson, T. J. (2014). Detection of significant cm to sub-mm band radio and γ-ray correlated variability in Fermi bright blazars. *MNRAS*, 441:1899–1909.

Gasparyan, S., Sahakyan, N., Baghmanyan, V., and Zargaryan, D. (2018). On the Multi-wavelength Emission from CTA 102. *ApJ*, 863:114.

Gaur, H., Mohan, P., Wierzcholska, A., and Gu, M. (2018). Signature of inverse Compton emission from blazars. *MNRAS*, 473:3638–3660.

Gehrels, N., Chincarini, G., Giommi, P., Mason, K. O., and Nousek, J. A. (2004). The Swift Gamma-Ray Burst Mission. *ApJ*, 611:1005–1020.

Ghisellini, G., Celotti, A., Fossati, G., Maraschi, L., and Comastri, A. (1998). A theoretical unifying scheme for gamma-ray bright blazars. *MNRAS*, 301:451–468.

Ghisellini, G. and Madau, P. (1996). On the origin of the gamma-ray emission in blazars. *MNRAS*, 280(1):67–76.

Ghisellini, G. and Maraschi, L. (1989). Bulk Acceleration in Relativistic Jets and the Spectral Properties of Blazars. *ApJ*, 340:181.

Ghisellini, G., Tagliaferri, G., Foschini, L., Ghirlanda, G., Tavecchio, F., Ceca, R. D., Haardt, F., Volonteri, M., and Gehrels, N. (2011). High-redshift Fermi blazars. *MNRAS*, 411(2):901–914.

Ghisellini, G. and Tavecchio, F. (2009). Canonical high-power blazars. *MNRAS*, 397:985–1002.

Ghisellini, G., Villata, M., Raiteri, C. M., Bosio, S., de Francesco, G., Latini, G., Maesano, M., Massaro, E., Montagni, F., Nesci, R., Tosti, G., Fiorucci, M., Pian, E., Maraschi, L., Treves, A., Comastri, A., and Mignoli, M. (1997). Optical-IUE observations of the gamma-ray loud BL Lacertae object S5 0716+714: data and interpretation. *A&A*, 327:61–71.

Giommi, P., Ansari, S. G., and Micol, A. (1995). Radio to X-ray energy distribution of BL Lacertae objects. *A&AS*, 109:267–291.

Gu, M., Cao, X., and Jiang, D. R. (2001). On the masses of black holes in radio-loud quasars. *MNRAS*, 327:1111–1115.

Gubbay, J., Legg, A. J., Robertson, D. S., Moffet, A. T., Ekers, R. D., and Seidel, B. (1969). Variations of Small Quasar Components at 2,300 MHz. *Nature*, 224(5224):1094–1095.

Gurwell, M. A., Peck, A. B., Hostler, S. R., Darrah, M. R., and Katz, C. A. (2007). Monitoring Phase Calibrators at Submillimeter Wavelengths. In Baker, A. J., Glenn, J., Harris, A. I., Mangum, J. G., and Yun, M. S., editors, *From Z-Machines to ALMA: (Sub)Millimeter Spectroscopy of Galaxies*, volume 375 of *Astronomical Society of the Pacific Conference Series*, page 234.

Hahn, J. (2015). GAMERA - a new modeling package for non-thermal spectral modeling. In Borisov, A. S., Denisova, V. G., Guseva, Z. M., Kanevskaya, E. A., Kogan, M. G., Morozov, A. E., Puchkov, V. S., Pyatovsky, S. E., Shoziyoev, G. P., Smirnova, M. D., Vargasov, A. V., Galkin, V. I., Nazarov, S. I., and Mukhamedshin, R. A., editors, *34th International Cosmic Ray Conference (ICRC2015)*, volume 34 of *International Cosmic Ray Conference*, page 917.

Hartman, R. C., Bertsch, D. L., Bloom, S. D., and Chen, A. W. (1999). The Third EGRET Catalog of High-Energy Gamma-Ray Sources. *ApJS*, 123:79–202.

Hayashida, M., Madejski, G. M., Nalewajko, K., and Sikora, M. (2012). The Structure and Emission Model of the Relativistic Jet in the Quasar 3C 279 Inferred from Radio to High-energy γ-Ray Observations in 2008-2010. *ApJ*, 754:114.

Hayashida, M., Nalewajko, K., Madejski, G. M., and Sikora, M. (2015). Rapid Variability of Blazar 3C 279 during Flaring States in 2013-2014 with Joint Fermi-LAT, NuSTAR, Swift, and Ground-Based Multiwavelength Observations. *ApJ*, 807:79.

Heidt, J. and Wagner, S. J. (1996). Statistics of optical intraday variability in a complete sample of radio-selected BL Lacertae objects. *A&A*, 305:42.

H.E.S.S. Collaboration, Abramowski, A., Acero, F., and Aharonian, F. (2013). H.E.S.S. discovery of VHE γ-rays from the quasar PKS 1510-089. *A&A*, 554:A107.

Hewett, P. C. and Wild, V. (2010). Improved redshifts for SDSS quasar spectra. *MNRAS*, 405:2302–2316.

Janiak, M., Sikora, M., Nalewajko, K., Moderski, R., and Madejski, G. M. (2012). On the Origin of the γ-Ray/Optical Lags in Luminous Blazars. *ApJ*, 760:129.

Jankowsky, F., Zacharias, M., Wierzcholska, A., Cologna, G., Mohamed, M., Schwemmer, S., and Wagner, S. (2015). Detection of renewed optical activity from the gamma-ray source PKS 1510-089 with ATOM. *The Astronomer's Telegram*, 7799.

Jorstad, S. G., Marscher, A. P., Lister, M. L., Stirling, A. M., Cawthorne, T. V., Gear, W. K., Gómez, J. L., Stevens, J. A., Smith, P. S., Forster, J. R., and Robson, E. I. (2005). Polarimetric Observations of 15 Active Galactic Nuclei at High Frequencies: Jet Kinematics from Bimonthly Monitoring with the Very Long Baseline Array. *AJ*, 130:1418–1465.

Jorstad, S. G., Marscher, A. P., Mattox, J. R., Aller, M. F., Aller, H. D., Wehrle, A. E., and Bloom, S. D. (2001). Multiepoch Very Long Baseline Array Observations of EGRET-detected Quasars and BL Lacertae Objects: Connection between Superluminal Ejections and Gamma-Ray Flares in Blazars. *ApJ*, 556:738–748.

Jorstad, S. G., Marscher, A. P., Smith, P. S., and Larionov, V. M. (2013). A Tight Connection between Gamma-Ray Outbursts and Parsec-scale Jet Activity in the Quasar 3C 454.3. *ApJ*, 773:147.

Kadota, A., Fujisawa, K., Sawada-Satoh, S., Wajima, K., and Doi, A. (2012). An Intrinsic Short-Term Radio Variability Observed in PKS 1510-089. *PASJ*, 64:109.

Kalberla, P. M. W., Burton, W. B., Hartmann, D., Arnal, E. M., Bajaja, E., Morras, R., and Pöppel, W. G. L. (2005). The Leiden/Argentine/Bonn (LAB) Survey of Galactic HI. Final data release of the combined LDS and IAR surveys with improved stray-radiation corrections. *A&A*, 440:775–782.

Kataoka, J., Madejski, G., Sikora, M., Roming, P., Chester, M. M., Grupe, D., Tsubuku, Y., Sato, R., Kawai, N., Tosti, G., Impiombato, D., Kovalev, Y. Y., Kovalev, Y. A., Edwards, P. G., Wagner, S. J., Moderski, R., Stawarz, Ł., Takahashi, T., and Watanabe, S. (2008). Multiwavelength Observations of the Powerful Gamma-Ray Quasar PKS 1510-089: Clues on the Jet Composition. *ApJ*, 672:787–799.

Kaur, N. and Baliyan, K. S. (2018). CTA 102 in exceptionally high state during 2016-2017. *A&A*, 617:A59.

Kellermann, K. I., Sramek, R., Schmidt, M., Shaffer, D. B., and Green, R. (1989). VLA observations of objects in the Palomar Bright Quasar Survey. *AJ*, 98:1195–1207.

Kelly, B. C., Sobolewska, M., and Siemiginowska, A. (2011). A Stochastic Model for the Luminosity Fluctuations of Accreting Black Holes. *ApJ*, 730:52.

Konigl, A. (1981). Relativistic jets as X-ray and gamma-ray sources. *ApJ*, 243:700–709.

Kushwaha, P., Gupta, A. C., Misra, R., and Singh, K. P. (2017). Multiwavelength temporal variability of the blazar 3C 454.3 during 2014 activity phase. *MNRAS*, 464:2046–2052.

Larionov, V. M., Jorstad, S. G., Marscher, A. P., Morozova, D. A., Blinov, D. A., Hagen-Thorn, V. A., Konstantinova, T. S., Kopatskaya, E. N., Larionova, L. V., Larionova, E. G., and Troitsky, I. S. (2013). The Outburst of the Blazar S5 0716+71 in 2011 October: Shock in a Helical Jet. *ApJ*, 768:40.

Larionov, V. M., Villata, M., Raiteri, C. M., Jorstad, S. G., and Marscher, A. P. (2016). Exceptional outburst of the blazar CTA 102 in 2012: the GASP-WEBT campaign and its extension. *MNRAS*, 461(3):3047–3056.

Li, X., Mohan, P., An, T., Hong, X., Cheng, X., Yang, J., Zhang, Y., Zhang, Z., and Zhao, W. (2018). Imaging and Variability Studies of CTA 102 during the 2016 January γ-ray Flare. *ApJ*, 854:17.

Liodakis, I., Marchili, N., Angelakis, E., Fuhrmann, L., Nestoras, I., Myserlis, I., Karamanavis, V., Krichbaum, T. P., Sievers, A., Ungerechts, H., and Zensus, J. A. (2017). F-GAMMA: variability Doppler factors of blazars from multiwavelength monitoring. *MNRAS*, 466:4625–4632.

Liu, H. T. and Bai, J. M. (2006). Absorption of 10-200 GeV Gamma Rays by Radiation from Broad-Line Regions in Blazars. *ApJ*, 653:1089–1097.

Lynds, C. R., Stockton, A. N., and Livingston, W. C. (1965). New Spectroscope Observations of Quasi-Stellar Sources. *ApJ*, 142:1667.

MAGIC Collaboration, Acciari, V. A., Ansoldi, S., and Antonelli, L. A. (2018). Detection of persistent VHE gamma-ray emission from PKS 1510-089 by the MAGIC telescopes during low states between 2012 and 2017. *A&A*, 619:A159.

MAGIC Collaboration, Albert, J., Aliu, E., and Anderhub, H. (2008). Very-High-Energy gamma rays from a Distant Quasar: How Transparent Is the Universe? *Science*, 320(5884):1752.

Mannheim, K. (1993). The proton blazar. *aap*, 269:67–76.

Mannheim, K. (1998). Possible production of high-energy gamma rays from proton acceleration in the extragalactic radio source markarian 501. *Science*, 279(5351):684–686.

Marscher, A. P. (2014). Turbulent, Extreme Multi-zone Model for Simulating Flux and Polarization Variability in Blazars. *ApJ*, 780:87.

Marscher, A. P. and Gear, W. K. (1985). Models for high-frequency radio outbursts in extragalactic sources, with application to the early 1983 millimeter-to-infrared flare of 3C 273. *ApJ*, 298:114–127.

Marscher, A. P., Jorstad, S. G., D'Arcangelo, F. D., Smith, P. S., Williams, G. G., Larionov, V. M., Oh, H., Olmstead, A. R., Aller, M. F., Aller, H. D., McHardy, I. M., Lähteenmäki, A., Tornikoski, M., Valtaoja, E., Hagen-Thorn, V. A., Kopatskaya, E. N., Gear, W. K., Tosti, G., Kurtanidze, O., Nikolashvili, M., Sigua, L., Miller, H. R., and Ryle, W. T. (2008). The inner jet of an active galactic nucleus as revealed by a radio-to-γ-ray outburst. *Nature*, 452:966–969.

Marscher, A. P., Jorstad, S. G., Larionov, V. M., and Aller, M. F. (2010). Probing the Inner Jet of the Quasar PKS 1510-089 with Multi-Waveband Monitoring During Strong Gamma-Ray Activity. *ApJL*, 710:L126–L131.

Massaro, E., Perri, M., Giommi, P., and Nesci, R. (2004). Log-parabolic spectra and particle acceleration in the BL Lac object Mkn 421: Spectral analysis of the complete BeppoSAX wide band X-ray data set. *A&A*, 413:489–503.

Matthews, T. A. and Sandage, A. R. (1963). Optical Identification of 3C 48, 3C 196, and 3C 286 with Stellar Objects. *ApJ*, 138:30.

Mattox, J. R., Bertsch, D. L., Chiang, J., Dingus, B. L., Digel, S. W., Esposito, J. A., Fierro, J. M., Hartman, R. C., Hunter, S. D., Kanbach, G., Kniffen, D. A., Lin, Y. C., Macomb, D. J., Mayer-Hasselwander, H. A., Michelson, P. F., von Montigny, C., Mukherjee, R., Nolan, P. L., Ramanamurthy, P. V., Schneid, E., Sreekumar, P., Thompson, D. J., and Willis, T. D. (1996). The Likelihood Analysis of EGRET Data. *ApJ*, 461:396.

Melia, F. and Konigl, A. (1989). The Radiative Deceleration of Relativistic Jets in Active Galactic Nuclei. *ApJ*, 340:162.

Miller, P., Rawlings, S., and Saunders, R. (1993). The radio and optical properties of the z < 0.5 BQS quasars. *MNRAS*, 263(2):425–460.

Mirzoyan, R. and MAGIC Collaboration (2015). ATel 7542: MAGIC detects an increased activity from PKS 1510-089 at very high energy gamma-rays. *The Astronomer's Telegram*, 7542.

Moore, R. L. and Stockman, H. S. (1981). The class of highly polarized quasars - Observations and description. *ApJ*, 243:60–75.

Mücke, A., Protheroe, R. J., Engel, R., Rachen, J. P., and Stanev, T. (2003). BL Lac objects in the synchrotron proton blazar model. *Astroparticle Physics*, 18(6):593–613.

Mukherjee, R., Bertsch, D. L., Bloom, S. D., and Dingus, B. L. (1997). EGRET Observations of High-Energy Gamma-Ray Emission from Blazars: An Update. *ApJ*, 490:116–135.

Nalewajko, K., Sikora, M., Madejski, G. M., Exter, K., Szostek, A., Szczerba, R., Kidger, M. R., and Lorente, R. (2012). Herschel PACS and SPIRE Observations of Blazar PKS 1510-089: A Case for Two Blazar Zones. *ApJ*, 760(1):69.

Narayan, R., Mahadevan, R., and Quataert, E. (1998). Advection-dominated accretion around black holes. In Abramowicz, M. A., Björnsson, G., and Pringle, J. E., editors, *Theory of Black Hole Accretion Disks*, pages 148–182.

Nenkova, M., Ivezić, Ž., and Elitzur, M. (2002). Dust Emission from Active Galactic Nuclei. *ApJL*, 570:L9–L12.

Netzer, H. (2015). Revisiting the Unified Model of Active Galactic Nuclei. *araa*, 53:365–408.

Nieppola, E., Tornikoski, M., and Valtaoja, E. (2006). Spectral energy distributions of a large sample of BL Lacertae objects. *A&A*, 445:441–450.

Nilsson, K., Pursimo, T., Villforth, C., Lindfors, E., and Takalo, L. O. (2009). The host galaxy of 3C 279. *A&A*, 505:601–604.

Nolan, P. L., Abdo, A. A., Ackermann, M., Ajello, M., Allafort, A., Antolini, E., Atwood, W. B., Axelsson, M., Baldini, L., Ballet, J., and et al. (2012). Fermi Large Area Telescope Second Source Catalog. *ApJS*, 199:31.

Nolan, P. L., Bertsch, D. L., Fichtel, C. E., Hartman, R. C., Hunter, S. D., Kanbach, G., Kniffen, D. A., Lin, Y. C., Mattox, J. R., Mayer-Hasselwander, H. A., Michelson, P. F., von Montigny, C., Schneid, E., Sreekumar, P., and Thompson, D. J. (1993). Observation of high-energy gamma rays from the quasi-stellar object CTA 102. *ApJ*, 414:82–85.

Orienti, M., Koyama, S., D'Ammando, F., Giroletti, M., Kino, M., Nagai, H., Venturi, T., Dallacasa, D., Giovannini, G., Angelakis, E., Fuhrmann, L., Hovatta, T., Max-Moerbeck, W., Schinzel, F. K., Akiyama, K., Hada, K., Honma, M., Niinuma, K., Gasparrini, D., Krichbaum, T. P., Nestoras, I., Readhead, A. C. S., Richards, J. L., Riquelme, D., Sievers, A., Ungerechts, H., and Zensus, J. A. (2013). Radio and γ-ray follow-up of the exceptionally high-activity state of PKS 1510-089 in 2011. *MNRAS*, 428(3):2418–2429.

Osterman Meyer, A., Miller, H. R., Marshall, K., Ryle, W. T., Aller, H., Aller, M., and Balonek, T. (2009). Simultaneous Multiwavelength and Optical Microvariability Observations of CTA 102 (PKS J2232+1143). *AJ*, 138:1902–1910.

Padovani, P., Alexander, D. M., Assef, R. J., De Marco, B., Giommi, P., Hickox, R. C., Richards, G. T., Smolčić, V., Hatziminaoglou, E., Mainieri, V., and Salvato, M. (2017). Active galactic nuclei: what's in a name? *aapr*, 25(1):2.

Padovani, P. and Giommi, P. (1995). A Sample-Oriented Catalogue of Bl-Lacertae Objects. *MNRAS*, 277:1477.

Paliya, V. S. (2015). Fermi-Large Area Telescope Observations of the Exceptional Gamma-Ray Flare from 3C 279 in 2015 June. *ApJL*, 808:L48.

Paliya, V. S., Diltz, C., Böttcher, M., Stalin, C. S., and Buckley, D. (2016). A HARD GAMMA-RAY FLARE FROM 3c 279 IN 2013 DECEMBER. *ApJ*, 817(1):61.

Paliya, V. S., Sahayanathan, S., and Stalin, C. S. (2015). Multi-Wavelength Observations of 3C 279 During the Extremely Bright Gamma-Ray Flare in 2014 March-April. *ApJ*, 803(1):15.

Patel, S. R., Shukla, A., Chitnis, V. R., Dorner, D., Mannheim, K., Acharya, B. S., and Nagare, B. J. (2018). Broadband study of blazar 1ES 1959+650 during flaring state in 2016. *A&A*, 611:A44.

Peterson, B. (2006). *The Broad-Line Region in Active Galactic Nuclei*, pages 77–100. Springer Berlin Heidelberg, Berlin, Heidelberg.

Pian, E., Falomo, R., and Treves, A. (2005). Hubble Space Telescope ultraviolet spectroscopy of blazars: emission-line properties and black hole masses. *MNRAS*, 361:919–926.

Pian, E., Urry, C. M., Maraschi, L., Madejski, G., McHardy, I. M., Koratkar, A., Treves, A., Chiappetti, L., Grandi, P., Hartman, R. C., Kubo, H., Leach, C. M., Pesce, J. E., Imhoff, C., Thompson, R., and Wehrle, A. E. (1999). Ultraviolet and Multiwavelength Variability of the Blazar 3C 279: Evidence for Thermal Emission. *ApJ*, 521(1):112–120.

Pier, E. A. and Krolik, J. H. (1992). Radiation-Pressure–supported Obscuring Tori around Active Galactic Nuclei. *ApJL*, 399:L23.

Pier, E. A. and Krolik, J. H. (1993). Infrared Spectra of Obscuring Dust Tori around Active Galactic Nuclei. II. Comparison with Observations. *ApJ*, 418:673.

Pittori, C., Lucarelli, F., Verrecchia, F., Raiteri, C. M., Villata, M., Vittorini, V., Tavani, M., Puccetti, S., Perri, M., Donnarumma, I., Vercellone, S., Acosta-Pulido, J. A., Bachev, R., Benítez, E., Borman, G. A., Carnerero, M. I., Carosati, D., Chen, W. P., Ehgamberdiev, S. A., Goded, A., Grishina, T. S., Hiriart, D., Hsiao, H. Y., Jorstad, S. G., Kimeridze, G. N., Kopatskaya, E. N., Kurtanidze, O. M., Kurtanidze, S. O., Larionov, V. M., Larionova, L. V., Marscher, A. P., Mirzaqulov, D. O., Morozova, D. A., Nilsson, K., Samal, M. R., Sigua, L. A., Spassov, B., Strigachev, A., Takalo, L. O., Antonelli, L. A., Bulgarelli, A., Cattaneo, P., Colafrancesco, S., Giommi, P., Longo, F., Morselli, A., and Paoletti, F. (2018). The Bright gamma-ray Flare of 3C 279 in 2015 June: AGILE Detection and Multifrequency Follow-up Observations. *apj*, 856(2):99.

Prince, R. (2019). Multi-frequency Variability Study of Ton 599 during the High Activity of 2017. *ApJ*, 871(1):101.

Prince, R., Majumdar, P., and Gupta, N. (2017). Long-term Study of the Light Curve of PKS 1510-089 in GeV Energies. *ApJ*, 844:62.

Prince, R., Raman, G., Hahn, J., Gupta, N., and Majumdar, P. (2018). Fermi-Large Area Telescope Observations of the Brightest Gamma-Ray Flare Ever Detected from CTA 102. *ApJ*, 866:16.

Protheroe, R. J. (1997). *High Energy Neutrinos from Blazars*, volume 121 of *Astronomical Society of the Pacific Conference Series*, page 585.

Protheroe, R. J. (2002). Factors Determining Variability Time in Active Galactic Nucleus Jets. *PASA*, 19:486–498.

Pushkarev, A. B., Kovalev, Y. Y., and Lister, M. L. (2010). Radio/Gamma-ray Time Delay in the Parsec-scale Cores of Active Galactic Nuclei. *ApJL*, 722:L7–L11.

Pushkarev, A. B., Kovalev, Y. Y., Lister, M. L., and Savolainen, T. (2009). Jet opening angles and gamma-ray brightness of AGN. *A&A*, 507:L33–L36.

Pushkarev, A. B., Kovalev, Y. Y., Lister, M. L., and Savolainen, T. (2017). MOJAVE - XIV. Shapes and opening angles of AGN jets. *MNRAS*, 468:4992–5003.

Raiteri, C. M., Villata, M., Aller, M. F., Gurwell, M. A., and Kurtanidze, O. M. (2011). The long-lasting activity of <ASTROBJ>3C 454.3</ASTROBJ>. GASP-WEBT and satellite observations in 2008-2010. *A&A*, 534:A87.

Raiteri, C. M., Villata, M., D'Ammando, F., Larionov, V. M., and Gurwell, M. A. (2013). The awakening of BL Lacertae: observations by Fermi, Swift and the GASP-WEBT. *MNRAS*, 436:1530–1545.

Raiteri, C. M., Villata, M., Smith, P. S., Larionov, V. M., Acosta-Pulido, J. A., Aller, M. F., D'Ammando, F., and Gurwell, M. A. (2012). Variability of the blazar 4C 38.41 (B3 1633+382) from GHz frequencies to GeV energies. *A&A*, 545:A48.

Rajput, B., Stalin, C. S., Sahayanathan, S., Rakshit, S., and Mandal, A. K. (2019). Temporal correlation between the optical and γ-ray flux variations in the blazar 3C 454.3. *MNRAS*, 486(2):1781–1795.

Ramakrishnan, V., León-Tavares, J., Rastorgueva-Foi, E. A., Wiik, K., and Jorstad, S. G. (2014). The connection between the parsec-scale radio jet and γ-ray flares in the blazar 1156+295. *MNRAS*, 445:1636–1646.

Rani, B., Krichbaum, T. P., Lee, S.-S., Sokolovsky, K., Kang, S., Byun, D.-Y., Mosunova, D., and Zensus, J. A. (2017). Probing the gamma-ray variability in 3C 279 using broad-band observations. *MNRAS*, 464:418–427.

Rani, B., Krichbaum, T. P., Marscher, A. P., Hodgson, J. A., Fuhrmann, L., Angelakis, E., Britzen, S., and Zensus, J. A. (2015). Connection between inner jet kinematics and broadband flux variability in the BL Lacertae object S5 0716+714. *A&A*, 578:A123.

Rani, B., Krichbaum, T. P., Marscher, A. P., Jorstad, S. G., Hodgson, J. A., Fuhrmann, L., and Zensus, J. A. (2014). Jet outflow and gamma-ray emission correlations in S5 0716+714. *A&A*, 571:L2.

Rees, M. J. (1966). Appearance of Relativistically Expanding Radio Sources. *Nature*, 211:468–470.

Richards, J. L., Max-Moerbeck, W., and Pavlidou, V. (2011). Blazars in the Fermi Era: The OVRO 40 m Telescope Monitoring Program. *ApJS*, 194(2):29.

Rowan-Robinson, M. (1977). On the unity of activity in galaxies. *ApJ*, 213:635–647.

Rybicki, G. B. and Lightman, A. P. (1979). *Radiative processes in astrophysics*.

Saito, S., Stawarz, Ł., Tanaka, Y. T., Takahashi, T., Madejski, G., and D'Ammando, F. (2013). Very Rapid High-amplitude Gamma-Ray Variability in Luminous Blazar PKS 1510-089 Studied with Fermi-LAT. *ApJL*, 766(1):L11.

Saito, S., Stawarz, Ł., Tanaka, Y. T., Takahashi, T., Sikora, M., and Moderski, R. (2015). Time-dependent Modeling of Gamma-Ray Flares in Blazar PKS1510–089. *ApJ*, 809(2):171.

Salpeter, E. E. (1964). Accretion of Interstellar Matter by Massive Objects. *apj*, 140:796–800.

Sambruna, R. M., Maraschi, L., and Urry, C. M. (1996). On the Spectral Energy Distributions of Blazars. *ApJ*, 463:444.

Sameer, Kaur, N., Ganesh, S., Kumar, V., and Baliyan, K. S. (2015). ATel 7495: Near Infrared flaring of the blazar FSRQ PKS 1510-089: MIRO Observations. *The Astronomer's Telegram*, 7495.

Sandage, A. and Wyndham, J. D. (1965). On the Optical Identification of Eleven New Quasi-Stellar Radio Sources. *ApJ*, 141:328.

Sanders, D. B., Phinney, E. S., Neugebauer, G., Soifer, B. T., and Matthews, K. (1989). Continuum energy distribution of quasars - Shapes and origins. *ApJ*, 347:29–51.

Sartori, L. F., Schawinski, K., Trakhtenbrot, B., Caplar, N., Treister, E., Koss, M. J., Urry, C. M., and Zhang, C. E. (2018). A model for AGN variability on multiple time-scales. *MNRAS*, 476:L34–L38.

Sbarrato, T., Padovani, P., and Ghisellini, G. (2014). The jet-disc connection in AGN. *MNRAS*, 445:81–92.

Schinzel, F. K., Lobanov, A. P., Taylor, G. B., Jorstad, S. G., Marscher, A. P., and Zensus, J. A. (2012). Relativistic outflow drives γ-ray emission in 3C 345. *A&A*, 537:A70.

Schlafly, E. F. and Finkbeiner, D. P. (2011). Measuring Reddening with Sloan Digital Sky Survey Stellar Spectra and Recalibrating SFD. *ApJ*, 737:103.

Schmidt, M. (1963). 3C 273 : A Star-Like Object with Large Red-Shift. *Nature*, 197:1040.

Schmidt, M. (1965). Large Redshifts of Five Quasi-Stellar Sources. *ApJ*, 141:1295.

Schneider, D. P., Richards, G. T., Hall, P. B., and Strauss, M. A. (2010). The Sloan Digital Sky Survey Quasar Catalog. V. Seventh Data Release. *AJ*, 139:2360.

Seyfert, C. K. (1943). Nuclear Emission in Spiral Nebulae. *ApJ*, 97:28.

Shah, Z., Jithesh, V., Sahayanathan, S., Misra, R., and Iqbal, N. (2019). Study on temporal and spectral behaviour of 3C 279 during 2018 January flare. *MNRAS*, 484:3168–3179.

Shakura, N. I. and Sunyaev, R. A. (1973). Black holes in binary systems. Observational appearance. *A&A*, 24:337–355.

Shukla, A., Mannheim, K., Patel, S. R., Roy, J., Chitnis, V. R., Dorner, D., Rao, A. R., Anupama, G. C., and Wendel, C. (2018). Short-timescale upgamma-ray variability in CTA 102. *ApJ*, 854(2):L26.

Sikora, M., Begelman, M. C., and Rees, M. J. (1994). Comptonization of diffuse ambient radiation by a relativistic jet: The source of gamma rays from blazars? *ApJ*, 421:153–162.

Sikora, M., Błażejowski, M., Begelman, M. C., and Moderski, R. (2001). Modeling the Production of Flares in Gamma-Ray Quasars. *ApJ*, 554:1–11.

Sinha, A., Shukla, A., Saha, L., Acharya, B. S., Anupama, G. C., Bhattacharjee, P., Britto, R. J., Chitnis, V. R., Prabhu, T. P., Singh, B. B., and Vishwanath, P. R. (2016). Long-term study of Mkn 421 with the HAGAR Array of Telescopes. *A&A*, 591:A83.

Smith, A. G. (1996). Multiple Timescales of AGN Variability. In Miller, H. R., Webb, J. R., and Noble, J. C., editors, *Blazar Continuum Variability*, volume 110 of *Astronomical Society of the Pacific Conference Series*, page 3.

Smith, P. S., Montiel, E., Rightley, S., Turner, J., Schmidt, G. D., and Jannuzi, B. T. (2009). Coordinated Fermi/Optical Monitoring of Blazars and the Great 2009 September Gamma-ray Flare of 3C 454.3. *arXiv e-prints*, page arXiv:0912.3621.

Sokolov, A. and Marscher, A. P. (2005). External Compton Radiation from Rapid Nonthermal Flares in Blazars. *ApJ*, 629:52–60.

Sokolov, A., Marscher, A. P., and McHardy, I. M. (2004). Synchrotron Self-Compton Model for Rapid Nonthermal Flares in Blazars with Frequency-dependent Time Lags. *ApJ*, 613:725–746.

Soldi, S., Türler, M., Paltani, S., Aller, H. D., and Aller, M. F. a. (2008). The multiwavelength variability of 3C 273. *A&A*, 486:411–425.

Spencer, R. E., McDowell, J. C., Charlesworth, M., Fanti, C., Parma, P., and Peacock, J. A. (1989). MERLIN and VLA observations of compact steep-spectrum radio sources. *MNRAS*, 240:657–687.

Stanghellini, C., O'Dea, C. P., Dallacasa, D., Baum, S. A., Fanti, R., and Fanti, C. (1998). A complete sample of GHz-peaked-spectrum radio sources and its radio properties. *A&AS*, 131:303–315.

Tavecchio, F., Ghisellini, G., Bonnoli, G., and Ghirlanda, G. (2010). Constraining the location of the emitting region in Fermi blazars through rapid γ-ray variability. *MNRAS*, 405:L94–L98.

The Fermi-LAT collaboration (2019). The Fourth Catalog of Active Galactic Nuclei Detected by the Fermi Large Area Telescope. *arXiv e-prints*, page arXiv:1905.10771.

Thompson, D. J., Bertsch, D. L., Dingus, B. L., and Esposito, J. A. (1995). The Second EGRET Catalog of High-Energy Gamma-Ray Sources. *ApJS*, 101:259.

Thompson, D. J., Bertsch, D. L., Fichtel, C. E., Hartman, R. C., Hofstadter, R., Hughes, E. B., Hunter, S. D., Hughlock, B. W., Kanbach, G., Kniffen, D. A., Lin, Y. C., Mattox, J. R., Mayer-Hasselwander, H. A., von Montigny, C., Nolan, P. L., Nel, H. I., Pinkau, K., Rothermel, H., Schneid, E. J., Sommer, M., Sreekumar, P., Tieger, D., and Walker, A. H. (1993). Calibration of the Energetic Gamma-Ray Experiment Telescope (EGRET) for the Compton Gamma-Ray Observatory. *ApJS*, 86:629.

Thompson, D. J., Djorgovski, S., and de Carvalho, R. (1990). Spectroscopy of radio sources from the Parkes 2700 MHz survey. *PASP*, 102:1235–1240.

Ulrich, M.-H., Maraschi, L., and Urry, C. M. (1997). Variability of active galactic nuclei. *Annual Review of Astronomy and Astrophysics*, 35(1):445–502.

Urry, C. M. and Padovani, P. (1995). Unified Schemes for Radio-Loud Active Galactic Nuclei. *PASP*, 107:803.

Valtaoja, E., Terasranta, H., Urpo, S., Nesterov, N. S., Lainela, M., and Valtonen, M. (1992). Five Years Monitoring of Extragalactic Radio Sources - Part Three - Generalized Shock Models and the Dependence of Variability on Frequency. *A&A*, 254:71.

Vaughan, S., Edelson, R., Warwick, R. S., and Uttley, P. (2003). On characterizing the variability properties of X-ray light curves from active galaxies. *MNRAS*, 345:1271–1284.

Vercellone, S., Chen, A. W., Vittorini, V., Giuliani, A., and D'Ammando, F. (2009). Multiwavelength Observations of 3C 454.3. I. The AGILE 2007 November campaign on the "Crazy Diamond". *ApJ*, 690:1018–1030.

Vercellone, S., D'Ammando, F., Vittorini, V., and Donnarumma, I. (2010). Multiwavelength Observations of 3C 454.3. III. Eighteen Months of Agile Monitoring of the "Crazy Diamond". *ApJ*, 712:405–420.

Vittorini, V., Tavani, M., and Cavaliere, A. (2017). Meeting the Challenge from Bright and Fast Gamma-Ray Flares of 3C 279. *ApJL*, 843(2):L23.

Wagner, S. J. and Witzel, A. (1995). Intraday variability in quasars and bl lac objects. *Annual Review of Astronomy and Astrophysics*, 33(1):163–197.

Wagner, S. J., Witzel, A., Heidt, J., Krichbaum, T. P., Qian, S. J., Quirrenbach, A., Wegner, R., Aller, H., Aller, M., Anton, K., Appenzeller, I., Eckart, A., Kraus, A., Naundorf, C., Kneer, R., Steffen, W., and Zensus, J. A. (1996). Rapid Variability in S5 0716+714 Across the Electromagnetic Spectrum. *AJ*, 111:2187.

Weaver, Z. R., Balonek, T. J., Jorstad, S. G., Marscher, A. P., Larionov, V. M., Smith, P. S., Boni, S. J., Borman, G. A., Chapman, K. J., Jenks, L. G., Kopatskaya, E. N., Larionova, E. G., Morozova, D. A., Nikiforova, A. A., Sabyr, A., Savchenko, S. S., Stahlin, R. W., Troitskaya, Y. V., Troitsky, I. S., and Zhang, S. (2019). The 2016 June Optical and Gamma-Ray Outburst and Optical Microvariability of the Blazar 3C 454.3. *ApJ*, 875:15.

Woo, J.-H. and Urry, C. M. (2002). Active Galactic Nucleus Black Hole Masses and Bolometric Luminosities. *ApJ*, 579(2):530–544.

Wu, L., Wu, Q., Yan, D., Chen, L., and Fan, X. (2018). Constraints on the Location of γ-Ray Sample of Blazars with Radio Core-shift Measurements. *ApJ*, 852:45.

Yan, D., Zhang, L., and Zhang, S.-N. (2015). Parameter constraints in a near-equipartition model with multifrequency NuSTAR, Swift, and Fermi-LAT data from 3C 279. *MNRAS*, 454:1310–1319.

Zacharias, M., Böttcher, M., Chakraborty, N., Cologna, G., Jankowsky, F., Lenain, J. P., Mohamed, M., Prokoph, H., Wagner, S., Wierzcholska, A., Zaborov, D., and H. E. S. S. Collaboration (2017a). The complex VHE and multiwavelength flaring activity of the FSRQ PKS 1510-089 in May 2015. In *6th International Symposium on High Energy Gamma-Ray Astronomy*, volume 1792 of *American Institute of Physics Conference Series*, page 050023.

Zacharias, M., Böttcher, M., Jankowsky, F., Lenain, J.-P., Wagner, S. J., and Wierzcholska, A. (2017b). Cloud Ablation by a Relativistic Jet and the Extended Flare in CTA 102 in 2016 and 2017. *ApJ*, 851:72.

Zamaninasab, M., Clausen-Brown, E., Savolainen, T., and Tchekhovskoy, A. (2014). Dynamically important magnetic fields near accreting supermassive black holes. *Nature*, 510:126–128.

Zhang, L. Z., Fan, J.-H., and Cheng, K.-S. (2002). The Multiwavelength Doppler Factors for a Sample of Gamma-Ray Loud Blazars. *PASJ*, 54:159–169.

Zhang, Y. H., Celotti, A., Treves, A., Chiappetti, L., Ghisellini, G., Maraschi, L., Pian, E., Tagliaferri, G., Tavecchio, F., and Urry, C. M. (1999). Rapid X-Ray Variability of the BL Lacertae Object PKS 2155-304. *ApJ*, 527(2):719–732.